Winter 2010

Solution Approximation for Atmospheric Flight Dynamics Using Volterra Theory

Ashraf Mohammed Kandeel Omran
Old Dominion University

SOLUTION APPROXIMATION FOR ATMOSPHERIC FLIGHT DYNAMICS USING VOLTERRA THEORY

by

Ashraf Mohammed Kandeel Omran
B.Sc. June 2002, Cairo University, Egypt
M.Sc. March 2006, Cairo University, Egypt

A Dissertation Submitted to the Faculty of
Old Dominion University in Partial Fulfillment of the
Requirement for the Degree of

DOCTOR OF PHILOSOPHY

AEROSPACE ENGINEERING

OLD DOMINION UNIVERSITY
December 2010

Approved by:

Brett Newman

Thomas Alberts

Colin Britcher

Zhao Sun

ABSTRACT

SOLUTION APPROXIMATION FOR ATMOSPHERIC FLIGHT DYNAMICS USING VOLTERRA THEORY

Ashraf Mohammed Kandeel Omran
Old Dominion University, December 2010
Director: Prof. Brett Newman

This dissertation introduces a set of novel approaches in order to facilitate and enrich Volterra theory as a nonlinear approximation technique for constructing mathematical solutions from the governing relationships describing aircraft dynamic behavior. These approaches reconnect Volterra theory and flight mechanics research, which has not been addressed in the technical literature for over twenty years. Volterra theory is known to be viable in modeling weak nonlinearities, but is not particularly well suited for directly describing high performance aircraft dynamics. In order to overcome these obstacles and restrictions of Volterra theory, the global Piecewise Volterra Approach has been developed. This new approach decomposes a strong nonlinearity into weaker components in several sub-regions, which individually only require a low order truncated series. A novel Cause-and-Effect Analysis of these low order truncated series has also been developed. This new technique in turn allows system prediction before employing computer simulation, as well as decomposition of existing simulation results. For a computationally complex and large envelope airframe system, a Volterra Parameter-Varying Model Approach has also been developed as a systematically efficient approach to track the aircraft dynamic model and its response across a wide range of operating conditions. The analytical and numerical solutions based on the proposed methodology show the ability of Volterra theory to help predict, understand, and analyze

nonlinear aircraft behavior beyond that attainable by linear theory, or more difficult to extract from nonlinear simulation, which in turn leads to a more efficient nonlinear preliminary design tool.

This dissertation is dedicated to my mother, Amina El Syaed.

ACKNOWLEDGMENTS

I would like to express my sincere thanks to my advisor Prof. Brett Newman, for how much he has constantly challenged me to make this dissertation up to the highest quality. There is a famous book of short-stories by Dave Eggers entitled "How We Are Hungry". The first story is about two guys challenging each other to ride horses on a very hot summer day. In my case, my horse was this dissertation and the hot summer day is that this is the very first dissertation on this particular subject. In Prof. Newman's case, he is the guy who challenges my creativity and innovation.

I extend many thanks to my committee for their patience and many hours spent editing this dissertation. Also, I would like to thank Prof. Terry Herdman, at Viriginia Tech for sharing his work with me, since Prof. Herdman was the first to investigate this research.

I would also like to offer special thanks to some people who have really affected my academic career: Dr. Ayman Kassem and Prof. Thomas Alberts. Dr. Kassem was my inspiration to pursue control and dynamics research. He still impresses me with his novel ideas and creativity. I consider Prof. Thomas Alberts to be my secondary advisor. I have gained a lot of valuable experience from working with him.

I also have a wonderfully supportive family. I am very thankful to them. My deepest thanks go to my mother, who has inspired me throughout my life. She is always supportive and she believes in me more than I believe in myself.

TABLE OF CONTENTS

LIST OF TABLES

LIST OF FIGURES

NOMENCLATURE

English and Greek Symbols

A	Input Amplitude, State transition matrix
B	Input Amplitude, Input distribution matrix
C	Output distribution matrix
D	Direct input-output matrix
E	Generic function
F	Generic function
G	Generic function
H	Altitude
M	Mach number
S	Reference area, Strength function
T	Total instantaneous engine thrust
V	Aircraft total velocity
a	Time constant
b	Wing span
e	Generic function
f	Generic function
g	Acceleration due to gravity, Generic function
h	Volterra kernel
i	Index
j	Index
k	Index
m	Airplane mass
p	Airplane roll rate
q	Airplane pitch rate

r	Airplane yaw rate
t	Time
τ	Time
u	Velocity component in X body axis, Input signal
v	Velocity component in Y body axis
w	Velocity component in Z body axis
x	State signal
y	Output signal
C_D	Total drag force coefficient
C_L	Total lift force coefficient
C_{L_T}	Total rolling moment coefficient
C_{L_p}	Roll rate roll moment coefficient
C_{L_r}	Yaw rate roll moment coefficient
$C_{L_{\delta a}}$	Aileron roll moment coefficient
$C_{L_{\delta r}}$	Rudder roll moment coefficient
C_{M_T}	Total pitching moment coefficient
C_M	Mean pitch moment coefficient
C_{M_q}	Pitch rate pitch moment coefficient
C_{N_T}	Total yawing moment coefficient
C_N	Mean yaw moment coefficient
C_{N_p}	Roll rate yaw moment coefficient
C_{N_r}	Yaw rate yaw moment coefficient
$C_{N_{\delta a}}$	Aileron yaw moment coefficient
$C_{N_{\delta r}}$	Rudder yaw moment coefficient
C_{X_T}	Total X axis force coefficient
C_X	Mean X axis force coefficient
C_{X_q}	Pitch rate X axis force coefficient

C_{Y_T}	Total Y axis force coefficient
C_{Y_p}	Roll rate Y axis force coefficient
C_{Y_r}	Yaw rate Y axis force coefficient
C_{Z_T}	Total Z axis force coefficient
C_Z	Mean Z axis force coefficient, Plunge force coefficient
C_{Z_q}	Pitch rate Z axis force coefficient
$C_{m\alpha}$	Pitch moment coefficient with angle of attack
$C_{m\delta e}$	Pitch moment coefficient with elevator deflection
H_e	Engine angular momentum
I_X	Moment of inertia about X body axis
I_Y	Moment of inertia about Y body axis
I_Z	Moment of inertia about Z body axis
I_{XZ}	Product of inertia with respect to X and Z body axes
α	Angle of attack
β	Sideslip angle
φ	Roll angle
θ	Pitch angle
ψ	Yaw angle
ζ	Damping ratio
δ_a	Aileron control surface deflection
δ_e	Elevator control surface deflection
δ_r	Rudder control surface deflection
δ_{th}	Throttle deflection
σ	Damping factor
ω_n	Undamped natural frequency
ω_d	Damped natural frequency
$\bar{c}$	Wing mean aerodynamic cord

$\bar{q}$	Dynamic pressure
$\bar{x}_{cg}$	Actual center of gravity location
$\bar{x}_{cg_r}$	Reference center of gravity location for aerodynamic data

CHAPTER 1

INTRODUCTION

1.1 Problem Motivation and Description

Constructing mathematical solutions from the governing relationships describing aircraft dynamic behavior is required for analysis, understanding, and synthesis. In the analytic sense, mathematical aircraft dynamic models are typically unsolvable for several reasons. First, the aircraft dynamic model is of high order, which is described by many coupled states, hundreds or thousands, due to actuator and sensor dynamics, airframe flexibility, unsteady aerodynamics, and other sub-system dynamics such as the engine and atmosphere. Second, many nonlinear components and their mathematical expressions appear in the aircraft equations of motion, for example, inertial coupling, gravity projections, rotating frame effects, kinematic relationships, and actuator saturation. Third, for most aircraft the aerodynamic and propulsive coefficients are presented in the form of look-up tables, sophisticated mathematical expressions, or high order polynomials. These factors make it extremely difficult to find analytic solution.

Nonlinear numeric simulation provides the most accurate solution procedure for the aircraft models. In a strict sense, nonlinear simulation results provide an approximate solution, especially when compared with experimentally derived responses from the physical system, which might be approximate as well due to test error. However, with careful treatment, results of the nonlinear simulation can be brought extremely close to exact solutions in cases where this information is derivable, and is assumed to be possible in cases where this information is not derivable. The residual solution errors can be reduced to a sufficiently small level where the accuracy of the model being solved becomes the critical issue, not the solution accuracy. Unfortunately, results based on nonlinear simulation have no underlying analytical structure. Tracing the aircraft motion

behavior characteristics back to their parametric origins based on specific numeric propagation is virtually impossible. Herein, nonlinear simulation is treated as the benchmark for evaluating the accuracy of other available solutions in the absence of experimental or exact results.

To circumvent these difficulties, many approximation techniques have been applied to solve the aircraft's dynamic equations of motion. Two main approximation methodologies exist: the model simplification approach and the solution simplification approach. In the model simplification approach, some techniques use assumptions coming from physical, experimental, or computational observations. For example, rigid body, non-rotating flat earth, and simple engine model assumptions are quite reasonable for many aircraft models. Other model simplification techniques consider the low order approximations such as longitudinal and lateral motions. This type of simplification is commonly referred as model order reduction. However, after applying these model simplification techniques, there remains a need to solve the resultant simplified models, since the aircraft's nonlinearities are still embedded in such models.

Linearization, as a model simplification technique, reshapes the aircraft equations of motion in the form of an inexpensive relational solvable model. Many time and frequency domain analyses using solution descriptions based on eigenvalue-eigenvector sets and transfer matrices (poles and zeros) have been proposed to characterize the linear model. These characterization tools have been and are still broadly used in flight mechanics for design and control. Unfortunately, the linear model validity is restricted to small variations from the equilibrium condition. Even using interpolation concepts to build a global linear parameter-varying model does not help in rendering some nonlinear phenomena, which have been observed in many classes of aircraft.

After realizing the linearization technique is inadequate to render phenomena such as wing rock, spin entry, and pilot-induced oscillation, the flight mechanics community has started to apply nonlinear solution simplification techniques. Bifurcation, describing

function, and perturbation expansion are common nonlinear solution simplification techniques for analyzing the onset behavior of aircraft to these phenomena. Although these techniques show potential for understanding and analyzing nonlinear behavior of aircraft, these techniques sometimes do not provide a precise cause-and-effect analysis. In fact, none of these techniques has the capability to construct a general conclusion for the nonlinearity consequences. This limitation is because of the assumptive, iterative, and computational details in developing a solution based on these techniques, which restrict any general development to nonlinear systems.

Volterra theory has emerged as a popular nonlinear solution simplification technique, primarily because of its extension of the impulse response concept from linear theory. In addition, Volterra theory has more analytical structure than other solution simplification techniques because of the so-called Volterra kernels. These kernels are unique signatures for the system, carrying the effect from the system parameters, and rendering the system behavior for any arbitrary input. These kernel features are not available in the other nonlinear solution simplification techniques. Volterra theory has had few applications to flight mechanics in the literature. The last efforts applying Volterra theory to flight mechanics date back to 1991. All these efforts have been abandoned because of computational difficulties in applying Volterra theory to strong nonlinearities in flight dynamic systems across the flight envelope. These observations underscore the need for new approaches that facilitate Volterra theory to be better suited for aircraft models.

This dissertation investigates solution approximation methodologies for atmospheric flight dynamics using Volterra theory. The aims of the dissertation are to develop such approaches for: 1) relaxing the computational and mathematical difficulties that have been faced by the previous attempts, 2) merging Volterra theory with model simplification concepts for constructing foundations that can qualify and predict the low

order flight dynamic motions, and 3) developing an overall Volterra model, which has the capability to render the aircraft movement across a wide array of operating conditions.

1.2 Literature Review

Approximation techniques including model simplification and solution simplification have been applied for many modeled and un-modeled physical systems to deliver a mathematical base through which the system behavior can be better understood. The literature has been filled by such techniques, for example, References 1-3 cite over 330 technical papers on model reduction alone as a model simplification technique. In this dissertation, the literature review will focus on approximation techniques applied to aircraft dynamics such as linear theory, bifurcation, describing function, and perturbation theory compared with Volterra theory, thus demonstrating why Volterra theory is much more promising than these techniques.

1.2.1 Classical Flight Dynamics Analysis

Mathematical modeling and solution of aircraft dynamic behavior for analysis, understanding, and synthesis requires an efficient and accurate technique, especially when the aircraft moves from one flight regime to another. This process is compounded by system nonlinearities, including but not limited to aerodynamic derivatives, inertial coupling, and actuation limits, all leading to significant changes in dynamic characteristics across the flight envelope. Therefore, universal approaches to explore and evaluate dynamic behavior over all flight regimes are sought.

One standard approach is based on the differential equation model and its nonlinear simulation. In this differential equation model, first principles of mechanics with a set of assumptions are used to describe the aircraft dynamic behavior in the form of differentiable and algebraic relationships. The differentiable relation formulates the state derivative vector as a nonlinear function of the state and input vectors. The algebraic

relation formulates the output vector as a nonlinear function of state and input vectors. These equations comprise the so-called "nonlinear state space" model. The nonlinear simulation based on this model provides an accurate and specific solution for overall motion.[4,5] However, the results based on the nonlinear simulation are relatively more computation costly and less structured analytically.

Linear analysis, on the other hand, provides inexpensive relational models and solutions, which are relatively less precise but much broader. Linearization theory starts by using Taylor series expansion for the differentiable and algebraic relationships with respect to the state and input vectors. By retaining only the first derivatives with respect to the state and input vector, the equations of motion are then approximated by the so-called "linear state space" model. This model has four matrices: state transition matrix, input distribution matrix, output distribution matrix, and direct input-output matrix. These matrices are constant for a given expansion point, but vary across the flight envelope. Many methods have been proposed to characterize and understand the aircraft dynamic motion based on this linear model in terms of eigenvalues, eigenvectors, transfer polynomial coefficients, and transfer polynomial roots. More details about the procedure of applying linear theory to the aircraft equations of motion have been reported in many scholarly books such as References 6 and 7.

Applying the linear theory in flight mechanics research has been studied more extensively than any other approximation technique. For characterizing aircraft dynamic behavior through linear theory, a basic technique is to relate the open- and closed-loop transfer function poles and zeros to fundamental parameters such as stability and control derivatives, thereby exposing insight to the dynamic mechanisms of the response. This approach is widely used in aircraft dynamics, such as the short period or dutch-roll approximations, which rely on a quadratic or second order model.[6-9] More advanced work for characterizing the aircraft open-loop and closed-loop behavior based on fourth order linear models have been listed in References 10-19 using the so-called "Literal Factors"

or "Symbolic Factoring" technique. Flying qualities, the acceptability of the airplane motion under manual control by the human pilot, have been widely qualified through linear models by defining acceptable ranges for various model parameters or transient responses.[20,21] For high order aircraft systems, the concept of equivalent flying quality metrics based on linear models has been considered.[22,23] Flying quality concept using linear modeling for elastic vehicles has also been proposed.[24]

Linear theory has been employed to understand some specific flight phenomena. In References 25 and 26, eigenvector analysis has been employed to reduce the three degrees of freedom spin motion model to two sub-models: a two degrees of freedom pitch-roll motion and one degree of freedom yaw motion. Routh-Hurwitz criterion has been applied to these reduced order sub-models. The results of such analysis have concluded that 1) for pitch-roll motion, the frequency term of the motion is controlled by the gyroscopic and rotary derivatives; whereas the damping term of the motion is controlled by the oscillatory derivatives, and 2) for yaw motion, a higher oscillatory derivative improves the stability of the motion. In Reference 27, linear sensitivity analysis has been used to understand the mechanism of stall recovery through the variation of both eigenvalues and eigenvectors with the flight condition (airspeed, altitude, etc.). Such analysis has concluded that 1) the airspeed has more influence on the short period mode than the phugoid mode, and 2) the center of gravity position drives the system to instability through the short period mode.

Model reduction based on linear theory for flight mechanics applications has been widely investigated. Many modern linear control synthesis techniques produce a controller with dynamic order at least equal to the plant dynamic order, which is undesirable for implementation. Thus, differing viewpoints exist for what to reduce, the original high order vehicle model or the resulting high order controller model. In addition to this, many strategies for order reduction exist. For example, in Reference 28, μ-synthesis has been used to reduce the order for the flexible B-52 bomber model.

Reference 29 has used a combined frequency-weighted internally balanced truncation-residualization procedure to obtain higher accuracy reduced order models intended for flight control design applications. Reference 30 considered using H_2 and H_∞ norms applied individual flexible mode transfer functions to identify their contribution to the overall transfer function of a flexible aircraft model for the purpose of order reduction. A full detailed survey about related research has been listed in Reference 31.

Many techniques have been proposed in the literature to design flight control systems based on the linear model. Reference 32 has provided an extensive survey for this topic up to 1969. Even after this date, the flight mechanics community is still heavily dependent on using linear theory. For example, in Reference 33, eigenstructure assignment based on linear theory has been used to design flight control systems for the L-1011 aircraft model using eigenvalue criteria and a gradient search to increase the damping. Reference 34 has proposed designing compensators of specified structure for shaping the closed-loop step response that uses linear quadratic output-feedback techniques with a glide slope coupler as an example. Reference 35 has applied the partial eignenstructure assignment approach via static output feedback to design a robust flight control system for a lateral stability augmentation system (SAS). In Reference 36, a flight control system has been developed for a XV-15 representation based on model inversion using the linear theory.

Linear theory has demonstrated the capability to be: 1) a characterization tool for aircraft behavior and performance,[8-24] 2) an understanding tool for the underlying mechanism of some flight phenomena,[25-27] 3) a model reduction tool for aircraft models,[28-31] and 4) a design tool for flight control systems.[32-36] Although these tools have proved that linear theory gives intuition about system behavior more than the nonlinear simulation, linear theory has failed to render phenomena such as pitch-up, stall, elevator or rudder control surface blockage, wing rock, roll-yaw spin inertial coupling, nose slice, falling leaf, and pilot-induced oscillation. These phenomena have been observed

following the onset of unusual attitudes and extreme maneuvers for many aircraft such as the F-14, F-15, and F-18. This lack of fidelity in the linear theory has pushed the flight mechanics research community to use more advanced nonlinear solution simplification techniques such as bifurcation and describing function, which are discussed next.

Bifurcation analysis starts first by computing the variation of equilibrium points with some parameters such as input signals, center of gravity, or aircraft mass. Then, the bifurcation diagram is constructed showing the dependency of these equilibrium points on the varying parameters. The point on this diagram, where the stability type changes, is called a bifurcation point. In the case of a high order system, the procedure is called "continuation". Full details about the bifurcation technique are given in References 37 and 38. The bifurcation diagram leads to many conclusions about the global behavior of the system, various characteristics like jump phenomenon, onsite of limit cycles, and chaotic behavior.

Bifurcation has been recognized as one the best methods to study nonlinear aircraft dynamics in a global sense. The earliest work applying bifurcation to study aircraft behavior has been reported in Reference 39 for the variable sweep F-14 fighter and a fixed swept-wing F-4 fighter. The outcomes of this work proved the bifurcation method's capability to understand some onset phenomena at high angle of attack such as wing rock, spin entry, and stall. In Reference 40, bifurcation and continuation methods have been applied to an F-15 fighter aircraft. This work has studied the influence of control augmentation on nonlinear motion and stability. The equilibrium and limit cycle solutions' variation with control surface deflections of the F-15 has been visualized. Based on such a visualization, it has been concluded that not only do the controls suppress wing rock, but also increase the divergence tendency and may lead to departure and spin. The effect of the center of gravity offset and engine dynamics on the spin entry and recovery has been investigated in Reference 41 for the Alpha Jet fighter using the bifurcation method. In Reference 42, the prediction for the onset of wing rock, spiral

divergence, and jump phenomena that cause the F-14 to enter a spin has been investigated by bifurcations. Based on this investigation, a simple feedback control system has been designed to eliminate the wing rock and spiral divergence instabilities. Besides the wing rock and spin entry phenomena, bifurcation has been also applied to study the pilot induced oscillation in Reference 43. Reference 44 represents many details about applying bifurcation methods to understand and expose the aircraft dynamic behavior during onset to various phenomena. Recently, the bifurcation method has been used to design flight control systems in References 45-47.

Describing function analysis has been mostly used to generate limit cycle behavior in many flight models as reported in References 48-50. In Reference 48, the classical sinusoidal describing function analysis has been used to accurately duplicate and predict the observed oscillatory characteristic due to the presence of Coulomb friction in a nozzle pivot mechanism. In References 49-50, the describing function technique has been employed to understand the effects of rate saturation on flight control systems undergoing pilot-induced oscillations. Because perturbation expansion analysis breaks down quickly in time or in parameter strength, the technique has been rarely applied in flight mechanics research. One example is given in Reference 51. Other techniques such as multiple time scales analysis as an extension of perturbation analysis in Reference 52 have also been used to describe the nonlinear dynamic behavior of aircraft, or to design and analyze flight trajectories as in Reference 53.

Although bifurcation, describing function, and perturbation analysis as nonlinear solution simplification techniques have shown a potential for understanding and analyzing nonlinear behavior of aircraft, these methods sometimes do not provide a precise cause-and-effect result, do not address transient behavior, or do not cover a sufficient range of time and/or parameter variation. In fact, none of these techniques has the capability to construct a general conclusion for the nonlinear consequences because of assumptive, iterative, and computational details, which restrict any general symbolic

development to nonlinear systems. In conclusion, there is a need for a more structural nonlinear approximation method, which has the same capability as the linear theory. Volterra theory is often considered as an extension of the impulse response concept from linear theory and possesses the desired analytic structure for characterization, and is thus reviewed in the next section.

1.2.2 Volterra Theory Background

Volterra theory is a nonlinear mathematical approximation for describing the input-output relationship of dynamic systems. Volterra theory is named in the honor of the Italian mathematician Vito Volterra, who develop the theory in 1887, with the first encompassing publication appearing in 1927 and later reprinted in 1959.[54] An early use of this theory has been reported in a series of technical reports at the Massachusetts Institute of Technology by Wiener[55] to study the response to Gaussian white noise of a series RLC circuit with nonlinear resistor. The work of Wiener was followed by Brilliant[56] and George[57] to apply the theory for communication problems. These reports have moved Volterra theory from the theoretical side to the practical-usage side. The outcomes of these reports have attracted the attention of other research communities to apply Volterra theory in different disciplines, one of them being aeronautical engineering.

The theory represents the input-output relationship as an infinite series of homogeneous linear and nonlinear sub-systems as an extension of Taylor's power series.[58] A system is called a degree-n homogeneous system, if an input $\alpha u(t)$ is applied to the system and the output is then $\alpha^n y(t)$, where $y(t)$ is the equivalent response for the input $u(t)$. The first term of the Volterra series is a degree-1 homogeneous sub-system, in which the change in output amplitude is proportional to the input amplitude. The second term is a degree-2 homogeneous sub-system, in which the change in output amplitude is proportional to the square of the input amplitude and so on. Each degree-n homogeneous sub-system is represented by an n dimensional convolution integral, while the input

signal is dynamically weighted by the so-called n^{th} order kernel. The n^{th} order kernel is an n-dimensional function in time or complex frequency, depending on the domain of interest. Each kernel appearing in the convolution integrals reflects a specific system behavior.

In general, kernels are of two classes: the state-dependent class and the state-input-dependent class. The only member of the state-dependent class is the zero order kernel, which represents the response of the output due to the initial system state. If the system motion is started at an equilibrium condition (both state and input values) and the equilibrium input is maintained, the zero order kernel equals zero. On the other hand, if the state value is mismatched to the equilibrium input, or vice versa, the zero order kernel is nonzero and can be interpreted as motion of the system from the initial state to the equilibrium state (stable), or the state reacting to the input. Sometimes the response of the zero order kernel can be a sustained oscillation representing a limit cycle, or possess a divergent behavior for an unstable equilibrium. The state-input-dependent class contains all other Volterra kernels starting with the first kernel. Those kernels represent the behavior of the system to any arbitrary input. In this class, each Volterra kernel is represented with the input in a multidimensional convolution integration. Both the state- and state-input-dependent class kernels are unique for a given system. For weak nonlinearities, all higher order kernels are seen to quickly tend to negligible values in the system representation. For a completely linear system, only the zero and first order kernels remain. The uniqueness of the Volterra kernels makes Volterra theory more promising than other nonlinear approximation techniques.[58,59]

Since the kernels are the backbone of Volterra theory, identifying these kernels has been the main concern of all research communities. Two categories have appeared in the literature to identify the kernel. The first identification category uses the observed input and output signals either in the time or frequency domain to estimate the kernels. The second identification category directly computes the kernel from the differential

equations. The first category is more suited for physically un-modeled dynamic systems such as biomedical, biological, and neuron systems.[60,61] For such identification, a discrete form of Volterra series is frequently used. Alper[62] proposed the first work to apply Volterra series in a discrete fashion. Alper's work has received an obvious acknowledgement to identify the kernels. In his method, the system is treated as a black or gray box. As the input starts to excite the system, the input and output signals are recorded, and based on the least square estimation (LSE) or other regression techniques, Volterra kernels are defined. LSE can be cast as a recursive algorithm[60,63] or a non-recursive algorithm.[64-66] Another method to estimate Volterra kernels from the system identification point of view has been provided by the use of sinusoidal or impulsive inputs.[67] The strategy is an extension from the use of impulsive and sinusoidal inputs to identify linear systems. This identification category captures only the input-output behavior of a system and disregards any internal structure.

For computing the Volterra kernels from the nonlinear differential equations, some analytical forms such as Lie derivatives, growing exponential method, Carleman linearization method, and variational expansion method have been developed. The idea of using Lie derivatives to compute Volterra kernel from the differential equation has been introduced in Reference 68. The Lie derivatives approach has been used to compute kernels analytically for biologically inspired motion detection through vision processing in Reference 61. The Lie derivative approach lacks tractability since the process constructs the kernels as a series. Each term in this series is defined as a function of Lie derivatives. Finding a closed-form expression for such a series is not always practical. Furthermore, divergence of these derivative expressions may restrict their utilization when approximated by a truncated series.

The growing exponential method provides the kernels by an n-dimensional Laplace transform. In this method, the input is assumed a finite sum of excitation in the form of exponents with different frequencies or eigenvalues and the same assumption is

set for the output. Equating each individual exponent term in the differential equation leads to a set of equations in terms of kernels. Solving this set of equations brings expressions for the kernels. The idea of the growing exponential method is an extension to the one-dimensional Laplace transform. More details of the algorithm are given in References 58 and 69. The use of the multivariable Laplace transform in system theory and interconnection rules was first introduced in Reference 57. The idea is developed through other research efforts in References 70 and 71. A number of methods for computing kernels or transfer functions corresponding to given differential equations have been proposed in References 72-74. The method has been applied to characterize some dynamic systems as listed in References 75 and 76. The growing exponential method often delivers the kernels in unwieldy forms, which restricts the applicability for nonlinear characterization.

The idea of using resubstitution or Picard iterations was the baseline to develop closed-form expressions of the kernels for a bilinear state vector equation.[77] Using Carleman linearization to obtain a bilinear state vector equation has been employed to develop approximate closed-form kernels for any nonlinear system. The Carleman linearization technique is discussed in Reference 78. In Reference 79, the Kronecker product has been used to enrich the Carleman linearization idea for developing analytical Volterra kernels. Carleman linearization or bilinearization for Volterra theory has been used in References 80 and 81. Although the method is mathematically simple and has the ability to deliver a general analytical solution for the kernels, the method lacks an ability to render certain highly nonlinear features such as a limit cycle because of the essential modeling assumptions of the method.

The variational expansion method was initially developed based on a perturbation point of view. The method starts by assuming the differential vector as a polynomial in terms of states and input. A state-equation description is then obtained for each degree-n homogeneous sub-system in a state space representation. It turns out that, although the

equation for the degree-k sub-system is coupled nonlinearly to the equations for the lower degree sub-systems, each of the equations has identical first order (linear) terms.[58] Although this expansion extends the n-dimensional problem to infinite dimension, the original nonlinearity of the system is broken into a sequence of pseudo-linear time invariant (PLTI) systems, which are solvable. The input of each PLTI system is a nonlinear function of all previous system states and the input. The first notable application for the variational expansion approach to show the capability of the method in approximating nonlinear differential systems was discussed in Reference 82. The method has also been employed in several flight mechanics studies, which highlight the capability of the method to capture nonlinearities imbedded in flight systems.[83-84] However, the method has not been employed to any significant extent for analytical purposes.

The first work, which applied Volterra series in the aeronautical field, was probably by Herdman.[85] Later on, the application of Volterra theory in aeronautical engineering has spread to several aeronautical disciplines. One of the remarkable pioneers in brining Volterra theory to aerospace engineering is Walter Silva, who has provided many research reports in this topic. Reference 86 is Silva's first work in applying Volterra series for aeroservoelastic analyses. In his Ph.D. dissertation,[87] Volterra series have been applied for many nonlinear aerodynamics examples using discrete Volterra models. Other research in the same area has been reported by Silva applying Volterra series as a model reduction technique to unsteady transonic aerodynamics[88] and to unsteady fluid-structure systems. [89,90]

For the aeroelasticity area, Silva and others have applied Volterra series through different algorithms for identification and characterization. In Reference 91, a discussion for identifying a nonlinear aeroelastic system based on Volterra theory is presented in the time domain for a wind-tunnel semi-span model using positive and negative step inputs in pitch. Reference 92 has introduced a Volterra kernel extrapolation technique to predict

the variation of kernels with flight conditions. The algorithm starts by identifying various kernels from input-output data at a specific number of flight conditions using a multi-wavelet based algorithm. A polynomial curve-fit extrapolation, for each kernel's parameters with flight condition, is then used to predict the Volterra kernels at a new flight condition. Volterra kernel extrapolation has been successfully applied to flight data from the F/A-18 Active Aeroelastic Wing. The research efforts in Reference 92 have demonstrated that the kernel can be characterized with the flight conditions. This idea will be extended in this dissertation as shown later.

In Reference 93, Volterra series have been used to predict aeroelastic instabilities with uncertainty analysis investigating the robustness of Volterra models. An interesting algorithm has been developed in Reference 94 to estimate the unmodeled nonlinearities in the aeroelastic dynamic system. The difference between the predicted linear behavior and the actual nonlinear behavior is employed to estimate the high order kernels. The algorithm has been successfully applied to a nonlinear pitch-plunge system. In References 95-96, a method to identify fluid basis functions with proper orthogonal decomposition using Volterra system realization is applied for two-dimensional inviscid flow over a bump with forcing. However, the listed work in References 91-96 has only applied the Volterra concept with numerical-based algorithms, which lack any analytical structure for understanding the influence of system parameters in Volterra kernels and system behavior.

Unlike most of the published numerical-based work in applying Volterra theory for aeronautical engineering, a few reports have recently appeared with an analytical-based fashion developing Volterra kernels from the system nonlinear differential equations. In Reference 97, a growing exponential method has been used to analytically compute the first three kernels of the two-dimensional lifting surface in an incompressible flow field. The analytical kernels were then used to analyze and determine the subcritical aeroelastic response and flutter instability with the influence of

geometric nonlinearities. This work has been extended in Reference 98 to the study of open- and closed-loop subcritical aeroelastic response and flutter prediction of simple nonlinear two-dimensional airfoils in an incompressible flow. More work for analytical kernels with aeronautic applications has been recently documented in Reference 99. However, most of these efforts have been applied to specific systems without any general parametric study, which enables one to achieve a more general conclusion. In contrast, this dissertation provides methodology for the generalized approach.

1.2.3 Current Research Focus

A few applications for Volterra methodology to flight mechanics appear in the literature. In 1983, Herdman documented the first work of using Volterra theory in flight dynamics in Reference 85. This work is also the first application for Volterra theory in aeronautical engineering as mentioned in Reference 99. The work was done under the motivation of the Flight Dynamics Laboratory, Air Force Wright Aeronautical Laboratories in Ohio for developing new nonlinear flight qualities metrics. The work aimed to set some mathematical bases for Volterra theory that can be used as a foundation in developing the nonlinear flight qualities. The work developed a six degree of freedom aircraft model with Euler angle representation. A transformation from Euler angle representation to four parameter quaternion representation has been used to reduce the order of kinematic nonlinearities. The Picard's successive approximation technique has been developed to construct the solution for the presented aircraft model. This work has summarized the mathematical foundation without any numerical or analytical results. The work was documented in a technical memorandum (TM) under contract with the United States Air Force. The project engineer of this work was Charles Suchomel, who continued the work as shown next.

Suchomel has developed many distinguished efforts to apply Volterra theory in flight dynamic research area during the second half of 1980s. His first work is given in

Reference 100, which has not been officially published, but in Reference 101, Suchomel has documented in detail the work of Reference 100. Volterra theory has been numerically evaluated by an application to an F-8 nonlinear aircraft model. Therein, the implemented F-8 aircraft model was a modified version of the model in Reference 102. The modifications involved the addition of a thrust and aerodynamic drag model. The analysis was restricted to the longitudinal motion. The source of nonlinearity in this F-8 model includes: 1) the product of the body velocities with pitch rate, 2) the products of the wing and tail lift and drag with sines and cosines of wing and tail angle of attacks, and 3) the wing and tail lift curve coefficients as a cubic polynomial with the angle of attack. A 2.2 deg pitch nose down pulse maneuver excited the Volterra model and the exact nonlinear model for 2 s out of the 20 s simulation. This maneuver generated a high amplitude variation in all the longitudinal states. For example, the angle of attack changed from +7 to -20 deg and the pitch rate changed from -25 to +24 deg/s. These ranges are categorized as a high amplitude maneuver for such an F-8 model. The results of the three term Volterra model provided a maximum absolute 5% error for all variables. The author highlighted that the accuracy of the results depends on the integration step time and the number of truncated terms. In addition, the author indicated that the kinematic nonlinearity has a 10% effect on the overall results. However, the author did not compare the Volterra model with the linear model to judge how nonlinear the F-8 model is.

Suchomel reported another remarkable attempt of applying Volterra theory to flight mechanics in Reference 101. This work proposed novel nonlinear flight quality metrics. The study started by a generic two state nonlinear model. This generic model has an affine form. The first and second derivative matrices of the aerodynamic coefficients were counted. A two term Volterra series is analytically derived. The step response is then selected as a methodology for the proposed nonlinear flight quality metrics. The first Volterra series term has two exponential functions with two distinct

eigenvalues. These two exponential functions are multiplied by eight coefficients. The first Volterra series term yields to the same linear flight qualities metrics given in Reference 20. The second Volterra series term has sixteen coefficients multiplied by all the permutated multiplications of the exponential functions. The work considered one of these coefficients as an example to define the nonlinear flight quality metrics through the dependency of such a coefficient on aerodynamic derivatives. The work has an un-matured form with no general conclusion or analysis. The idea, which Suchomel brought in this work, was very promising for a new attitude to qualify the performance aircrafts. Regrettably, Suchomel did not continue developing his novel idea.

Directly after Suchomel's efforts, other work appeared in References 83 and 84 by a research group in the Mathematics Department at the Virginia Polytechnic Institution. One of the co-authors was Herdman. The work studied two common observed phenomena for high performance aircraft: stall limit cycle and wing rock. A simplified longitudinal dynamic model of the T-2C high performance aircraft model was selected therein. The model has been taken from Reference 103 and has been modified by replacing the look-up table plunging force coefficient behavior with a set of polynomials for pre-stall, pre-stall/stall, stall/post-stall, and post-stall regimes. The plunging force coefficient dependency with angle of attack has a linear polynomial in both pre-stall and post-stall regimes, while a quadratic polynomial is present in pre-stall/stall and stall/post-stall regimes. The differential form of Volterra theory is then used to compare the linear-based model with the Volterra-based model. The results show a high accuracy level by the Volterra model to capture the aircraft limit cycle behavior, while the linear model failed to render this limit cycle phenomenon. The second example in this work was given for the wing rock phenomenon. Although Volterra analysis showed the ability to capture the limit cycle, the Volterra model was still restricted to a certain equilibrium region.

The work in References 83 and 84 has been extended in Reference 104 to a global approach, which replaces the integral kernels with a repeatedly updated regression model

using state-input memory values from the past three time steps and 24 regression coefficients. Although the approach showed satisfactory results, the approach is limited by only allowing system representation through finite sets of numerical coefficients and memory bits, thus destroying the underlying analytical function framework. The work in Reference 104 was more oriented to discrete control. The authors employed these truncated Volterra series to construct a nonlinear control algorithm. The controller used the truncated Volterra model to build an estimator. The model assumes that both angle of attack and pitch rate are measurable at the moment k-1 and then the Volterra model is used to estimated the value of angle of attack and pitch rate at the next moment k. A control law is then developed in terms of angle of attack error. Also the model was constructed in a nonlinear adaptive fashion, such that the regression coefficients are updated with each sampling time. The adaptive version of the controller has performance, which was slightly worse than the non-adaptive case. However, comparing this nonlinear adaptive controller based on the Volterra model with the linear adaptive controller, the outcomes prove the superiority of Volterra-based model with a noticeable difference especially for the smoothness of the controller action time histories.

All the previously cited works for applying Volterra series in flight mechanics emphasize the ability of Volterra series to describe the aircraft behavior during aggresive maneuvers and to be a good estimator for nonlinear adaptive control. These efforts have been abandoned for almost 20 years (the last work was published in 1991) because of computational difficulties in applying Volterra theory to strong nonlinearities in flight dynamic systems across the envelope. This dissertation brings Volterra theory back to the flight mechanics research community by proposing a set of new approaches. These approaches enrich and facilitate Volterra theory to be more applicable for flight dynamic characterization. These approaches include:

1. Relaxing the computational cost to apply Volterra theory for strong nonlinearities as in the aircraft dynamics case.

2. Developing a nonlinear cause-and-effect parametric study for the low order atmospheric flight motions that can be used as a foundation to qualify the high performance aircraft.
3. Constructing a global model with the capability to render the aircraft behavior across a wide range of maneuvers and operating conditions.

Recall the work in References 83 and 84, the resultant Volterra-based model was restricted to certain equilibrium regions, which restricts the ability to capture the aircraft behavior while moving from one flight region to another. Even the global approach proposed in Reference 104 has a discrete form, which put a ceiling on any analytical foundation. For that reason, this dissertation aims to face these difficulties by proposing a "Piecewise Volterra Approach". This approach breaks down the strong nonlinear model to a set of weak nonlinear sub-models, and a proper interpolation is then employed to move between the sub-models. This reduction in computation simplifies the required mathematical manipulation to employ Volterra theory in flight mechanics. For example, attack angle and associated aerodynamic behavior is classified as pre-stall, stall, and post-stall. These domains can reflect different stability tendencies. In pre-stall, the behavior is usually linear, but in the stall regime, the aerodynamics can be strongly nonlinear. In the post-stall domain, the behavior can also be nonlinear but to a lesser extent. For investigating the feasibility of this global approach, a piecewise fashion is initially applied to a nonlinear pitch-plunge model for a high performance aircraft. A set of Volterra series sub-models can be generated for these various domains. Thus, the system behavior can be rendered from one sub-domain (pre-stall, pre-stall/stall, stall/post-stall, post-stall) to another sub-domain. An impulse response technique is used to estimate the Volterra kernels. For computational efficiency, reduced order Volterra terms are addressed. The order of the model is determined from a generic strength index metric. Subsequently, a piecewise Volterra kernel technique is used to switch between the Volterra sub-models. Feasibility of the universal piecewise approach is determined by

several input test cases. The test cases are compared with solutions generated from numerical integration of the nonlinear differential equations. Also, the proposed approach is compared with a global linear piecewise approach.

Based on the results of the global piecewise Volterra approach, it has been shown that a truncated two term Volterra series is enough to capture the behavior of the nonlinear dynamic system in a specific sub-domain. The nonlinearity in this sub-domain is mathematically given in the form of quadratic and bilinear nonlinearities, which leads to a significant reduction in the mathematical manipulation. This reduction is then used to develop the second approach, which is called herein "Nonlinear Cause-and-Effect Analysis". The cause-and-effect analysis provides a general analytical framework to predict the nonlinear behavior for the first and second order single degree of freedom (SDOF) sub-systems. The work is considered a demonstration tool to understand and analyze the nonlinear phenomena observed in aircraft dynamic behaviors. Symbolic nonlinear SDOF first and second order systems of generic nature are investigated as basic representations for system dynamics. The nonlinearity herein is mathematically considered as state quadratic terms, an input quadratic term, and as state-input bilinear terms. A variational expansion methodology, one of the most efficient analytical Volterra techniques, is used to develop an approximate nonlinear solution. The solution is given as a two term truncated Volterra series. The two terms symbolize the first and second kernels, which are sufficient to capture the quadratic and bilinear information initially assumed in the nonlinear systems. Such an analytical solution is visualized in the time domain for understanding the effect of each nonlinear and linear term in the kernels' structures. Also, this parametric study illuminates the cause of the observed deviation between the linear and nonlinear simulations. This deviation appears in the steady state response, settling time response, the phase shift response, and in general the transient response shape for any input. For that reason, these analyses are called the "Cause-and-Effect". Following the same rationale of linear analyses in the literature, a parametric

exploration for a nonlinear step response is conducted to characterize the overall system response. Feasibility of the proposed implementation is assessed by four examples: surge, pitch, roll, and yaw motions.

The third approach represents a global modeling technique for Volterra series based on a more computationally efficient interpolation to make the global Volterra technique more systematic than the piecewise Volterra approach. The method is called herein "Volterra Parameter-Varying Approach", which is suited for an aircraft's complex and large envelope (such as the F-16) more than the piecewise approach. The VPV algorithm starts by applying the local two term Volterra series sub-model in the differential form. This sub-model captures the quadratic and bilinear characteristics represented by inertial coupling nonlinearity, gravitational nonlinearity, kinematic nonlinearity, and aerodynamic and propulsive nonlinearity. The total flight speed and the altitude define the operating condition or the varying parameter. Other equivalent sub-models are generated at different operating conditions over the entire flight envelope. The coefficients of these local sub-models are then tabulated with the varying parameter (total speed and altitude). Different interpolation techniques are then investigated to select the most proper systematic interpolation. The algorithm employs the flight condition dependency to slide over the original nonlinearities hyper-surfaces and projects it as a Volterra parameter variation with the flight condition. The proposed VPV model has many advantages, which include:

- The model has the capability to render the aircraft behavior across wide ranging maneuvers, while the linear model is restricted to only mild maneuvers.
- The model provides a tractable analysis by linking Volterra kernels to the high order stability and control derivatives, while the linear model is restricted to the first order derivatives only.
- The cause-and-effect Volterra approach analyses can be applied to the global reduced order models taken from this VPV model providing an efficient nonlinear

preliminary design tool in qualifying the aircraft responses before computer simulation is invoked, or as an analysis tool to dissect a given simulation trace.

The VPV model is applied in this dissertation to the F-16 longitudinal motion to move across the flight envelope showing a superior matching compared to the linear parameter-varying (LVP) model. The kernel variations due to total velocity and altitude are visualized over the entire flight envelope to show the merit of Volterra kernels to characterize the longitudinal motion.

1.3 Research Contribution

Novel techniques to facilitate and enrich Volterra theory have been proposed. These techniques bring Volterra theory back to the flight mechanics research community twenty years after the last related publication. Volterra theory has been known for modeling weak nonlinearities, which is not well suited for high performance aircrafts. In order to overcome these obstacles and restrictions on Volterra theory, the global Volterra approach (piecewise approach and parameter-varying approach) has been developed.[105-107] This global approach opens a new window for practical use of Volterra theory when applied to systems with a strong overall nonlinearity by decomposing the nonlinearity into weaker component nonlinearities appearing in several operational sub-regions only requiring a low order truncated series. A novel cause-and-effect analysis of these low ordered truncated series has been developed, which provides system prediction before employing computer simulation.[108-112] Modeling the aircraft dynamics implementing these approaches in Volterra theory offers more efficient nonlinear preliminary design techniques than have been offered by other linear and nonlinear approximation techniques.

1.4 Dissertation Outline

This dissertation is composed of six chapters, including the current Chapter 1. Chapter 2 introduces some foundations for Volterra theory and techniques to identify Volterra kernels from the observed input-output signals and from the nonlinear differential equations. Chapter 3 is dedicated to the piecewise global Volterra technique. This method is a novel approach that increases the practical use of Volterra theory when applied to systems with a strong overall nonlinearity requiring several high order kernels by decomposing the nonlinearity into weaker component nonlinearities appearing in several operational sub-regions requiring fewer kernels. The piecewise Volterra model is recommended for low order dynamics. Chapter 4 presents the cause-and-effect analyses for the first and seconded order single degree of freedom system. A two term truncated Volterra series, which is enough to capture the quadratic and bilinear nonlinearities, is developed for first and second order generalized nonlinear single degree of freedom systems. The resultant models are given in the form of first and second kernels. A parametric study of the influence of each linear and nonlinear term on kernel structures is investigated. A step input is then employed to quantify and qualify the nonlinear response characteristics followed by some low order atmospheric flight examples. In Chapter 5, a Volterra parameter-varying modeling approach is proposed to model the high order aircraft dynamics. The global analytical kernels based on the VPV approach is visualized over the flight envelope. This visualization emphasizes the capability of Volterra theory to analytically characterize the aircraft dynamics more than other approximation techniques. The dissertation is concluded in Chapter 6, which contains proposals for future investigation.

CHAPTER 2

VOLTERRA THEORY

This chapter provides the necessary background of Volterra theory and different methods to estimate the so-called Volterra kernels. This background is used throughout the dissertation to develop the proposed approaches. Section 2.1 introduces the mathematical and dynamical insights of Volterra theory. Section 2.2 discusses the nature of the kernels and their shapes. Section 2.3 outlines a numerical procedure, which estimates Volterra kernels via an impulsive technique. Three analytical techniques to develop Volterra kernels from the differential equations are discussed in Section 2.4.

2.1 Mathematical and Dynamical Foundation

Many physical systems can be described across a set of nonlinear differential and algebraic equations between input, state, and output signals. A commonly used representation is the nonlinear state space form

$$\begin{aligned} \dot{x}(t) &= f\{t, x(t), u(t)\} \\ y(t) &= g\{t, x(t), u(t)\} \end{aligned} \tag{2.1}$$

where $x \in R^n$ denotes the state vector, $u \in R^m$ the input vector, and $y \in R^p$ the output vector. Vectors $f \in R^n$ and $g \in R^p$ denote the system nonlinearities and $t \in R^1$ is time. Volterra series represents the input-output relation of a nonlinear system as an infinite sum of multidimensional convolution integrals.

$$y(t) = h_o(t) + \sum_{k=1}^{\infty} \int_0^{\infty}\int_0^{\infty} \cdots \int_0^{\infty} h_k(\tau_1, \tau_2, \ldots, \tau_k) \cdot \prod_{i=1}^{k} u(t-\tau_i) d\tau_i \tag{2.2}$$

In Equation (2.2), $h_k(\tau_1, \tau_2, \ldots, \tau_k)$ denotes the k^{th} order Volterra kernel.

To solidify the mathematical applicability of Equation (2.2) and its origins, a conceptual derivation is given first.[58] The theory supposes that output $y(t)$ of a system at a

particular time t depends nonlinearly on all values of the input at times equal and prior to t. In other words, $y(t)$ depends on $u(t-\tau)$ for all $\tau \geq 0$. If $u(t-\tau)$ can be quantified by the set $u_1(t)$, $u_2(t)$, ..., then output $y(t)$ is expressible as a nonlinear function of these quantities.

$$y(t) = \psi\{u_1(t), u_2(t), \ldots\} \tag{2.3}$$

The theory supposes the input $u(t-\tau)$ is given by an infinite series involving products of $u_i(t)$ with functions $\phi_i(\tau)$ serving as an orthonormal basis for the appropriate functional input vector space.

$$u(t-\tau) = \sum_{i=1}^{\infty} u_i(t)\phi_i(\tau) \tag{2.4}$$

$$\int_0^{\infty} \phi_i(\tau)\phi_j(\tau)d\tau = \begin{cases} 1 & for \quad i = j \\ 0 & for \quad i \neq j \end{cases} \tag{2.5}$$

Exploiting the orthogonality property of $\phi_i(\tau)$, quantities $u_i(t)$ are computed as

$$u_i(t) = \int_0^{\infty} u(t-\tau)\phi_i(\tau)d\tau \tag{2.6}$$

Finally expand Equation (2.3) with a general power series, or

$$y(t) = \theta_0 + \sum_{i_1=1}^{\infty} \theta_{i_1} u_{i_1}(t) + \sum_{i_1=1}^{\infty}\sum_{i_2=1}^{\infty} \theta_{i_1 i_2} u_{i_1}(t) u_{i_2}(t) + \ldots\ldots \tag{2.7}$$

and substitute from Equation (2.6) yielding

$$\begin{aligned} y(t) = \theta_0 &+ \int_0^{\infty} \sum_{i_1=1}^{\infty} \theta_{i_1} \phi_{i_1}(\tau_1) u(t-\tau_1) d\tau_1 \\ &+ \int_0^{\infty}\int_0^{\infty} \sum_{i_1=1}^{\infty}\sum_{i_2=1}^{\infty} \theta_{i_1 i_2} \phi_{i_1}(\tau_1)\phi_{i_2}(\tau_2) u(t-\tau_1) u(t-\tau_2) d\tau_1 d\tau_2 + \ldots\ldots \end{aligned} \tag{2.8}$$

Equation (2.8) has a term-by-term correspondence with Equation (2.2) authenticating, for the purpose here, the Volterra series solution. A more rigorous mathematical proof can be found in Reference 58.

Although the previous derivation gives a conceptual understanding of Volterra theory's mathematical origin, it is also beneficial to look at the dynamical intuition of the Volterra representation. The theory represents the input-output relationship as an infinite series of homogeneous linear and nonlinear sub-systems expanding upon Taylor's power series.[58] Homogeneity, in general, means that the change in the amplitude of the input generates a change in the amplitude of the response without any change in the shape. If the shape of the response of the system distorts with change in amplitude of the input, then the system is a non-homogeneous one. A linear system is an example of a homogeneous system at $n = 1$, whereas a nonlinear system is typically non-homogeneous, but not in all cases.

The n^{th} term of the Volterra series is a single input single output degree-n homogeneous stationary nonlinear system, which is defined through the generalized convolution integral as

$$\begin{aligned} y_n(t) &= \int_{-\infty}^{\infty} \cdots \int_{-\infty}^{\infty} h_n(\tau_1, \cdots, \tau_n) u(t-\tau_1) \cdots u(t-\tau_n) d\tau_1 \cdots d\tau_n \\ &= \int_{-\infty}^{\infty} \cdots \int_{-\infty}^{\infty} h_n(t-\tau_1, \cdots, t-\tau_n) u(\tau_1) \cdots u(\tau_n) d\tau_1 \cdots d\tau_n \end{aligned} \tag{2.9}$$

where $h_n(\tau_1, \cdots, \tau_n)$ is the kernel of the system defined for $\tau_i \in (-\infty, \infty)$, i =1,2, .., n. In Equation (2.9), $y_n(t)$ denotes the system output and $u(t)$ denotes the system input. This system is called a degree-n homogeneous system, because if an input $\alpha u(t)$ is applied to the system, the output is then $\alpha^n y_n(t)$, where $y_n(t)$ is the equivalent response for the input $u(t)$. The first term of the Volterra series is a degree-1 homogeneous sub-system, in which the change in output amplitude is proportional to the input amplitude. The second term is a degree-2 homogeneous sub-system, in which the change in output amplitude is proportional to the square of the input amplitude and so on. Each degree-n homogeneous sub-system is represented by an n dimensional convolution integral, while the input signal is dynamically weighted by the so-called n^{th} order kernel. The n^{th} order kernel is an

n-dimensional function in time or complex frequency, depending on the domain of interest. Each kernel appearing in the convolution integrals reflects a specific system behavior.

2.2 Kernel Nature and Shape

In Equation (2.9), the kernel is a one-sided function in each argument τ_i due to the causality of the system. Thus, the system response at a certain time cannot depend on future values of the input. This one-sided characteristic implies that "0" can replace the infinite lower limit of the integration. Also, the input signal is considered to have a zero value prior to $t = 0$, which leads to the replacement of the upper limit of the integration by t. Both changes yield

$$\begin{aligned} y(t) &= \int_0^t \cdots \int_0^t h_n(\tau_1, \cdots, \tau_n) u(t-\tau_1) \cdots u(t-\tau_n) d\tau_1 \cdots d\tau_n \\ &= \int_0^t \cdots \int_0^t h_n(t-\tau_1, \cdots, t-\tau_n) u(\tau_1) \cdots u(\tau_n) d\tau_1 \cdots d\tau_n \end{aligned} \tag{2.10}$$

The structure of the kernel $h_n(\tau_1, \cdots, \tau_n)$ is described in terms of arguments τ_1, τ_2, . . . , τ_n. Three forms of the kernel commonly appear: symmetric kernel, triangular kernel, and regular kernel. The symmetric kernel for a stationary system is defined to be

$$h_{nsym}(\tau_1, \cdots, \tau_n) = h_n(\tau_{\pi(1)}, \cdots, \tau_{\pi(n)}) \tag{2.11}$$

where $\pi(.)$ denotes any permutation of the integers 1,2,...,*n*. For some computational algorithms, kernel symmetry is not guaranteed. In such a case, a symmetrization technique could be applied to h_n yielding h_{nsym} as[58]

$$h_{nsym}(\tau_1, \cdots, \tau_n) = \frac{1}{n!} \sum_{\pi(.)} h_n(\tau_{\pi(1)}, \cdots, \tau_{\pi(n)}) \tag{2.12}$$

For example, if the system has an asymmetric kernel as

$$h_2(\tau_1,\tau_2)=g(\tau_1)f(\tau_1,\tau_2) \tag{2.13}$$

the symmetric kernel is then computed as

$$h_{2sym}(\tau_1,\tau_2)=\frac{1}{2}[g(\tau_1)f(\tau_1,\tau_2)+g(\tau_2)f(\tau_2,\tau_1)] \tag{2.14}$$

Although the symmetric kernel in Equation (2.14) has more terms than the one in Equation (2.13), such symmetrization brings the kernel into the most standard form.

A triangular kernel is the second special form of the kernel. The triangular kernel is defined such that $h_{ntri}(\tau_1,\cdots,\tau_n)=0$ for $\tau_{i+j} > \tau_j$ for i, j positive integers. Figure 2.1 shows an example of the operating domain over which the degree-2 $h_{2tri}(\tau_1,\tau_2)$ kernel could be defined. However, the operating domain of a triangular kernel is not unique. For a degree-n kernel, there are $n!$ possibilities to define the domain.

The third special form is the regular kernel. This form is developed from a triangular kernel as follows. For a system with a triangular kernel, the output is given as

$$\begin{aligned} y(t) &= \int_0^t \int_0^{\sigma_1} \cdots \int_0^{\sigma_{n-1}} h_n(\sigma_1,\cdots,\sigma_n)u(t-\sigma_1)\cdots u(t-\sigma_n)d\sigma_1\cdots d\sigma_n \\ &= \int_0^t \cdots \int_0^t h_{ntri}(\sigma_1,\cdots,\sigma_n)u(t-\sigma_1)\cdots u(t-\sigma_n)d\sigma_1\cdots d\sigma_n \end{aligned} \tag{2.15}$$

where

$$h_{ntri}(\sigma_1,\cdots,\sigma_n)=h_n(\sigma_1,\cdots,\sigma_n)\Delta(\sigma_1-\sigma_2)\Delta(\sigma_2-\sigma_3)\cdots\Delta(\sigma_{n-1}-\sigma_n)$$

and $\Delta(\sigma)$ denotes the unit step function. Replace σ_1 by $\tau_1 = \sigma_1-\sigma_2$ where σ_2 is treated as a constant, then

$$\begin{aligned} y(t) = \int_0^t \cdots \int_0^t & h_{ntri}(\tau_1+\sigma_2,\sigma_2,\sigma_3,\cdots,\sigma_n)u(t-\tau_1-\sigma_2)\times \\ & u(t-\sigma_2)\cdots u(t-\sigma_n)d\tau_1 d\sigma_2 d\sigma_3\cdots d\sigma_n \end{aligned} \tag{2.16}$$

Replace σ_2 by $\tau_2 = \sigma_2-\sigma_3$ where σ_3 is a constant, then

$$y(t)=\int_0^t\cdots\int_0^t h_{ntri}(\tau_1+\tau_2+\sigma_3,\tau_2+\sigma_3,\sigma_3,\cdots,\sigma_n)u(t-\tau_1-\tau_2-\sigma_3)u(t-\tau_2-\sigma_3)\times u(t-\sigma_3)\cdots u(t-\sigma_n)d\tau_1 d\tau_2 d\sigma_3\cdots d\sigma_n \tag{2.17}$$

Continuing this process, one finds

$$y(t)=\int_0^t\cdots\int_0^t h_{ntri}(\tau_1+\cdots+\tau_n,\tau_2+\cdots+\tau_n,\tau_{n-1}+\tau_n,\tau_n)\times u(t-\tau_1-\cdots-\tau_n)u(t-\tau_2-\cdots-\tau_n)\cdots u(t-\tau_n)d\tau_1 d\tau_2\cdots d\tau_n \tag{2.18}$$

In this way, the regular kernel is defined as

$$h_{nreg}(\tau_1,\tau_2,\cdots,\tau_n)=h_{ntrig}(\tau_1+\cdots+\tau_n,\tau_2+\cdots+\tau_n,\tau_{n-1}+\tau_n,\tau_n) \tag{2.19}$$

This structure leads to writing the input-output representation for the degree-*n* stationary homogeneous system as

$$y(t)=\int_0^t\cdots\int_0^t h_{nreg}(\tau_1,\tau_2,\cdots,\tau_n)u(t-\tau_1-\cdots-\tau_n)\times u(t-\tau_2-\cdots-\tau_n)\cdots u(t-\tau_n)d\tau_1 d\tau_2\cdots d\tau_n \tag{2.20}$$

The main reason for this conversion from the triangular kernels to regular kernels is to generate kernels with an orthant domain instead of a triangular domain without bringing any discontinuity. For example, if a triangular kernel is defined as

$$h_{2tri}(\tau_1,\tau_2)=\{\cos(\tau_1)\sin(\tau_2)+3\sin(\tau_1)\}\Delta(\tau_1-\tau_2) \tag{2.21}$$

Both symmetric and regular kernels, equivalent for this triangular kernel, are computed as

$$\begin{aligned} h_{2sym}(\tau_1,\tau_2)&=\frac{1}{2}[\{\cos(\tau_1)\sin(\tau_2)+3\sin(\tau_1)\}\Delta(\tau_1-\tau_2)\\ &\quad+\{\cos(\tau_2)\sin(\tau_1)+3\sin(\tau_2)\}\Delta(\tau_2-\tau_1)]\\ h_{2reg}(\tau_1,\tau_2)&=\cos(\tau_1+\tau_2)\sin(\tau_2)+3\sin(\tau_1+\tau_2)\end{aligned} \tag{2.22}$$

The three kernels of Equations (2.21) and (2.22) are shown in Figures 2.2-2.4 to emphasize the philosophy behind the regular kernel generation, since a symmetric kernel shows discontinuity, while a regular kernel does not.

Volterra theory represents the system as an infinite sum of multidimensional convolution integrals by

$$y(t) = h_o(t) + \sum_{k=1}^{\infty} \int_0^{\infty} \int_0^{\infty} \cdots \int_0^{\infty} h_k(\tau_1, \tau_2, \ldots, \tau_k) \cdot \prod_{i=1}^{k} u(t - \tau_i) d\tau_i \tag{2.23}$$

Each term k in such a series is a homogeneous sub-system of degree-k, which has kernel $h_k(\tau_1, \tau_2, \ldots, \tau_k)$ as mentioned before. Volterra kernels are causal homogeneous functions with respect to their arguments. These kernels represent the behavior of the system to any arbitrary input, which concludes that kernels are unique signatures for the system. Each kernel appearing in the convolution integrals reflects a specific system behavior. For example, the first kernel h_1 represents the linear behavior of the system. The merit of using Volterra theory is that such series for many nonlinear systems can be truncated by a certain number of terms when considering a bounded time interval and input amplitude. In this way, the input-output relation of a nonlinear system can be approximated as a "finite" sum of multidimensional convolution integrals. However, it is difficult to find such bounds of input and time. Most weak nonlinear systems only require between two and three terms and more nonlinearities means more terms.

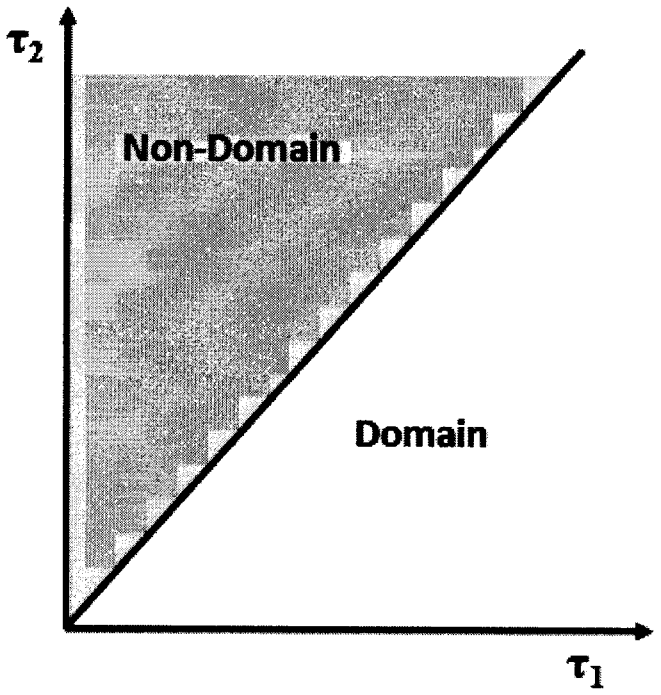

Figure 2.1 Triangular Domain for Degree-2 Kernel

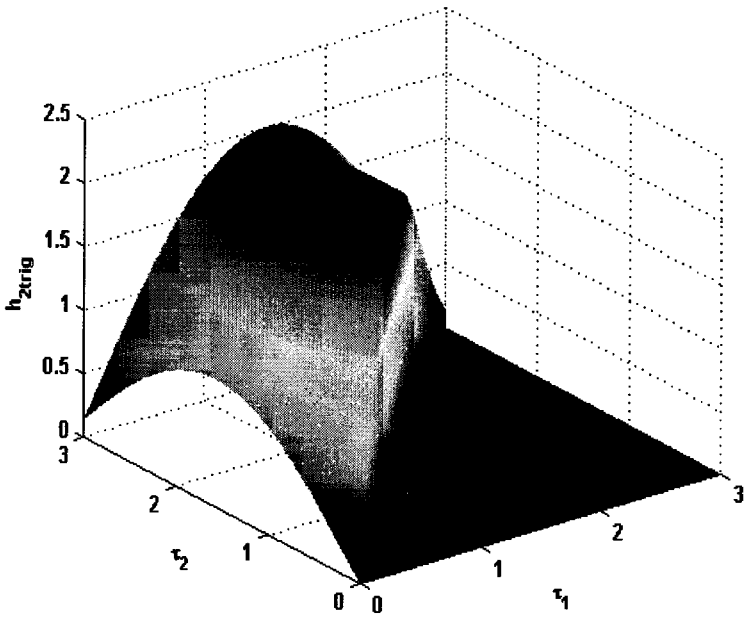

Figure 2.2 Triangular Kernel

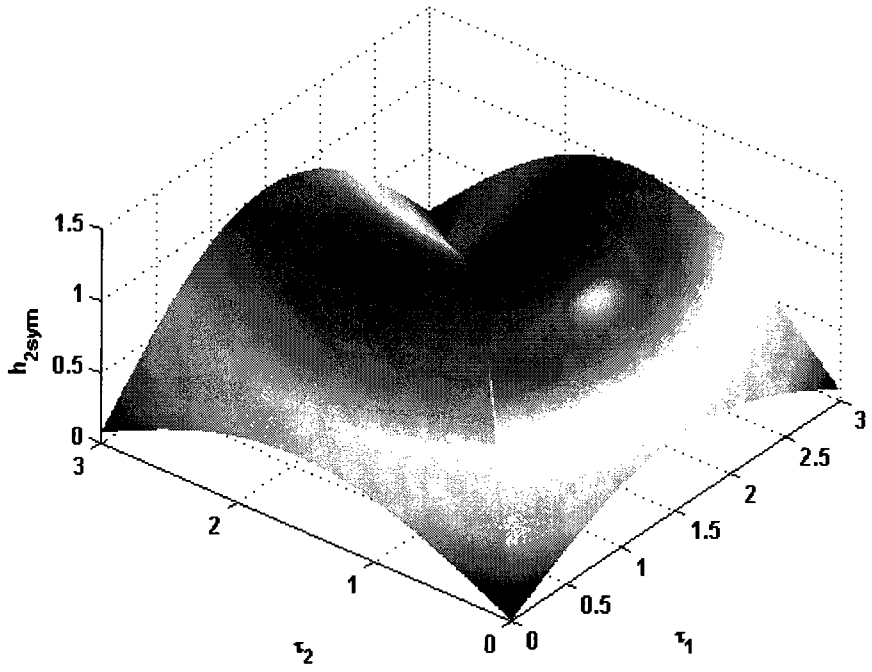

Figure 2.3 Symmeterized Kernel

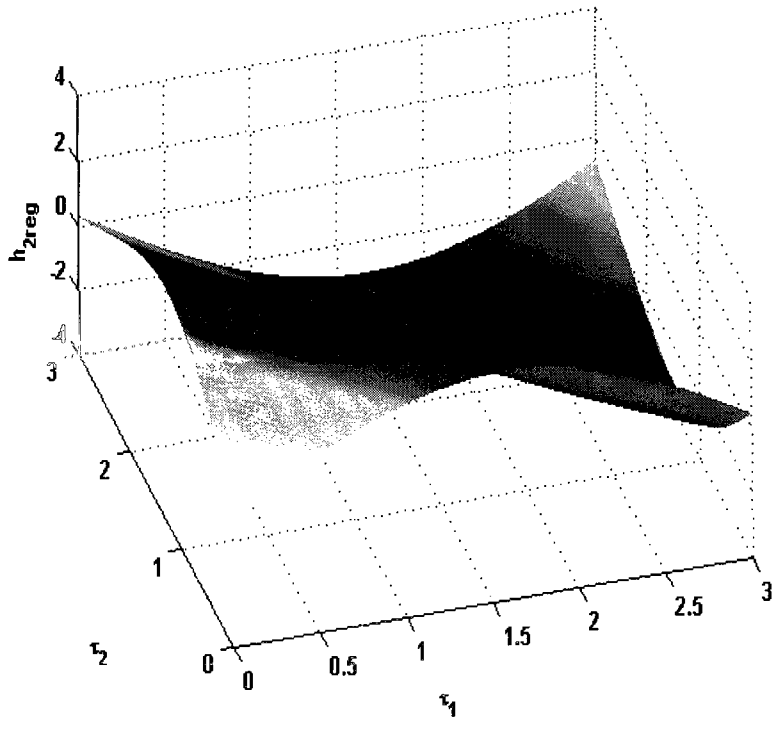

Figure 2.4 Regularized Kernel

2.3 Kernel Identification based on Input-Output Signals

Since, kernels are the backbone of Volterra theory, they must be constructed by some means. Several methodologies have been addressed to estimate the Volterra kernels. Some methods are iterative and numerical in nature, identifying the nonlinear system as a black box or gray box. For example, one of these numerical techniques is based on linear regression or least square estimation (LSE). LSE can be cast as a recursive algorithm or a non-recursive algorithm. Another method to estimate Volterra kernels from the system identification point of view is provided by the use of sinusoidal or impulsive inputs. The strategy is an extension from the use of these inputs to identify linear systems. This strategy captures only the input-output behavior of a system and disregards any internal structure.

In this section, Volterra kernel estimation via impulsive input is implemented. The kernels are estimated from a time domain system identification perspective. As the input $u(t)$ is applied to and the output $y(t)$ is recorded from the undefined system, the waveform of the output and input signals are used to estimate the kernels. This methodology is especially favorable for reflecting the operational meaning of Volterra kernels. For an impulsive input, every kernel indicates the response of the system as a function of time and a certain number of distinct time lags. For example, a second order kernel is a function of both time and time lag τ_L, or $h_2(t,t-\tau_L)$, which reflects how the system memory (nonlinearity) from an applied input at previous time $(t-\tau_L)$ affects the response of the system with input at time t. Based on the operational meaning of the kernel and the input time lag, kernel identification can be realized by inputting a signal waveform of multiple impulses with variable amplitude and variable time lag.

A procedure is given in Reference 58 for first and second order kernel estimation which is generalized here to n^{th} order. The diagonal values of n kernels are estimated first by applying a sequence of variable strength impulse inputs one at a time as

$$u_i(t) = A_i\delta(t) \quad , \qquad i = 0,1,2,...,n \tag{2.24}$$

where $\delta(t)$ denotes the unit impulse function. Each input generates a corresponding response $y_i(t)$ as

$$y_i(t) = h_o(t) + A_i h_1(t) + A_i^2 h_2(t,t) + ... + A_i^n h_n(t,t,...,t) \quad \text{and} \quad i = 0,1,2,...,n \tag{2.25}$$

Equation (2.25) represents a set of simultaneous equations for the diagonal kernel values. These diagonal values are computed as

$$\begin{aligned} &h(t) = A^{-1}y(t) \\ &h(t) = [h_0(t) \quad h_1(t) \quad h_2(t,t) \quad ... \quad h_n(t,t,...,t)]^T \\ &y(t) = [y_0(t) \quad y_1(t) \quad ... \quad y_n(t)]^T \\ &A = \begin{bmatrix} 1 & A_0 & A_0^2 & ... & A_0^n \\ 1 & A_1 & A_1^2 & ... & A_1^n \\ \vdots & & & & \vdots \\ 1 & A_n & A_n^2 & ... & A_n^n \end{bmatrix} \end{aligned} \tag{2.26}$$

This computation is carried out at each point in the time series. The impulse strengths must be selected to ensure excitation of relevant nonlinearities and invertibility of the $(n+1)\times(n+1)$ matrix A.

This methodology can be extended to estimate off-diagonal values of the high order kernels by exciting the system through a sequence of time delayed impulses. The m off-diagonal kernel values are estimated by applying a sequence of variable strength time delayed impulse inputs one at a time.

$$u_i(t) = A_i\delta(t) + B_i\delta(t - t_L) \quad , \qquad i = 1,2,\cdots,m \tag{2.27}$$

The produced responses corresponding to these inputs are

$$
\begin{aligned}
y_i(t) = {} & h_o(t) + A_i h_1(t) + B_i h_1(t - t_L) + A_i^2 h_2(t,t) \\
& + 2A_i B_i h_2(t, t - t_L) + B_i^2 h_2(t - t_L, t - t_L) + \cdots \\
& + A_i^n h_n(t,t,\cdots,t) + \frac{n}{1} A_i^{n-1} B_i h_n(t,\cdots,t,t - t_L) \\
& + \frac{n(n-1)}{1 \cdot 2} A_i^{n-2} B_i^2 h_n(t,\cdots,t,t - t_L, t - t_L) \\
& + \cdots + \frac{n(n-1)}{1 \cdot 2} A_i^2 B_i^{n-2} h_n(t,t,t - t_L,\cdots,t - t_L) \\
& + \frac{n}{1} A_i \, B_i^{n-1} h_n(t, t - t_L,\cdots,t - t_L) + B_i^n h_n(t - t_L, t - t_L,\cdots,t - t_L) \\
& i = 1,2,\cdots,m \qquad , \qquad m = \sum_{i=1}^{n-1} i
\end{aligned}
\tag{2.28}
$$

Equation (2.28) also represents a set of simultaneous equations, this time for the off-diagonal kernel values. These off-diagonal values are computed as

$$
h'(t) = [AB]^{-1} y'(t) \tag{2.29}
$$

where

$$
h'(t) = \begin{bmatrix}
h_2(t, t - t_L) \\
h_3(t,t,t - t_L) \\
h_3(t, t - t_L, t - t_L) \\
\vdots \\
h_n(t,\cdots,t,t - t_L) \\
h_n(t,\cdots,t,t - t_L, t - t_L) \\
\vdots \\
h_n(t,t,t - t_L,\cdots,t - t_L) \\
h_n(t, t - t_L,\cdots,t - t_L)
\end{bmatrix}
$$

$$[AB]=\begin{bmatrix} 2A_1B_1 & 3A_1^2B_1 & 3A_1B_1^2 & \cdots & \frac{n}{1}A_1^{n-1}B_1 & \frac{n(n-1)}{1\cdot 2}A_1^{n-2}B_1^2 & \cdots & \frac{n(n-1)}{1\cdot 2}A_1^2B_1^{n-2} & \frac{n}{1}A_1B_1^{n-1} \\ 2A_2B_2 & 3A_2^2B_2 & 3A_2B_2^2 & \cdots & \frac{n}{1}A_2^{n-1}B_2 & \frac{n(n-1)}{1\cdot 2}A_2^{n-2}B_2^2 & \cdots & \frac{n(n-1)}{1\cdot 2}A_2^2B_2^{n-2} & \frac{n}{1}A_2B_2^{n-1} \\ \vdots & & & & & & & & \\ \vdots & & & & & & & & \\ 2A_mB_m & 3A_m^2B_m & 3A_mB_m^2 & \cdots & \frac{n}{1}A_m^{n-1}B_m & \frac{n(n-1)}{1\cdot 2}A_m^{n-2}B_m^2 & \cdots & \frac{n(n-1)}{1\cdot 2}A_m^2B_m^{n-2} & \frac{n}{1}A_mB_m^{n-1} \end{bmatrix}$$

$$y'(t)=\begin{bmatrix} y_1(t)-h_0(t)-A_1h_1(t)-B_1h_1(t-t_L)-A_1^2h_2(t,t)-B_1^2h_2(t-t_L,t-t_L) \\ -\cdots-A_1^nh_n(t,t,\cdots,t)-B_1^nh_n(t-t_L,t-t_L,\cdots,t-t_L) \\ y_2(t)-h_0(t)-A_2h_1(t)-B_2h_1(t-t_L)-A_2^2h_2(t,t)-B_2^2h_2(t-t_L,t-t_L) \\ -\cdots-A_2^nh_n(t,t,\cdots,t)-B_2^nh_n(t-t_L,t-t_L,\cdots,t-t_L) \\ \vdots \\ \vdots \\ \vdots \\ y_m(t)-h_0(t)-A_mh_1(t)-B_mh_1(t-t_L)-A_m^2h_2(t,t)-B_m^2h_2(t-t_L,t-t_L) \\ -\cdots-A_m^nh_n(t,t,\cdots,t)-B_m^nh_n(t-t_L,t-t_L,\cdots,t-t_L) \end{bmatrix}$$

This computation is carried out at each point in the time series. The impulse strengths are selected to strongly excite the nonlinearities of interest and to avoid singularity of the $m \times m$ matrix $[AB]$. By varying the value of t_L from zero to t_H, the desired temporal horizon of the Volterra model, the value of any kernel at an off-diagonal point in the domain can be defined numerically. It is only necessary to calculate the kernels over half of the domain with this procedure, the remaining half is obtained from kernel symmetry. If only two kernels through $h_2(t,t\text{-}t_L)$ are sought, the above general technique simplifies considerably. Equation (2.28) reduces to a single equation and the matrix inverse solution in Equation (2.29) is replaced by scalar division.

$$
\begin{aligned}
y(t) &= h_o(t) + Ah_1(t) + Bh_1(t - t_L) + A^2 h_2(t,t) \\
&\quad + 2ABh_2(t, t - t_L) + B^2 h_2(t - t_L, t - t_L) \\
h_2(t, t - t_L) &= \frac{1}{2AB}\{y(t) - h_o(t) - Ah_1(t) \\
&\quad - Bh_1(t - t_L) - A^2 h_2(t,t) - B^2 h_2(t - t_L, t - t_L)\}
\end{aligned} \tag{2.30}
$$

Estimating Volterra kernels based on the impulsive response is used in this dissertation only within Chapter 3.

2.4 Kernel Identification from Differential Equations

Identifying the kernels from the input-output signals is quite general but captures only the input-output behavior of a system and disregards any internal structure. On the other hand, the usage of analytical methods exposes internal structure but is more restricted in applicability. Three analytical methods to develop the Volterra kernels from the nonlinear differential equation are discussed in this section: Carleman linearization method, growing exponential method, and variational expansion method. A brief discussion is presented to show the procedure, capability, and limitation of each method in the next three subsections.

2.4.1 Carleman Linearization Approach

The single input single output state space representation of the nonlinear affine system is defined as

$$
\begin{aligned}
\dot{x}(t) &= F(x(t),t) + G(x(t),t)u(t) \\
y(t) &= H(x(t),t)
\end{aligned} \tag{2.31}
$$

where $x \in R^n$ denotes the state vector, $u \in R^1$ the scalar input, and $y \in R^1$ the scalar output. Vectors $F \in R^n$, $G \in R^n$, and $H \in R^1$ denote the nonlinear analytical functions in x and continuous function in t, where $t \in R^1$ is time. The system in Equation (2.31) is also called a linear-analytical state equation. The Carleman linearization approach can be applied to $F(x(t),t)$, $G(x(t),t)$, and $H(x(t),t)$ as

$$
\begin{aligned}
F(x(t),t) &= A_1(t)x(t) + A_2(t)x^{(2)}(t) + \cdots + A_i(t)x^{(i)}(t) + \cdots \\
G(x(t),t) &= B_o(t) + B_1(t)x^{(1)}(t) + B_2(t)x^{(2)}(t) + \cdots + B_i(t)x^{(i)}(t) + \cdots \\
H(x(t),t) &= C_1(t)x(t) + C_2(t)x^{(2)}(t) + \cdots + C_i(t)x^{(i)}(t) + \cdots
\end{aligned}
\tag{2.32}
$$

where

$$
\begin{aligned}
x^{(0)}(t) &= 1 \\
x^{(1)}(t) &= x(t) \\
x^{(2)}(t) &= x(t) \otimes x(t) \\
x^{(3)}(t) &= x(t) \otimes x(t) \otimes x(t) \\
&\vdots \\
x^{(i)}(t) &= x(t) \prod_{k=1}^{i-1} \otimes x(t)
\end{aligned}
\tag{2.33}
$$

and $x(t)$, $u(t)$, and $y(t)$ now denote signals referenced to the expansion point. In Equation (2.33), $\otimes$ is the Kronecker product. The Kronecker product for two matrices P of the dimension $N_P \times M_P$ and Q of the dimension $N_Q \times M_Q$ is defined as

$$
P \otimes Q = \begin{bmatrix} P_{11}Q & \cdots & P_{1M_P}Q \\ \vdots & \ddots & \vdots \\ P_{N_P1}Q & \cdots & P_{N_PM_P}Q \end{bmatrix}
\tag{2.34}
$$

The resultant matrix $P \otimes Q$ has dimension $(N_P N_Q) \times (M_P M_Q)$.

After considering Carleman linearization for N terms only, Equation (2.31) is then approximated as

$$
\begin{aligned}
\dot{x}(t) &\approx \sum_{k=1}^{N} A_k(t)x^{(k)}(t) + \sum_{k=0}^{N-1} B_k(t)x^{(k)}(t)u(t) \\
y(t) &\approx \sum_{k=1}^{N} C_k(t)x^{(k)}(t)
\end{aligned}
\tag{2.35}
$$

Equation (2.35) and the index notation to follow is modestly generalized from that in Reference 58. The system in Equation (2.35) can be formulated as a bilinear system by considering the differential equation of $x^{(i)}(t)$ as[58]

$$\dot{x}^{(i)}(t)=\sum_{k=i}^{N}A_{i,k}(t)x^{(k)}(t)+\sum_{k=i-1}^{N-1}B_{i,k}(t)x^{(k)}(t)u(t) \tag{2.36}$$

where

$$A_{i,k}(t)=A_{k-i+1}(t)\left(\prod_{j=1}^{i-1}\otimes I_n\right)+I_n\otimes A_{k-i+1}(t)\left(\prod_{j=1}^{i-2}\otimes I_n\right)+\cdots+\left(\prod_{j=1}^{i-1}I_n\otimes\right)A_{k-i+1}(t)$$

$$B_{i,k}(t)=B_{k-i+1}(t)\left(\prod_{j=1}^{i-1}\otimes I_n\right)+I_n\otimes B_{k-i+1}(t)\left(\prod_{j=1}^{i-2}\otimes I_n\right)+\cdots+\left(\prod_{j=1}^{i-1}I_n\otimes\right)B_{k-i+1}(t) \tag{2.37}$$

$$B_{i,i-1}(t)=iB_o(t)$$

and $k=i,i+1,i+2,\cdots,N$

In Equation (2.37), there are (i-1) Kronecker products in each $A_{i,k}(t)$ and $B_{i,k}(t)$ terms. The derivation of Equation (2.37) is a sequential one. The first step of the derivation is presented as

$$\begin{aligned}
\frac{d}{dt}\left[x^{(2)}(t)\right]&=\frac{d}{dt}\left[x^{(1)}(t)\otimes x^{(1)}(t)\right]=\dot{x}^{(1)}(t)\otimes x^{(1)}(t)+x^{(1)}(t)\otimes\dot{x}^{(1)}(t)\\
\frac{d}{dt}\left[x^{(2)}(t)\right]&=\left\{\sum_{k=1}^{N-1}A_k(t)x^{(k)}(t)+\sum_{k=0}^{N-2}B_k(t)x^{(k)}(t)u(t)\right\}\otimes x^{(1)}(t)\\
&\quad+x^{(1)}(t)\otimes\left\{\sum_{k=1}^{N-1}A_k(t)x^{(k)}(t)+\sum_{k=0}^{N-2}B_k(t)x^{(k)}(t)u(t)\right\}+\cdots\\
\frac{d}{dt}\left[x^{(2)}(t)\right]&=\sum_{k=1}^{N-1}\underbrace{\left[A_k(t)\otimes I_n+I_n\otimes A_k(t)\right]}_{A_{2,k}(t)}x^{(k+1)}(t)\\
&\quad+\sum_{k=0}^{N-2}\underbrace{\left[B_k(t)\otimes I_n+I_n\otimes B_k(t)\right]}_{B_{2,k}(t)}x^{(k+1)}(t)u(t)+\cdots\\
\frac{d}{dt}\left[x^{(2)}(t)\right]&\approx\sum_{k=1}^{N-1}A_{2,k}(t)x^{(k+1)}(t)+\sum_{k=0}^{N-2}B_{2,k}(t)x^{(k+1)}(t)u(t)
\end{aligned} \tag{2.38}$$

In Equation (2.38), the upper limit of the summation of A_k terms has been reduced to N-1 to remove the $(N+1)^{th}$ order terms $x^{(N+1)}$. Also, the upper limit of the summation of A_k terms has been reduced to N-2 to remove the $(N+1)^{th}$ order terms $x(N)u(t)$. The differential equations of $x^{(i)}(t)$ for i =1,..., N can be collected in a state space model as

$$\begin{aligned} \dot{x}^{\otimes}(t) &= \overline{A}(t)x^{\otimes}(t) + \overline{B}_0(t)u(t) + \overline{B}_1(t)x^{\otimes}(t)u(t) \\ y(t) &= \overline{C}(t)x^{\otimes}(t) \end{aligned} \tag{2.39}$$

with

$$\overline{A}(t) = \begin{bmatrix} A_{1,1} & A_{1,2} & \cdots & A_{1,N} \\ 0 & A_{2,2} & \cdots & A_{2,N} \\ 0 & 0 & \cdots & A_{3,N} \\ \vdots & \vdots & \vdots & \vdots \\ 0 & 0 & \cdots & A_{N,N} \end{bmatrix}, \quad x^{\otimes}(t) = \begin{bmatrix} x(t) \\ x^{(2)}(t) \\ x^{(3)}(t) \\ \vdots \\ x^{(N)}(t) \end{bmatrix}, \quad \overline{B}_0(t) = \begin{bmatrix} B_{1,0} \\ 0 \\ 0 \\ \vdots \\ 0 \end{bmatrix} u(t)$$

$$\overline{B}_1(t) = \begin{bmatrix} B_{1,1} & B_{1,2} & \cdots & B_{1,N-1} & 0 \\ B_{2,1} & B_{2,2} & \cdots & B_{2,N-1} & 0 \\ 0 & B_{3,2} & \cdots & B_{3,N-1} & 0 \\ \vdots & \vdots & \vdots & \vdots & \vdots \\ 0 & 0 & \cdots & B_{N,N-1} & 0 \end{bmatrix}, \quad \overline{C}(t) = \begin{bmatrix} C_1(t) & C_2(t) & \cdots & C_N(t) \end{bmatrix}$$

The last term in each row of $\overline{B}_1(t)$ has been deleted to remove the $(N+1)^{th}$ order terms $x^{(N)}(t)u(t)$. The closed-form expression of the Volterra kernels are analytically defined as

$$\begin{aligned} &h_o(t) = \overline{C}(t)\Phi(t,0)x_0^{\otimes} \\ &h_k(t,\tau_1,\cdots,\tau_k) = \\ &\overline{C}(t)\overline{\Phi}(t,\tau_1)\overline{B}_1(\tau_1)\overline{\Phi}(\tau_1,\tau_2)\overline{B}_1(\tau_2)\cdots\overline{B}_1(\tau_{k-1})\overline{\Phi}(\tau_{k-1},\tau_k)\overline{B}_1(\tau_k)\overline{\Phi}(\tau_k,0)x_0^{\otimes} \\ &+\overline{C}(t)\overline{\Phi}(t,\tau_1)\overline{B}_1(\tau_1)\overline{\Phi}(\tau_1,\tau_2)\overline{B}_1(\tau_2)\cdots\overline{B}_1(\tau_{k-1})\overline{\Phi}(\tau_{k-1},\tau_k)\overline{B}_0(\tau_k) \end{aligned} \tag{2.40}$$

Note the kernels of the bilinear system are of the triangular form.

2.4.2 Growing Exponential Approach

Assume the input as a sum of excitations in the form of

$$u(t) = \sum_{i=1}^{N} e^{\lambda_i t} \tag{2.41}$$

and the output is assumed as

$$y(t) = \sum_{i=1}^{N} G_{m_1,\cdots,m_i,0,\cdots,0}(\lambda_1,\cdots,\lambda_i)e^{(m_1\lambda_1+\cdots+m_i\lambda_i)t} \tag{2.42}$$

where m_i is a counter for each parameter λ_i. By substituting the assumed input and output forms in the differential equation and solving for $G_{1,0,\cdots,0}(\lambda_1), G_{1,1,0,\cdots,0}(\lambda_1,\lambda_2), \cdots, G_{1,1,\cdots,1}(\lambda_1,\lambda_2,\cdots,\lambda_N)$, a set of linear algebraic equations is generated for the kernels in the complex Laplace domain. By equating the coefficients of like exponents, the symmetric kernels are computed as

$$\begin{aligned} H_1(s) &= cG_{1,0,\cdots,0}(\lambda_1) \\ H_2(s_1,s_2) &= \frac{c}{2!}G_{1,1,0,\cdots,0}(\lambda_1,\lambda_2) \\ &\vdots \\ H_N(s_1,s_2,\cdots,s_N) &= \frac{c}{N!}G_{1,1,\cdots,1}(\lambda_1,\lambda_2,\cdots,\lambda_N) \end{aligned} \tag{2.43}$$

where s denotes complex frequency and

$$H_k(s_1,\cdots,s_k) = \int\cdots\int h_k(\tau_1,\cdots,\tau_k)e^{-(s_1\tau_1+\cdots+s_k\tau_k)}d\tau_1\cdots d\tau_k \tag{2.44}$$

2.4.3 Variational Approach

The variational method assumes the state vector derivative $\dot{x}$ is expandable as an infinite power series in terms of the state vector $x \in R^n$ and scalar input $u \in R^1$ around an arbitrary point, defined by (x_o, u_o), as

$$\dot{x} = f(x,u) = \sum_{i=0}^{\infty}\sum_{j=0}^{\infty}\tilde{K}_{ij}x^{(i)}u^j \quad , \quad x^{(i)} = x\prod_{k=1}^{i-1}\otimes x \quad \text{and} \quad x^{(0)} = 1 \quad , \quad x^{(1)} = x \tag{2.45}$$

The matrix $\tilde{K}_{ij}$ of dimension $n \times n^i$ is defined as

$$\tilde{K}_{ij} = \begin{bmatrix} (K_{11})_{ij} & \cdots & (K_{1n^i})_{ij} \\ \vdots & \ddots & \vdots \\ (K_{n1})_{ij} & \cdots & (K_{nn^i})_{ij} \end{bmatrix}, \quad i,j \in \{0,1,2,\cdots,\infty\} \quad \text{and} \quad \tilde{K}_{00} = 0 \tag{2.46}$$

Note $\tilde{K}_{00}$ has a null value. Thus, the expansion holds around an equilibrium point ($\dot{x} = 0$). The matrix $\tilde{K}_{ij}$ represents the derivatives of the vector function $f(x,u)$ with respect

to $x^{(i)}$ and u^i at point (x_o,u_o). The input u is generalized to be $\alpha u(t)$, where α is a tracking parameter that ultimately will be set to unity. In this case, the response $x(t)$ can be expanded in terms of α as

$$x = \sum_{i=1}^{\infty} \alpha^i x_i \tag{2.47}$$

By substituting in Equation (2.45) and rearranging according to the coefficients of α^i (i = *1, 2, ...*), a set of differential equations is generated as

$$\begin{aligned}
\dot{x}_1 &= \tilde{K}_{10}x_1 + \tilde{K}_{01}u \\
\dot{x}_2 &= \tilde{K}_{10}x_2 + \tilde{K}_{20}x_1^{(2)} + \tilde{K}_{11}x_1u + \tilde{K}_{02}u^2 \\
\dot{x}_3 &= \tilde{K}_{10}x_3 + \tilde{K}_{30}x_1^{(3)} + \tilde{K}_{20}\left[x_1 \otimes x_2 + x_2 \otimes x_1\right] \\
&\quad + \tilde{K}_{11}x_2u + \tilde{K}_{21}x_1^{(2)}u + \tilde{K}_{12}x_1u^2 + \tilde{K}_{03}u^3 \\
&\vdots
\end{aligned} \tag{2.48}$$

Equation (2.48) represents the system as an infinite set of differential equations. Although this expansion extends the n-dimensional problem to infinite dimension, the original nonlinearity of the system is broken into a sequence of pseudo-linear time invariant (PLTI) systems, which are solvable. The input of each PLTI system is a nonlinear function of all previous system states and the input u. Figure 2.5 shows the schematic diagram of the method for the PLTI systems through the k^{th} term.

In Figure 2.5, the first PLTI system has a linear transition matrix $\Phi(t\text{-}t_0)$ based on the square matrix $\tilde{K}_{10}$, which is excited by an input u multiplied by the column vector $\tilde{K}_{01}$. The state response of this system x_1 has a closed-form convolution integral solution in term of u. This solution is mapped to the next PLTI system by a nonlinear function $f_1(x_1,u)$. This sequence is repeated for a certain number k, which provides satisfactory results. Note that $f_{i-1}(x_1,x_2,\ldots,x_{i-1},u)$, where $i = 2,3,\ldots,k$, automatically keeps the order of input u to the power i. For example, $f_1(x_1,u)$ is a sum of u^2, x_1u, and $x_1^{(2)}$. By substituting for x_1 as a convolution integral of u, the bilinear term x_1u and the state quadratic term $x_1^{(2)}$

become a function of u^2. Then, x_2 is defined as a convolution integral of u^2. In general, this condition is not essential to the method, but it is necessary to extract the kernels.

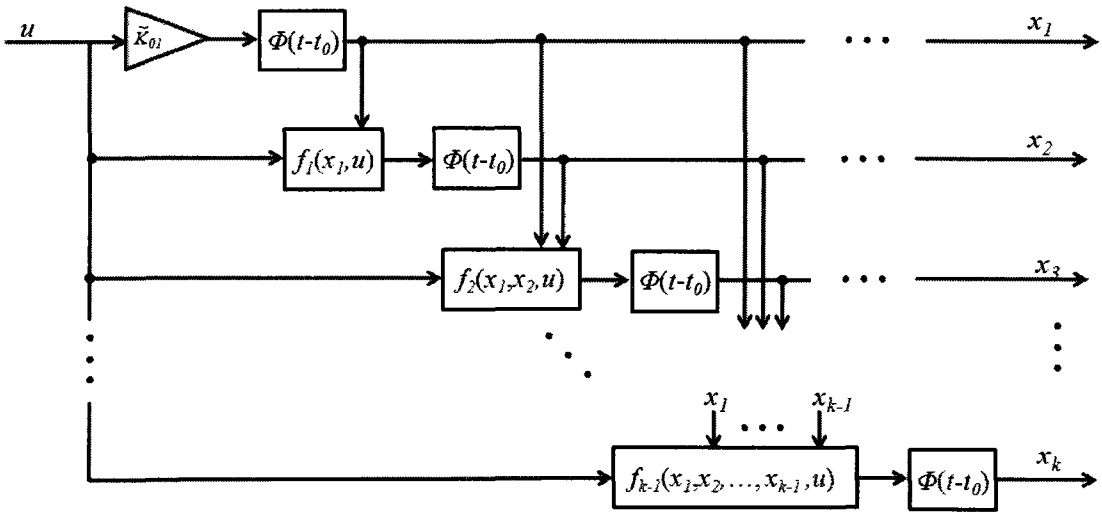

Figure 2.5 Variational Expansion Method Schematic Diagram

The Carleman linearization method, growing exponential method, and variational expansion method have been proposed for single input single output systems. More investigation is required to extend these methods for multiinput multioutput systems. The growing exponential method provides the kernels as a set of N-dimensional Laplace domain transfers. However, the method delivers the kernels in unwieldy forms, which restricts the applicability for nonlinear characterization. The Carleman linearization or bilinearization method delivers the kernels in a triangular form. The method is mathematically simple. However, the method replaces the nonlinear system by a higher order bilinear system, which limits practical usage to only affine systems. The differential method is more general. The generated kernels are not necessarily restricted to being symmetric or triangular as in the other methods. However, the method requires many special mathematical manipulations during conversion to integral form. In this dissertation, the variational method is used throughout Chapters 3-5.

CHAPTER 3

PIECEWISE VOLTERRA APPROACH

This chapter is dedicated to the piecewise Volterra approach, which facilitates the use of Volterra theory in a piecewise fashion for strong nonlinearity. In Section 3.1, the theory of the global Volterra methodology is presented. Section 3.2 starts by introducing the strength index to determine the order of the Volterra series for different sub-models. Subsequently, an algorithm based on this strength index to switch between the Volterra sub-models is listed. As a demonstration, the approach is applied to a simplified nonlinear model of a high performance aircraft longitudinal dynamics given in Section 3.3. Feasibility of the universal approach is determined by several input test cases in Section 3.4. Extracting the global kernels is discussed in Section 3.5.

3.1 Global Methodology

The number of Volterra series terms required to model the system behavior depends on two main attributes. The first is the strength of the nonlinearity involved in the system reflecting the number of required Volterra series terms in the sense of more terms for more nonlinearity. For example, a single degree of freedom first order system with a cubic nonlinearity defined by $\dot{x} = f(x) = ax^3 + bx + u$, where x is the state, u is the input, $f(x)$ is the system's state space function, and a and b are constants. Changing the ratio between a to b changes the strength of the nonlinearity. Figure 3.1 shows the shape of $f(x)$ for different values of a and b. In Case 1, the system is linear and then the first term of the Volterra series is enough to capture the system's behavior. The inherent twist or the curvature in the function $f(x)$ increases with the increase in the case number on Figure 3.1. More specifically, in Case 3, the system has more curvature or twist (more nonlinearity) than in Case 2. The dynamical analysist can then tell that the number of Volterra series terms to render the system behavior in Case 3 is more than in Case 2.

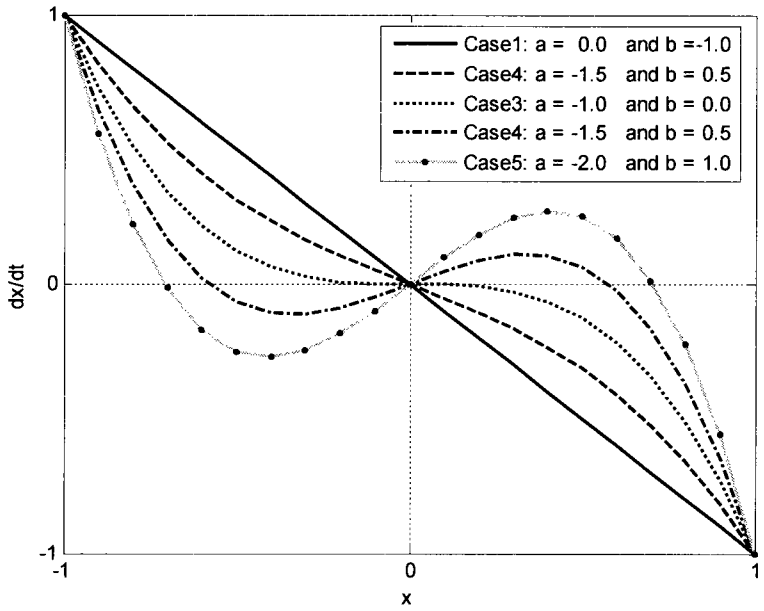

Figure 3.1 Cubic Nonlinearity Strength

The second attribute is the operating space range to be covered by the model. Hence the series is expanded around an operating point, and a wider range to be captured by the model requires more terms in the series. For example, recall Case 5 on Figure 3.1 and consider that three different Volterra series around the origin are required to cover three different operating spaces R_1, R_2, and R_3 as shown in Figure 3.2. It is clear that the number of terms in the Volterra series to cover the space R_3 is more than space R_2, which is more than the space R_1. However, in the case of nonlinearity strength (see Figure 3.1) or in the range case (see Figure 3.2), there is no quantitative scale or gauge to tell exactly how many term are required in each case. In the next section, the concept of "Strength Index" is developed to measure the required number terms of the Volterra series (strength of the nonlinearity) to render the system behavior in a certain region.

These two attributes show that sometimes the overall behavior of the system can not, or should not, be represented by a single series high order expansion. Hence if the series is expanded around an operating point, increasing the range and/or the strength of the nonlinearity to be captured by the model will require more terms in the series. Unfortunately the convolution integral becomes ever more computationally expensive

with more terms. For example, take the case in Figure 3.2. If a series is expanded around $x_0 = 0$ or $u_0 = 0$ and the required covered range is $|x| < 1$, an n^{th} order Volterra series will be required then. For this case in Figure 3.2, n is at least seven and may be more. The model will involve a potentially prohibitive n^{th} (at least 7^{th}) dimensional integral. Instead, the entire range can be replaced by five sub-models of k^{th} (2^{nd} or 3^{rd}) order Volterra series as shown in Figure 3.3. The new model has in general k kennels instead of n kernels, where $k < n$. This reduction in the number of the kernels not only reduces the computational cost, but also facilitates the process of understanding the dynamical insight of the system. Thus, visualizing and analyzing a two dimensional surface of the 2^{nd} order kernel is much easier than a five dimensional surface of the 5^{th} order kernel.

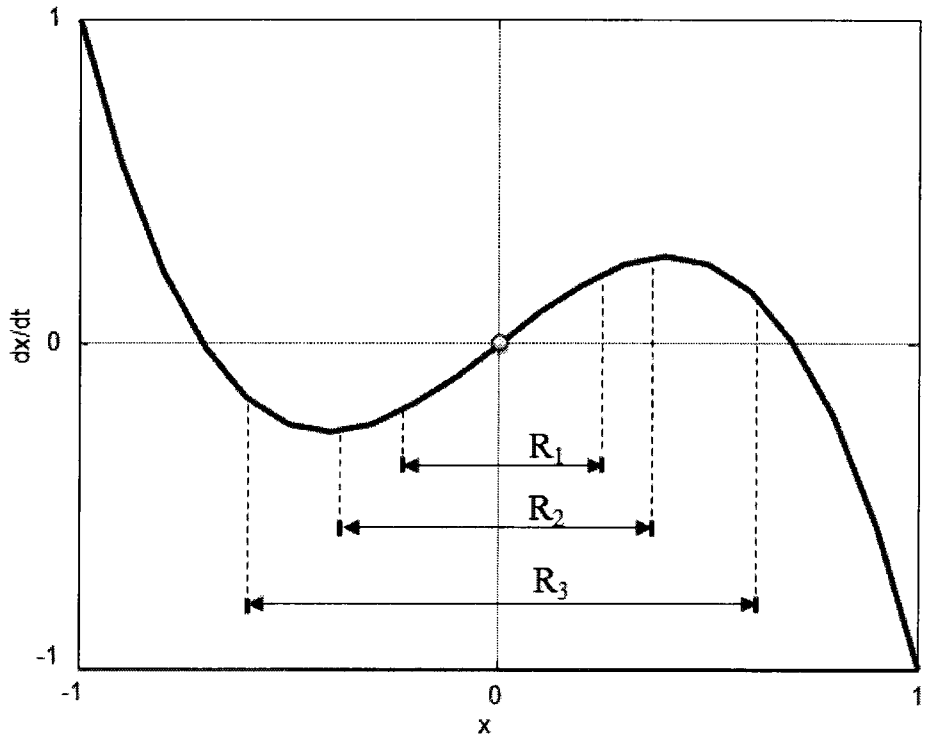

Figure 3.2 Operating Space Range of Cubic Nonlinearity

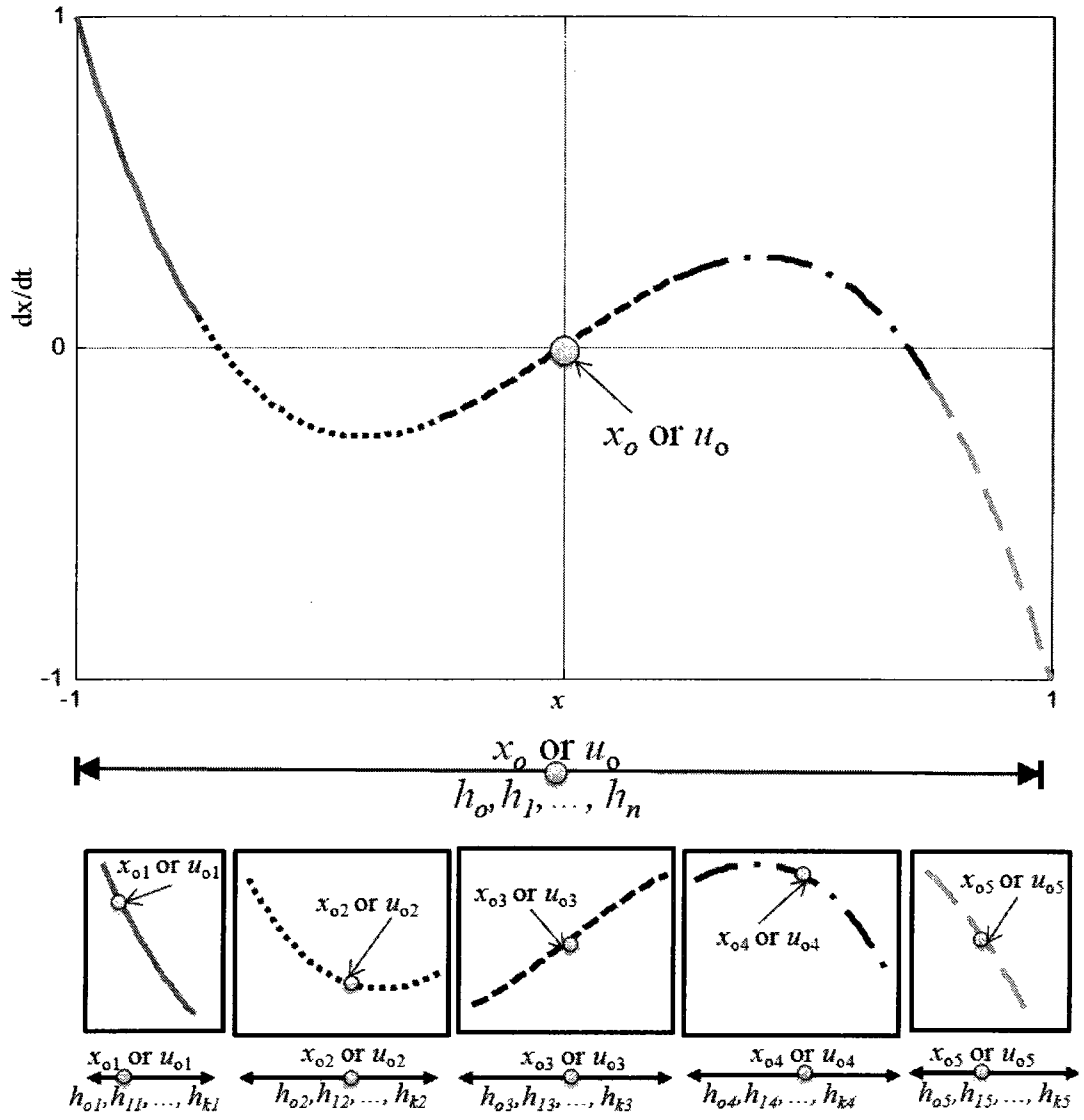

Figure 3.3 Schematic Diagram of Piecewise Approach

The global Volterra approach is proposed here to assemble the kernels in all of the sub-regions. This assembly process is constructed through interpolation or modeling techniques such as piecewise, linear, spline, or design of experiments. The assembly or the modeling process considers the operating conditions (x_o or u_o) to be the interpolation factor. This interpolation factor will increase the kernel dimension, as the kernel must be scheduled according to the current value of the factor. For example, in the case of the 1st kernel $h_1(t)$ of the system in Figure 3.3, a new modeling or interpolation dimension will be added making $h_1(t, x_o)$ or $h_1(t,u_o)$. In this chapter, piecewise interpolation is used to

switch between the sub-systems in the simulation process. The piecewise Volterra approach is more suited for a handy nonlinearity as in the given example (see Figure 3.3), where one can manually break down the nonlinearity or the range to pieces. The assembly process should be then considered carefully in order to retain smoothness and continuity when switching between these sub-regions. Other important issues in this process are determining the number of sub-regions, the range or amplitude of each sub-region, and the operating point location within each sub-region. A systematic algorithm to apply the piecewise interpolation and to address these other issues is given in the next section.

3.2 Strength Index and Piecewise Switching Algorithm

The traditional technique to determine the number of required terms in the series for modeling the system dynamics is based on trial and error. First a model with n terms is initially constructed. The model is then compared to the nonlinear simulation for selected test cases. New terms are included, or existing terms are deleted, depending on the comparison results. The technique is a trade-off between number of terms and response accuracy. This technique is time consuming, and the simulated test cases can not cover all possibilities of system behavior. For these reasons, a new function called the "Strength Index" S is proposed in the current research. This index uses the estimated diagonal values of each input dependent kernel, instead of the extensive simulation across all kernels, to judge their importance. The index S_i is defined as a convolution line integral over the diagonal kernel of i^{th} order multiplied by the same order of input, as demonstrated in Equation (3.1). An absolute value applied to the integral argument will be preferred to avoid the possibility of integral area cancelling.

$$S_i = \int_0^{t_H} \left| h_i(\tau, \tau, \cdots, \tau) u(\tau)^i \right| d\tau \qquad \text{and} \qquad i = 1, 2, 3, \cdots, n \tag{3.1}$$

Each index S_i is considered as a gauge to measure the magnitude of each term in the system model. Thus a large strength index value for S_i, relative to S_1, means that the corresponding kernel has a significant contribution in rendering the system behavior, and vice versa. In this way, Equation (3.1) is used to determine how many terms should be considered in the model.

An important issue concerns the switching between sub-model Volterra series, when the system transitions from one operating point to another across several sub-ranges. Global linear models are typically constructed based on the interpolation between the linear sub-models at different operating points. A linear gain scheduled control system is a prime example. In this way, use of a global Volterra series is proposed. This approach is addressed by employing the sub-model Volterra kernels in an interpolation procedure. Effectively a new dimension is added to the series kernels. For example the first kernel will have two arguments instead of one, or $h_1(t,u_o)$ instead of $h_1(t)$, where u_o is the operating point around which the sub-model is constructed. An interpolation technique is used to move through the tables of Volterra kernels. The number of sub-models and the range of each model may have a large effect on global model accuracy, therefore an intelligent sequence is outlined here to find an appropriate number of the sub-models, the range of each one, and the operating point locations. The sequence is organized as shown next.

1) Select an operating point within a candidate sub-space. The selected operating points should lay in a region of stability. In this way, all the estimated kernels either diminish or oscillate as the time arguments (τ_1, τ_2, ...) grow to infinity.
2) Assume an n^{th} order Volterra series model as an initial trial.
3) Use Equation (2.26) to compute the state dependent kernel and the diagonal value of each input dependent kernel.
4) Compute the strength index of each input dependent kernel using Equation (3.1).

5) Compare the strength index value of each kernel with respect to the first one. If the strength ratio is more than 10%, then the kernel is considered to be significant in the model.
6) Reduce or expand the order of the model based on the strength ratio results.
7) Render the sub-space by exciting the approximate model by a step input with different amplitudes and compare the response to the nonlinear simulation. The sub-space is defined as the region where the response error is within a specified tolerance.
8) Sweep the operating point forward and backward across the sub-space and return to Step 2 to maximize the range and minimize the number of kernels.

Since convergence of the Volterra series generation is excitation amplitude dependent, these amplitudes must be carefully chosen. Amplitude selection is based on constraining the responses to remain within the sub-region of interest while simultaneously forcing the responses to transit nearly all of the sub-region. Selecting amplitude in this way allows for identification of nonlinearities residing within the sub-region of interest and avoids convergence issues associated with computing higher order kernels across all sub-regions with large amplitude excitation. Since accuracy of the Volterra series is strength index cutoff dependent, the cutoff must be chosen for the intended application. For the application of system analysis, rather than high fidelity simulation, a cutoff of 10% is reasonable.

3.3 Longitudinal Aircraft Example

A simplified longitudinal dynamic model of a high performance aircraft is chosen as an example for the proposed piecewise Volterra approach. The model is addressed in References 83 and 104 for the short period mode, where the motion involves rapid changes to the angle of attack and pitch attitude at roughly constant airspeed. The suitability of this model is that the dynamics cover both linear and nonlinear flight

behavior through an extensive range in angle of attack. The model is mathematically described as

$$\dot{\alpha} = q + 9.168C_Z(\alpha) - 1.834(\delta_e + 7^o) + 7.362$$
$$\dot{q} = 5.730(C_{m\alpha}\alpha + C_{m\delta e}\delta_e) + 2.865$$
$$C_Z(\alpha) = \begin{cases} -0.07378\,\alpha & , \quad \alpha \le 14.36^o \\ 0.09722\alpha^2 - 2.865\,\alpha + 20.04 & , \quad 14.36^o \le \alpha \le 15.6^o \\ -0.01971\alpha^2 + 0.7439\alpha - 7.808 & , \quad 15.6^o \le \alpha \le 19.6^o \\ -0.4733 - 0.01667\alpha & , \quad 19.6^o \le \alpha \end{cases} \tag{3.2}$$

In Equation (3.2), α is the angle of attack in degree, q is the pitch rate in degree per second, δ_e is the elevator control surface deflection in degree, $C_Z(\alpha)$ is the plunging force coefficient, $C_{m\delta e}$ is the pitch moment coefficient with elevator deflection, and $C_{m\alpha}$ is the pitch moment coefficient with angle of attack. The model is simplified further by fixing the pitching coefficients as $C_{m\alpha}$ = -1 1/deg and $C_{m\delta e}$ = -1.5 1/deg. The sole nonlinearity in the model is the plunging force coefficient $C_Z(\alpha)$. The coefficient behavior is shown in Figure 3.4. The nonlinearity approximates stall and lift recovery at high attack angles. The $C_Z(\alpha)$ model originally was discrete data points collected from a wind tunnel test. The coefficients in Equation (3.2) were then numerically computed to provide a fit for these points over the corresponding α intervals as mentioned in References 83 and 104.

Figure 3.4 shows how the plunging force coefficient has different slope values. Every distinct slope demonstrates different characteristics in system behavior. The constant slope value in the pre-stall and post-stall regions renders linear system behavior. From the linear perspective, the system is plunge axis statically stable in these regions. Thus, a negative rate of change in plunging force coefficient creates a damping plunge force counteracting the original perturbation. Along with the negative pitch axis static stability ($C_{m\alpha} < 0$), this damping force contributes to the aircraft returning to trimmed equilibrium flight in the sense of dynamic stability. Note in the pre-stall regime, the settling time is less than in the post-stall regime, because of the larger slope value in

Figure 3.4. On the other hand, the significant curvature in the stall regime renders nonlinear system behavior. The stall regime can be split into two sub-regimes. The first one is the pre-stall/stall regime. In this sub-regime, the slope switches from negative to positive or from stability to instability. The second one is the stall/post-stall regime, where the slope switches from instability to stability. Both sub-regimes capture the nonlinear behavior of the system as unstable and stable limit cycles. Note the classical pitch static margin characterization of stability is not applicable to the Equation (3.2) model having a fixed $C_{m\alpha}$ but independently varying nonlinear $C_Z(\alpha)$. Also note the nonlinearity is a function of the angle of attack, but elevator deflection is the core mechanism to move through the various regimes. In the case of stable linear behavior, the analogous value of elevator deflection is below -9.5 deg or above -11 deg, and in between these values both unstable and stable limit cycle behavior is experienced.

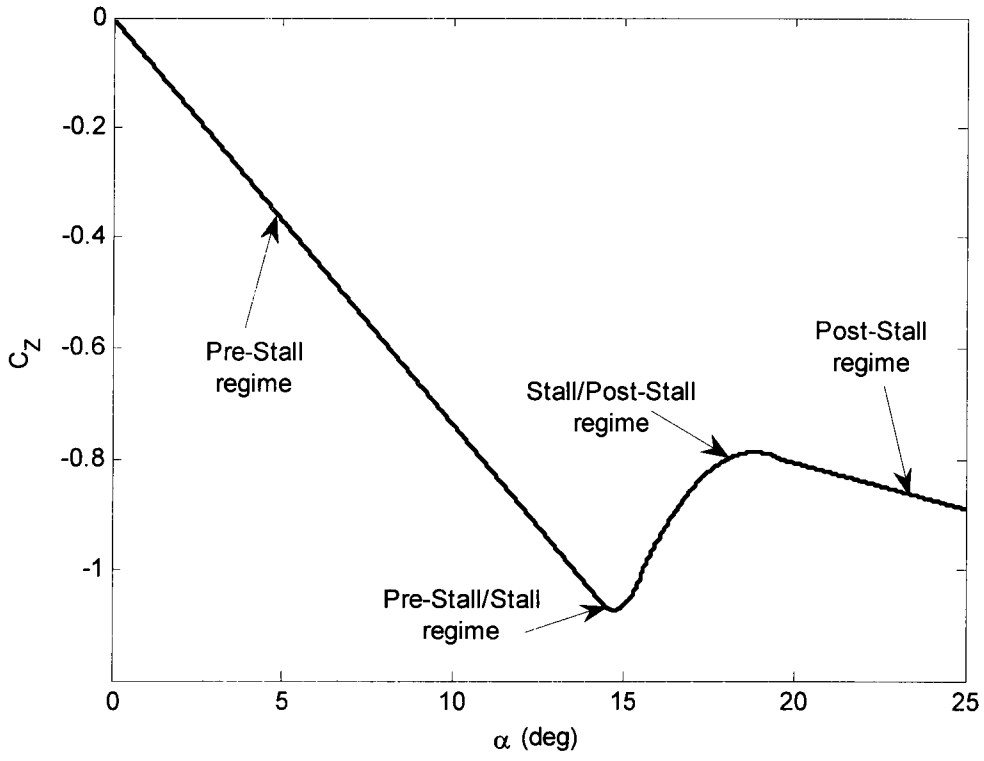

Figure 3.4 Nonlinear Plunging Force Coefficient $C_z(\alpha)$

Here the space is divided into four sub-spaces based on the range of elevator deflection, consistent with Equation (3.2). Two sub-spaces exist for linear behavior in the pre-stall and the post-stall regions, and two for nonlinear behavior in the stall regimes also exist. For the two nonlinear sub-spaces, the points around which the series were expanded were selected to have a negative slope. For example, in the pre-stall/stall sub-space, C_Z initially decreases with increasing angle of attack (negative slope) until a minimum point (α = 14.74 deg or δ_{eo} = -9.5 deg) is reached. After this minimum point, C_Z increases with an increasing angle of attack (positive slope). To avoid expanding on unstable behavior (positive slope), the operating point is selected to be δ_{eo} = -9.5 deg. In the same way, the operating point is selected in the stall/post-stall sub-space. This careful selection is a critical feature for success but it places the expansion points near the edge of the sub-regions.

After selecting the operating points, a fifth order Volterra series model is initially assumed as mentioned in Section 3.2. The diagonal waveforms of the kernels are computed for an angle of attack output signal, expanded around α = 0 deg and the elevator operating point value δ_{eo}, as a set of simultaneous equations as in Equation (2.26). One test case of the diagonal kernels is presented in Figure 3.5 for the stall/post-stall sub-space. These diagonal kernel waveforms are estimated around an operating point defined by δ_{eo} = -11 deg. Note the operating point can be defined by elevator deflection or the corresponding angle of attack at trim. Figure 3.5 shows that the first kernel is the most significant one followed by the second diagonal kernel. This qualitative observation can help in deciding how to reduce the order of the sub-model, but it is preferable to base this judgment on quantitative numerical criteria such as the strength index.

A strength index is used to evaluate the number of terms required to render the system's behavior in each sub-space. Table 3.1 mentions the value of the strength indices in each sub-space. Each index is computed by numerical integration. A 20 s time span and a unit step input are considered. Several iterations are conducted searching for

optimal operating points and ranges (see Table 3.1) based on the sequence listed in Section 3.2. The ratios between the strength of the first kernel S_1 and higher order strengths change from one sub-space to another depending on the level of nonlinearity. In the first sub-space, the strength index of the first kernel is the only significant value compared to the others. The strength index of the second kernel S_2 is raised in the second sub-space to be approximately 10% of the strength index of the first kernel. This quantification means the nonlinearity starts to appear in a significant way. The ratio of S_2 to S_1 in the second sub-space is the same as in the third sub-space implying the level of nonlinearity in the second and third sub-spaces is the same. In the fourth sub-space, the ratio S_2/S_1 decreases to 7% indicating reduced but still significant nonlinearity. The strength indices of the third and higher order kernels have very small values with less than 2% strength of S_1 in all sub-spaces. All these results indicate that the first and second order kernels are sufficient to render the system angle of attack behavior in all sub-spaces. The off-diagonal second order kernel values are then constructed. This overall kernel generation procedure was implemented on a desktop computer with reasonable turnaround time.

Table 3.1 Kernel Strength Indices

Sub-Space Index	Range (deg)	δ_{eo} (deg)	S_1 (deg)	S_2 (deg)	S_3 (deg)	S_4 (deg)	S_5 (deg)
1	$\alpha \leq 14.3$	0	7.7	2×10^{-12}	2.0×10^{-12}	9.9×10^{-12}	1.7×10^{-12}
2	$14.3 \leq \alpha \leq 15.6$	-9.5	23.7	2.3	0.57	0.22	0.082
3	$15.6 \leq \alpha \leq 19.6$	-11	24.6	2.2	0.45	0.15	0.055
4	$19.6 \leq \alpha$	-14	25.1	1.8	0.27	0.08	0.027

The accuracy of each sub-model is evaluated by step input excitation. A step input is used with different amplitudes. The estimated response is compared to the result of the nonlinear simulation. Figure 3.6 shows a comparison between the stall/post-stall Volterra series second order model and the nonlinear simulation response to a step input of -0.5 deg from the initial operating values δ_{eo} = -11 deg and α = 0 deg. The 2nd order sub-model is sufficiently accurate, even as the angle of attack crosses all four regions. However an increase in the amplitude of the input leads to a decrease in the accuracy. The results show how the reduced second order model of the Volterra series is able to render the system behavior in the four sub-spaces.

Combining the four sub-models into a global model, and assessing the accuracy across the entire operating range, is addressed next. For numerical simulation, a differential equation form of the Volterra series is more convenient than the integral form. This differential form is based on breaking down the original nonlinear differential equations into a sequence of pseudo-linear time invariant systems (PLTI) where the input to the next system is a nonlinear function of the previous system output. Based on Table 3.1, two terms of a Volterra series are enough to capture the system behavior for all regions using this piecewise interpolation technique. Thus, Equation (3.2) is broken down as the two pseudo linear differential equation sets

$$\begin{bmatrix}\dot{\alpha}_1\\ \dot{q}_1\end{bmatrix}=\begin{bmatrix}A_{11} & 1\\ -5.73 & 0\end{bmatrix}\begin{bmatrix}\alpha_1\\ q_1\end{bmatrix}+\begin{bmatrix}-1.834\\ 8.595\end{bmatrix}(\delta_e-\delta_{eo})$$

$$\begin{bmatrix}\dot{\alpha}_2\\ \dot{q}_2\end{bmatrix}=\begin{bmatrix}A_{11} & 1\\ -5.73 & 0\end{bmatrix}\begin{bmatrix}\alpha_2\\ q_2\end{bmatrix}+\begin{bmatrix}g(\alpha_1)\\ 0\end{bmatrix} \tag{3.3}$$

where A_{11}, δ_{eo}, and $g(\alpha_1)$ have different values for each sub-space as given in Table 3.2, and the output α equals the summation of states α_1 and α_2. Along with nonlinear simulation, the piecewise global Volterra approach is also compared to a linear piecewise global approach. The model is previously derived in Reference 83 for local behavior

evaluation. The model is a piecewise linear model of $C_z(\alpha)$. The state space model is documented in Equation (3.4).

$$\begin{aligned}
\begin{bmatrix}\dot{\alpha}\\ \dot{q}\end{bmatrix} &= \begin{bmatrix}-0.668 & 1\\ -5.73 & 0\end{bmatrix}\begin{bmatrix}\alpha\\ q\end{bmatrix} + \begin{bmatrix}-1.834\\ 8.595\end{bmatrix}\delta_e + \begin{bmatrix}12.84\\ 2.865\end{bmatrix} && \alpha \le 14.74^o\\
\begin{bmatrix}\dot{\alpha}\\ \dot{q}\end{bmatrix} &= \begin{bmatrix}0.811 & 1\\ -5.73 & 0\end{bmatrix}\begin{bmatrix}\alpha\\ q\end{bmatrix} + \begin{bmatrix}-1.834\\ 8.595\end{bmatrix}\delta_e + \begin{bmatrix}-34.60\\ 2.865\end{bmatrix} && 14.74^o < \alpha \le 17.4^o\\
\begin{bmatrix}\dot{\alpha}\\ \dot{q}\end{bmatrix} &= \begin{bmatrix}0.312 & 1\\ -5.73 & 0\end{bmatrix}\begin{bmatrix}\alpha\\ q\end{bmatrix} + \begin{bmatrix}-1.834\\ 8.595\end{bmatrix}\delta_e + \begin{bmatrix}-25.73\\ 2.865\end{bmatrix} && 17.4^o < \alpha \le 18.87^o\\
\begin{bmatrix}\dot{\alpha}\\ \dot{q}\end{bmatrix} &= \begin{bmatrix}-0.153 & 1\\ -5.73 & 0\end{bmatrix}\begin{bmatrix}\alpha\\ q\end{bmatrix} + \begin{bmatrix}-1.834\\ 8.595\end{bmatrix}\delta_e + \begin{bmatrix}8.715\\ 2.865\end{bmatrix} && 18.87^o < \alpha \le 28^o
\end{aligned} \tag{3.4}$$

Table 3.2 Differential Volterra Parameters of Equation (3.3)

Sub-space Index	A_{11} (1/s)	δ_{eo} (deg)	$g(\alpha_1)$ (deg/s)
1	-0.668	0	0
2	-0.671	-9.5	$0.891\ \alpha_1^2$
3	0.459	-11	$-0.181\ \alpha_1^2$
4	-0.153	-14	0

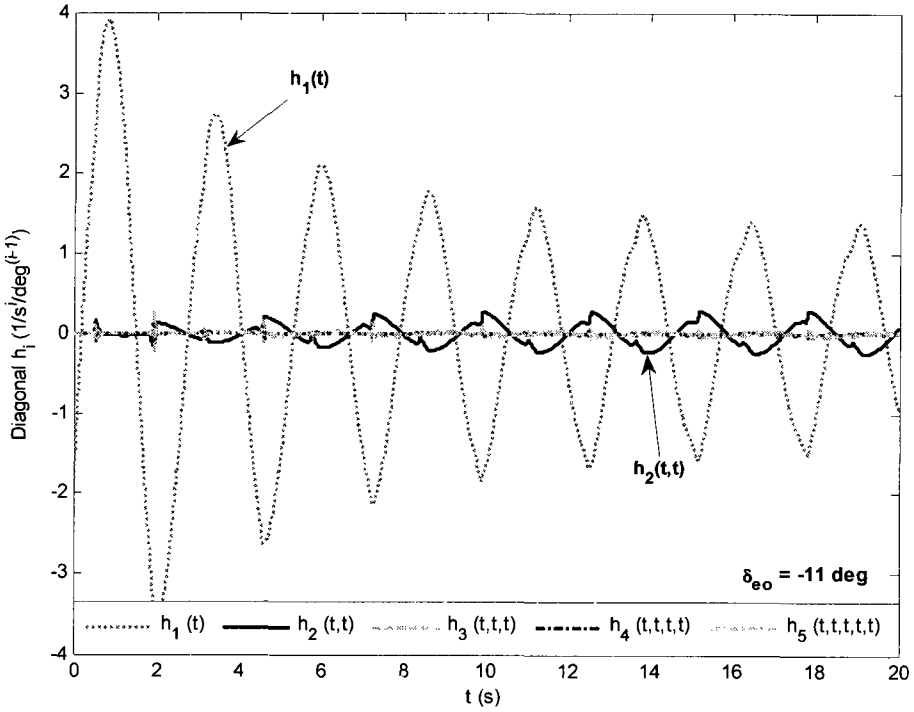

Figure 3.5 Diagonal Kernels of Fifth Order Model in Stall/Post-Stall Sub-Space

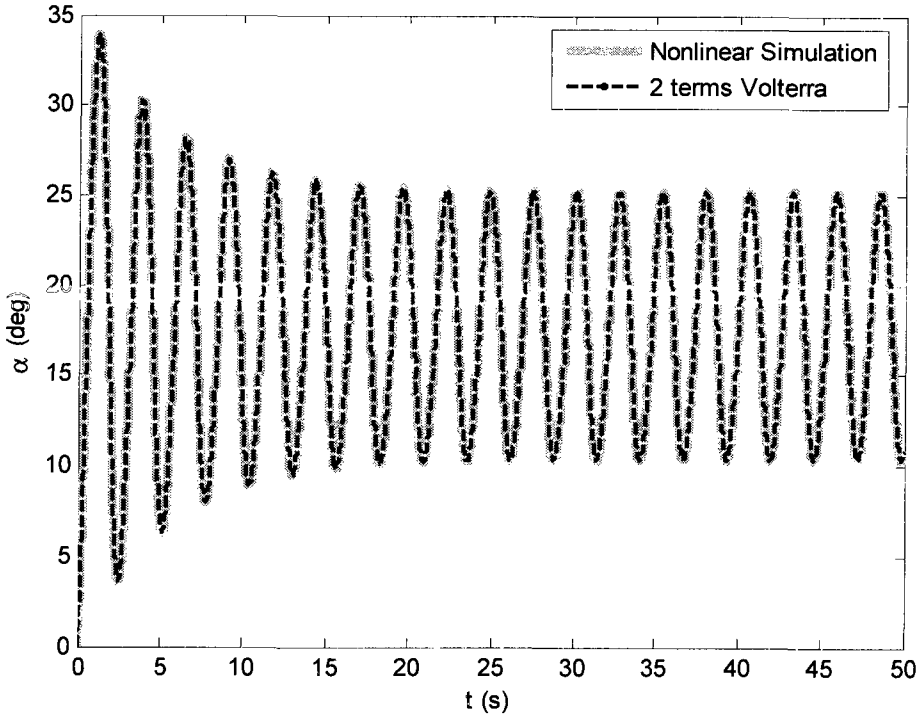

Figure 3.6 Angle of Attack Step Response of Stall/Post-Stall Sub-Model

3.4 Piecewise Volterra Model Validation

The piecewise global Volterra approach and its accuracy are evaluated by three test cases with different input waveforms. The first input signal is assigned to primarily validate the sub-models and the local behavior around certain operating conditions. The input is designed to have a fast smooth change from 0 deg to -9.5 deg within 5 s. The input is then held at -9.5 deg as shown in Figure 3.7. The final value is selected to lie inside a nonlinear region (pre-stall/stall). During the first 5 s, there is no large difference between the linear model and the Volterra model as shown in Figure 3.8. When the input starts to settle at δ_e = -9.5 deg, the nonlinearity becomes dominant and its signature appears in the system behavior as a limit cycle waveform. In this period, the linear model shows a significant inability to capture this phenomenon. The linear model responds as an oscillatory damped system, since this model has no mechanism to generate a limit cycle phenomenon. On the other hand, the Volterra model shows more adequacy to render the system behavior through the 2nd order kernel h_2. The maximum amplitude error from the Volterra model for this approximately 4.5 deg amplitude angle of attack limit cycle is 0.5 deg compared to 4.5 deg error in the linear model case. Both models do a good job of predicting the oscillation frequency. Based on this test case, the Volterra model shows ample ability to capture nonlinear behavior with reasonable qualitative and quantitative accuracy in the sub-models (see Figure 3.8).

In addition to the time response, a parametric time track is visualized over the phase plane for further analysis as shown in Figure 3.9, where the rate of attack angle is plotted against the attack angle from t = 0 s to t = 100 s. During the first 5 s, there is no difference between the linear model track and the Volterra model track compared to the nonlinear simulation track. As the tracks start to intersect the vertical line of α = 14.7 deg (minimum value of C_z, see Figure 3.4), each track heads in a different direction. The linear model track forms a spiral orbit converging at the attractor point (α = 14.7 deg and

$d\alpha/dt = 0$). This track is a damped oscillatory response. In contrast, the Volterra model and nonlinear simulation tracks head away to form a limit cycle with a semi cardioid shape. To the left side of the line $\alpha = 14.7$ deg, the cardioid path has a tendency to move towards the attractor point or a tendency for stability (negative slope of C_z). After the track crosses to the right of this line, the tendency is inverted to instability or divergence (positive slope of C_z). Hence the indentation near $\alpha = 14.7$ deg and $d\alpha/dt > 0$ appears when moving from a stable C_Z to an unstable C_Z, and likewise the protuberance near $\alpha = 14.7$ deg and $d\alpha/dt < 0$ appears when moving from an unstable C_Z to a stable C_Z. Eventually a balance between these two competing effects ensues and the system forms a limit cycle with smooth curvature around the line $\alpha = 14.7$ deg. Note the linear model track crosses this line with a slope discontinuity. Observations based on the phase plane (see Figure 3.9) imply the Volterra model has high capability to render smooth inversion of the slope of C_Z from negative to positive values in the same way as the nonlinear simulation, which the linear model can not provide.

The second input is assigned to have more excitation range and to move over and return across the sub-regions in rapid succession. The input starts to excite the dynamic behavior from the pre-stall linear region going through the entire space (from $\delta_e = 0$ deg to $\delta_e = -14$ deg), returning back to the pre-stall linear region ($\delta_e = -5$ deg), and finally settling in the pre-stall/stall nonlinear region as shown in Figure 3.10. Although both linear and Volterra models have a close qualitative behavior in rendering system dynamics during the first 50 s, the linear system proves very poor in rendering system behavior in the final duration (from $t = 50$ s to $t = 120$ s). This observation from the second test case (see Figure 3.11) indicates that linear and Volterra models have the same level of accuracy if switching between regions is very fast (sharp change in input). The breakdown of the linear model beyond $t = 50$ s is again due to an inability to perform sustained oscillation. The Volterra model again has less than 0.5 deg error in angle of attack across the entire test case relative to the nonlinear simulation. Also the phase plane

shown in Figure 3.12 leads to the same conclusion from the time response. Thus the linear model and Volterra model tracks have the same performance during the fast change in the input. However the linear track loses its accuracy when the input is held in the pre-stall/stall nonlinear region.

Because of the insensitivity to rapid input changes, test case three assigns an input with smooth movement over the entire space as shown in Figure 3.13. This input tries to imitate the real movement of input experienced in practice (generated from bio-pilot or autopilot), which should be dynamically smooth. Figure 3.14 shows that linear and Volterra models are quantitatively close. The maximum error developed by the linear model is 1.2 deg compared to 0.4 deg developed by the Volterra model for an overall 25 deg change in angle of attack. From the qualitative perspective, the Volterra model is more adequate (see Figure 3.14), especially in rendering system hysteresis. In the first duration (from t = 0 s to t = 15 s), both linear and Volterra models provide close results. Conversely, the linear model starts to have less accuracy in the second half of the maneuver (from t = 20 s to t = 40 s). Thus some residual state is accumulated in the system memory when passing through the nonlinear region in the first duration. This accumulated memory appears in the second half of the maneuver, primarily as amplitude growth. Such a phenomenon can not be captured by the linear model as the Volterra model does. After the memory effect dissipates both systems return to the same equilibrium at t = 45 s.

Because of the large excitation in this test case, a phase plane is plotted in two segments. Figure 3.15 shows the phase plane in the first 10 s for when the system crosses from the linear region to the nonlinear regions. As it appears in Figure 3.15, both linear and Volterra model tracks follow the nonlinear simulation. However the linear model track starts to deviate as the system enters the nonlinear region. Figure 3.16 shows the second window of the phase plane from t = 10 s to t = 25 s. The three tracks rotate around the point defined by α = 14.7 deg and $d\alpha/dt$ = 0 deg/s by cardioid orbits (pre-stall/stall

region). The input then moves the track to rotate in another circular orbit (stall/post-stall region) around the point defined by α = 23 deg and $d\alpha/dt$ = 0 deg/s. Although linear and Volterra model tracks have the same shape, the Volterra model shows a superior performance with higher accuracy than the linear model. The linear track is incapable of producing the radius of this circular orbit in the nonlinear system. All these test cases validate the capability of the Volterra model to be quite adequate in rendering the global behavior of the system with nonlinear phenomena (limit cycle and amplitude hysteresis memory effect).

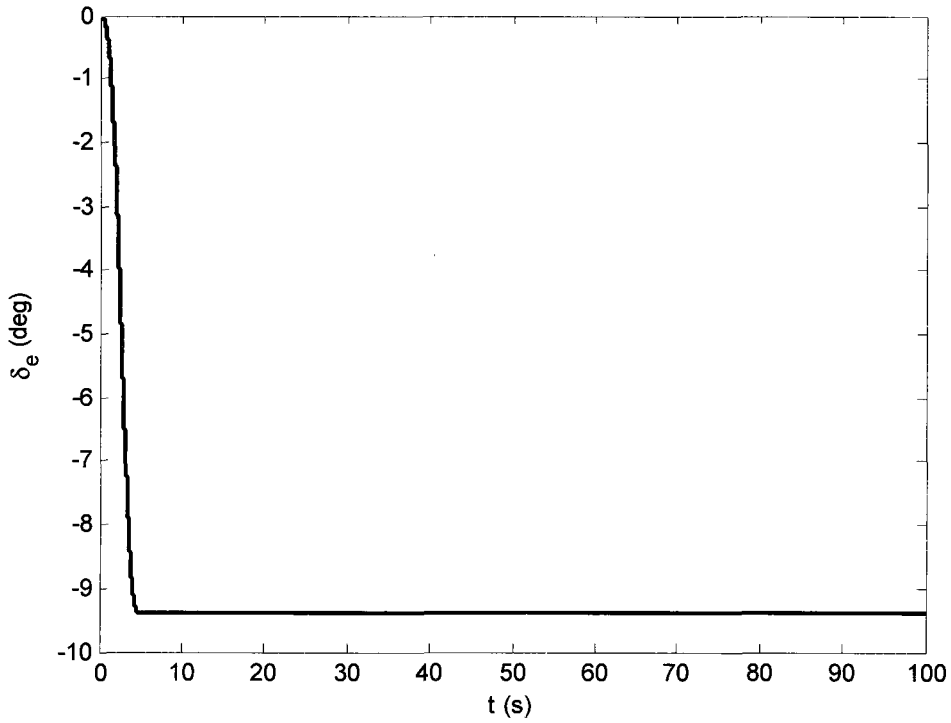

Figure 3.7 Step Input Test Case

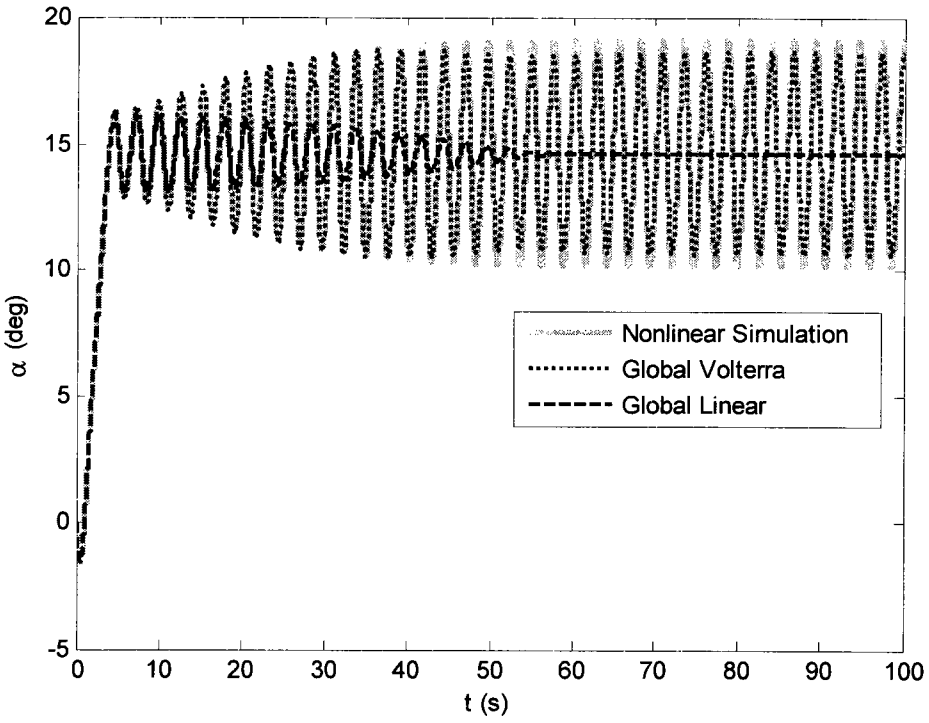

Figure 3.8 Step Response Test Case

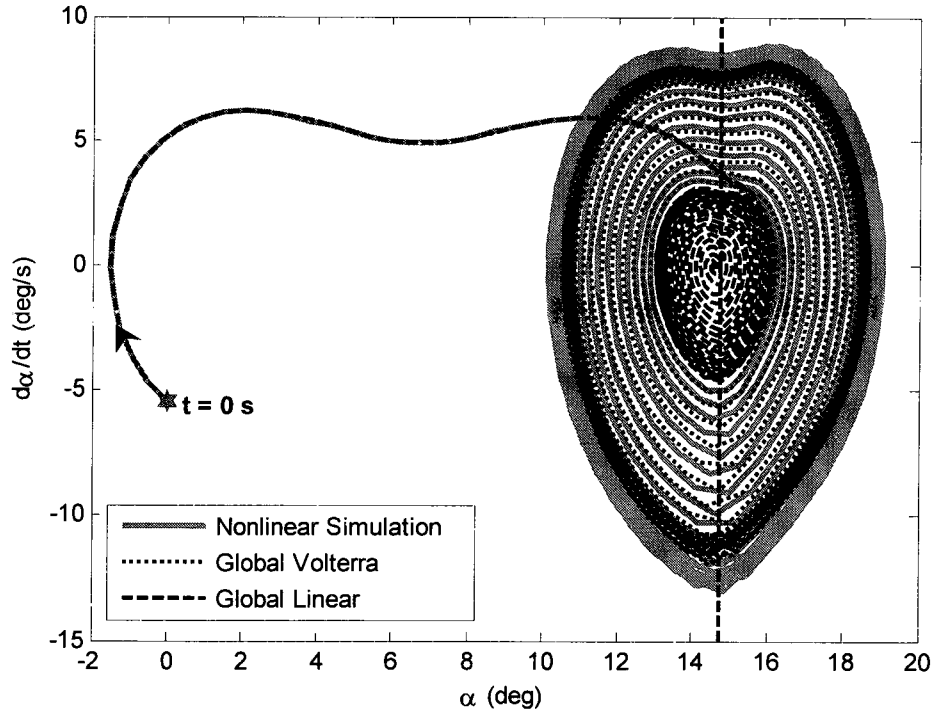

Figure 3.9 Phase Plane of Step Response Test Case

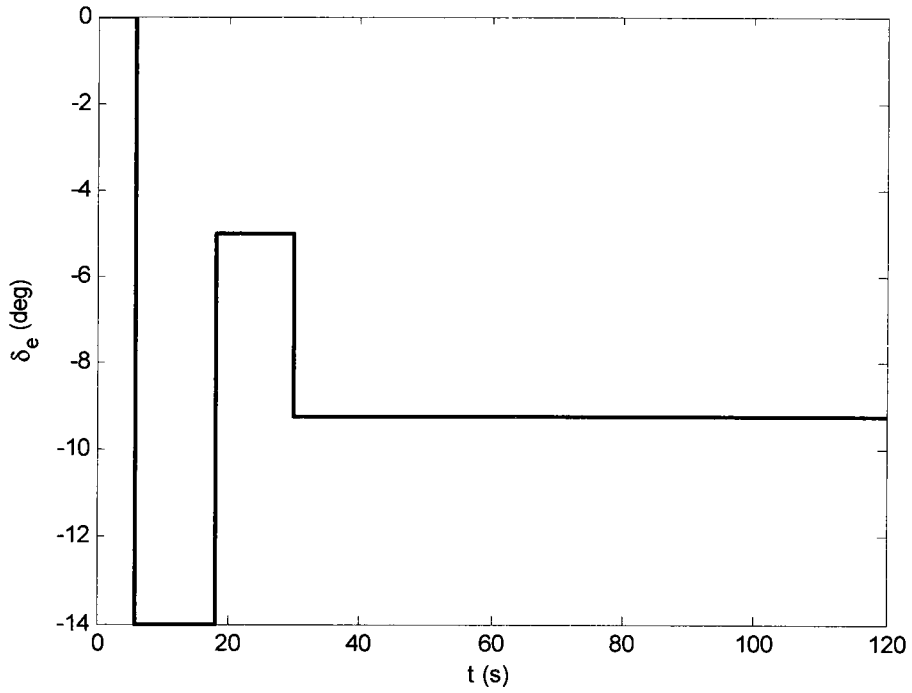

Figure 3.10 Bang-Bang Input Test Case

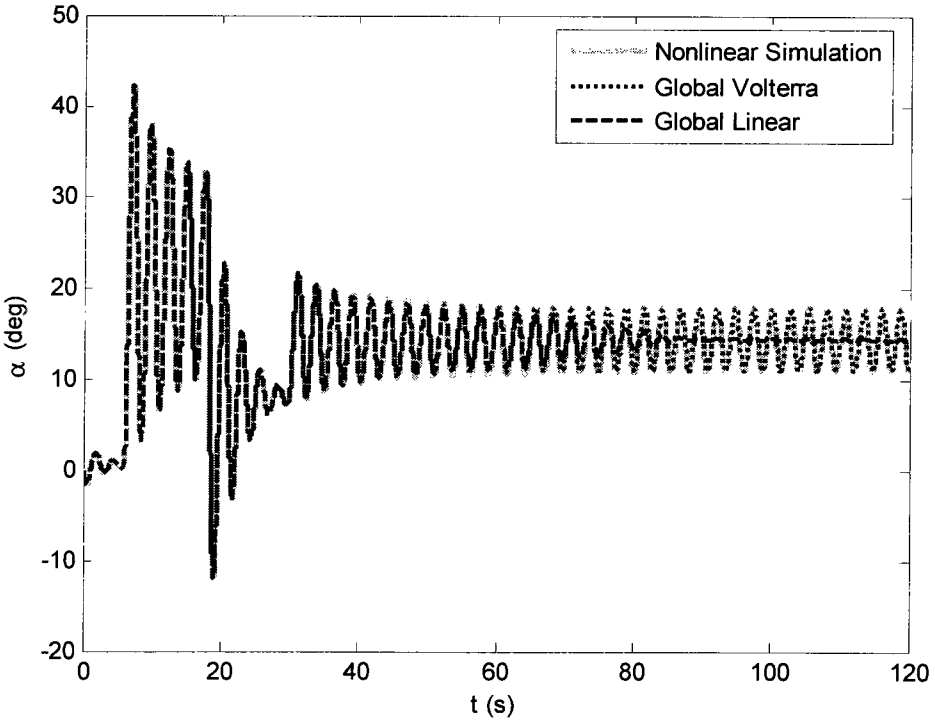

Figure 3.11 Bang-Bang Response Test Case

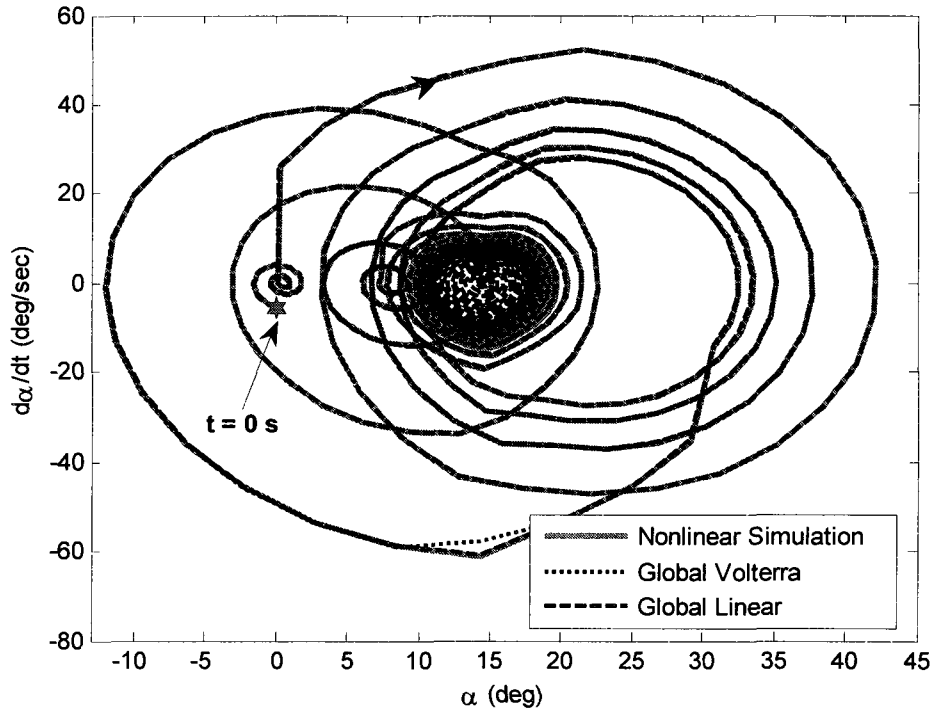

Figure 3.12 Phase Plane of Bang-Bang Response Test Case

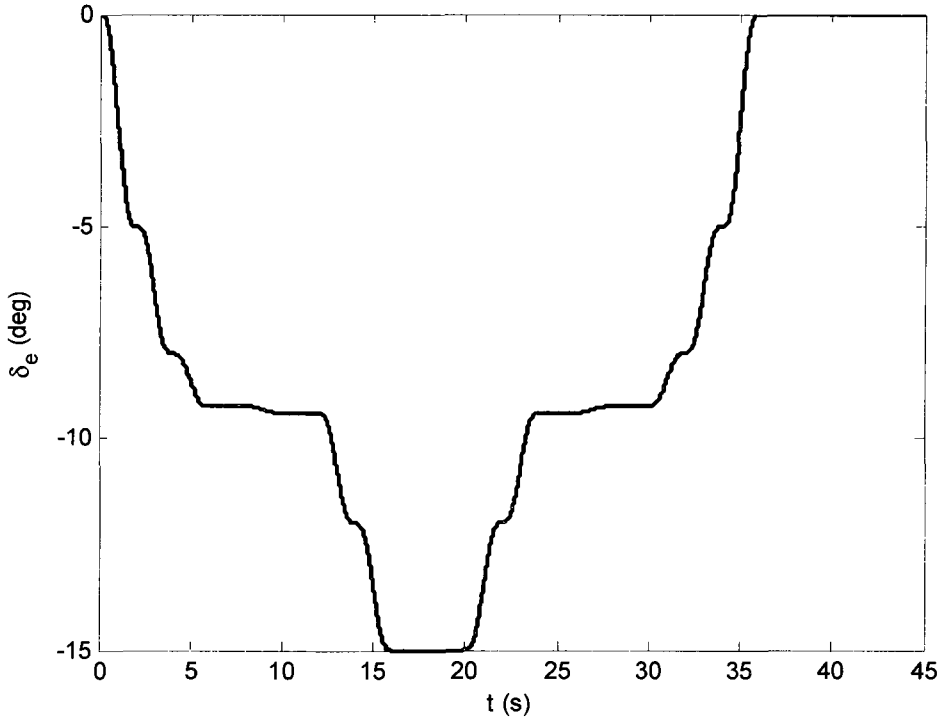

Figure 3.13 Stair Input Test Case

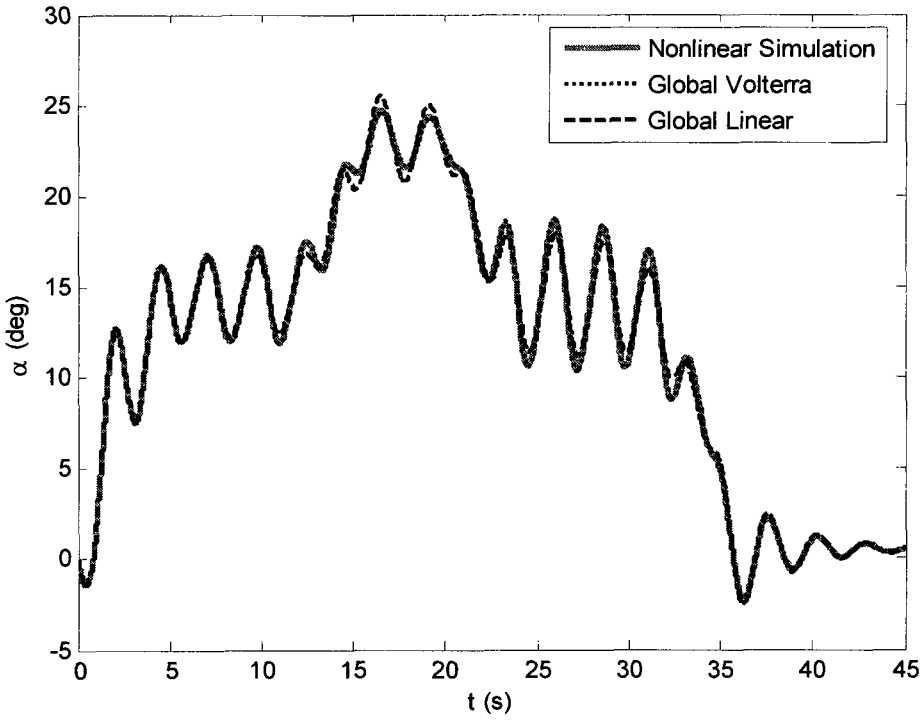

Figure 3.14 Stair Response Test Case

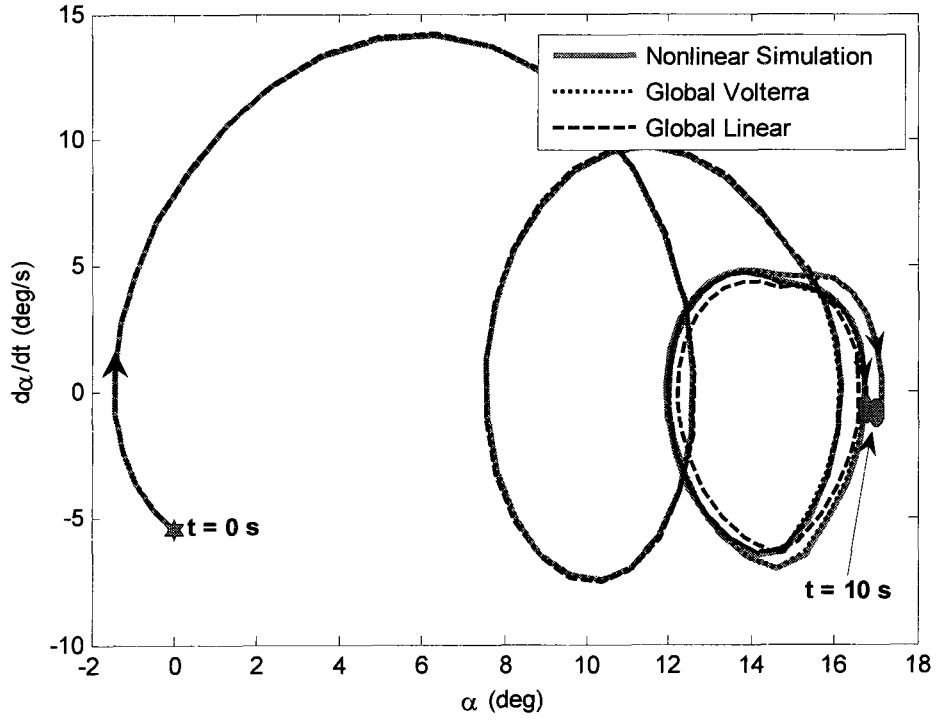

Figure 3.15 Phase Plane from $t = 0$ s to $t = 10$ s for Stair Response Test Case

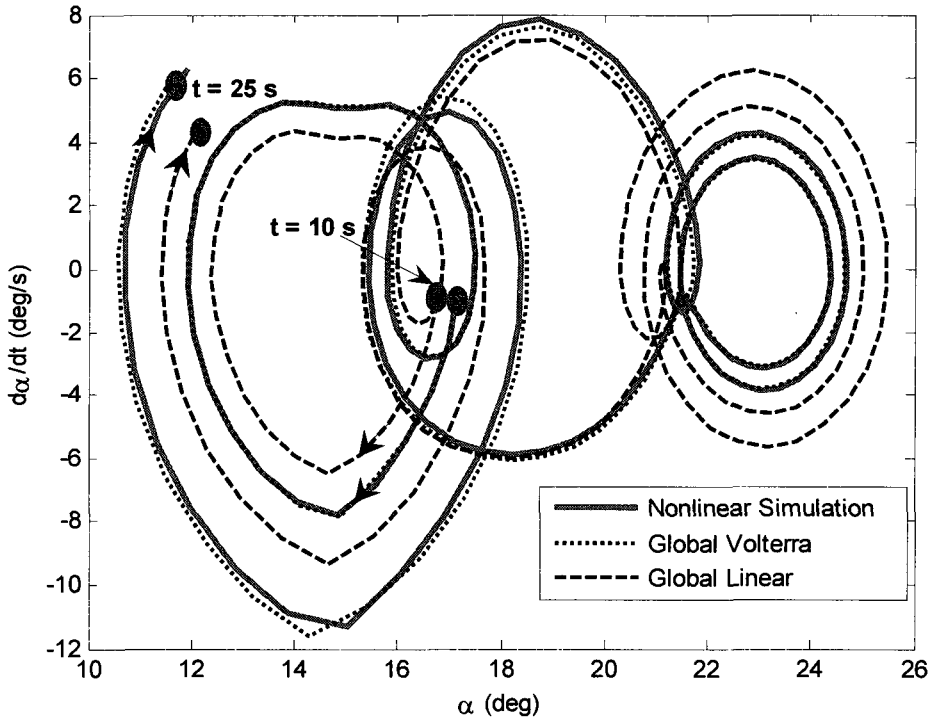

Figure 3.16 Phase Plane from t =10 s to t =25 s for Stair Response Test Case

3.5 Global Kernel Evaluation

Analysis of flight vehicle dynamic behavior, based on the Volterra model kernels, is addressed next. Although a differential form of Volterra theory using piecewise interpolation was implemented for simulation accuracy purposes, the integral form can also be used in creating the global model. Developing the kernel from this differential form requires many mathematical manipulations. For now, as a fast computational tool to validate the globality of the method, the impulsive identification technique is used to estimate these kernels. Later in Chapter 4 and Chapter 5, the analytical kernels will be computed from the differential form. The primary intent here is dynamic analysis based on the integral kernel framework. To that effect, the sub-models of local Volterra kernels are employed in a look-up table procedure using linear interpolation. In this way a new dimension is added to the series kernels. For example, the first input kernel will have two

arguments, $h_1(t_1,\delta_{eo})$, instead of one, $h_1(t_1)$, where δ_{eo} is the operating point around which the sub-model is constructed. Figure 3.17 and Figure 3.18 show the global Volterra kernels for zero and first orders. These kernels appear as surfaces across the two independent variables. The values of the zero order kernel $h_0(t_1,\delta_{eo})$ and the first order kernel $h_1(t_1,\delta_{eo})$ are nonzero across all sub-spaces. On the other hand, the second kernel $h_2(t_1,t_2,\delta_{eo})$ is nonzero in three regions (pre-stall/stall, stall/post-stall, and post-stall), and has a zero value elsewhere. The hyper-surface representing the second kernel can not be fully plotted in three dimensions. For visualization, Figure 3.19 shows the second kernel hyper-subsurface for the pre-stall/stall region.

The surface shown in Figure 3.17 reflects how the zero kernel's nature changes temporally, and from one flight regime to another. This surface primarily represents the initial condition response. First note that for all elevator values, the kernel, with respect to time, starts at zero. This initial value is consistent with how the kernels were computed for $\alpha = 0$ deg initially. At a low value of δ_{eo}, $h_0(t_1,\delta_{eo})$ has a linear characteristic waveform with respect to the time axis. The waveform of $h_0(t_1,\delta_{eo})$ looks like an under-damped second order system. As time increases the amplitude of the conducted oscillation decreases and tends to zero, leaving a nonzero steady state value. The frequency and damping values from this region are consistent with those from Equation (3.4). Conversely, at a high value of δ_{eo}, the nonlinearity becomes important, and $h_0(t_1,\delta_{eo})$ exhibits a nonlinear or non-exponential shaped waveform. The nonlinearity appears here as a self-starting or initial condition excited limit cycle within $h_0(t_1,\delta_{eo})$. As time increases the amplitude of this oscillation is constant at an approximate value of 9.5 deg, while the corresponding frequency is 2.4 rad/s. In between the δ_{eo} extremes, $h_0(t_1,\delta_{eo})$ gradually changes from a linear to a nonlinear waveform proportional to elevator setting.

The waveform of $h_1(t_1,\delta_{eo})$ can be fairly well modeled as an under-damped second order system over the entire space in the sense that $h_1(t_1,\delta_{eo})$ represents the linear portion of the system. The characteristic of this linear waveform changes from one sub-space to

another. Figure 3.18 shows how the characteristics of the plunging force coefficient C_Z have been projected on to the $h_1(t_1,\delta_{eo})$ waveform. The observation indicates a higher damped oscillatory response (relatively high negative slope of C_Z) in the pre-stall sub-space, and a lower damped oscillatory response in the post-stall sub-space (relatively low negative slope of C_Z). In the post-stall region, the oscillation amplitude continues to decrease for large time but at a rather slow rate. The frequency and damping values for the two regions in Figure 3.18 roughly correspond to values extracted from the linear model in Equation (3.4). In between the two distinct regions in Figure 3.18, a sharp change is observed in the two stall sub-spaces. This sharp change is expected, since the difference between the operated elevator deflection in the pre-stall/stall sub-space (δ_{eo} = -9.5 deg) and stall/post-stall sub-space (δ_{eo} = -11 deg) is only 1.5 deg. This difference means that any small change in δ_e leads to a significant change in system behavior or a sharp change in $h_1(t_1,\delta_{eo})$.

Figure 3.19 shows the second kernel in the pre-stall/stall sub-space. This kernel represents the source of input excited limit cycle behavior. Thus the waveform of this kernel reflects a sustained constant amplitude oscillation. Note the frequency of oscillation in Figure 3.19, when moving along the diagonal, is 4.4 rad/s, approximately twice that in Figure 3.17 for high δ_{eo} values. However, when moving along only one of the time axes, the frequency is 2.2 rad/s, consistent with Figure 3.17 and observed oscillations in all three test case responses. Based on all these observations, it can be indicated that the h_0 kernel represents one of the nonlinearity's signatures imbedded in the system's memory (homogeneous induced limit cycle), the h_1 kernel represents a linear behavior (damped oscillatory response) of the system with an arbitrary input, and the h_2 kernel is the nonlinear behavior of the system with the input history (non-homogeneous induced limit cycle). Building such global kernels provides a tool to predict and evaluate the system behavior from one flight region to another before exercising the nonlinear simulation tool.

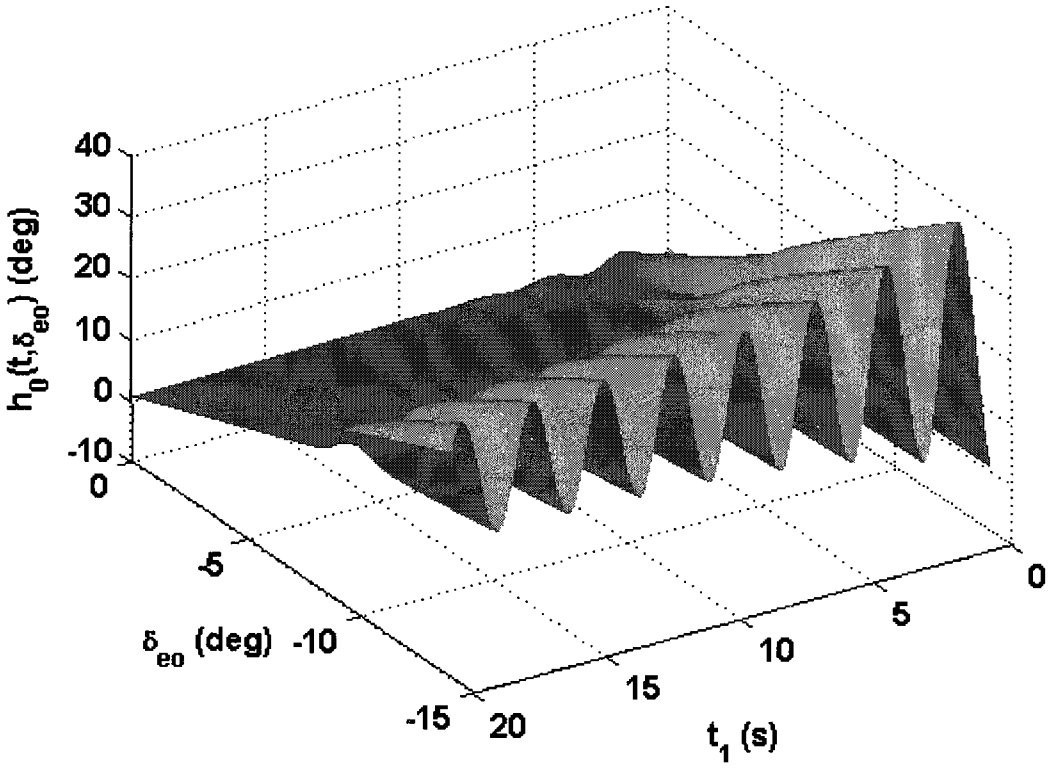

Figure 3.17 Global Zero Order Volterra Kernel

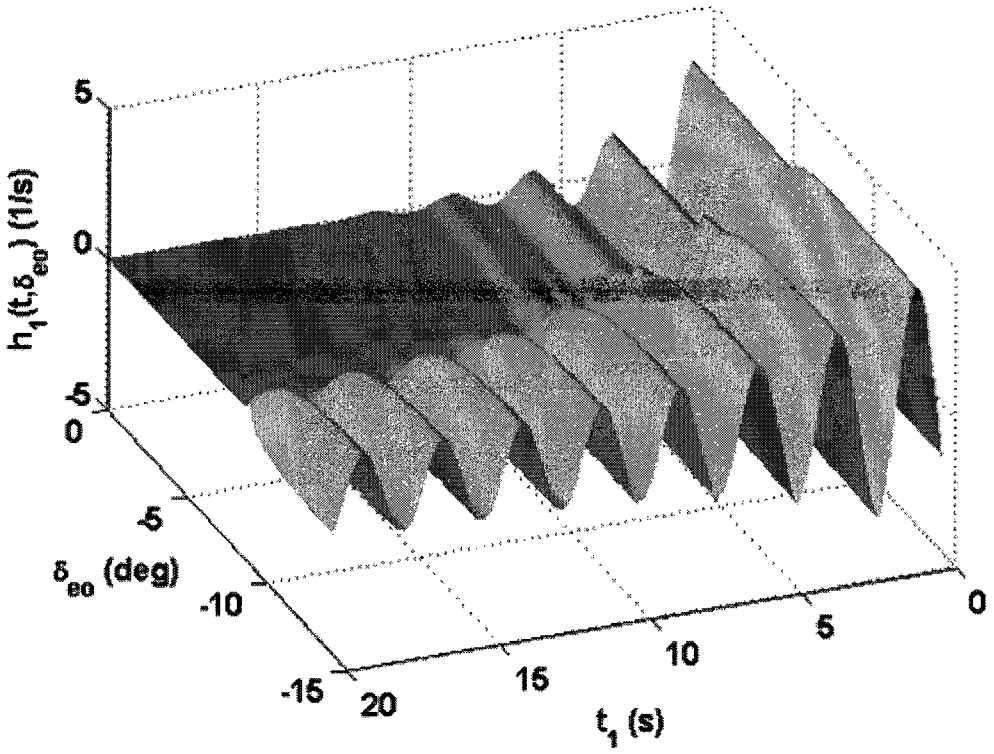

Figure 3.18 Global First Order Volterra Kernel

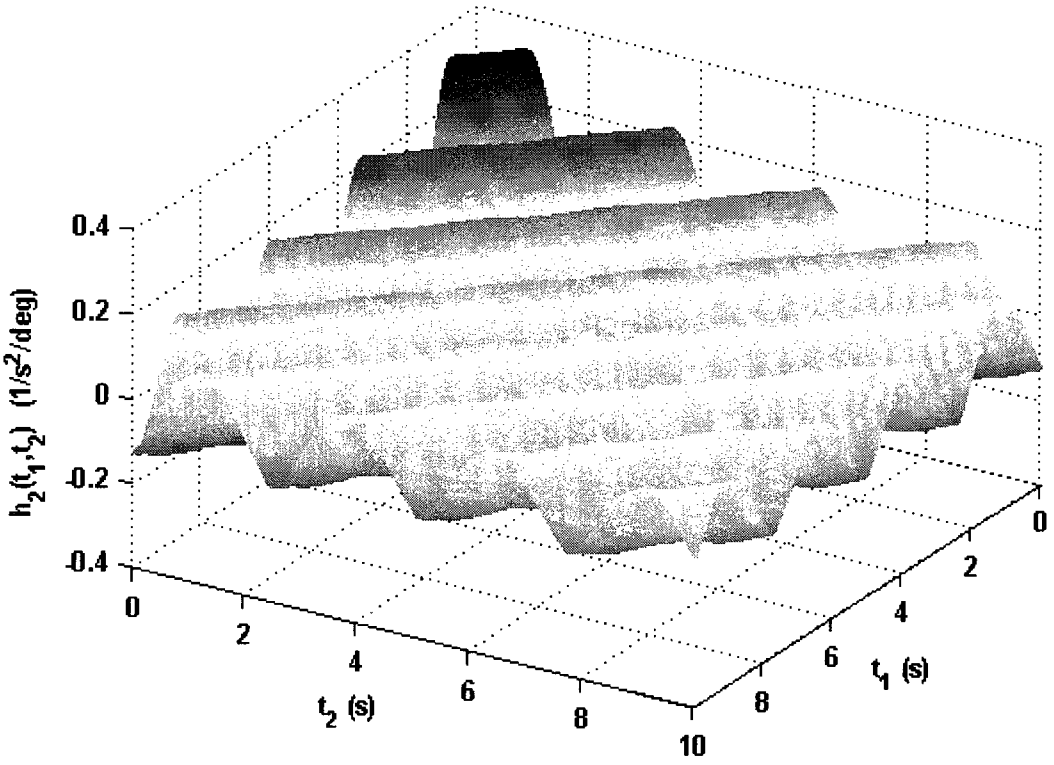

Figure 3.19 Second Order Volterra Kernel in Pre-Stall/Stall Sub-Space

CHAPTER 4

NONLINEAR CAUSE-AND-EFFECT ANALYSIS

In Chapter 3, the globality of the Volterra model has been validated through a piecewise fashion. Relying on this fact, in this chapter, an analytical methodology is presented to conduct dynamical assembly of simple low order nonlinear responses for system synthesis and prediction. The procedure is set forth generically and then applied to several atmospheric flight examples. A two term truncated Volterra series, which is enough to capture the quadratic and bilinear nonlinearities, is developed analytically for a first order system in Section 4.1 and the analytical step response is also visualized and parametrically investigated in Section 4.2. For the second order system, the same analyses are given in Sections 4.3 and 4.4. Reducing the full order aircraft dynamics to a set of low order flight dynamic sub-systems while preserving the link to the more general model is given in Section 4.5. Finally, in Section 4.6, uniaxial surge, pitch, roll, and yaw motions are presented as examples of the low order flight dynamic systems to show the ability of the proposed analytical Volterra-based models to predict, understand, and analyze the nonlinear aircraft behavior beyond that attainable by linear-based models.

4.1 First Order System Analytical Volterra Kernels

The main purpose of this section is to develop Volterra kernels for a nonlinear first order single degree of freedom (SDOF) system. The general governing equation can be expressed as

$$\dot{x} = f(x,u) \tag{4.1}$$

where $x \in R^1$ denotes the state variable, $u \in R^1$ the input, and $f \in R^1$ the system nonlinearity. Using the Taylor series expansion of $f(x,u)$ and assuming coordinates are chosen such that $x_0 = 0$ and $u_0 = 0$, the differential equation can be represented as

$$\dot{x} = \sum_{i=0}^{\infty}\sum_{j=0}^{\infty} k_{ij} x^i u^j = k_{10}x + k_{20}x^2 + k_{30}x^3 + \cdots + k_{01}u + k_{11}xu + k_{21}x^2u + \cdots + k_{02}u^2 + k_{12}xu^2 + \cdots + k_{03}u^3 + \cdots \tag{4.2}$$

where k_{ij} is the corresponding coefficient to the term $x^i u^j$ and $i, j = 0,1,2,3,\ldots$ and $k_{00} = 0$. Based on the global Volterra approach in Chapter 3, a small set of linear and nonlinear terms is enough to specify the system characteristics in a certain domain. Therefore, the bilinear state-input, quadratic state, and quadratic input terms in addition to the linear terms in Equation (4.2) are considered to be sufficient. As a function of these terms, the system is reduced to

$$\dot{x} \approx ax + k_{01}u + k_{20}x^2 + k_{11}xu + k_{02}u^2 \tag{4.3}$$

Note the linear state term coefficient has been re-symbolized by a instead of k_{10}. This re-symbolization has the purpose to emphasize the uniqueness of this term by comparison to the others, as clearly indicated later in this section.

The variational method is now applied to develop the Volterra kernels. The state x can be then expressed as a sum of infinite terms.

$$x = \alpha x_1 + \alpha^2 x_2 + \alpha^3 x_3 + \cdots \tag{4.4}$$

By substituting in Equation (4.3) and equating α^i coefficients, where $i = 1,2,3, \ldots$, a set of pseudo differential equations is generated as

$$\begin{aligned} \dot{x}_1 &= ax_1 + k_{01}u \\ \dot{x}_2 &= ax_2 + k_{20}x_1^2 + k_{11}x_1u + k_{02}u^2 \\ \dot{x}_3 &= ax_3 + 2k_{20}x_1x_2 + k_{11}x_2u + k_{21}x_1^2u + k_{12}x_1u^2 \\ &\vdots \end{aligned} \tag{4.5}$$

The solution of the first differential equation for x_1 with zero initial condition is

$$x_1 = k_{01}\int_0^t e^{a(t-\tau)}u(\tau)d\tau \tag{4.6}$$

The solution of x_2 is then given as

$$x_2 = k_{20}\int_0^t e^{a(t-\tau)}x_1^2(\tau)d\tau + k_{11}\int_0^t e^{a(t-\tau)}x_1(\tau)u(\tau)d\tau + k_{02}\int_0^t e^{a(t-\tau)}u^2(\tau)d\tau$$
$$= x_2^{qs} + x_2^{bsi} + x_2^{qi} \qquad (4.7)$$

where x_2^{qs}, x_2^{bsi}, and x_2^{qi} represent the quadratic state, bilinear state-input, and quadratic input component contributions in x_2.

Replacing the solution of x_1 in the quadratic state component x_2^{qs} by the convolution integral in Equation (4.6) leads to

$$x_2^{qs} = k_{20}\int_0^t e^{a(t-\tau)}x_1^2(\tau)d\tau = k_{20}k_{01}^2\int_0^t e^{a(t-\tau)}\int_0^\tau e^{a(\tau-\tau_1)}u(\tau_1)d\tau_1\int_0^\tau e^{a(\tau-\tau_2)}u(\tau_2)d\tau_2 d\tau \qquad (4.8)$$

or

$$x_2^{qs} = k_{20}k_{01}^2\int_0^t e^{a(t-\tau)}\int_0^t e^{a(\tau-\tau_1)}\Delta(\tau-\tau_1)u(\tau_1)d\tau_1\int_0^t e^{a(\tau-\tau_2)}\Delta(\tau-\tau_2)u(\tau_2)d\tau_2 d\tau$$
$$= k_{20}k_{01}^2\int_0^t\int_0^t e^{a(t-\tau_1-\tau_2)}\left[\int_0^t e^{a(\tau)}\Delta(\tau-\tau_1)\Delta(\tau-\tau_2)d\tau\right]u(\tau_1)u(\tau_2)d\tau_1 d\tau_2 \qquad (4.9)$$

The step function $\Delta(\tau-\tau_1)$ is defined by

$$\Delta(x) = \begin{cases} 1 & x \geq 0 \\ 0 & x < 0 \end{cases} \qquad (4.10)$$

Use of the minimum function min(τ_1, τ_2) can replace the two step functions $\Delta(\tau-\tau_1)$ and $\Delta(\tau-\tau_2)$ as

$$x_2^{qs} = k_{20}k_{01}^2\int_0^t\int_0^t e^{a(t-\tau_1-\tau_2)}\left[\int_{-\min(-\tau_1,-\tau_2)}^t e^{a(\tau)}d\tau\right]u(\tau_1)u(\tau_2)d\tau_1 d\tau_2 \qquad (4.11)$$

where min(x,y) refers to the minimum values between x and y. The quadratic state component x_2^{qs} is then written as

$$x_2^{qs} = \frac{k_{20}k_{01}^2}{a}\int_0^t\int_0^t e^{a(t-\tau_1)}e^{a(t-\tau_2)}\left[1-e^{-a\min(t-\tau_1,t-\tau_2)}\right]u(\tau_1)u(\tau_2)d\tau_1 d\tau_2 \qquad (4.12)$$

The quadratic input component x_2^{qi} yields the standard Volterra form

$$x_2^{qi} = k_{02}\int_0^t e^{a(t-\tau)}u^2(\tau)d\tau = k_{02}\int_0^t\int_0^t e^{a(t-\tau_1)}\delta(\tau_1-\tau_2)u(\tau_1)u(\tau_2)d\tau_1 d\tau_2 \tag{4.13}$$

where $\delta(\tau_1\text{-}\tau_2)$ is the impulse function.

For the bilinear state-input component x_2^{bsi}, the convolution integral is substituted for x_1 as

$$x_2^{bsi} = k_{11}\int_0^t e^{a(t-\tau)}x_1(\tau)u(\tau)d\tau \;= k_{11}k_{01}\int_0^t e^{a(t-\tau_1)}\int_0^{\tau_1} e^{a(\tau_1-\tau_2)}u(\tau_2)d\tau_2 u(\tau_1)d\tau_1 \tag{4.14}$$

or

$$x_2^{bsi} = k_{11}k_{01}\int_0^t\int_0^t e^{a(t-\tau_2)}\Delta(\tau_1-\tau_2)u(\tau_1)u(\tau_2)d\tau_1 d\tau_2 \tag{4.15}$$

Unlike the quadratic components x_2^{qs} and x_2^{qi}, the bilinear component x_2^{bsi} has a triangular form, which means that the double convolution integral is defined over a triangular domain $\Delta(\tau_1\text{-}\tau_2)$. To keep all the components in the same form, a symmetrization approach is used. The transformation between triangular and symmetric kernels is listed as[58]

$$h_{sym}(t_1,\cdots,t_n) = \frac{1}{n!}\sum_{\pi(.)} h_{tri}\left(t_{\pi(1)},\cdots,t_{\pi(n)}\right) \tag{4.16}$$

where $\pi(.)$ denotes any permutation of integers 1,2,...,n. Applying this transformation, the symmetric form of the bilinear component is

$$\begin{aligned} x_2^{bsi} &= \frac{k_{11}k_{01}}{2}\int_0^t\int_0^t\left[e^{a(t-\tau_2)}\Delta(\tau_1-\tau_2)+e^{a(t-\tau_1)}\Delta(\tau_2-\tau_1)\right]u(\tau_1)u(\tau_2)d\tau_1 d\tau_2 \\ &= \frac{k_{11}k_{01}}{2}\int_0^t\int_0^t\left[e^{a\max(t-\tau_1,t-\tau_2)}\right]u(\tau_1)u(\tau_2)d\tau_1 d\tau_2 \end{aligned} \tag{4.17}$$

The operator max(x, y) refers to the maximum value between x and y.

Adding the quadratic and bilinear components to the linear term offers an approximate solution for x as

$$x \approx \int_0^t h_1(t-\tau)u(\tau)d\tau + \int_0^t \int_0^t h_2(t-\tau_1, t-\tau_2)u(\tau_1)u(\tau_2)d\tau_1 d\tau_2 \tag{4.18}$$

where

$$h_1(\tau) = k_{01}e^{a(\tau)} \tag{4.19}$$

$$\begin{aligned} h_2(\tau_1,\tau_2) &= h_2^{qs} + h_2^{bsi} + h_2^{qi} \\ &= \frac{k_{20}k_{01}^2}{a} e^{a(\tau_1)}e^{a(\tau_2)}\left[1 - e^{-a\min(\tau_1,\tau_2)}\right] + \frac{k_{11}k_{01}}{2} e^{a\max(\tau_1,\tau_2)} + k_{02}e^{a(\tau_1)}\delta(\tau_1 - \tau_2) \end{aligned} \tag{4.20}$$

The resultant approximate solution is given by the two kernels h_1 and h_2. For any arbitrary input $u(t)$, one can compute the response x using convolution integrals or the pseudo state space representation. These kernels are a unique signature of the first order SDOF system being functions of the nonlinear system parameters. For understanding how the system behavior varies with these parameters, their influence on each kernel is presented next.

The first kernel h_1 is an exponential function with a gain k_{01} and power factor a. It is clear that this power factor a controls the divergence or convergence of the first kernel histories. For a positive a, the value of h_1 keeps increasing with time to be infinite as time tends to infinity. This observation concludes that the system has a divergent or unstable response for any input. If a is null, the first kernel is constant with time, which means that the system linear response is the input integration. In case of negative a, at time zero, the value of h_1 is k_{01}. This value keeps decreasing with time, yielding zero at time equal to infinity. Figure 4.1 shows the normalized generic shape of h_1 for negative a. The normalized kernel starts at 1 with a downward slope with angle φ = arctan(a). This slope is an indication for the initial or maximum speed by which the system responds for any arbitrary input. If a 2% value is considered as a tolerance for approximate steady state,

the required time to be inside this zero vicinity is labeled here as the linear kernel settling time τ_{ks}^{l}. This time is computed as a function of a to be

$$\tau_{ks}^{l} = \frac{-\ln(0.02)}{|a|} \approx \frac{4}{|a|} \quad \text{for} \quad a < 0 \tag{4.21}$$

The second kernel has three components: quadratic state kernel h_2^{qs}, quadratic input kernel h_2^{qi}, and bilinear state-input kernel h_2^{bsi}. Each component is a two dimensional surface as a function of τ_1 and τ_2. The quadratic state kernel h_2^{qs} has three exponential terms. The linear coefficient a controls the divergence and convergence of this surface. For null a, the surface is defined by $k_{20}k_{01}^2$ min(τ_1, τ_2) using l'Hopital's rule. This minimum operator represents two ramp surfaces τ_1 and τ_2 merged at the diagonal line, which implies that if the system is critically stable in the linear sense (a = 0), the state quadratic term has a divergent kernel shape (instability). Such a conclusion is not accessible using the linear analysis. For positive a, the surface starts at the zero value heading upwards to a divergence referring to unstable behavior for any external excitation. If the value of a is negative, the surface starts at zero and diminishes at infinite time arguments τ_1 and τ_2. The exponential term with the minimum operation in the exponent works on directing the surface upward and enforcing the surface edges to be zero, while the two regular exponential terms of τ_1 and τ_2 work on heading the surface downward. The irregular exponential term competes with the two regular terms reaching a maximum surface value at $\tau_1 = \tau_2 = \ln(2)/|a| \approx 0.7/|a|$, beyond which this effect diminishes. The two standard exponential terms then dominate the shape of the surface, yielding zero as the two arguments τ_1 and τ_2 go to infinity. One example of this surface is given in Figure 4.2, where a = -5 1/s. The overall shape of this kernel is determined by its diagonal ($\tau_1 = \tau_2$). The normalized general shape of this diagonal is shown in Figure 4.3. The surface has a maximum value $0.25k_{20}k_{01}^2 / a$ at time $\tau_{km}^{qs} = \ln(2)/|a| \approx 0.7/|a|$. Also, the

required time by which the surface is considered as zero is referred to here as the quadratic state kernel's settling time τ_{ks}^{qs}. This time is computed to be

$$\tau_{ks}^{qs} = \frac{1}{|a|} \ln\left\{\frac{2}{1-\sqrt{1-4\times 0.02\times 0.25}}\right\} \approx \frac{5.3}{|a|} \qquad (4.22)$$

The surface of the quadratic input kernel component h_2^{qi} is an exponential impulse sheet oriented vertically on the $\tau_1 = \tau_2$ diagonal, which has the same shape and characteristics as the first kernel in Figure 4.1 but with a different gain k_{02} instead of k_{01}.

The surface of the bilinear state-input kernel component h_2^{bsi} is an exponential function including a maximum operator in the power. This operator divides the domain into two triangles $\Delta(\tau_i\text{-}\tau_j)$, where i and $j = \{1,2\}$. Over the domain $\Delta(\tau_i\text{-}\tau_j)$, the normalized surface starts at value 0.5 at $\tau_i = \tau_j = 0$. The surface heads to zero (stable or convergent) as τ_i tends to infinity in the case of negative a, or heads to infinity (unstable or divergent) in the case of positive a. Thus, the exponential function of the argument τ_i is the active one over this domain. For null a, the normalized surface is a flat one with a value 0.5. For positive or negative a, the two surfaces merge at the diagonal line where $\tau_1 = \tau_2$ or at the intersection of the two triangles. Figure 4.4 shows an example of the bilinear state-input kernel at a = -5 1/s. The diagonal shape of this kernel is the same as the linear first kernel but with different gain (see Figure 4.5). The gain here is $k_{01}k_{11}/2$. The initial slope angle φ is arctan(a) and τ_{ks}^{bsi} is defined as

$$\tau_{ks}^{bsi} = \frac{-\ln(0.02)}{|a|} \approx \frac{4}{|a|} \qquad \text{for} \qquad a < 0 \qquad (4.23)$$

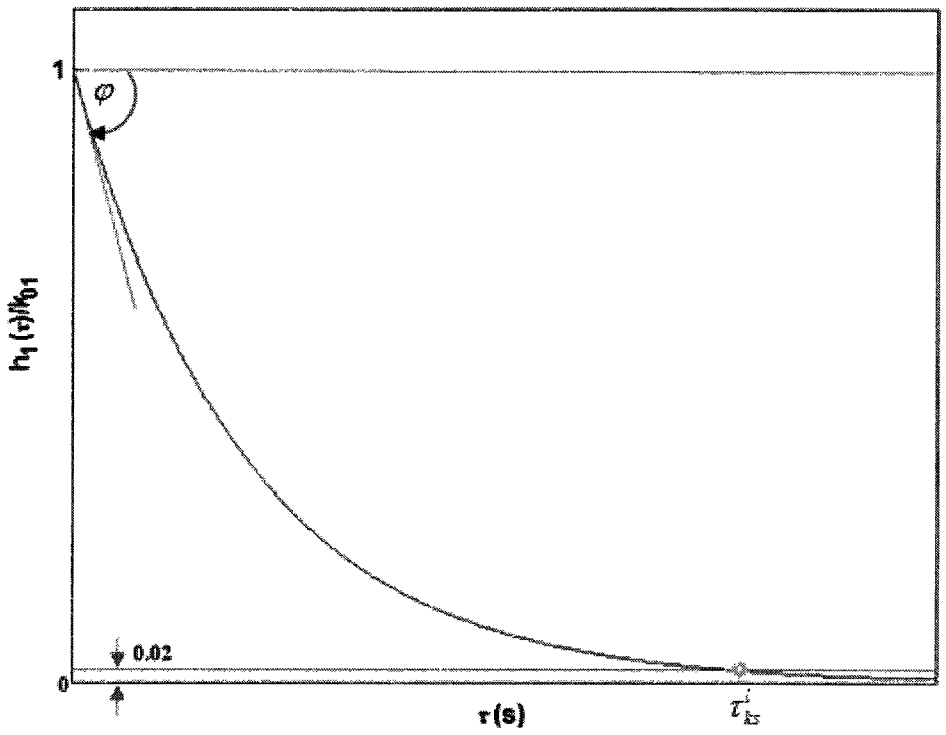

Figure 4.1 First Order System First Kernel ($a < 0$)

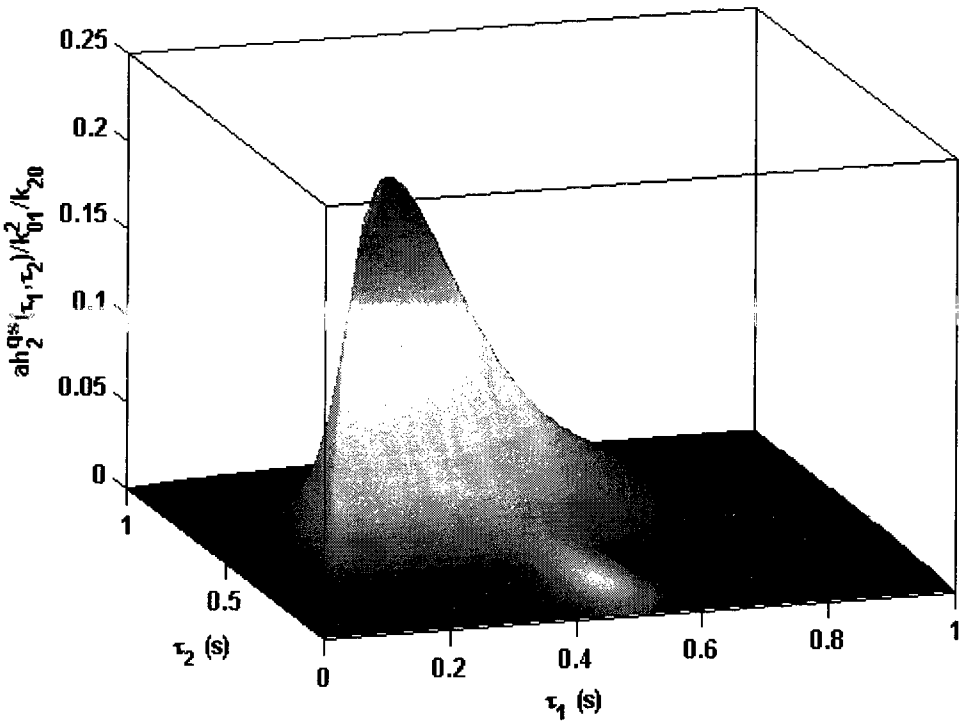

Figure 4.2 First Order System Quadratic State Second Kernel (a = -5 1/s)

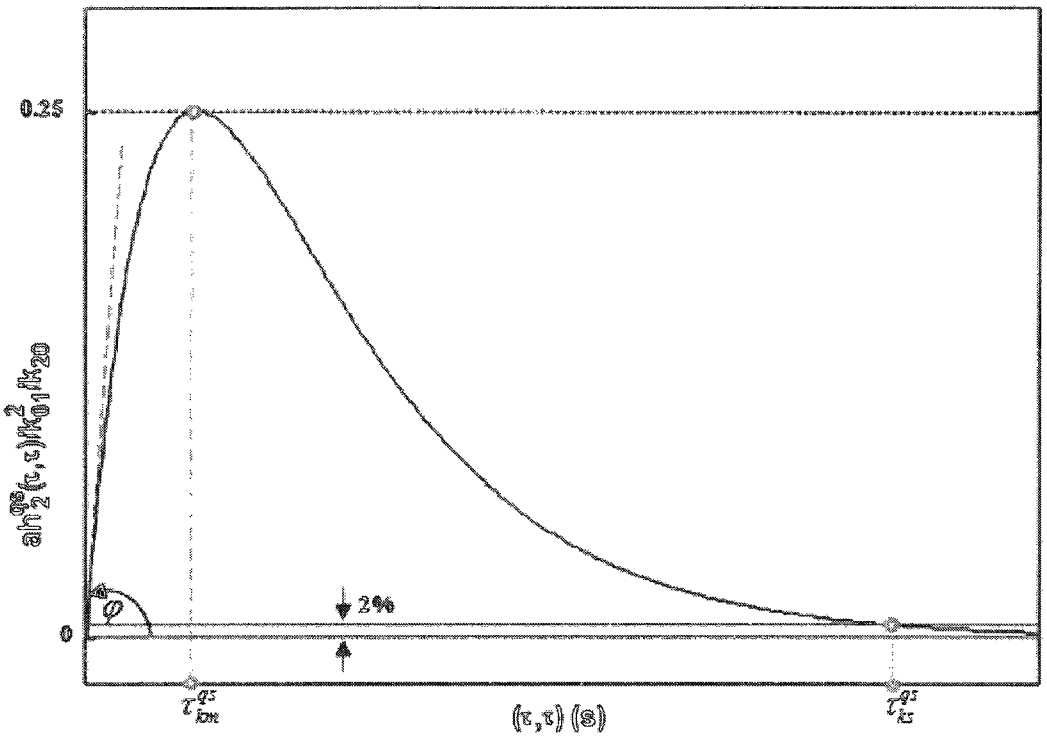

Figure 4.3 First Order System Quadratic State Second Kernel Diagonal ($a < 0$)

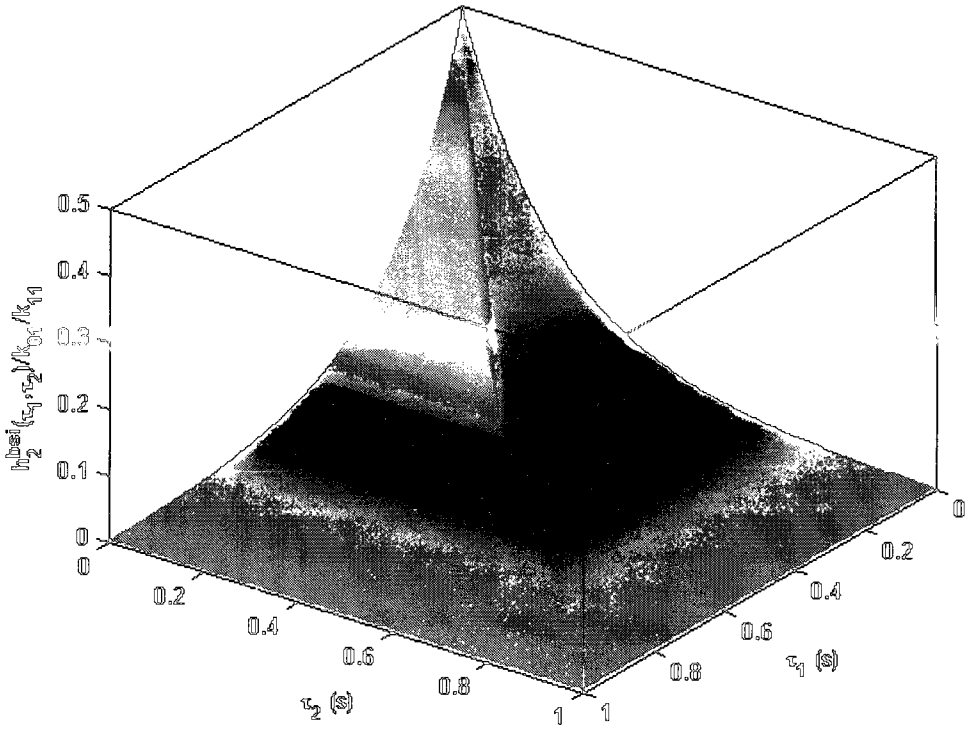

Figure 4.4 First Order System Bilinear State-Input Second Kernel (a = -5 1/s)

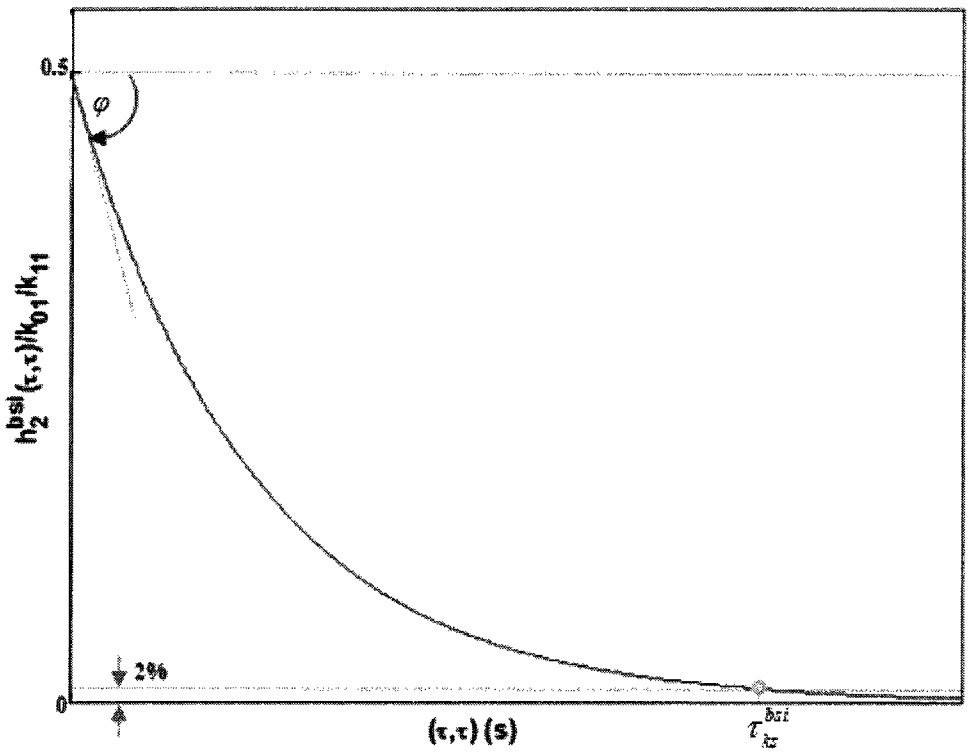

Figure 4.5 First Order System Bilinear State-Input Second Kernel Diagonal ($a < 0$)

4.2 Analytical Step Response of First Order System

The response to a step input is selected herein as the baseline to characterize the system behavior. The system overall step response is computed by summing individual components as

$$
\begin{aligned}
& x \approx x_1 + x_2^{qs} + x_2^{bsi} + x_2^{qi} \\
& x_1 = \frac{Ak_{01}}{a}\left(e^{at} - 1\right), \qquad x_2^{qi} = \frac{A^2 k_{02}}{a}\left(e^{at} - 1\right) \\
& x_2^{qs} = \frac{A^2 k_{01}^2 k_{20}}{a^3}\left(e^{2at} - 2ate^{at} - 1\right), \quad x_2^{bsi} = \frac{A^2 k_{01} k_{11}}{a^2}\left(1 - e^{at} + ate^{at}\right)
\end{aligned}
\tag{4.24}
$$

In Equation (4.24), A is the step input amplitude. The four terms x_1, x_2^{qs}, x_2^{bsi}, and x_2^{qi} are the contributions of the linear, quadratic, and bilinear components in the system behavior. Assembling these components together presents the overall response. To show each

component effect on the overall behavior, the generic shape of each term is individually visualized as shown in Figure 4.6 and
Figure 4.7 for the stable case ($a < 0$). Both linear and quadratic input components have the same mathematical structure except for the steady gain as shown in Figure 4.6. Although the normalized state quadratic and bilinear components have different mathematical structure, both yield the same generic shape as shown in
Figure 4.7 but with different parameters.

All responses start at zero and head upward. The initial slope of the normalized linear and input quadratic terms is $\tan(\varphi) = a$, while both the normalized state quadratic and bilinear terms have a zero initial slope. This observation indicates that both state quadratic and bilinear terms have no influence on the initial rate by which the system behaves for any input excitation. The initial rate $\dot{x}(0)$ is a function of the ratio between the linear coefficient k_{01} and the quadratic input coefficient k_{02} in addition to the input amplitude A.

Both the quadratic state x_2^{qs} and bilinear state-input x_2^{bsi} responses have a noticeable lag. The duration of lag in the quadratic state component x_2^{qs} is longer than for the bilinear state-input x_2^{bsi}, but its transient rise is steeper. Thus, the quadratic state kernel h_2^{qs} has zero edges and the bilinear state-input kernel h_2^{bsi} has nonzero edges. Referring to these two lags as τ_{rl}^{qs} and τ_{rl}^{bsi}, if 2% is considered as the required threshold to leave the vicinity of such a lag, then these two lags are approximately found to be $0.45/|a|$ and $0.2/|a|$. Note that the quadratic state and bilinear state-input step responses include a ramp function multiplied by an exponential function, which sets hurdles in computing their lag times analytically; a reason for which numerical fitting is considered. These time lags are the instances at which a deviation between linear and nonlinear simulation starts to be significant in the case of a zero quadratic input coefficient.

This deviation widens due to an increase in the slopes of the quadratic state and bilinear state-input components after exiting from their lag vicinity. At a certain point, the

rate of each component reaches its maximum value followed by a rapid decreasing. Sequentially, each term settles to its steady value at an equivalent settling time $\tau_{rs}^{l} = \tau_{rs}^{qi} = 4/|a|$ for the linear term and the quadratic input component, $\tau_{rs}^{qs} = 6.6/|a|$ for the quadratic state component, and $\tau_{rs}^{bsi} = 5.8/|a|$ for the bilinear state-input component. The overall response settles at

$$x_{ss} = \frac{Ak_{01}}{|a|} + \frac{A^2 k_{01}^2 k_{20}}{|a|a^2} + \frac{A^2 k_{01} k_{11}}{a^2} + \frac{A^2 k_{02}}{|a|} \tag{4.25}$$

The time for reaching this steady value depends on the ratio between the coefficients of each term and the input amplitude.

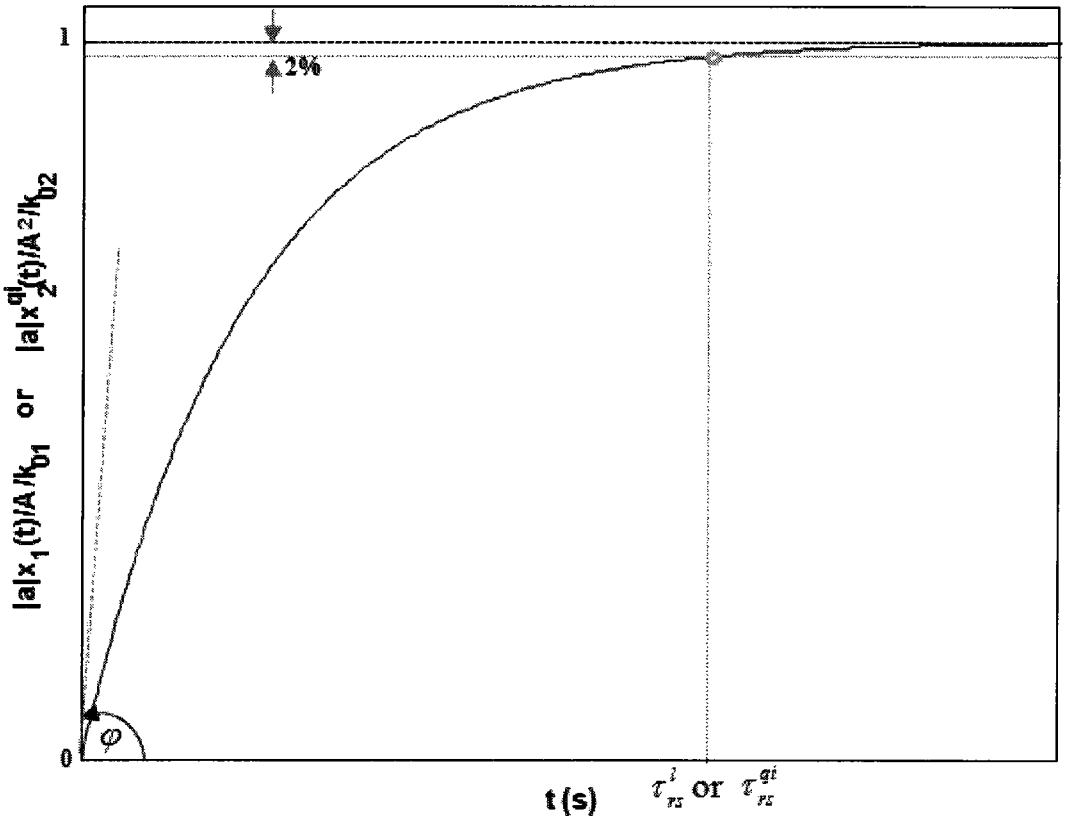

Figure 4.6 First Order System Linear or Quadratic Input Response to Step Input ($a < 0$)

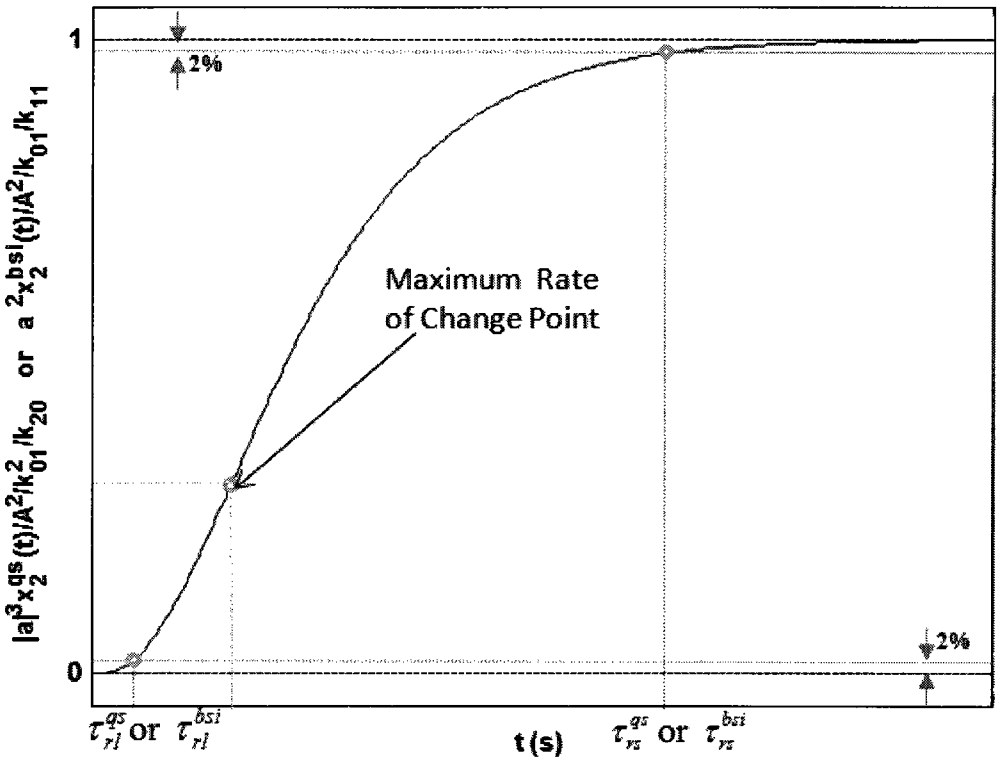

Figure 4.7 First Order System Quadratic State or Bilinear State-Input Response to Step Input ($a < 0$)

4.3 Second Order System Analytical Volterra Kernels

Following the same sequence for the nonlinear second order SDOF system, and assuming that quadratic and bilinear terms are enough to capture system nonlinearity in a certain neighborhood, the system is defined below.

$$\begin{aligned} &\ddot{x} = k_{100}x + k_{010}\dot{x} + k_{200}x^2 + k_{110}x\dot{x} + k_{020}\dot{x}^2 \quad + k_{001}u + k_{101}xu + k_{011}\dot{x}u + k_{002}u^2 \\ &\text{or} \\ &\dot{x} = v \\ &\dot{v} = -\omega_n^2 x - 2\zeta\omega_n v + k_{200}x^2 + k_{110}xv + k_{020}v^2 \quad + k_{001}u + k_{101}xu + k_{011}vu + k_{002}u^2 \end{aligned} \tag{4.26}$$

The parameter k_{lmn} is the corresponding coefficient to the term $x^l v^m u^n$ and l, m, n = 0,1,2. Note that the linear terms have been re-symbolized by $-2\zeta\omega_n$ instead of k_{010} and $-\omega_n^2$ instead of k_{100}. This re-symbolization is for the purpose of keeping the discussion in the

sense of undamped natural frequency ω_n and damping ratio ζ. The variational method is used to develop the Volterra kernels. The method assumes that the input is αu where α is any arbitrary constant. The state position x and state rate v can be then be expressed as a sum of infinite terms.

$$\begin{aligned} x &= \alpha x_1 + \alpha^2 x_2 + \alpha^3 x_3 + \cdots \\ v &= \alpha v_1 + \alpha^2 v_2 + \alpha^3 v_3 + \cdots \end{aligned} \tag{4.27}$$

By equating coefficients of α^i, a set of pseudo differential equations is generated.

$$\begin{aligned} \begin{bmatrix} \dot{x}_1 \\ \dot{v}_1 \end{bmatrix} &= \begin{bmatrix} 0 & 1 \\ -\omega_n^2 & -2\zeta\omega_n \end{bmatrix} \begin{bmatrix} x_1 \\ v_1 \end{bmatrix} + \begin{bmatrix} 0 \\ k_{001} \end{bmatrix} u \\ \begin{bmatrix} \dot{x}_2 \\ \dot{v}_2 \end{bmatrix} &= \begin{bmatrix} 0 & 1 \\ -\omega_n^2 & -2\zeta\omega_n \end{bmatrix} \begin{bmatrix} x_2 \\ v_2 \end{bmatrix} + \begin{bmatrix} 0 \\ k_{200} x_1^2 \end{bmatrix} + \begin{bmatrix} 0 \\ k_{110} x_1 v_1 \end{bmatrix} \\ &\quad + \begin{bmatrix} 0 \\ k_{020} v_1^2 \end{bmatrix} + \begin{bmatrix} 0 \\ k_{101} x_1 u \end{bmatrix} + \begin{bmatrix} 0 \\ k_{011} v_1 u \end{bmatrix} + \begin{bmatrix} 0 \\ k_{002} u^2 \end{bmatrix} \\ \begin{bmatrix} \dot{x}_3 \\ \dot{v}_3 \end{bmatrix} &= \begin{bmatrix} 0 & 1 \\ -\omega_n^2 & -2\zeta\omega_n \end{bmatrix} \begin{bmatrix} x_3 \\ v_3 \end{bmatrix} + \cdots \\ &\vdots \end{aligned} \tag{4.28}$$

Under the piecewise Volterra approach, two terms are considered sufficient to describe the system in a certain sub-domain. The first linear state space model is defined by state, input, output coefficient matrices *A, B, C* as

$$A = \begin{bmatrix} 0 & 1 \\ -\omega_n^2 & -2\zeta\omega_n \end{bmatrix}, \; C = \begin{bmatrix} 1 & 0 \\ 0 & 1 \end{bmatrix}, \; B = \begin{bmatrix} 0 \\ k_{001} \end{bmatrix} \tag{4.29}$$

The transition matrix Φ of this system is computed as

$$\Phi(t) = e^{At} = \begin{bmatrix} \dfrac{e^{-\sigma t}}{\sqrt{1-\zeta^2}} \sin(\omega_d t + \varphi) & \dfrac{e^{-\sigma t}}{\omega_d} \sin(\omega_d t) \\ \dfrac{-\omega_n^2}{\omega_d} e^{-\sigma t} \sin(\omega_d t) & \dfrac{-e^{-\sigma t}}{\sqrt{1-\zeta^2}} \sin(\omega_d t - \varphi) \end{bmatrix}, \; \varphi = \cos^{-1}(\zeta) \tag{4.30}$$

In Equation (4.30), $\sigma = \zeta\omega_n$ denotes the system's damping factor and $\omega_d = \sqrt{1-\zeta^2}\,\omega_n$ is the system damped natural frequency. The solution of the first linear pseudo sub-system $[x_1\ v_1]^T$ for zero initial condition is then computed as

$$\begin{bmatrix} x_1 \\ v_1 \end{bmatrix} = \int_0^t C\Phi(t-\tau)Bu(\tau)d\tau \tag{4.31}$$

Substituting the system state space matrices leads to

$$\begin{aligned} x_1 &= \frac{k_{001}}{\omega_d}\int_0^t e^{-\sigma(t-\tau)}\sin(\omega_d(t-\tau))u(\tau)d\tau \\ v_1 &= \frac{-k_{001}}{\sqrt{1-\zeta^2}}\int_0^t e^{-\sigma(t-\tau)}\sin(\omega_d(t-\tau)-\varphi)u(\tau)d\tau \end{aligned} \tag{4.32}$$

For the second pseudo sub-system $[x_2\ v_2]^T$, the solution of x_2 is sought as a sum of six components

$$x_2 = x_2^{qs} + x_2^{bsr} + x_2^{qr} + x_2^{bsi} + x_2^{bri} + x_2^{qi} \tag{4.33}$$

where $x_2^{qs}, x_2^{bsr}, x_2^{qr}, x_2^{bsi}, x_2^{bri}$, and x_2^{qi} are quadratic state, bilinear state-rate, quadratic rate, bilinear state-input, bilinear rate-input, and quadratic input components respectively. The second pseudo state space is then rewritten as

$$\begin{aligned} \begin{bmatrix} \dot{x}_2 \\ \dot{v}_2 \end{bmatrix} &= \underbrace{\begin{bmatrix} 0 & 1 \\ -\omega_n^2 & -2\zeta\omega_n \end{bmatrix}}_{A}\begin{bmatrix} x_2 \\ v_2 \end{bmatrix} + \underbrace{\begin{bmatrix} 0 \\ k_{200} \end{bmatrix}}_{B_{qs}} x_1^2 + \underbrace{\begin{bmatrix} 0 \\ k_{110} \end{bmatrix}}_{B_{bsr}} x_1 v_1 + \underbrace{\begin{bmatrix} 0 \\ k_{020} \end{bmatrix}}_{B_{qr}} v_1^2 \\ &+ \underbrace{\begin{bmatrix} 0 \\ k_{101} \end{bmatrix}}_{B_{bsi}} x_1 u + \underbrace{\begin{bmatrix} 0 \\ k_{011} \end{bmatrix}}_{B_{bri}} v_1 u + \underbrace{\begin{bmatrix} 0 \\ k_{002} \end{bmatrix}}_{B_{qi}} u^2 \end{aligned} \tag{4.34}$$

Defining a new output coefficient matrix $C_x = [1\ \ 0]$, the solution of the quadratic state component x_2^{qs} is computed as

$$
\begin{aligned}
x_2^{qs} &= \int_0^t C_x \Phi(t-\tau) B_{qs} x_1(\tau) x_1(\tau) d\tau \\
&= \frac{k_{200} k_{001}^2}{\omega_d^3} \int_0^t e^{-\sigma(t-\tau)} \sin(\omega_d (t-\tau)) \int_0^\tau e^{-\sigma(\tau-\tau_1)} \sin(\omega_d (\tau-\tau_1)) u(\tau_1) d\tau_1 \\
&\quad \times \int_0^\tau e^{-\sigma(\tau-\tau_2)} \sin(\omega_d (\tau-\tau_2)) u(\tau_2) d\tau_2 d\tau \qquad (4.35) \\
&= \frac{k_{200} k_{001}^2}{\omega_d^3} \int_0^t e^{-\sigma(t-\tau)} \sin(\omega_d (t-\tau)) \int_0^t e^{-\sigma(\tau-\tau_1)} \sin(\omega_d (\tau-\tau_1)) \Delta(\tau-\tau_1) u(\tau_1) d\tau_1 \\
&\quad \times \int_0^t e^{-\sigma(\tau-\tau_2)} \sin(\omega_d (\tau-\tau_2)) \Delta(\tau-\tau_2) u(\tau_2) d\tau_2 d\tau
\end{aligned}
$$

If the -min(-τ_1, -τ_2) operator replaces the multiplication of the two step functions $\Delta(\tau-\tau_1)$ $\Delta(\tau-\tau_2)$ in addition to some mathematical and trigonometric manipulations, then Equation (4.35) becomes

$$
\begin{aligned}
x_2^{qs} &= \frac{k_{200} k_{001}^2}{2\omega_d^3} \int_0^t \int_0^t \int_{-\min(-\tau_1,-\tau_2)}^t e^{-\sigma(t-\tau)} e^{-\sigma(t-\tau_1)} e^{-\sigma(t-\tau_2)} \\
&\times \{\cos(\omega_d((t-\tau_1)-(t-\tau_2)))\sin(\omega_d(t-\tau)) \qquad (4.36) \\
&- \cos(\omega_d((t-\tau_1)+(t-\tau_2)))\sin(2\omega_d(t-\tau))\sin(\omega_d(t-\tau)) - \\
&- \sin(\omega_d((t-\tau_1)+(t-\tau_2)))\cos(2\omega_d(t-\tau))\sin(\omega_d(t-\tau))\} u(\tau_1) u(\tau_2) d\tau \, d\tau_1 d\tau_2
\end{aligned}
$$

Computing the integration with respect to τ brings the solution of the quadratic state component x_2^{qs} to the form

$$
x_2^{qs} = \int_0^t \int_0^t h_2^{qs}(t-\tau_1, t-\tau_2) u(\tau_1) u(\tau_2) d\tau_1 d\tau_2 \qquad (4.37)
$$

where

$$
\begin{aligned}
h_2^{qs}(\tau_1,\tau_2) &= \frac{k_{200} k_{001}^2}{2\omega_d^4} e^{-\sigma\tau_1} e^{-\sigma\tau_2} \\
&\times \{M_1 \cos(\omega_d(\tau_1-\tau_2)) + M_2 \cos(\omega_d(\tau_1+\tau_2)) + M_3 \sin(\omega_d(\tau_1+\tau_2))\}
\end{aligned} \qquad (4.38)
$$

$$M_1(\tau_1,\tau_2)=(1-\zeta^2)\left\{1+\frac{e^{\sigma\min(\tau_1,\tau_2)}}{\sqrt{1-\zeta^2}}\sin(\omega_d\min(\tau_1,\tau_2)-\varphi)\right\} \tag{4.39}$$

$$\begin{aligned}M_2(\tau_1,\tau_2)=&\frac{(1-\zeta^2)}{2}\left\{1+\frac{e^{\sigma\min(\tau_1,\tau_2)}}{\sqrt{1-\zeta^2}}\sin(\omega_d\min(\tau_1,\tau_2)-\varphi)\right\}\\&-\frac{3(1-\zeta^2)}{2(9-8\zeta^2)}\left\{1+\sqrt{\frac{9-8\zeta^2}{9-9\zeta^2}}e^{\sigma\min(\tau_1,\tau_2)}\sin(3\omega_d\min(\tau_1,\tau_2)-\hat{\varphi})\right\}\end{aligned} \tag{4.40}$$

$$\begin{aligned}M_3(\tau_1,\tau_2)=&\frac{\zeta\sqrt{1-\zeta^2}}{2}\left\{1-\frac{e^{\sigma\min(\tau_1,\tau_2)}}{\zeta}\cos(\omega_d\min(\tau_1,\tau_2)-\varphi)\right\}\\&-\frac{\zeta\sqrt{1-\zeta^2}}{2(9-8\zeta^2)}\left\{1-\frac{\sqrt{9-8\zeta^2}}{\zeta}e^{\sigma\min(\tau_1,\tau_2)}\cos(3\omega_d\min(\tau_1,\tau_2)-\hat{\varphi})\right\}\end{aligned} \tag{4.41}$$

where $\cos(\hat{\varphi})=\zeta/\sqrt{9-8\zeta^2}$.

It is clear that the only difference between quadratic state expression and bilinear state-rate one is a phase shift $-\varphi$ for the terms $\omega_d\tau_2$ in addition to the gain difference (see Equations (4.32) and (4.35)). One can use the same steps to derive the bilinear state-rate solution as

$$x_2^{bsr}=\int_0^t\int_0^t h_2^{bsr}(t-\tau_1,t-\tau_2)u(\tau_1)u(\tau_2)d\tau_1 d\tau_2 \tag{4.42}$$

where

$$\begin{aligned}h_2^{bsr}(\tau_1,\tau_2)=&\frac{-k_{110}k_{001}^2}{2\sqrt{1-\zeta^2}\,\omega_d^3}e^{-\sigma\tau_1}e^{-\sigma\tau_2}\{M_1\cos(\omega_d(\tau_1-\tau_2)+\varphi)\\&+M_2\cos(\omega_d(\tau_1+\tau_2)-\varphi)+M_3\sin(\omega_d(\tau_1+\tau_2)-\varphi)\}\end{aligned} \tag{4.43}$$

In case of the quadratic rate component, the shift $-\varphi$ appears in both terms $\omega_d\tau_1$ and $\omega_d\tau_2$. The expression of the quadratic rate component is

$$x_2^{qr}=\int_0^t\int_0^t h_2^{qr}(t-\tau_1,t-\tau_2)u(\tau_1)u(\tau_2)d\tau_1 d\tau_2 \tag{4.44}$$

where

$$h_2^{qr}(\tau_1,\tau_2)=\frac{-k_{020}k_{001}^2}{2(1-\zeta^2)\omega_d^2}e^{-\sigma\tau_1}e^{-\sigma\tau_2}\{M_1\cos(\omega_d(\tau_1-\tau_2))$$
$$+M_2\cos(\omega_d(\tau_1+\tau_2)-2\varphi)+M_3\sin(\omega_d(\tau_1+\tau_2)-2\varphi)\} \quad (4.45)$$

Note for x_2^{bsr} and x_2^{qr}, the factors M_1, M_2, and M_3 are the same as in Equations (4.39-4.41).

For the bilinear state-input component, the expression is developed as

$$x_2^{bsi}=\int_0^t C_x\Phi(t-\tau)B_{bsi}x_1(\tau)u(\tau)d\tau$$
$$=\frac{k_{001}k_{101}}{\omega_d^2}\int_0^t e^{-\sigma(t-\tau_1)}\sin(\omega_d(t-\tau_1))\int_0^{\tau_1}e^{-\sigma(\tau_1-\tau_2)}\sin(\omega_d(\tau_1-\tau_2))u(\tau_2)d\tau_2u(\tau_1)d\tau_1 \quad (4.46)$$
$$=\frac{k_{001}k_{101}}{\omega_d^2}\int_0^t\int_0^t e^{-\sigma(t-\tau_2)}\sin(\omega_d(t-\tau_1))\sin(\omega_d(\tau_1-\tau_2))\Delta(\tau_1-\tau_2)u(\tau_1)u(\tau_2)d\tau_1d\tau_2$$

The kernel of this component is triangular. Employing the symmetrization approach as in the case of the first order system gives the solution of the bilinear state-input component in the form of

$$x_2^{bsi}=\int_0^t\int_0^t h_2^{bsi}(t-\tau_1,t-\tau_2)u(\tau_1)u(\tau_2)d\tau_1d\tau_2 \quad (4.47)$$

where

$$h_2^{bsi}(\tau_1,\tau_2)=\frac{k_{001}k_{101}}{2\omega_d^2}e^{-\sigma\max(\tau_1,\tau_2)}$$
$$\times\{\sin(\omega_d\min(\tau_1,\tau_2))\sin(\omega_d\max(\tau_1,\tau_2)-\omega_d\min(\tau_1,\tau_2))\} \quad (4.48)$$

The difference between the bilinear state-input x_2^{bsi} and the bilinear rate-input x_2^{bri} components is a shift $-\varphi$ in the term $\omega_d(\tau-\tau_2)$ in addition to the gain differences. The solution of the bilinear rate-input component is thus

$$x_2^{bri}=\int_0^t\int_0^t h_2^{bri}(t-\tau_1,t-\tau_2)u(\tau_1)u(\tau_2)d\tau_1d\tau_2 \quad (4.49)$$

where

$$h_2^{bri}(\tau_1,\tau_2)=\frac{-k_{001}k_{011}}{2\sqrt{1-\zeta^2}\,\omega_d}e^{-\sigma\max(\tau_1,\tau_2)} \times\{\sin(\omega_d\min(\tau_1,\tau_2))\sin(\omega_d\max(\tau_1,\tau_2)-\omega_d\min(\tau_1,\tau_2)-\varphi)\} \tag{4.50}$$

The quadratic input component, as in the case of first order systems, yields

$$\begin{aligned} x_2^{qi} &= k_{002}\int_0^t \frac{e^{-\sigma(t-\tau)}}{\omega_d}\sin(\omega_d(t-\tau))u^2(\tau)d\tau \\ &= k_{002}\int_0^t\int_0^t \frac{e^{-\sigma(t-\tau_1)}}{\omega_d}\sin(\omega_d(t-\tau_1))\delta(\tau_1-\tau_2)u(\tau_2)u(\tau_1)d\tau_2 d\tau_1 \end{aligned} \tag{4.51}$$

where

$$h_2^{qi}(\tau_1,\tau_2)=\frac{k_{002}e^{-\sigma(\tau_1)}}{\omega_d}\sin(\omega_d\tau_1)\delta(\tau_1-\tau_2) \tag{4.52}$$

The overall second kernel is a sum of the six components quadratic state h_2^{qs}, bilinear state-rate h_2^{bsr}, quadratic rate h_2^{qr}, bilinear state-input h_2^{bsi}, bilinear rate-input h_2^{bri}, and quadratic input h_2^{qi}. The resultant second kernel along with the first kernel represents an approximate Volterra-based model for the second order SDOF system.

$$\begin{aligned} x &\approx \int_0^t h_1(t-\tau)u(\tau)d\tau+\int_0^t\int_0^t h_2(t-\tau_1,t-\tau_2)u(\tau_1)u(\tau_2)d\tau_1 d\tau_2 \\ h_2 &= h_2^{qs}+h_2^{bsr}+h_2^{qr}+h_2^{bsi}+h_2^{bri}+h_2^{qi} \end{aligned} \tag{4.53}$$

The Volterra-based model presents the system as two analytically developed kernels. These analytical forms are used to understand each kernel characteristic as a function of system parameters for the second order SDOF system.

The first kernel h_1 is an exponential sinusoidal function with a gain k_{001}/ω_d, frequency ω_d, and a damping factor σ. If the damping factor is less than zero, then the system lacks the damping required to stabilize the response for any excitation. Thus, the positive exponential power shapes a divergent kernel. When taking the damping factor off (null damping factor), the remaining sine term keeps the kernel shape as an oscillatory

one. For positive damping factor, it is better to parameterize the kernel by the damping ratio ζ. If the damping ratio is more than or equal to unity, then the sine term diminishes and the resultant first kernel is a sum of two exponential terms, which is the case in the first order system. These two exponential terms become equal at $\zeta = 1$. For less than unity damping ratio $\zeta < 1$, the generic shape of the first kernel is shown in Figure 4.8. In this case, the kernel starts at zero and oscillates around zero. The amplitude of such oscillation decreases with time, where the loci of minimum and maximum points are located along the envelope functions $h_{1\max}$ and $h_{1\min}$.

$$h_{1\max}(t) = \frac{k_{001}}{\omega_d} e^{-\sigma t} \quad , \quad h_{1\min}(t) = -\frac{k_{001}}{\omega_d} e^{-\sigma t} \tag{4.54}$$

The maximum points occur at times $(2n\pi+\varphi)/\omega_d$, while the minimum points occur at times $((2n+1)\pi+\varphi)/\omega_d$, where $n = 0,1,2,\ldots$ The kernel h_1 settles down inside a 2% band around zero at time

$$\tau_{ks}^{1} = \frac{-\ln(0.02)}{\sigma} \approx \frac{4}{\sigma} \qquad \text{for} \qquad 0 < \zeta < 1 \tag{4.55}$$

There are six terms for the second kernel: quadratic state h_2^{qs}, bilinear state-rate h_2^{bsr}, quadratic rate h_2^{qr}, bilinear state-input h_2^{bsi}, bilinear rate-input $h_2^{br_i}$, and quadratic input h_2^{qi}, each being a two dimensional surface in τ_1 and τ_2. The expression of the quadratic state kernel h_2^{qs} has three coefficients M_1, M_2, and M_3, which depend on the minimum operator. These operator coefficients work as dynamic weighting factors for three two-dimensional periodic signals multiplied by two-dimensional damping signals. Also, these operator coefficients force the edges of the kernel shape to be zero. Thus, all these coefficients have zero value edges. If the system lacks damping (negative σ), the generated quadratic state kernel h_2^{qs} has zero edges heading upward to infinity as τ_1 and τ_2 go to infinity. The surface becomes a constant amplitude two-dimensional sinusoidal surface for a zero damping factor. In case of positive damping factor, the overall kernel has a damped sinusoidal shape. One example for this surface is given in Figure 4.9 for $\zeta =$

0.1 and ω_n = 2 rad/s. The generic shape of the normalized quadratic state kernel diagonal $h_2^{qs}(\tau,\tau)$ is shown in Figure 4.10. The most interesting feature of the diagonal histories is that they do not oscillate around zero as would be expected. The shape oscillates around another shape, which is similar to the one in Figure 4.3, the quadratic state diagonal kernel $h_2^{qs}(\tau,\tau)$ of the first order system. During the oscillation, a set of maximum and minimum points are generated with a frequency ω_d. The time of the maximum points is $((2n+1)\pi)/\omega_d$, while the minimum point times are $(2n\pi)/\omega_d$, where n = 0,1,2,..... The loci of the signal maximum or minimum points are defined by

$$h_{2\min}^{qs} = \frac{k_{200}k_{001}^2}{\omega_d^4}\psi_1(\zeta)\left(e^{-2\sigma t} - e^{-\sigma t}\right), \quad h_{2\max}^{qs} = \frac{k_{200}k_{001}^2}{\omega_d^4}\psi_1(\zeta)\left(e^{-2\sigma t} + e^{-\sigma t}\right)$$
$$\psi_1(\zeta) = \frac{3\left(1-\zeta^2\right)^2}{\left(9-8\zeta^2\right)} \tag{4.56}$$

where $h_{2\min}^{qs}$ and $h_{2\max}^{qs}$ are the lower and upper loci. As shown in Figure 4.10, the upper locus settles after the lower locus. The settling time of the upper locus is a solution of a second order quadratic equation in $e^{-\sigma t}$. Each coefficient in this equation is a function of ζ. The settling time of the surface (or the diagonal) is computed to be

$$\tau_{ks}^{qs} = \frac{1}{\sigma}\ln\left\{\frac{2}{-1+\sqrt{1+0.08/\psi_1(\zeta)}}\right\} \quad \text{for} \quad 0<\zeta<1 \tag{4.57}$$

The bilinear state-rate kernel h_2^{bsr} is mathematically the same as the quadratic state kernel h_2^{qs} except a phase shift $-\varphi$ is added to $\omega_d(\tau-\tau_2)$. This phase shift has a significant effect on the shape of the kernel. The produced bilinear state-rate kernel starts at zero value. The damping ratio controls the convergent and divergent behavior of the surface as the case in the quadratic state kernel; $\zeta < 0$ divergent, $\zeta > 0$ convergent, and $\zeta = 0$ neutral oscillatory surface. In case of $\zeta > 0$, as the damping ratio moves closer to unity, there is less oscillation. If the damping ratio is less than unity, the surface oscillates around zero. This oscillation damps with time to zero at infinity. Figure 4.11 is an example of this

surface at ζ = 0.1 and ω_n = 2 rad/s. The generic shape of the normalized diagonal $h_2^{bsr}(\tau,\tau)$ in case of 0 < ζ < 1 is shown in Figure 4.12. During the oscillation of the surface, two sets of maximum and minimum points appear at times $(6n\pi\text{-}4\varphi)/3/\omega_d$ and $(6n\pi+4\varphi)\ /3/\omega_d$ respectively. The loci of these peaks are an indication of the surface settling time. These loci are defined from the steady envelope of the kernel, which are

$$\begin{aligned} h_{2\max}^{bsr} &= \frac{-k_{110}k_{001}^2}{2\sqrt{1-\zeta^2}\omega_d^3}\left\{\psi_2(\zeta)e^{-2\sigma t}+\psi_3(\zeta)e^{-\sigma t}\right\} \\ h_{2\min}^{bsr} &= \frac{-k_{110}k_{001}^2}{2\sqrt{1-\zeta^2}\omega_d^3}\left\{\psi_4(\zeta)e^{-2\sigma t}+\psi_5(\zeta)e^{-\sigma t}\right\} \end{aligned} \tag{4.58}$$

$$\begin{aligned} \psi_2(\zeta) &= \zeta(1-\zeta^2)+\frac{(1-\zeta^2)(3-4\zeta^2)}{(9-8\zeta^2)}\cos\left(\frac{5\varphi}{3}\right)+\frac{4\zeta(1-\zeta^2)^{3/2}}{(9-8\zeta^2)}\sin\left(\frac{5\varphi}{3}\right) \\ \psi_3(\zeta) &= \sqrt{1-\zeta^2}\left\{\zeta\sin\left(\frac{\varphi}{3}\right)-\frac{1}{2}\sin\left(\frac{7\varphi}{3}-\hat{\varphi}\right)\right\}-\frac{1}{2}\sqrt{\frac{1-\zeta^2}{9-8\zeta^2}}\sin\left(\frac{4\varphi}{3}\right) \\ \psi_4(\zeta) &= \frac{(1-\zeta^2)}{(9-8\zeta^2)}\left\{\zeta(9-8\zeta^2)+(3-4\zeta^2)\cos(11\varphi/3)-4\zeta\sqrt{1-\zeta^2}\sin(11\varphi/3)\right\} \\ \psi_5(\zeta) &= \frac{\sqrt{1-\zeta^2}}{2}\left\{\sin(4\varphi/3)-2\zeta\sin(7\varphi/3)+\frac{1}{\sqrt{9-8\zeta^2}}\sin(\varphi/3+\hat{\varphi})\right\} \end{aligned} \tag{4.59}$$

Based on these loci the settling time of the surface is a solution of a quadratic second order equation in terms of $e^{-\sigma t}$. By observation, the upper locus settles after the lower one. Using the upper locus, the settling time is computed as

$$\tau_{ks}^{bsr} = \frac{1}{\sigma}\ln\left\{\frac{2\psi_4(\zeta)}{-\psi_5(\zeta)+\sqrt{\psi_5^2(\zeta)+0.08\psi_4(\zeta)}}\right\} \quad \text{for} \quad 0<\zeta<1 \tag{4.60}$$

The 2% vicinity is considered from the normalized gain of the bilinear state-rate kernel.

The quadratic rate kernel h_2^{qr} is similar to the quadratic state kernel h_2^{qs} except the phase shift $-\varphi$ in the two arguments. This phase shift warps the diagonal lines of the kernel surface. The damping ratio controls the surface divergence or convergence (ζ > 0

convergent surface, $\zeta = 0$ oscillatory surface, and $\zeta < 0$ divergent surface). One example for the surface of the quadratic rate kernel h_2^{qr} is given in Figure 4.13 at $\zeta = 0.1$ and $\omega_n = 2$ rad/s. The surface diagonal generic shape for $0 < \zeta < 1$ is shown in Figure 4.14. The quadratic rate diagonal kernel $h_2^{qr}(\tau,\tau)$ has a set of periodic maximum and minimum points appearing at times $(2n+1)\pi/\omega_d$ and $2n\pi/\omega_d$ respectively. Because of phase shift, there is one non-periodic maximum point appearing at time $4\varphi/3\omega_d$ (see Figure 4.13). The loci of the periodic maximum and minimum points is defined as

$$
\begin{aligned}
h_{2\min}^{qr} &= \frac{k_{020}k_{001}^2}{2\left(1-\zeta^2\right)\omega_d^2}\psi_6(\zeta)\left(e^{-2\sigma t}-e^{-\sigma t}\right) \\
h_{2\max}^{qr} &= \frac{k_{020}k_{001}^2}{2\left(1-\zeta^2\right)\omega_d^2}\psi_6(\zeta)\left(e^{-2\sigma t}+e^{-\sigma t}\right) \\
\psi_6(\zeta) &= 1-\zeta^2+\frac{\left(1-\zeta^2\right)\left(4-3\zeta^2\right)}{\left(9-8\zeta^2\right)}\left\{\cos(2\varphi)+\frac{4\zeta\sqrt{1-\zeta^2}}{\left(4-3\zeta^2\right)}\sin(2\varphi)\right\}
\end{aligned}
\qquad (4.61)
$$

where $h_{2\min}^{qr}$ and $h_{2\max}^{qr}$ are the lower and upper loci. The settling time of the surface is computed to be

$$
\tau_{ks}^{qr} = \frac{1}{\sigma}\ln\left\{\frac{2}{-1+\sqrt{1+0.08/\psi_1(\zeta)}}\right\} \quad \text{for} \quad 0<\zeta<1 \qquad (4.62)
$$

The value of τ_{ks}^{qr} in Equation (4.62) changes from $3.55/\sigma$ ($\zeta = 0.1$) to $3.6/\sigma$ ($\zeta = 0.7$), which can be approximated by $3.6/\sigma$.

For the bilinear state-input kernel, the normalized expression has the same structure as the corresponding first order system term, but multiplied by two sine functions. The damping factor σ controls the divergence and convergence of the surface. For the positive damping factor, using the damping ratio, there are three cases: $0 < \zeta < 1$, $\zeta = 0$, and $\zeta \geq 1$. For null damping ratio, the normalized surface starts at zero and keeps oscillating around 0.25. For $\zeta \geq 1$, the function reduces two first order systems with two different damping coefficients. These coefficients become the same at $\zeta = 1$. If $\zeta < 1$ the

normalized surface starts oscillating from a zero value at the two frequencies and with an amplitude damped after successive oscillations, while the two arguments τ_1 and τ_2 go to infinity. Figure 4.15 is an example for the bilinear state-input kernel at $\zeta = 0.1$ and $\omega_n = 2$ rad/s. The generic shape of the $2\tau_2 = \tau_1$ diagonal time histories is shown in Figure 4.16. Starting at zero, the kernel oscillates upward generating two sets of maximum and minimum points determined by frequency ω_d. The maximum points occur at time $(2n+1)\pi/\omega_d$, while the minimum ones occur at time $2n\pi/\omega_d$. The envelope of the kernel is defined by $h_{2\max}^{bsi}(\tau,0.5\tau) = 0.5e^{-\sigma t}$ and $h_{2\min}^{bsi}(\tau,0.5\tau) = 0$, where $h_{2\max}^{bsi}$ and $h_{2\min}^{bsi}$ are the upper and lower locus, respectively. Using the upper locus, the surface settling time is computed as $\tau_{ks}^{bsi} = 4/\sigma$.

The bilinear rate-input kernel is similar to the bilinear state-input kernel with phase shift. This phase shift makes the surface oscillate around zero with a frequency ω_d. The damping ratio controls the divergence and convergence of the surface as well as the other surfaces. Figure 4.17 is an example for the bilinear rate-input kernel at $\zeta = 0.1$ and $\omega_n = 2$ rad/s. The generic shape of the $\tau_2 = \tau_1$ diagonal time histories is shown in Figure 4.18. There are two sets of maximum and minimum points determined by frequency ω_d. The maximum points occur at time $(2n\pi+\varphi)/\omega_d$, while the minimum ones occur at time $((2n+1)\pi+\varphi)/\omega_d$. The bounding curves for these sets are defined by $h_{2\max}^{bri}(\tau,\tau) = (1-\zeta^2)e^{-\sigma t}$ and $h_{2\min}^{bri}(\tau,\tau) = -(1-\zeta^2)e^{-\sigma t}$, where $h_{2\max}^{bri}$ and $h_{2\min}^{bri}$ are the upper and lower loci, respectively. Using the upper locus, the surface settling time is computed as $\tau_{ks}^{bri} = -\ln(0.02/(1-\zeta^2))/\sigma$. The settling time values change from $3.9/\sigma$ at ζ =0.1 to $2.25/\sigma$ at ζ=0.9.

The quadratic input h_2^{qi} kernel is an impulsive sheet over the diagonal kernel line. The amplitude of this sheet has the same shape as the first kernel as shown in Figure 4.8.

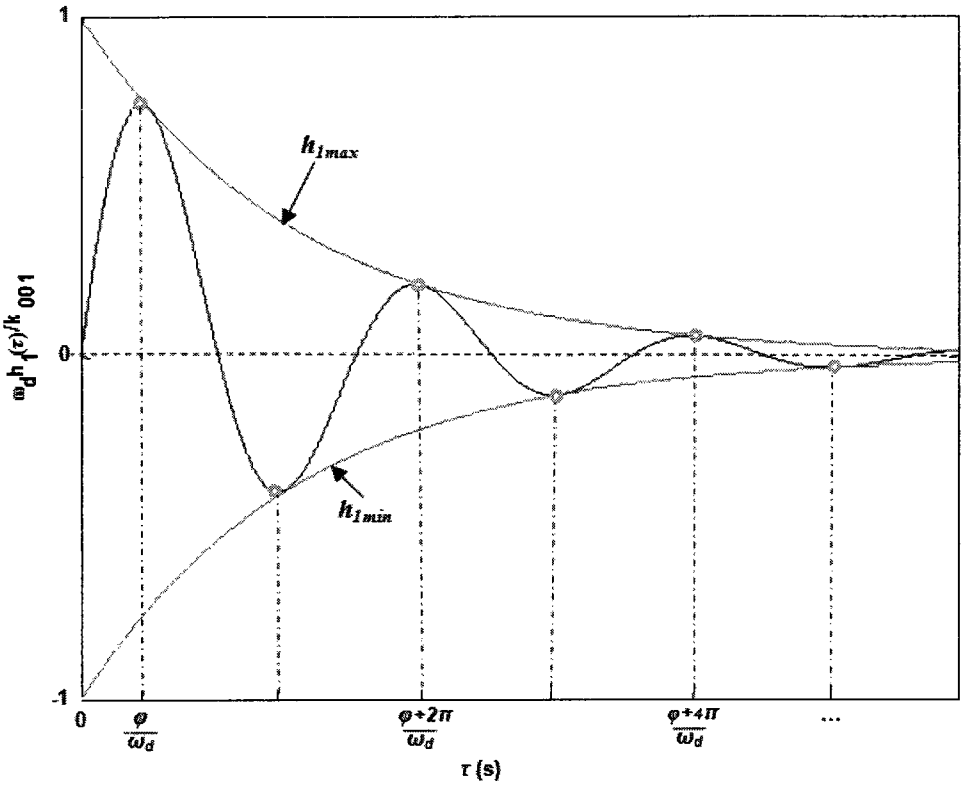

Figure 4.8 Second Order System First Kernel ($0 < \zeta < 1$)

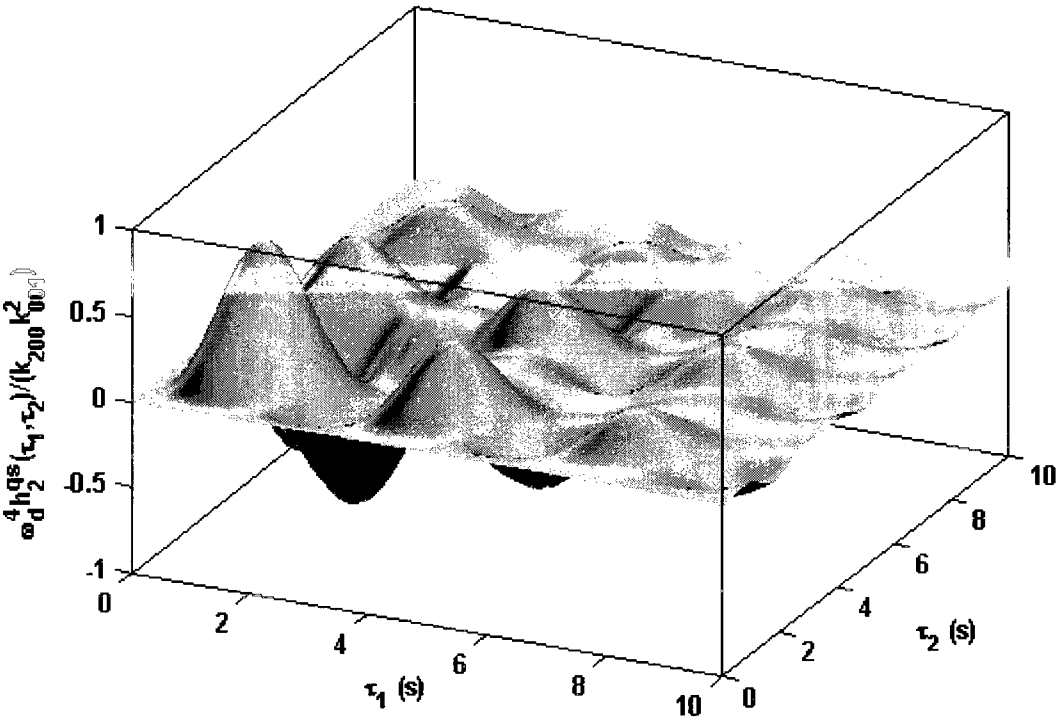

Figure 4.9 Second Order System Quadratic State Kernel ($\zeta = 0.1$and $\omega_n = 2$ rad/s)

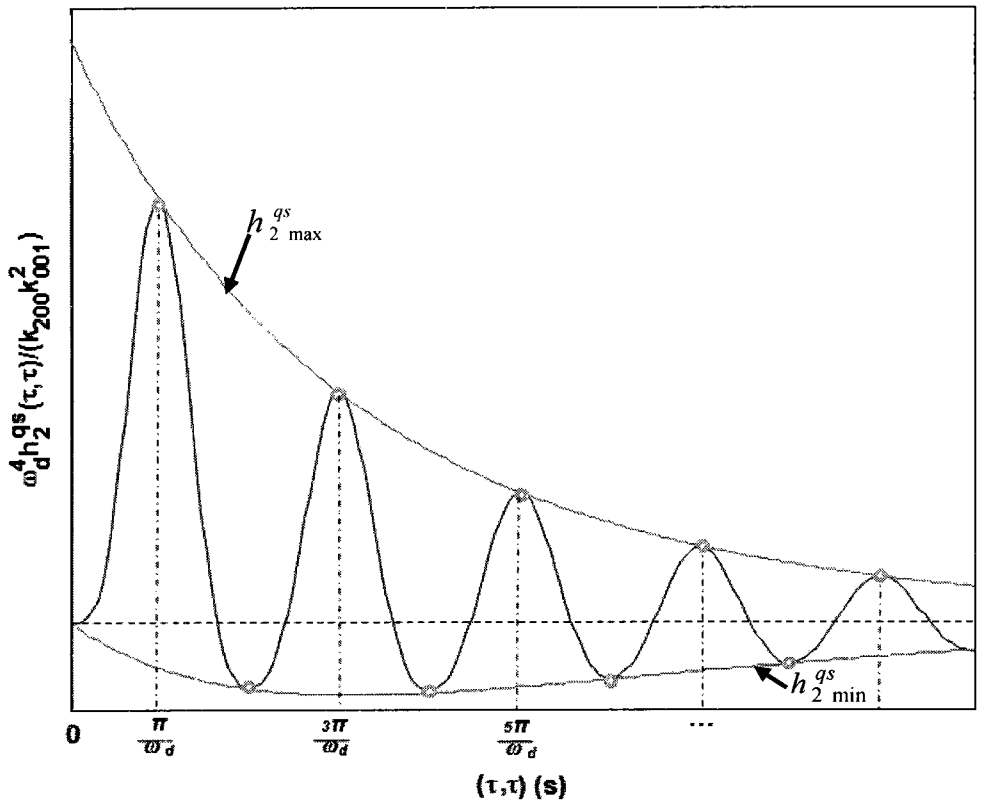

Figure 4.10 Second Order System Quadratic State Kernel Diagonal ($0 < \zeta < 1$)

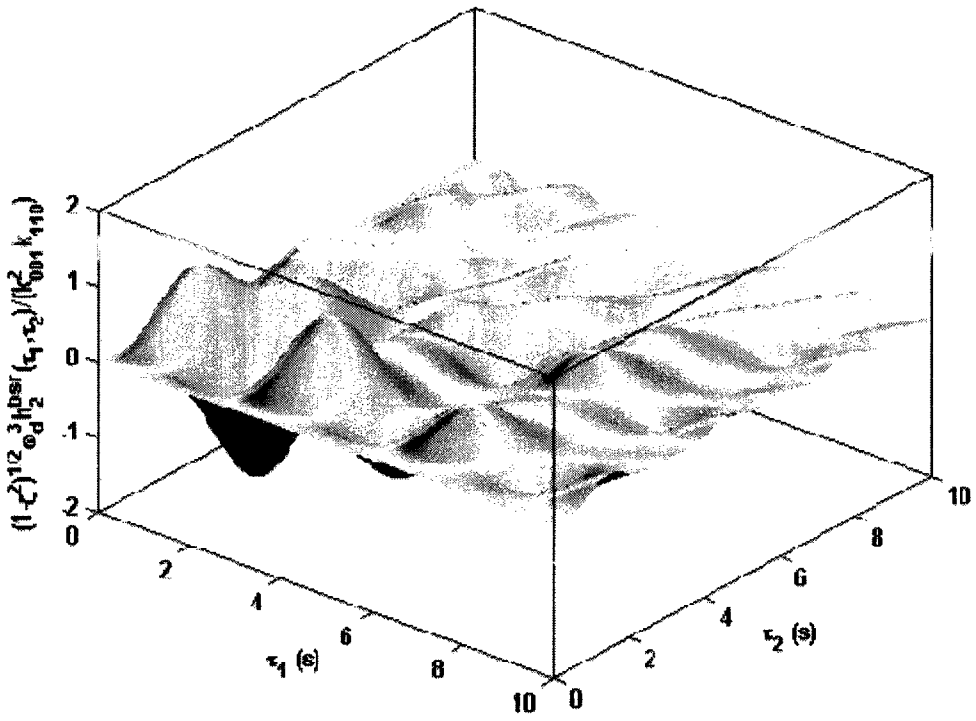

Figure 4.11 Second Order System Bilinear State-Rate Kernel ($\zeta = 0.1$ and $\omega_n = 2$ rad/s)

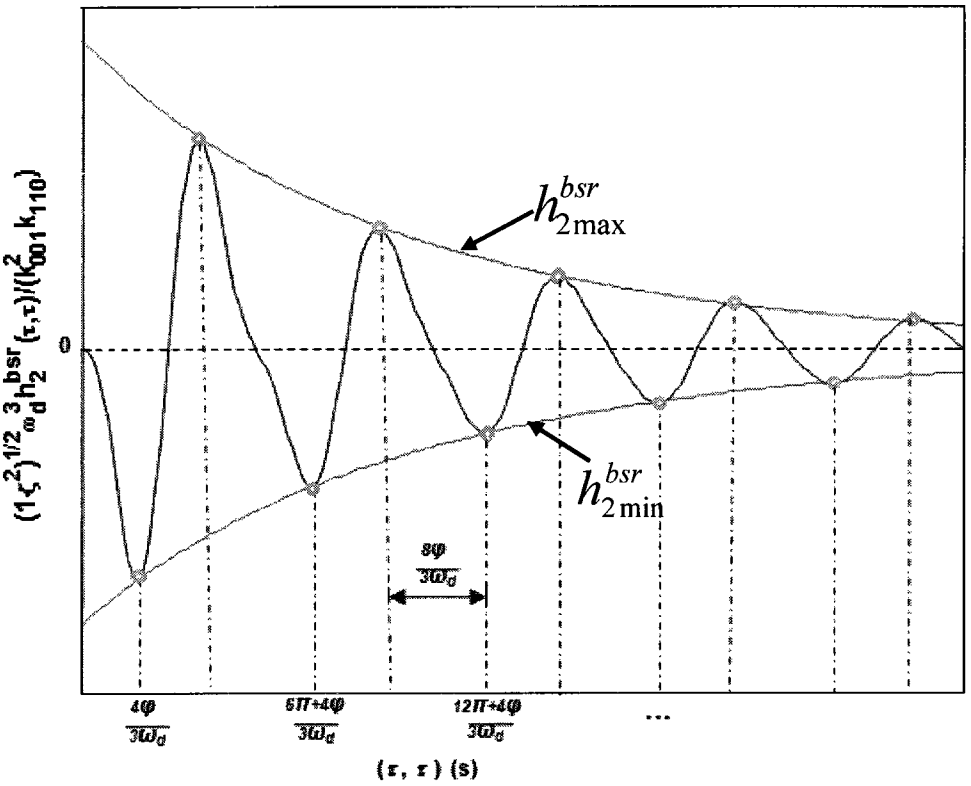

Figure 4.12 Second Order System Bilinear State-Rate Kernel Diagonal ($0 < \zeta < 1$)

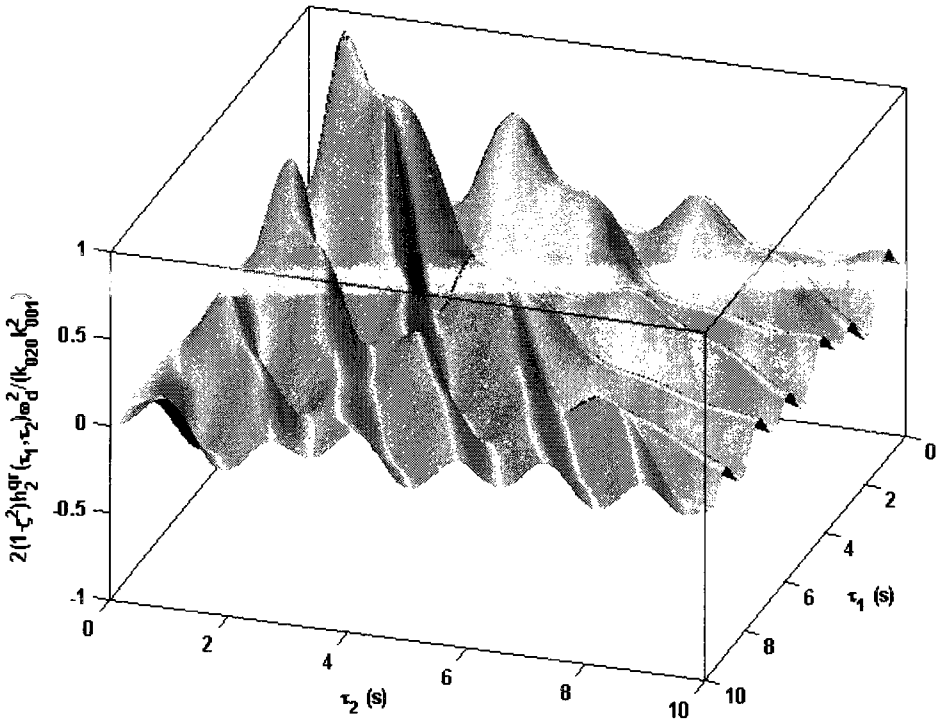

Figure 4.13 Second Order System Quadratic Rate Kernel ($\zeta = 0.1$ and $\omega_n = 2$ rad/s)

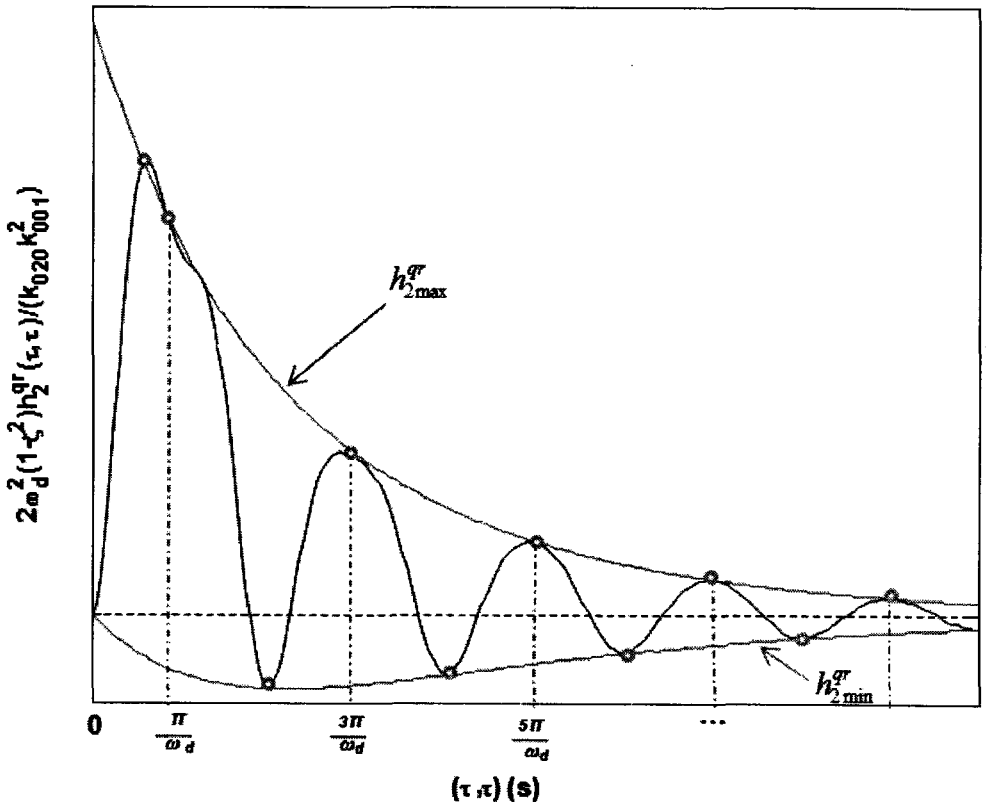

Figure 4.14 Second Order System Quadratic Rate Kernel Diagonal ($0 < \zeta < 1$)

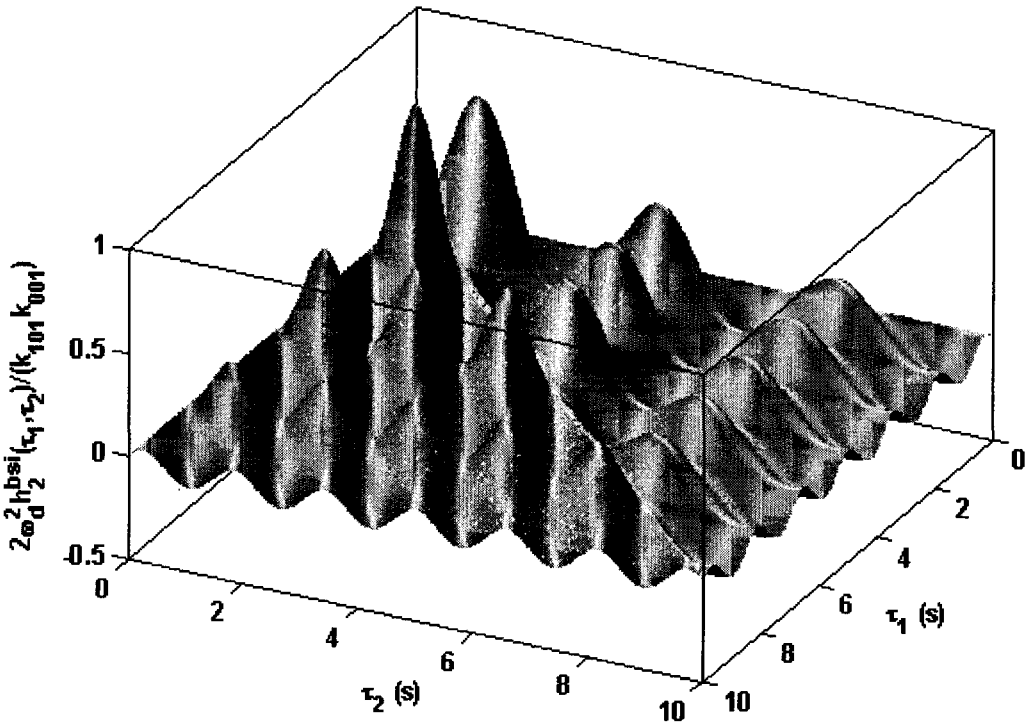

Figure 4.15 Second Order System Bilinear State-Input Kernel ($\zeta = 0.1$ and $\omega_n = 2$ rad/s)

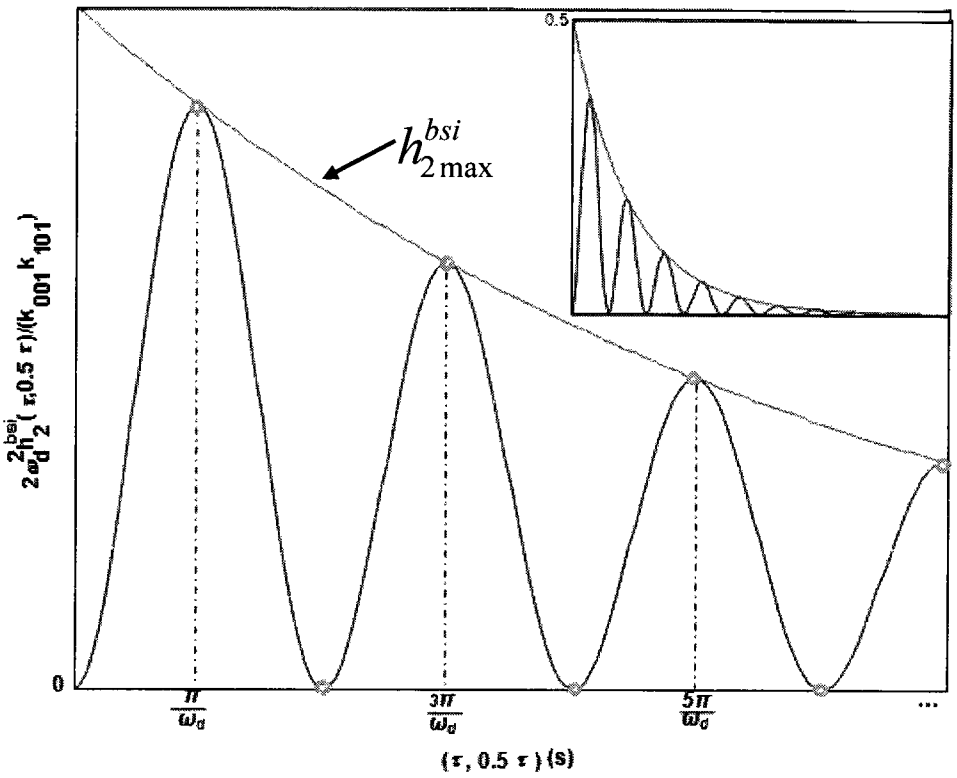

Figure 4.16 Second Order System Bilinear State-Input Kernel Diagonal ($0 < \zeta < 1$)

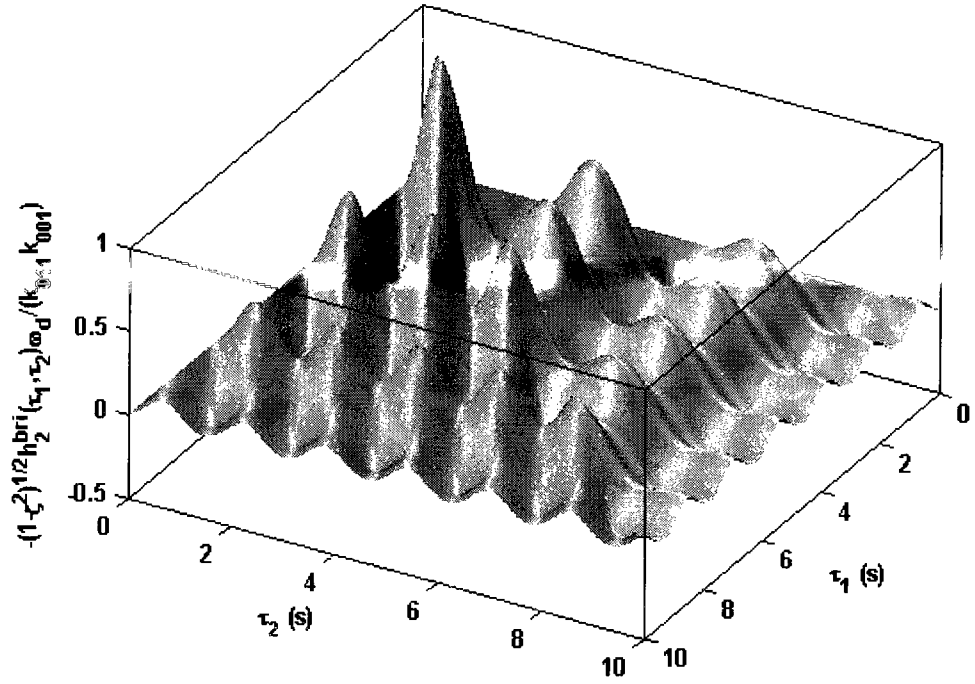

Figure 4.17 Second Order System Bilinear Rate-Input Kernel ($\zeta = 0.1$ and $\omega_n = 2$ rad/s)

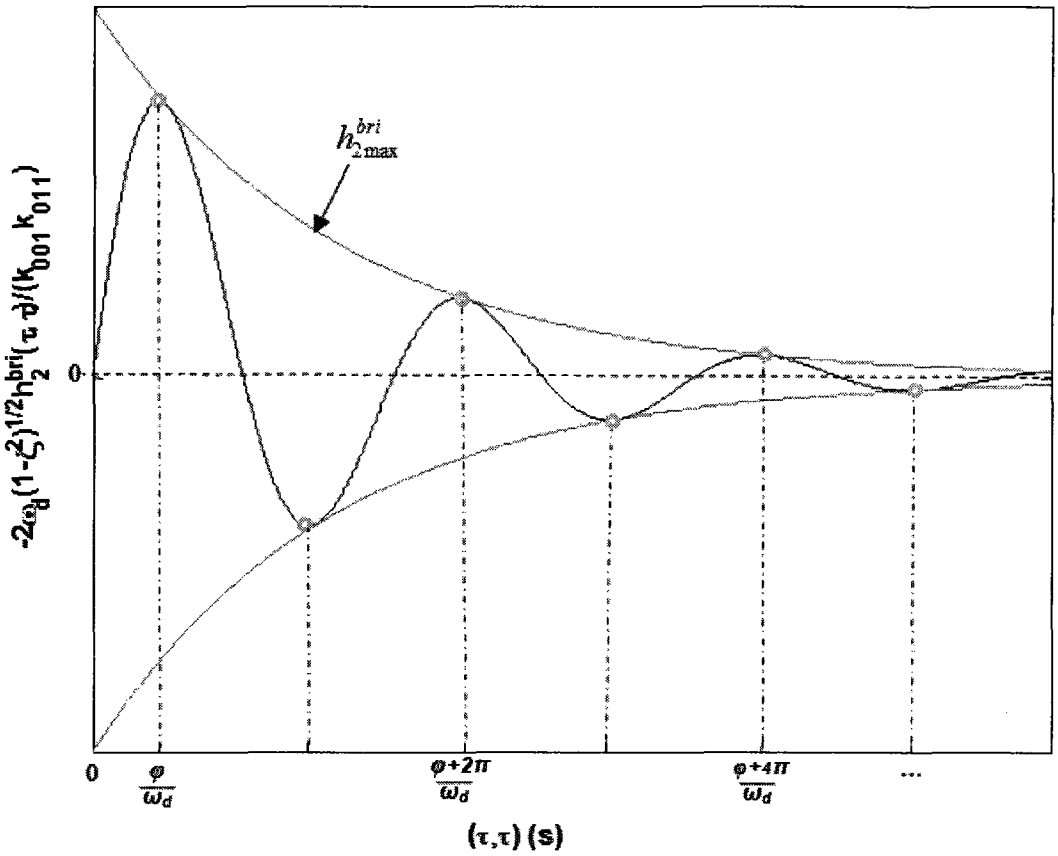

Figure 4.18 Second Order System Bilinear Rate-Input Kernel Diagonal ($0 < \zeta < 1$)

4.4 Analytical Step Response of Second Order System

The step response of this approximate nonlinear system is computed as

$$x = x_1 + x_2^{qs} + x_2^{bsr} + x_2^{qr} + x_2^{bsi} + x_2^{bri} + x_2^{qi} \tag{4.63}$$

with

$$x_1 = \frac{k_{001}A}{\omega_n^2}\left\{1 - \frac{e^{-\sigma t}}{\sqrt{1-\zeta^2}}\sin(\omega_d t + \varphi)\right\} \tag{4.64}$$

$$\begin{aligned} x_2^{qs} = \frac{k_{001}^2 k_{200} A^2}{\omega_n^6}\Bigg\{1 + \frac{e^{-\sigma t}}{4(1-\zeta^2)^{3/2}}\Big[4\omega_d t\cos(\omega_d t+\varphi) - 2(3-2\zeta^2)\sin(\omega_d t+\varphi) \\ - \sin(\omega_d t + 3\varphi) - \frac{1}{\sqrt{9-8\zeta^2}}\sin(\omega_d t - 2\varphi - \hat{\varphi})\Big] \\ + \frac{e^{-2\sigma t}}{4(1-\zeta^2)}\left[2 + \frac{1}{\sqrt{1-\zeta^2}}\sin(2\omega_d t + 3\varphi) - \frac{1}{\sqrt{1-\zeta^2}\sqrt{9-8\zeta^2}}\sin(2\omega_d t + 2\varphi + \hat{\varphi})\right]\Bigg\} \end{aligned} \tag{4.65}$$

$$x_2^{bsr} = \frac{k_{001}^2 k_{110} A^2}{\omega_n^5} \frac{e^{-\sigma t}}{2(1-\zeta^2)^{3/2}(9-8\zeta^2)}$$
$$\times \left\{ \left[16\zeta(1-\zeta^2)^{3/2} - (9-8\zeta^2)(\omega_d t)\right] \cos(\omega_d t) + \left[3-2\zeta^2\right]\sin(\omega_d t) \right. \tag{4.66}$$
$$\left. + \sqrt{1-\zeta^2}\, e^{-\sigma t}\left[(3-4\zeta^2)\cos(2\omega_d t+\varphi) + 4\zeta\sqrt{1-\zeta^2}\,\sin(2\omega_d t+\varphi) + \zeta(9-8\zeta^2)\right] \right\}$$

$$x_2^{qr} = \frac{k_{001}^2 k_{020} A^2}{4\omega_d^3 \omega_n} \left\{ e^{-2\sigma t}\left(2\sin(\varphi) + \sin(2\omega_d t+\varphi) - \frac{1}{\sqrt{9-8\zeta^2}}\sin(2\omega_d t+\hat{\varphi}) \right) \right. \tag{4.67}$$
$$\left. + e^{-\sigma t}\left(2\sin(\omega_d t-\varphi) - \sin(\omega_d t+\varphi) - \frac{1}{\sqrt{9-8\zeta^2}}\sin(2\omega_d t-\hat{\varphi}) \right) \right\}$$

$$x_2^{bsi} = \frac{k_{001} k_{101} A^2}{\omega_n^4}$$
$$\times \left\{ 1 - \frac{e^{-\sigma t}}{2(1-\zeta^2)^{3/2}} \left[\zeta \sin(\omega_d t) + 2(1-\zeta^2)\sin(\omega_d t+\varphi) - \omega_d t \cos(\omega_d t+\varphi) \right] \right\} \tag{4.68}$$

$$x_2^{bri} = \frac{k_{001} k_{011} A^2 e^{-\sigma t}}{2\omega_d^3} \left\{ \sin(\omega_d t) - t\omega_d \cos(\omega_d t) \right\} \tag{4.69}$$

$$x_2^{qi} = \frac{k_{002} A^2}{\omega_n^2} \left\{ 1 - \frac{e^{-\sigma t}}{\sqrt{1-\zeta^2}} \sin(\omega_d t+\varphi) \right\} \tag{4.70}$$

where A is the input amplitude. Assembling the linear term x_1 along with all the nonlinear components x_2^{qs}, x_2^{bsr}, x_2^{qr}, x_2^{bsi}, x_2^{bri}, and x_2^{qi} gives the overall system response for a step input. Each term has different influences on the overall behavior. Figures 4.19-4.24 show the generic shape of each individual component for $0 < \zeta < 1$. The resultant generic shapes in Figures 4.19-4.24 are specifically taken at $\zeta = 0.1$ or less in some cases in order to show all the feature of each response. As in the case of the first order system, both linear and quadratic input terms have the same generic shape but with different gain; $k_{001} A / \omega_n^2$ for the linear term and $k_{002} A^2 / \omega_n^2$ for the quadratic input component.

All responses start at zero with a zero rate (initial conditions), and head upward or downward depending on their equivalent sign. The nonlinear components $x_2^{qs}, x_2^{bsr}, x_2^{qr}, x_2^{bsi}$, and x_2^{bri} have observed initial time lags. If a 2% tolerance is considered to define this lag vicinity, the equivalent time lags are computed as

$$\tau_{rl}^{qs} = \frac{1.5\zeta - 0.05}{\sigma}, \quad \tau_{rl}^{bsr} = \frac{1.33\zeta - 0.05}{\sigma}, \quad \tau_{rl}^{qr} = \frac{0.38\zeta - 0.03}{\sigma}$$
$$\tau_{rl}^{bsi} = \frac{0.97\zeta - 0.02}{\sigma}, \quad \tau_{rl}^{bri} = \frac{0.33\zeta - 0.02}{\sigma} \tag{4.71}$$

where $\tau_{rl}^{qs}, \tau_{rl}^{bsr}, \tau_{rl}^{qr}, \tau_{rl}^{bsi}$, and τ_{rl}^{bri} are the time lags for $x_2^{qs}, x_2^{bsr}, x_2^{qr}, x_2^{bsi}$, and x_2^{bri} respectively. Note because of the expression complexity of these nonlinear components, a fitting technique is employed to find approximate expressions for the equivalent time lags as listed in Equation (4.71) and as shown in Figure 4.25. Linear approximations are adequate for a wide range of damping ratio. The 2% threshold is defined by the steady value of each term for x_{rl}^{qs} and x_{rl}^{bsi} and the maximum value for x_{rl}^{qr}, x_{rl}^{bsr}, and x_{rl}^{bri}. The linear term and the quadratic input component do not have such time lags. Both start immediately to rise to their steady value. This observation is consistent with the one in the first order system case, which emphasizes that any noticeable change in the initial slope of the nonlinear response, from that given by the linear model, is traced back to the quadratic input nonlinearity. Also, the time lags are the instances at which a deviation between linear and nonlinear simulation starts to be significant in the case of a zero quadratic input coefficient, which is frequently observed in aircraft applications.

After leaving the 2% vicinities, all responses oscillate around their equivalent steady values. All terms correlated with the rate, x_2^{bsr}, x_2^{qr}, and x_2^{bri}, oscillate around a zero value. This observation means that they do not have any influence on the overall response's steady value. Thus, for the stable case $\zeta > 0$, when the total system behavior settles down, its rate settles at zero ($v = v_1 + v_2 + \ldots = 0$). Then, these terms diminish.

All terms oscillate with the same frequency ω_d generating a set of maximum and minimum points. Both quadratic state x_2^{qs} and bilinear state-input x_2^{bsi} components achieve their minimum and maximum values at the same times, which are $(4n+5)\pi/2/\omega_d$ and $(4n+3)\pi/2/\omega_d$ respectively, where $n = 0,1,2,\ldots$ The remaining components including the linear term have minimum and maximum values at times $(2n+3)\pi/\omega_d$ and $(2n+2)\pi/\omega_d$, where $n = 0,1,2,\ldots$ Based on these results, both quadratic state x_2^{qs} and bilinear state-

input x_2^{bsi} components produce a phase shift in the observed peaks especially after the linear behavior settles down.

The loci of the maximum and minimum points are achieved by retaining only the steady effect of the oscillation terms in the original expressions (see Equations (4.64-4.70)) as

$$x_{1\min} = \frac{k_{001}A}{\omega_n^2}\left\{1-\frac{e^{-\sigma t}}{\sqrt{1-\zeta^2}}\right\} \quad , \quad x_{1\max} = \frac{k_{001}A}{\omega_n^2}\left\{1+\frac{e^{-\sigma t}}{\sqrt{1-\zeta^2}}\right\} \tag{4.72}$$

$$x_{2\min}^{qs} = \frac{k_{001}^2 k_{200}A^2}{\omega_n^6}\left\{1-\psi_7(\zeta)e^{-\sigma t}+\psi_8(\zeta)e^{-2\sigma t}\right\}$$

$$x_{2\max}^{qs} = \frac{k_{001}^2 k_{200}A^2}{\omega_n^6}\left\{1+\psi_7(\zeta)e^{-\sigma t}+\psi_8(\zeta)e^{-2\sigma t}\right\}$$

$$\psi_7 = \frac{1}{4\left(1-\zeta^2\right)^{3/2}}\left[4\omega_d t\sin(\varphi)+2(3-2\zeta^2)\cos(\varphi)+\cos(3\varphi)+\frac{1}{\sqrt{9-8\zeta^2}}\cos(2\varphi+\hat{\varphi})\right] \tag{4.73}$$

$$\psi_8 = \frac{1}{4\left(1-\zeta^2\right)}\left[2-\frac{1}{\sqrt{1-\zeta^2}}\sin(3\varphi)+\frac{1}{\sqrt{1-\zeta^2}\sqrt{9-8\zeta^2}}\sin(2\varphi+\hat{\varphi})\right]$$

$$x_{2\min}^{bsr} = \frac{k_{001}^2 k_{110}A^2}{\omega_n^5}\left\{\frac{-\omega_d t e^{-\sigma t}}{2\left(1-\zeta^2\right)^{3/2}}+\frac{8\zeta}{9-8\zeta^2}\left(e^{-2\sigma t}-e^{-\sigma t}\right)\right\}$$

$$x_{2\max}^{bsr} = \frac{k_{001}^2 k_{110}A^2}{\omega_n^5}\left\{\frac{\omega_d t e^{-\sigma t}\left(9+8\zeta^2\right)}{2\left(1-\zeta^2\right)^{3/2}\left(9-8\zeta^2\right)}-\frac{8\zeta}{9-8\zeta^2}\left(e^{-2\sigma t}-e^{-\sigma t}\right)\right\} \tag{4.74}$$

$$x_{2\min}^{qr} = \frac{3k_{001}^2 k_{020}A^2\left(4-9\zeta^2+4\zeta^4\right)}{2\omega_d^4\left(9-8\zeta^2\right)}\left(e^{-2\sigma t}-e^{-\sigma t}\right)$$

$$x_{2\max}^{qr} = \frac{3k_{001}^2 k_{020}A^2\left(4-9\zeta^2+4\zeta^4\right)}{2\omega_d^4\left(9-8\zeta^2\right)}\left(e^{-2\sigma t}+e^{-\sigma t}\right) \tag{4.75}$$

$$x_{2\min}^{bsi} = \frac{k_{001}k_{101}A^2}{\omega_n^4}\left\{1-\frac{e^{-\sigma t}}{2\left(1-\zeta^2\right)^{3/2}}\left[\zeta\left(3-2\zeta^2\right)+\omega_d t\sqrt{1-\zeta^2}\right]\right\}$$

$$x_{2\max}^{bsi} = \frac{k_{001}k_{101}A^2}{\omega_n^4}\left\{1+\frac{e^{-\sigma t}}{2\left(1-\zeta^2\right)^{3/2}}\left[\zeta\left(3-2\zeta^2\right)+\omega_d t\sqrt{1-\zeta^2}\right]\right\} \tag{4.76}$$

$$x_{2\min}^{bri} = \frac{-k_{001}k_{011}A^2}{2\omega_d^3}\left\{t\omega_d e^{-\sigma t}\right\} \quad , \quad x_{2\max}^{bri} = \frac{k_{001}k_{011}A^2}{2\omega_d^3}\left\{t\omega_d e^{-\sigma t}\right\} \tag{4.77}$$

$$x_{2\max}^{qi} = \frac{k_{002}A^2}{\omega_n^2}\left\{1-\frac{e^{-\sigma t}}{\sqrt{1-\zeta^2}}\right\} \quad , \quad x_{2\min}^{qi} = \frac{k_{002}A^2}{\omega_n^2}\left\{1+\frac{e^{-\sigma t}}{\sqrt{1-\zeta^2}}\right\} \tag{4.78}$$

where $x_{j\min}^{i}$ and $x_{j\max}^{i}$ are the loci of minimum and maximum points for the term x_j^i, where $i = \{(), qs, bsr, qr, bsi, bri, qi\}$ and $j = \{1, 2\}$. These loci are good estimators for the settling time of each component. For the linear term and quadratic input component, the response settling time based on their equivalent loci is $\tau_{rs}^{l} = \tau_{rs}^{qi} = 4/\sigma$. By solving a quadratic equation formed by equating Equation (4.75) to a 2% value, the settling time of the quadratic rate component is

$$\tau_{rs}^{qr} = \frac{1}{\sigma}\ln\left\{\frac{2}{-1+\sqrt{1+0.08/\psi_9(\zeta)}}\right\} \quad \text{for} \quad 0<\zeta<1$$
$$\psi_9(\zeta) = \frac{6\left(4-9\zeta^2+4\zeta^4\right)}{\left(9-8\zeta^2\right)} \tag{4.79}$$

For the rest of terms $x_2^{qs}, x_2^{bsr}, x_2^{bsi}$, and x_2^{bri}, a fitting technique is used based on the results in Figure 4.26 to present the settling times as

$$\tau_{rs}^{qs} = \frac{6.8\zeta^2-8.2\zeta+9.0}{\sigma} \quad , \quad \tau_{rs}^{bsr} = \frac{-0.23\zeta^2-0.54\zeta+6.8}{\sigma}$$
$$\tau_{rs}^{bsi} = \frac{7.4\zeta^2-8.3\zeta+8.2}{\sigma} \quad , \quad \tau_{rs}^{bri} = \frac{-2.2\zeta^2-2.7\zeta+7.4}{\sigma} \tag{4.80}$$

Quadratic approximations are needed here to cover a range of damping ratio. The overall settling time depends on the ratio between the coefficients, undamped natural frequency, and damping ratio.

Based on the solution in Equations (4.63-4.70), if the system has low frequency, the nonlinearity of the system starts to be significant even when the system has small nonlinear coefficients, but influence of this frequency on the settling time is the same as in the linear case. On the other hand, the damping ratio ζ does not change the ratio between the linear and nonlinear terms, but changes the overall settling time. In addition, the sign ratio between the coefficients plays an important role in the settling time.

Negative nonlinear coefficients may lead to improvement of the settling time or make it longer. Using this assembly, the estimated overall steady value x_{ss} is

$$x_{ss} = \frac{k_{001}A}{\omega_n^2} + \frac{k_{001}^2 k_{200}A^2}{\omega_n^6} + \frac{k_{001}k_{101}A^2}{\omega_n^4} + \frac{k_{002}A^2}{\omega_n^2} \tag{4.81}$$

This steady value depends on the system parameters as well as the input amplitude.

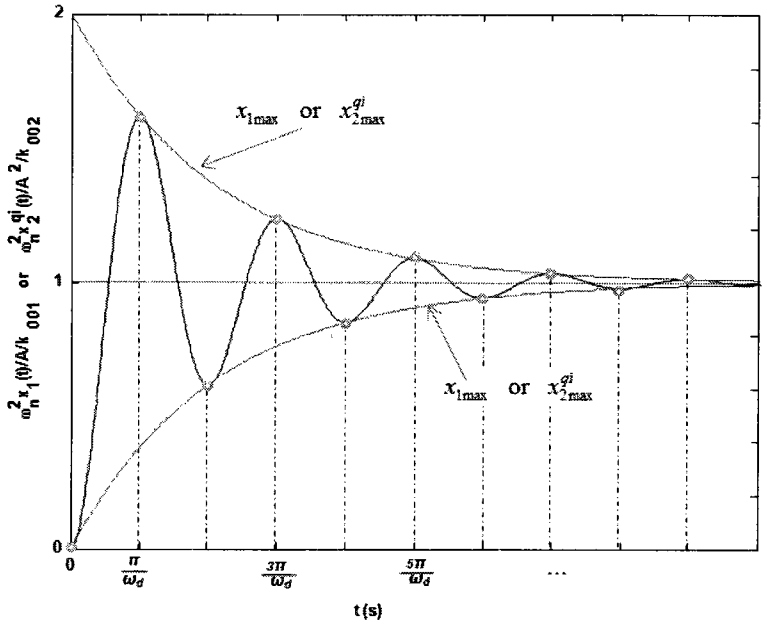

Figure 4.19 Linear or Quadratic Input Response to Step Input ($0 < \zeta < 1$)

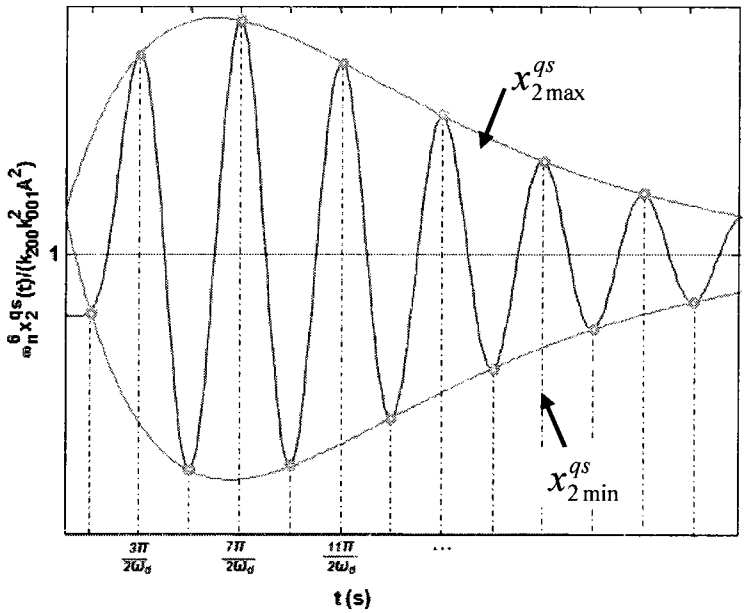

Figure 4.20 Quadratic State Response to Step Input ($0 < \zeta < 1$)

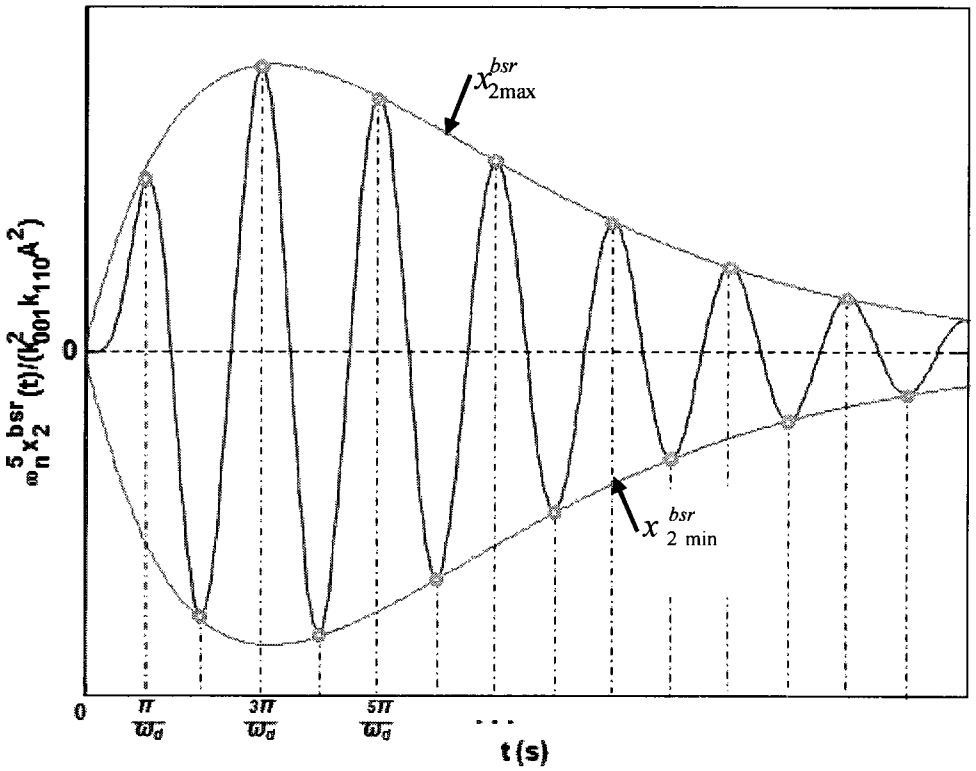

Figure 4.21 Bilinear State-Rate Response to Step Input ($0 < \zeta < 1$)

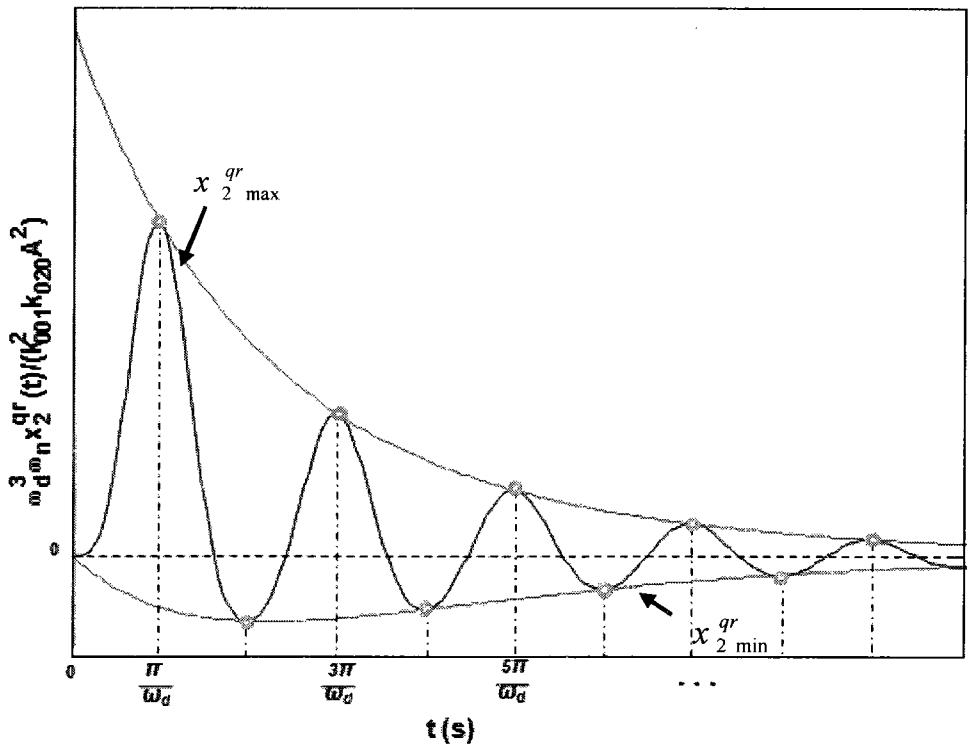

Figure 4.22 Quadratic Rate Response to Step Input ($0 < \zeta < 1$)

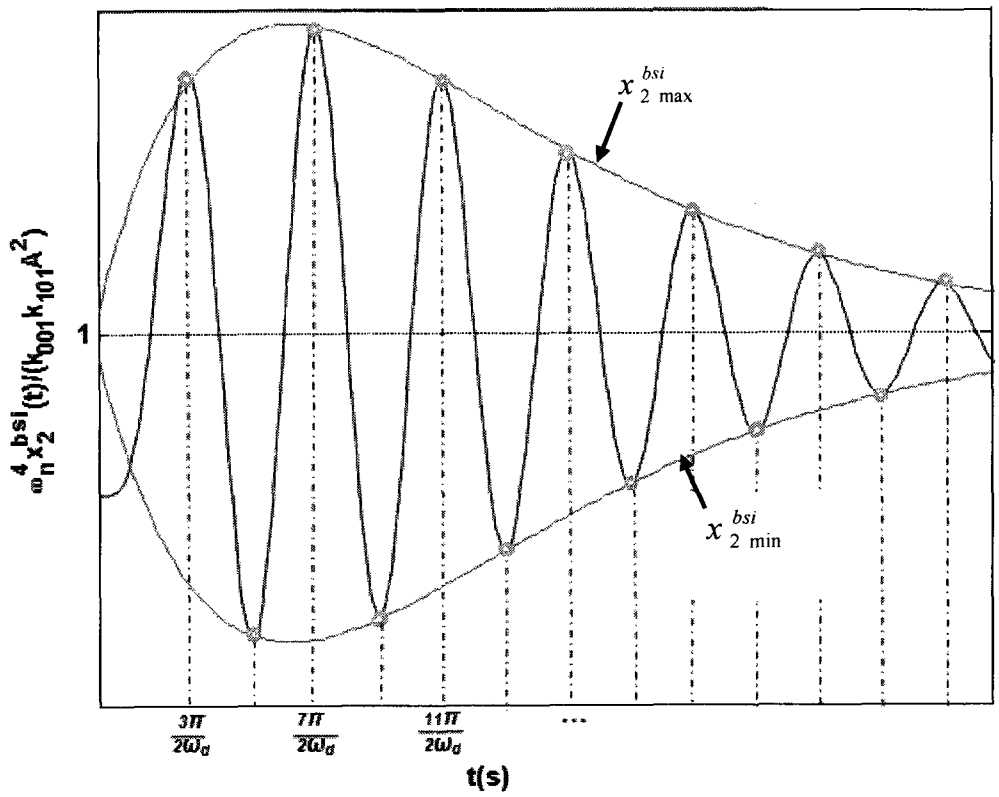

Figure 4.23 Bilinear State-Input Response to Step Input ($0 < \zeta < 1$)

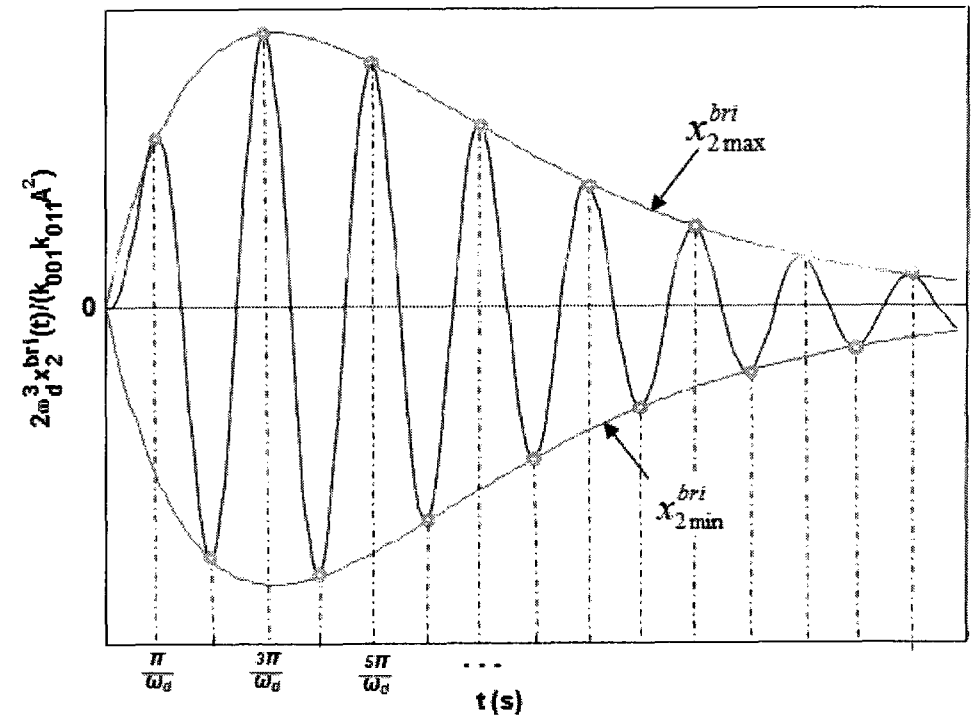

Figure 4.24 Bilinear Rate-Input Response to Step Input ($0 < \zeta < 1$)

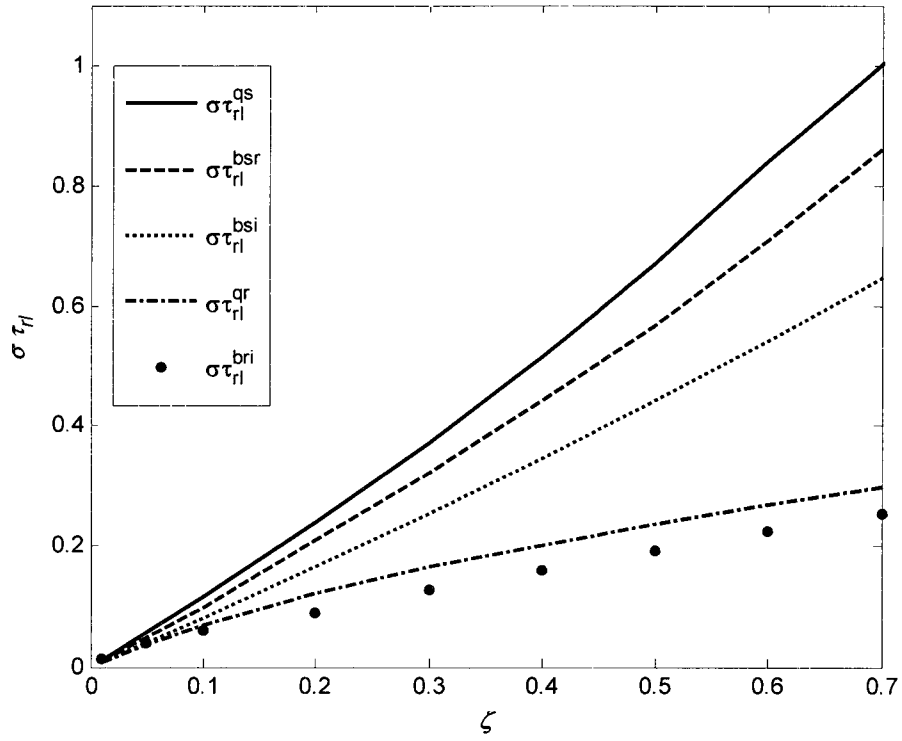

Figure 4.25 Lag Time Variation for Nonlinear Components

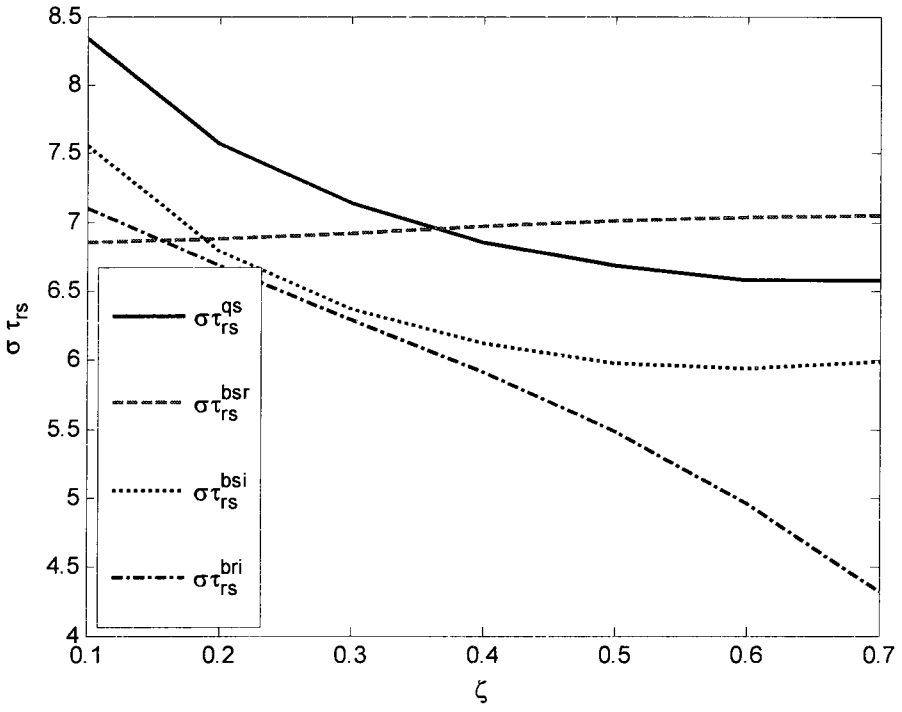

Figure 4.26 Settling Time Variation for Nonlinear Components

4.5 Low Order Uniaxial Flight Dynamic Sub-Systems

This section shows how the full order aircraft dynamic model can be represented as a set of low order flight dynamic sub-systems while preserving the link to the more general model. The four low order system examples: surge, pitch, roll, and yaw motions, are offered herein as demonstrations. Each example represents a SDOF uniaxial motion. Reference 113 contains a frequently cited full order dynamic model of a high performance aircraft. This model is considered under many assumptions: the aircraft is a rigid body with six degrees of freedom (6DOF) except for an internal constant spinning engine rotor, the aircraft mass is constant, the aircraft body is symmetric about the *XZ* plane, the atmosphere is stationary, and the earth is flat with constant gravity. Based on those assumptions the nonlinear equations of motion, derived from Newtonian mechanics, are

$$\dot{u} = rv - qw - g\sin\theta + \frac{\bar{q}S}{m}C_{X_T} + \frac{T}{m} \tag{4.82}$$

$$\dot{v} = pw - ru + g\cos\theta\sin\varphi + \frac{\bar{q}S}{m}C_{Y_T} \tag{4.83}$$

$$\dot{w} = qu - pv + g\cos\theta\cos\varphi + \frac{\bar{q}S}{m}C_{Z_T} \tag{4.84}$$

$$\dot{p} = \frac{I_Y - I_Z}{I_X}qr + \frac{I_{XZ}}{I_X}\left(\dot{r} + pq\right) + \frac{\bar{q}Sb}{I_X}C_{L_T} \tag{4.85}$$

$$\dot{q} = \frac{I_Z - I_X}{I_Y}pr + \frac{I_{XZ}}{I_Y}\left(r^2 - p^2\right) + \frac{\bar{q}S\bar{c}}{I_Y}C_{M_T} - H_e r \tag{4.86}$$

$$\dot{r} = \frac{I_X - I_Y}{I_Z}pq + \frac{I_{XZ}}{I_Z}\left(\dot{p} - qr\right) + \frac{\bar{q}Sb}{I_Z}C_{N_T} + H_e q \tag{4.87}$$

The aerodynamic and engine data used in the aircraft model have been developed by test at the NASA Langley Research Center in 1979 as listed in Reference 113. This test was conducted in low-speed wind tunnel facilities. The model data represents the

total aerodynamic coefficients ($C_{X_T}, C_{Y_T}, C_{Z_T}, C_{L_T}, C_{M_T}, C_{N_T}$) corresponding to angle of attack α, sideslip angle β, elevator deflection δ_e, aileron deflection δ_a, and rudder deflection δ_r. In Reference 5, a simplified model of the F-16 aerodynamics is represented. Simplification comes about by programming leading edge flap movement as a function of angle of attack and Mach number (an actual schedule in the F-16 control system) and combining associated tabular aerodynamic data, along with additional approximation of sideslip dependency. The new model has the capability to reduce the computational time with acceptable accuracy, but the simplicity of this model restricts the angle of attack range to -10° /+45° and the sideslip angle range to -30°/+30°. For completeness, the equations for the aerodynamic coefficients of the simplified model will be listed here. More details are given in Reference 5.

$$C_{X_T} = C_X(\alpha, \delta_e) + \frac{\bar{c}q}{2V} C_{Xq}(\alpha) \tag{4.88}$$

$$C_{Y_T} = -0.02\beta + 0.021\left(\frac{\delta_a}{20}\right) + 0.086\left(\frac{\delta_r}{30}\right) + \frac{br}{2V} C_{Yr}(\alpha) + \frac{bp}{2V} C_{Yp}(\alpha) \tag{4.89}$$

$$C_{Z_T} = C_Z(\alpha)\left[1 - \left(\frac{\beta}{57.3}\right)^2\right] - 0.19\left(\frac{\delta_e}{25}\right) + \frac{\bar{c}q}{2V} C_{Zq}(\alpha) \tag{4.90}$$

$$C_{L_T} = C_L(\alpha, \beta) + C_{L\delta_a}(\alpha, \beta)\left(\frac{\delta_a}{20}\right) + C_{L\delta_r}(\alpha, \beta)\left(\frac{\delta_r}{30}\right) + \frac{br}{2V} C_{Lr}(\alpha) + \frac{bp}{2V} C_{Lp}(\alpha) \tag{4.91}$$

$$C_{M_T} = C_M(\alpha, \delta_e) + C_{Z_T}\left(\bar{x}_{cg_r} - \bar{x}_{cg}\right) + \frac{\bar{c}q}{2V} C_{Mq}(\alpha) \tag{4.92}$$

$$\begin{aligned} C_{N_T} = {} & C_N(\alpha, \beta) + C_{N\delta_a}(\alpha, \beta)\left(\frac{\delta_a}{20}\right) + C_{N\delta_r}(\alpha, \beta)\left(\frac{\delta_r}{30}\right) \\ & + \frac{br}{2V} C_{Nr}(\alpha) + \frac{bp}{2V} C_{Np}(\alpha) - C_{Y_T}\left(\bar{x}_{cg_r} - \bar{x}_{cg}\right)\frac{\bar{c}}{b} \end{aligned} \tag{4.93}$$

The equivalent aerodynamic tables of this model are given in Reference 5. All tabular data are valid only for the bounds on angle of attack, sideslip angle, and control surface deflections (see Table 4.1 where the given data is from Reference 5).

Table 4.1 Control Surface Limits

Control Surface	Travel Limit (deg)	Rate Limit (deg/s)	Time Constant (s)
Elevator	±25	60	0.0495
Aileron	±21.5	80	0.0495
Rudder	±30	120	0.0495

The afterburner turbofan engine model is considered a first order lag for actual power level. The lag time constant is related to actual power and commanded power (linear function of throttle deflection) levels by a linear function with different slopes, and the thrust is then computed from tabular data corresponding to the actual power level, altitude, and Mach number. All the numerical values of the engine model are given in Reference 5. Even though this first order lag models engine thrust spool up or spool down, the angular momentum of the engine rotor (H_e) appearing in the aircraft pitch and yaw acceleration equations is assumed constant. The control surface actuators are assumed to be first order lags with some nonlinearities in actuation limitation.

The dominant behavior of a conventional aircraft can be fairly well described by a symmetric motion (longitudinal) and an asymmetric motion (lateral-directional), if the engine angular momentum H_e is assumed zero. For symmetric longitudinal flight, the lateral-directional variables are exactly zero due to airplane symmetry about the XZ plane. In this case, the aircraft motion can be described by a reduced nonlinear longitudinal model as

$$\dot{u} = -qw - g\sin\theta + \frac{\bar{q}S}{m} C_{X_T}(\alpha, q, \delta_e) + \frac{T}{m} \tag{4.94}$$

$$\dot{w} = qu + g\cos\theta + \frac{\bar{q}S}{m} C_{Z_T}(\alpha, q, \beta = 0, \delta_e) \tag{4.95}$$

$$\dot{q} = \frac{\bar{q}S\bar{c}}{I_Y} C_{M_T}(\alpha, q, \beta = 0, \delta_e) \tag{4.96}$$

$$\dot{\theta} = q \tag{4.97}$$

Using the stability axes and the relations $w = V\sin(\alpha)$, $u = V\cos(\alpha)$, and $V^2 = u^2 + w^2$, one can replace the surge u and heave w equations by

$$\dot{V} = \frac{\cos(\alpha)}{m} T(M, H, \delta_{th}) - \frac{\bar{q}S}{m} C_D(\alpha, q, \delta_e) - g\sin(\theta - \alpha) \tag{4.98}$$

$$\dot{\alpha} = q - \frac{\sin(\alpha)}{mV} T(M, H, \delta_{th}) - \frac{\bar{q}S}{mV} C_L(\alpha, q, \delta_e) + \frac{g}{V}\cos(\theta - \alpha) \tag{4.99}$$

and

$$\begin{aligned} C_D &= -C_{X_T}\cos(\alpha) - C_{Z_T}\sin(\alpha) \\ C_L &= -C_{Z_T}\cos(\alpha) + C_{X_T}\sin(\alpha) \end{aligned} \tag{4.100}$$

where V is the total velocity.

If an autopilot is assumed to hold the altitude to a constant value H_o and the flight path angle $\gamma_o = \theta_o - \alpha_o$ at zero value along with $q_o = 0$, then variation of the total velocity is given as

$$\dot{V} = \frac{\cos(\alpha_o)}{m} T(V, H_o, \delta_{th}) - \frac{\rho V^2 S}{2m} C_D(\alpha_o, \delta_{eo}) = f(V, \delta_{th}, \hat{\theta}) \tag{4.101}$$

where α_o and δ_{eo} are the trimmed angle of attack and elevator deflection along with trimmed throttle δ_{tho}, which are determined by the specified parameter vector $\hat{\theta} = [H_o \; V_o]^T$. Equation (4.101) represents a first order SDOF system for total velocity with throttle as the input. The perturbation form of Equation (4.101) is then given by introducing the first order and second order (quadratic and bilinear) derivatives of the function f as

$$\Delta\dot{V} \approx \frac{\partial f}{\partial V}\left(\hat{\theta}\right)\Delta V + \frac{\partial f}{\partial \delta_{th}}\left(\hat{\theta}\right)\Delta\delta_{th} + \frac{1}{2!}\frac{\partial^2 f}{\partial V^2}\left(\hat{\theta}\right)\Delta V^2 + \frac{\partial^2 f}{\partial V \partial \delta_{th}}\left(\hat{\theta}\right)\Delta V\Delta\delta_{th} + \frac{1}{2!}\frac{\partial^2 f}{\partial \delta_{th}^2}\left(\hat{\theta}\right)\Delta\delta_{th}^2 + \cdots \tag{4.102}$$

The two perturbed quantities ΔV and $\Delta\delta_{th}$, not necessarily small, are measured from the nominal values defined at the operating condition. Equation (4.102) is a specific case of the more general Equation (4.2). Since the aerodynamic and engine models of the aircraft are given in the form of look-up tables, a finite difference technique is an appropriate choice to compute the derivatives appearing in Equation (4.102). The second derivative of f with respect to δ_{th}, is zero for the equivalent engine model.

Another example of a longitudinal low order flight sub-system is the nonlinear pitching motion. In such motion, the total velocity is assumed constant in magnitude ($V = V_o$) and direction ($\gamma = \gamma_0 = 0$, $\theta = \alpha$). The pitch motion, assuming it to be much faster than heave motion, is then described as a second order SDOF sub-system as

$$\begin{aligned} \dot{\theta} &= q \\ \dot{q} &= \frac{\bar{q}S\bar{c}}{I_Y} C_{M_T}(\theta, q, \delta_e) = f\left(\theta, q, \delta_e, \hat{\theta}\right) \end{aligned} \tag{4.103}$$

where θ and q are the position and rate, while δ_e is the input signal. The parameter vector $\hat{\theta}$ is introduced through $\bar{q}$. Expanding the nonlinear function f around the nominal point, defined by $\hat{\theta}$, leads to

$$\begin{aligned} \Delta\dot{\theta} &= \Delta q \\ \Delta\dot{q} &\approx \frac{\partial f}{\partial \theta}\left(\hat{\theta}\right)\Delta\theta + \frac{\partial f}{\partial q}\left(\hat{\theta}\right)\Delta q + \frac{\partial f}{\partial \delta_e}\left(\hat{\theta}\right)\Delta\delta_e + \frac{1}{2!}\frac{\partial^2 f}{\partial \theta^2}\left(\hat{\theta}\right)\Delta\theta^2 + \frac{1}{2!}\frac{\partial^2 f}{\partial q^2}\left(\hat{\theta}\right)\Delta q^2 \\ &+ \frac{\partial^2 f}{\partial \theta \partial q}\left(\hat{\theta}\right)\Delta\theta\Delta q + \frac{\partial^2 f}{\partial \theta \partial \delta_e}\left(\hat{\theta}\right)\Delta\theta\Delta\delta_e + \frac{\partial^2 f}{\partial q \partial \delta_e}\left(\hat{\theta}\right)\Delta q\Delta\delta_e + \frac{1}{2!}\frac{\partial^2 f}{\partial \delta_e^2}\left(\hat{\theta}\right)\Delta\delta_e^2 + \cdots \end{aligned} \tag{4.104}$$

Equation (4.104) corresponds to Equation (4.26) in the general case. Here, the second derivative of the function f with respect to q is zero, since the pitching moment is a linear function of q. Also, the coupled derivative with respect to q and δ_e is zero in the aircraft

model. The perturbed quantities $\Delta\theta$, Δq and $\Delta\delta_e$ are defined from the nominal value determined by the operating condition $\hat{\theta} = [H_o \ V_o]^T$.

For the lateral-directional sub-systems, roll motion and yaw motion are considered as examples. Recall the governing roll rate expression in Equation (4.85). If the pitch and yaw rates are assumed zero ($q = q_o = 0$, $r = r_o = 0$), the roll motion is represented as

$$\dot{p} = \frac{\bar{q}Sb}{I_X} C_{L_T}(\alpha, \beta, \delta_a, \delta_r, p) = f(p, \alpha, \hat{\theta}) \tag{4.105}$$

where $\hat{\theta}$ represents the operating condition $[H_o \ V_o \ p_o \ \ q_o \ r_o]^T$. Thus, the angle of attack is considered as an input signal, which changes the roll rate. If there is a sideslip angle hold system activated ($\beta = \beta_o$, $\delta_a = \delta_{ao}$, $\delta_r = \delta_{ro}$, all determined from the specific $\hat{\theta}$), the equation of the roll motion then approximately matches the first order SDOF generic model as

$$\begin{aligned} \Delta\dot{p} \approx & \frac{\partial f}{\partial p}(\hat{\theta})\Delta p + \frac{\partial f}{\partial \alpha}(\hat{\theta})\Delta\alpha + \frac{1}{2!}\frac{\partial^2 f}{\partial p^2}(\hat{\theta})\Delta p^2 \\ & + \frac{\partial^2 f}{\partial \alpha \partial p}(\hat{\theta})\Delta\alpha\Delta p + \frac{1}{2!}\frac{\partial^2 f}{\partial \alpha^2}(\hat{\theta})\Delta\alpha^2 + \cdots \end{aligned} \tag{4.106}$$

The two perturbed quantities Δp and $\Delta\alpha$ are measured from the operating condition. The nonzero trim rolling rate is denoted by p_o. Several of the f derivatives appearing in Equation (4.106) are zero for the aircraft model. However, the roll moment is linearly dependent on the roll rate. This linear relation between roll moment and roll rate has a significant variation with the angle of attack, which appears as a bilinear term in the model. The main purpose of this model is to show the angle of attack influence on the steady roll rate.

For the low order yaw motion sub-system, at constant total speed ($V = V_o$) and zero roll angle, pitch rate, and flight path angle ($\varphi = \varphi_o = 0$, $q = q_o = 0$, $\gamma = \gamma_o = 0$), the

sideslip is then equal to the negative of the yaw angle (β = -ψ). The yaw moment equation is then given as

$$\begin{aligned} \dot{\psi} &= \frac{r}{\cos(\alpha_o)} \\ \dot{r} &= \frac{\bar{q}Sb}{I_Z} C_{N_T}(\alpha_o, -\psi, r, \delta_r, \delta_{ao}) = f(\psi, r, \delta_r, \hat{\theta}) \end{aligned} \tag{4.107}$$

Replacing the nonlinear function f of the yawing moment by a Taylor expansion around the nominal point defined by $\hat{\theta} = [H_o\ V_o]^T$ which determines the nominal values α_o, δ_{eo}, δ_{tho} (all nonzero) and β_o, δ_{ao}, δ_{ro} (all zero), the model conforms to the standard nonlinear second order SDOF model as

$$\begin{aligned} \Delta\dot{\psi} &= \frac{1}{\cos(\alpha_0)} \Delta r \\ \Delta\dot{r} &\approx \frac{\partial f}{\partial \psi}(\hat{\theta})\Delta\psi + \frac{\partial f}{\partial r}(\hat{\theta})\Delta r + \frac{\partial f}{\partial \delta_r}(\hat{\theta})\Delta\delta_r + \frac{1}{2!}\frac{\partial^2 f}{\partial \psi^2}(\hat{\theta})\Delta\psi^2 + \frac{1}{2!}\frac{\partial^2 f}{\partial r^2}(\hat{\theta})\Delta r^2 \\ &+ \frac{\partial^2 f}{\partial \psi \partial r}(\hat{\theta})\Delta\psi\Delta r + \frac{\partial^2 f}{\partial \psi \partial \delta_r}(\hat{\theta})\Delta\psi\Delta\delta_r + \frac{\partial^2 f}{\partial r \partial \delta_r}(\hat{\theta})\Delta r\Delta\delta_r + \frac{1}{2!}\frac{\partial^2 f}{\partial \delta_r^2}(\hat{\theta})\Delta\delta_r^2 + \cdots \end{aligned} \tag{4.108}$$

In this low order model, the rudder deflection is the input signal. Several of these derivatives are again zero. The aileron is taken as zero since there is no roll. Changing the rudder deflection leads to an insignificant change in the roll motion that can be neglected for simplicity. Note that for the aircraft model, the rate of change in the rolling moment due to rudder deflection is less than 10% of the rate of change due to aileron deflection.

4.6 Low Order Motion Examples

A set of four low order flight systems (surge, pitch, roll, and yaw), previously developed in Section 4.5, are employed to demonstrate the dynamical assembly methodology given in Sections 4.1-4.4, to predict the behavior of such systems. For each motion, the trim values of the total nonlinear aircraft model are computed at certain operating conditions. These conditions are selected to represent the behavior of the aircraft near the boundaries of the flight envelope. The low order flight systems are then

extracted from the overall model. These low order systems still have the aerodynamic-propulsive coefficients represented by look-up tables. After that, the finite difference technique generates both first and second order stability and control derivatives around the previously considered operating condition. These derivatives are passed to linear-based and Volterra-based models, while the look-up tables are used for the nonlinear simulation. Table 4.2 shows the operating conditions, initial conditions, and the linear/nonlinear aerodynamic-propulsive derivatives for surge and roll motions.

Table 4.2 Numerical Data for Surge and Roll Motions

	V_o (ft/s)	H_o (kft)	α_o (deg)	a (k_{10}) (1/s, 1/s)	k_{01} (ft/s^2, 1/s^2)	k_{20} (1/ft, 1/rad)	k_{11} (1/s,1/s)
Surge Motion	300	10	15.85	-0.0285	13.44	-4.57×10^{-5}	4.06×10^{-3}
Roll Motion	300	10	10	-1.0358	0.065	0	0.024

Based on previous analysis, several nonlinear features that describe the system can be predicted without the need for nonlinear simulation. For the surge motion, considering the step response more specifically, two nonlinearities appear in the model, quadratic state x_2^{qs} and bilinear state-input x_2^{bsi}. The linear term a (k_{10} = -0.0285 1/s) has a low value indicating that quadratic nonlinearity x_2^{qs} is more dominant than the bilinear nonlinearity x_2^{bsi} according to the respective gains in Equation (4.24). Thus, the quadratic component is proportional to $k_{20}k^2_{01}/a^3$ = 356.7 ft/s, while the bilinear component is proportional to $k_{11}k_{01}/a^2$ = 67.2 ft/s. The lag time of each nonlinear component is τ_{rl}^{qs} = 0.45/|a| = 15 s and τ_{rl}^{bsi} = 0.2/|a| = 7 s. The linear term has a settling time 4/|a| = 140.4 s, while the two nonlinear components have settling times τ_{rs}^{qs} = 6.6/|a| = 231.6 s and τ_{rs}^{bsi} = 5.8/|a| = 203.5 s. Since the quadratic state component x_2^{qs} has a negative value and it is

more dominant than the bilinear component x_2^{bsi}, the overall settling time is expected to be less than the linear one depending on the input amplitude. At a low amplitude input, the settling time is almost the linear settling time 140 s, while at a high amplitude input, the settling time is much less than 140 s. In other words, increasing the input's amplitude reduces the settling time. Recall Equation (4.25), the steady value as a function of input amplitude is $\Delta V_{ss} = 471.6\Delta\delta_{th} - 289.5\Delta\delta_{th}^2$ ft/s.

For a specific response example, assume an input excitation $\Delta\delta_{th}$=15% with δ_{tho} = 43% and δ_{eo} = -11.07 deg. Figure 4.27 shows the response of each nonlinear component. Assembling the two nonlinear components along with the linear term provides the overall estimated response as shown in Figure 4.28. Both nonlinear and linear responses start with the same slope or velocity (quadratic state and bilinear terms do not change the initial rate due to time lag). At time t = 15 s, the linear model deviates from the nonlinear one. This time is the quadratic time lag. The linear-based model has a steady value $V_{ss}^{linear} = 300 + 471.6\Delta\delta_{th}\big|_{0.15} = 371$ ft/s, while the Volterra-based model has a steady value $V_{ss}^{\text{Volterra}} = 300 + \left(471.6\Delta\delta_{th} - 289.5\Delta\delta_{th}^2\right)\big|_{0.15} = 364.3$ ft/s. The nonlinear simulation has a steady value 365 ft/s. This result shows how the quadratic component has a significant influence on the steady value. The quadratic component in this model represents the second derivative of the X axis total force with velocity, which is the drag and thrust variation with the velocity squared. The required time to achieve the steady values in the case of the linear model is $\tau_{rs}^{\text{linear}} = \tau_{rs}^{1} = 4/|a| = 140$ s. In the case of the Volterra model, by recalling Equation (4.24) and noting the Volterra steady state response is 2% below that of the linear steady state response, the estimated settling time is then $\tau_{rs}^{\text{Volterra}} = \ln(0.02 + 0.02)/a = 3.2/|a| = 113$ s. The nonlinear simulation has a total settling time of 118 s, which is much less than the linear settling time and the Volterra settling time well approximates here because of the negative sign of the quadratic position component.

In the case of roll motion, the only source of nonlinearity is the bilinear component as listed in Table 4.2. The nominal rolling condition corresponds to p_0 = 1 rad/s, β_o = -5 deg, δ_{eo} = 1.04 deg, δ_{ao} = -1.3 deg, δ_{ro} = 0 deg, and δ_{tho} = 28%. Consider the step response as a more specific case, the contribution of the nonlinear component p_2^{bsi} can be described using the previous analysis: lag time $\tau_{rl}^{bsi} = 0.2/|a| = 0.192$ s, the settling time $\tau_{rs}^{bsi} = 5.8/|a| = 5.6$ s, and a steady value $p_{ss}^{bsi} = A^2 k_{01} k_{11} / a^2 = 1.5\times10^{-3}\Delta\alpha^2$ rad/s (see Equation (4.25)). Note the bilinear component response is always positive regardless of the input direction while the linear component response depends on the input direction. For the positive input excitation, the settling time is expected to be more than for the linear system and vice versa.

For an input amplitude $\Delta\alpha$ = -6 deg, while α_o = 10 deg, the response of p_2^{bsi} is shown in Figure 4.29. Adding the nonlinear component p_2^{bsi} to the linear term p_1 provides the estimated Volterra model shown in Figure 4. **30**. The three responses: nonlinear, Volterra, and linear start at the same initial value with the same rate. The deviation between nonlinear and linear responses occurs earlier than in the previous surge example, since the bilinear lag time is only $\tau_{rl}^{bsi} = 0.2$ s. Using Equation (4.25), the three models settle at different steady values: 0.69 rad/s (nonlinear), 0.68 rad/s (Volterra), and 0.62 rad/s (linear), indicating 10% error in the prediction of the linear model and 1.5% error in the prediction of the Volterra model. The increment in steady state roll rate due to nonlinear aerodynamics is predictable from Equation (4.25), specifically the term $A^2 k_{01} k_{11} / a^2$. The required time to settle each model to its steady value is computed to be 3.3 s (nonlinear), 3.2 s (Volterra), and 3.8 s (linear).

The pitch motion example is considered at an altitude H_o = 40 kft and total velocity V_o = 530 ft/s. For a rectilinear motion, the computed trimming variables are θ_o = α_o = 15.6 deg, δ_{eo} = -2.6 deg, and δ_{tho} = 98.8%. Using the finite difference technique, the reduced pitch equations of motion, equivalent to Equation (4.104), are

$$\Delta\dot{\theta} = \Delta q$$
$$\Delta\dot{q} = \underbrace{-0.79}_{k_{100}}\Delta\theta \underbrace{-0.36}_{k_{010}}\Delta q \underbrace{-3.15}_{k_{001}}\Delta\delta_e + \underbrace{1.05}_{k_{200}}\Delta\theta^2 + \underbrace{0.16}_{k_{110}}\Delta\theta\Delta q + \underbrace{0.29}_{k_{101}}\Delta\theta\Delta\delta_e \underbrace{-0.0014}_{k_{002}}\Delta\delta_e^2 \qquad (4.109)$$

In Equation (4.109), the quadratic rate coefficient k_{020} = 0 and the bilinear rate-input coefficient k_{011} = 0. Thus, both plunge force and pitch moment coefficients are linear related to the pitch rate q with a zero correlation to the elevator deflection δ_e. The pitch motion model has a damping ratio ζ = 0.2, damping factor σ = 0.18 1/s, undamped natural frequency ω_n = 0.89 rad/s, and damped natural frequency ω_d = 0.87 rad/s. The first kernel starts at zero with a negative slope and keeps oscillating with a frequency ω_d = 0.87 rad/s. The amplitude of this oscillation decreases with time and settles inside a 2% band of the gain $|k_{001}/\ \omega_n|$ = 3.54 at time $\tau_{ks}^{l} = 4/|\sigma| =$ 22.2 s. The second kernel has four components. The influence of each component on the total second kernel, from highest to lowest, is: quadratic state component h_2^{qs} (with a weight $k_{200}k_{001}^2/2\omega_d^4$ = 9.05), bilinear state-rate component h_2^{bsr} (with a weight $k_{110}k_{001}^2/2\omega_d^3\sqrt{1-\zeta^2}$ = 1.19), bilinear state-input component h_2^{bsi} (with a weight $k_{101}k_{001}/2\omega_d^2$ = -0.59), and quadratic input component h_2^{qi} (with a weight k_{002}/ω_d = -0.0016). Although the nonlinear coefficients in Equation (4.109) are in the same range, the analysis based on the Volterra model shows that some nonlinearities dominate the others because of the operating frequency and damping ratio. The contribution of the quadratic input term is almost zero and can be removed from the model. Since the quadratic state component has the highest weight with a big difference compared to the other components, the total second kernel is expected to be close in shape to the quadratic state component h_2^{qs} . The individual settling time of each component is τ_{ks}^{qs} = 19.47 s, τ_{ks}^{bsr} = 19.34 s, and $\tau_{ks}^{bsi} = \tau_{ks}^{qi}$ = 22.23 s. Since the quadratic state component is dominant, the expected overall settling time is roughly close to $\tau_{ks}^{Volterra}$ ≈ 19.47 s.

The developed first and second kernels of the pitch motion provide the structure to predict and understand the system behavior of any input. The step response analysis in

Section 4.4 is now recalled and used. The step response of each component can be specified by the following characteristics:

1- Time lags of each component in Equation (4.71) as τ_{rl}^{qs} = 1.41 s, τ_{rl}^{bpr} = 1.22 s, τ_{rl}^{bsi} = 0.98 s, and τ_{rl}^{qi} = 0 s.

2- Settling times in Equation (4.80) as τ_{rs}^{qs} = 41.9 s, τ_{rs}^{bsr} = 37.1 s, τ_{rs}^{bsi} = 37.9 s, and τ_{rs}^{qi} = 22.2 s.

3- Steady values in Equation (4.81) as $\theta_{ss}^{qs} = 20.96\,\Delta\delta_e^2$ rad, $\theta_{ss}^{bsr} = 0\,\Delta\delta_e^2$ rad, θ_{rs}^{bsi} = -1.44 $\Delta\delta_e^2$ rad, and θ_{ss}^{qi} = -0.0017 $\Delta\delta_e^2$ rad, where $\Delta\delta_e$ is in rad.

The linear response, on the other hand, has a settling time τ_{rs}^{l} = 22.2 s and a steady value θ_{rs}^{l} = -3.98 $\Delta\delta_e$ rad. As a test case, the response of each nonlinear component is shown in Figure 4.31 for an input of $\Delta\delta_e$ = 0.75 deg. Figure 4.32 shows the result of assembling the linear term to the nonlinear components in a comparison with the linear response, while the nonlinear simulation is the benchmark. The three responses (linear, Volterra, and nonlinear) start at 15.6 deg heading downward. The linear model deviates from both the nonlinear simulation and Volterra-based model at $t \approx 1.5$ s (almost equal to τ_{rl}^{qs}), when the nonlinear components start to be energetic.

There is a difference in the times of the peak overshoot and undershoot between the linear and nonlinear simulation. Based on the Volterra model, this difference in time traces back to the x_2^{qs} and x_2^{bsi} components, which lead by $\Delta t = \pi/2/\omega_d$ = 1.8 s from the linear simulation. However, the x_2^{bsi} component does not really contribute in such a time difference as well as the x_2^{bsr} component because of its low strength. Volterra model is consistent with the nonlinear simulation and provides accurate times of the first three overshoot peaks at 6.76 s, 13.67 s, and 20.47 s. The linear model, on the other hand, provides these times at 7.22 s, 14.43 s, and 21.64 s. It is clear how the time difference propagates with time to reach a phase shift 90 deg by the third cycle. The equivalent percentage maximum overshoots at these times are 7.5%, 3.2%, and 1.5% based on the linear model and 8.0%, 3.9%, and 2.1% based on the Volterra model, which is the same

as the nonlinear simulation. The differences in estimating the maximum overshoot values and their equivalent times emphasize that developed analytical models based on Volterra theory provides a better tool in predicting the transient response of the aircraft especially for tracking applications when these differences are a matter of concern. The developed analytical Volterra model not only proves the capability to render the transient response but also the steady response as $\theta_{ss}^{volterra}$ = 12.79 deg compared to θ_{ss}^{linear} = 12.6 deg from the linear model with an error 7%. The estimated settling time to reach this value is $\tau_{rs}^{linear} = 19.4$ s and $\tau_{s}^{Volterra} = 24.6$ s.

The operating condition of the yaw motion is considered at V_o = 1000 ft/s, H_o = 5 kft, α_o = 10 deg, δ_{eo} = -1.4 deg, δ_{tho} = 55%. The resultant equations of motion are

$$\begin{aligned} \Delta\dot{\psi} &= \Delta r \\ \Delta\dot{r} &= \underbrace{-36.22}_{k_{001}}\Delta\psi \underbrace{-0.86}_{k_{010}}\Delta r \underbrace{-0.23}_{k_{001}}\Delta\delta_r \underbrace{-0.089}_{k_{101}}\Delta\psi\Delta\delta_r \end{aligned} \tag{4.110}$$

The model in Equation (4.110) has a damping ratio of ζ = 0.072, undamped natural frequency ω_n = 6.02 rad/s, and damped natural frequency ω_d = 6 rad/s. Because the model has a relatively high frequency and low input bilinear strength, the nonlinearity has almost no effect on the steady value and the settling time. Figure 4.33 shows the contribution of the bilinear state-input nonlinearity for an input signal $\Delta\delta_r$ = -10 deg, while the overall response is shown in Figure 4.34. The nonlinearity here is insignificant. The only signature of the nonlinearity appears as shift in the times of maximum peak points, especially after the linear part settles down. Thus, the input bilinear term has minimum and maximum peaks at times $(4n+5)\pi/2/\omega_d$ and $(4n+3)\pi/2/\omega_d$ respectively, while the linear term has these peaks at times $2(n+1)\pi/\omega_d$ and $(2n+1)\pi/\omega_d$ respectively, where n = 0,1,2,.... The difference in peak times between linear and input bilinear traces produces such shift. The results from this model and the previous ones show the necessity for counting the high order stability and control derivatives to characterize aircraft behavior near outlying regions of the flight envelope,

or anywhere nonlinearity is significant. The analytically developed Volterra-based models efficiently employ these high order derivatives and trace their influence on the system behavior. Such mechanism would not be accessible in linear analyses.

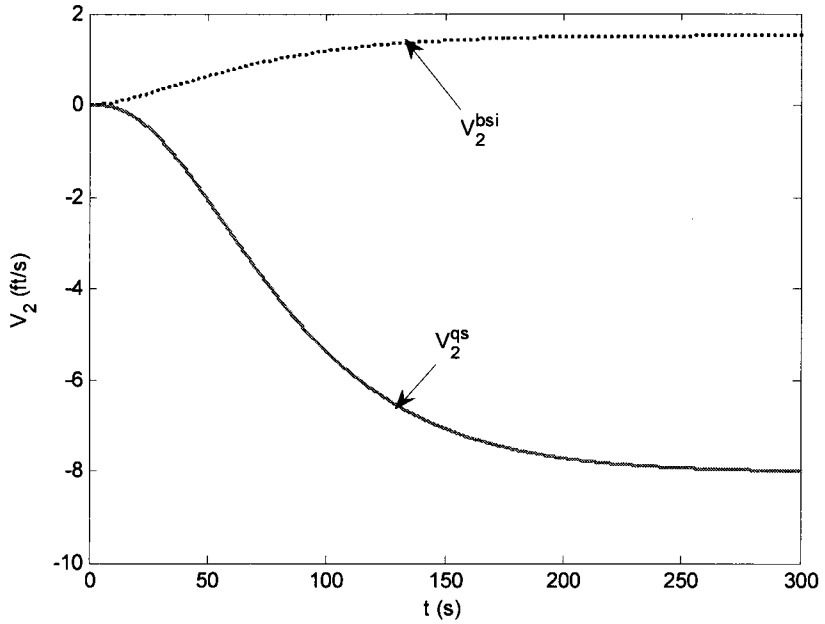

Figure 4.27 Surge Motion Nonlinear Step Response Components for $\Delta\delta_{th}$ = 15%

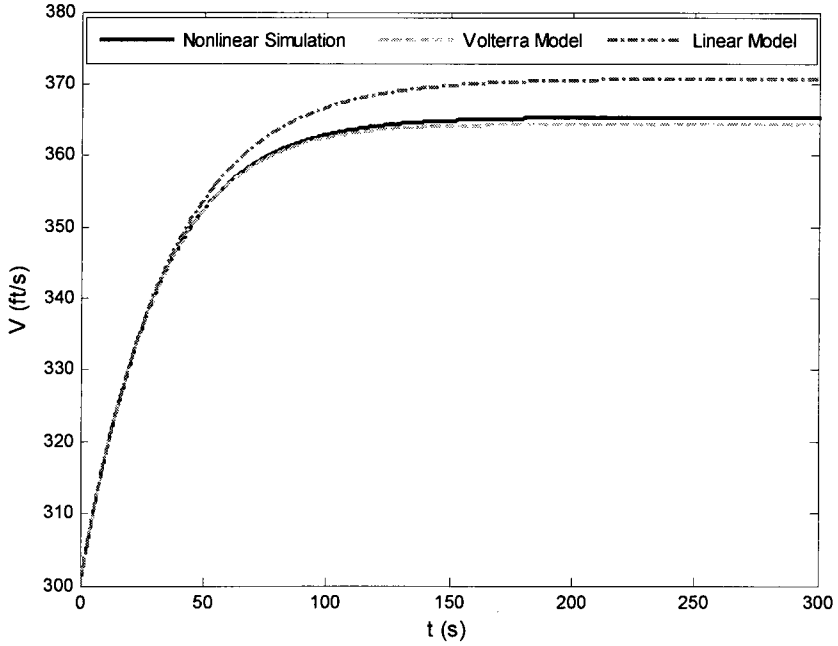

Figure 4.28 Surge Motion Step Response for $\Delta\delta_{th}$ = 15%

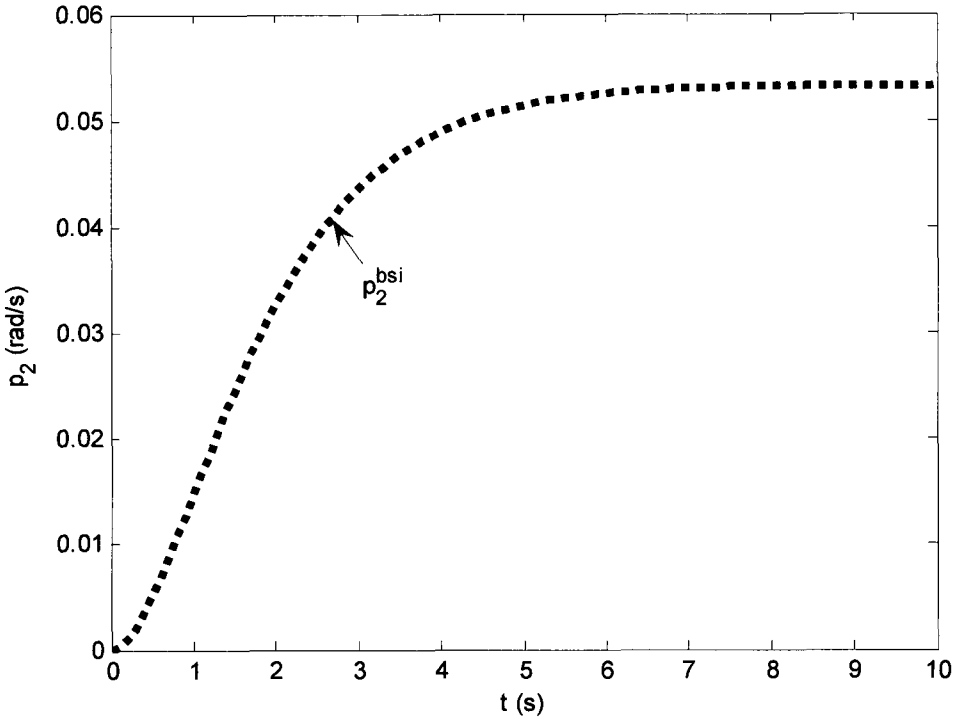

Figure 4.29 Roll Motion Nonlinear Step Response Components for $\Delta\alpha$ = -6 deg

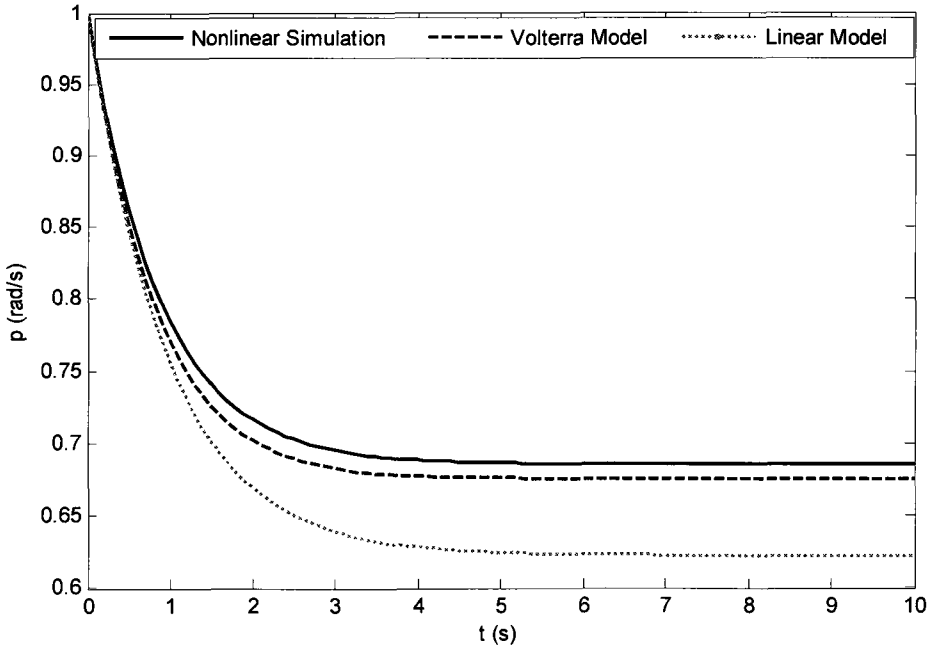

Figure 4. 30 Roll Motion Step Response for $\Delta\alpha$ = -6 deg

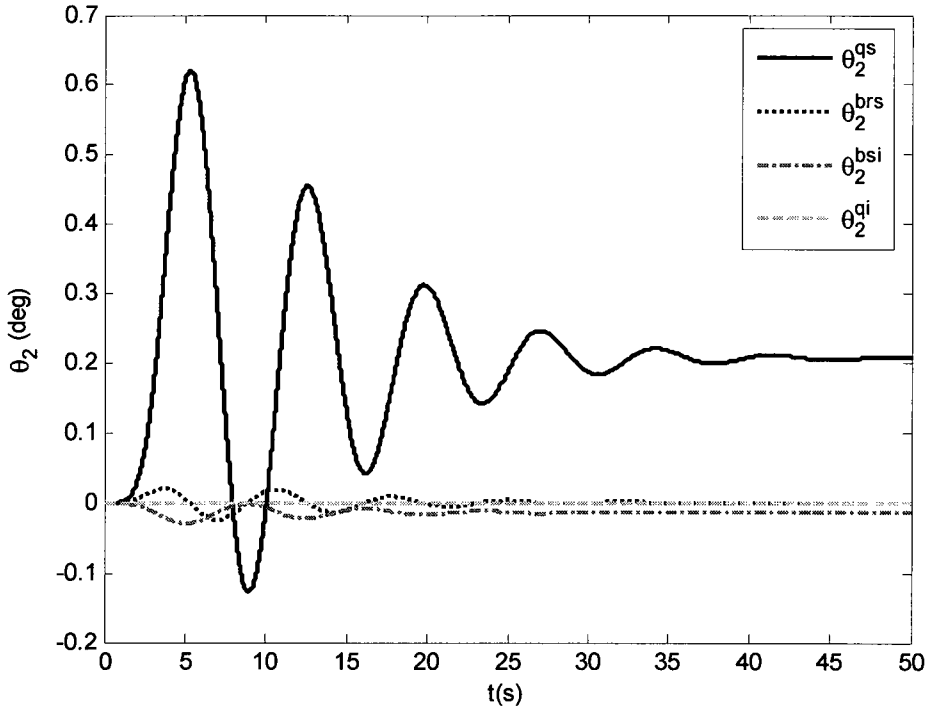

Figure 4.31 Pitch Motion Nonlinear Step Response Components for $\Delta\delta_e = 0.75$ deg

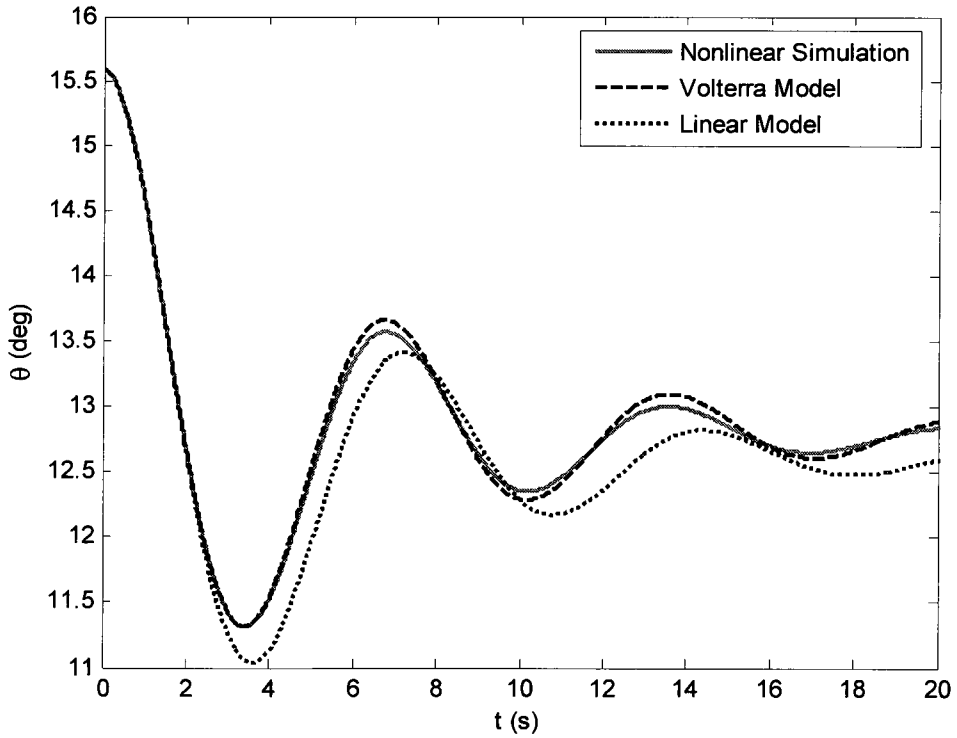

Figure 4.32 Pitch Motion Step Response for $\Delta\delta_e = 0.75$ deg

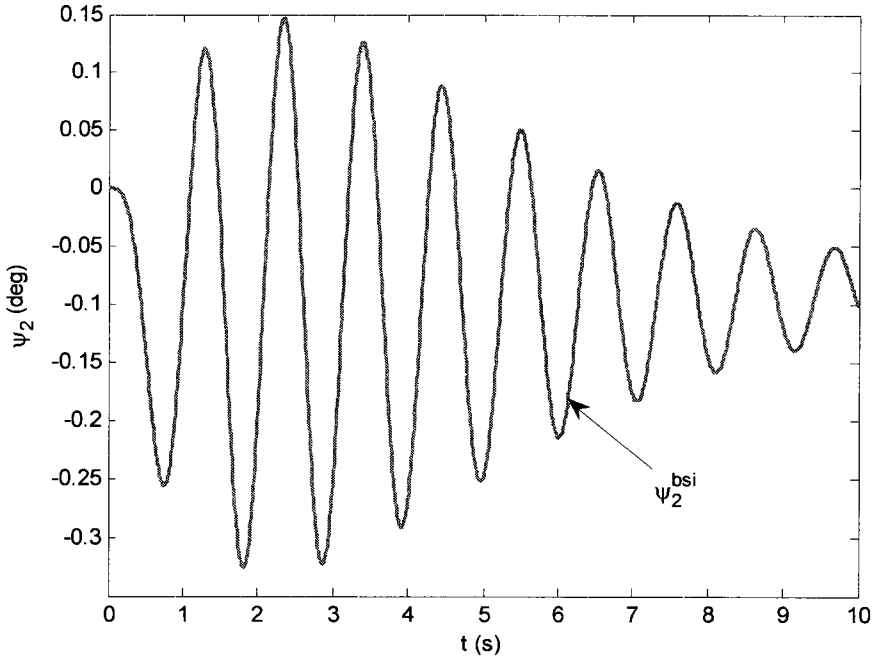

Figure 4.33 Yaw Motion Nonlinear Step Response Component for $\Delta\delta_r$ = -10 deg

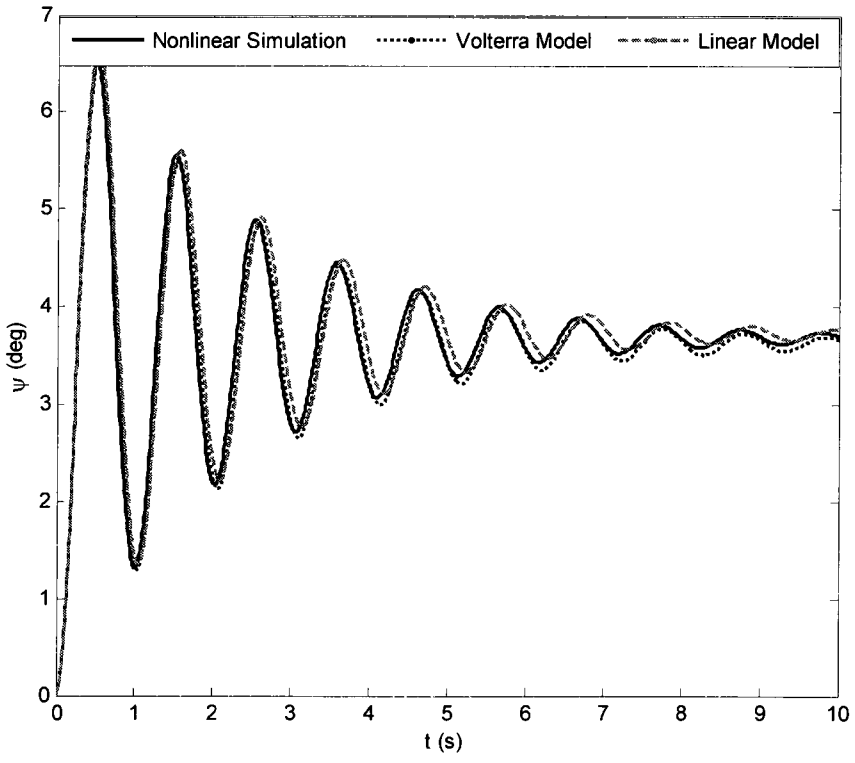

Figure 4.34 Yaw Motion Step Response for $\Delta\delta_r$ = -10 deg

CHAPTER 5

VOLTERRA PARMETER-VARYING APPROACH

The piecewise Volterra approach in Chapter 3 has been used as a demonstration tool to prove the universality of Volterra models. However, the approach requires a lot of mathematical manipulation and manual intervention. In this chapter, a more systematic and computationally efficient approach is introduced. This methodology is called the volterra parameter-varying (VPV) approach, which is considered an extension for the linear parameter-varying (LPV) approach. Throughout this chapter the F-16 longitudinal motion is used to assess the proposed approach. The approach starts by generating a local differential Volterra sub-model at a specific operating condition based on variable expansion as shown in Section 5.1. In Section 5.2, the local Volterra kernels based on the differential sub-model are analytically developed. Such analytical expression provides an understanding for the aircraft dynamics. Finally, in Section 5.3, the VPV model is assembled. Many interpolation techniques are investigated to select the proper one followed by some test cases to compare the VPV to LPV, while the nonlinear simulation is used as a benchmark. Characterizing the aircraft dynamics over the entire flight envelope is visualized throughout the variation of Volterra kernels with total speed and altitude.

5.1 Local Differential Model

In this section, the local VPV model in the form of a power series of the motion function derivatives is developed for the longitudinal motion of an F-16 model. This model has been previously discussed in Chapter 4. Recall the symmetric longitudinal motion, developed in that chapter.

$$\dot{V} = \frac{1}{2m}\rho S V^2 \underbrace{\left(C_{X_T} C_\alpha + C_{Z_T} S_\alpha\right)}_{-C_D} + \frac{T}{m} C_\alpha - g S_{\theta-\alpha} = f_1(V, \alpha, q, \theta, \delta_e) \tag{5.1}$$

$$\dot{\alpha} = q + \frac{1}{2m}\rho S V \underbrace{\left(C_{Z_T} C_\alpha - C_{X_T} S_\alpha\right)}_{-C_L} - \frac{T}{mV} S_\alpha + \frac{g}{V} C_{\theta-\alpha} = f_2(V, \alpha, q, \theta, \delta_e) \tag{5.2}$$

$$\dot{q} = \frac{\rho S \bar{c}}{2I_Y} V^2 C_{M_T} = f_3(V, \alpha, q, \theta, \delta_e) \tag{5.3}$$

$$\dot{\theta} = q = f_4(V, \alpha, q, \theta, \delta_e) \tag{5.4}$$

Here the thrust is considered constant and the throttle is assumed fixed, thus functions f_1, f_2, f_3, and f_4 show no explicit dependence on δ_{th}. Replace the state vector and input vector by the expanded forms.

$$\begin{bmatrix} V \\ \alpha \\ q \\ \theta \end{bmatrix} = \begin{bmatrix} V_o \\ \alpha_o \\ q_o \\ \theta_o \end{bmatrix} + \lambda \underbrace{\begin{bmatrix} V_1 \\ \alpha_1 \\ q_1 \\ \theta_1 \end{bmatrix}}_{x_1} + \lambda^2 \underbrace{\begin{bmatrix} V_2 \\ \alpha_2 \\ q_2 \\ \theta_2 \end{bmatrix}}_{x_2} + \ldots$$

$$\delta_e = \delta_{eo} + \lambda \delta_{e1} \tag{5.5}$$

Substituting into the nonlinear state space model in Equations (5.1-5.4), expanding nonlinearities with Taylor theory, and equating the coefficients of λ and λ^2 leads to the following VPV local differential model

$$\begin{aligned} \dot{x}_1 &= A(\hat{\theta}) x_1 + B(\hat{\theta}) \delta_{e1} \\ \dot{x}_2 &= A(\hat{\theta}) x_2 + B_{xx}(\hat{\theta}) x_1^{[2]} + B_{xu}(\hat{\theta}) x_1 \delta_{e1} + B_{uu}(\hat{\theta}) \delta_{e1}^2 \end{aligned} \tag{5.6}$$

Applying the Kronecker operator directly to the vector $x_1 = [V\ \alpha\ q\ \theta]^T$ leads to $x_1^{(2)} = \begin{bmatrix} V^2 & V\alpha & Vq & V\theta & \alpha V & \alpha^2 & \alpha q & \alpha\theta & qV & q\alpha & q^2 & q\theta & \theta V & \theta\alpha & \theta q & \theta^2 \end{bmatrix}^T$, which has many redundant elements in addition that terms q^2, $q\theta$, and θ^2 do not influence the dynamics. By eliminating this redundancy and the terms q^2, $q\theta$, and θ^2, a reduced Kronecker product denoted with a square-bracket superscript $x_1^{[2]} = \begin{bmatrix} V^2 & V\alpha & Vq & V\theta & \alpha^2 & \alpha q & \alpha\theta \end{bmatrix}^T$ is used herein. Dimension of five matrices in Equation (5.6) are $A \in R^{4\times4}$, $B \in R^{4\times1}$, $B_{xx} \in R^{4\times7}$, $B_{xu} \in R^{4\times4}$, and $B_{uu} \in R^{4\times1}$. The parameters dependency vector is denoted by $\hat{\theta} = \begin{bmatrix} H_o & V_o \end{bmatrix}^T$ indicating the operating condition. The structure of these five matrices A, B, B_{xx}, B_{xu}, and B_{uu} are

$$A=\begin{bmatrix} f_{1V} & f_{1\alpha} & f_{1q} & f_{1\theta} \\ f_{2V} & f_{2\alpha} & f_{2q} & f_{2\theta} \\ f_{3V} & f_{3\alpha} & f_{3q} & 0 \\ 0 & 0 & 1 & 0 \end{bmatrix} \quad B=\begin{bmatrix} f_{1\delta_e} \\ f_{2\delta_e} \\ f_{3\delta_e} \\ 0 \end{bmatrix} \quad B_{xu}=\begin{bmatrix} f_{1V\delta_e} & f_{1\alpha\delta_e} & 0 & 0 \\ f_{2V\delta_e} & f_{2\alpha\delta_e} & 0 & 0 \\ f_{3V\delta_e} & f_{3\alpha\delta_e} & 0 & 0 \\ 0 & 0 & 0 & 0 \end{bmatrix}$$

$$B_{xx}=\begin{bmatrix} \frac{1}{2}f_{1V^2} & f_{1V\alpha} & f_{1Vq} & 0 & \frac{1}{2}f_{1\alpha^2} & f_{1\alpha q} & f_{1\alpha\theta} \\ \frac{1}{2}f_{2V^2} & f_{2V\alpha} & 0 & f_{2V\theta} & \frac{1}{2}f_{2\alpha^2} & f_{2\alpha q} & f_{2\alpha\theta} \\ \frac{1}{2}f_{3V^2} & f_{3V\alpha} & f_{3Vq} & 0 & \frac{1}{2}f_{3\alpha^2} & f_{3\alpha q} & 0 \\ 0 & 0 & 0 & 0 & 0 & 0 & 0 \end{bmatrix} \quad B_{uu}=\begin{bmatrix} \frac{1}{2}f_{1\delta_e^2} \\ \frac{1}{2}f_{2\delta_e^2} \\ \frac{1}{2}f_{3\delta_e^2} \\ 0 \end{bmatrix} \tag{5.7}$$

The derivatives f_{ij}, where $i = \{1, 2, 3\}$ and $j = \{V, \alpha, q, \theta, V^2, V\alpha, Vq, V\theta, \alpha^2, \alpha q, \alpha\theta, \delta_e, \delta_e^2\}$, are correlated to the aerodynamic and propulsive coefficients and their derivatives as

$$f_{1V}=\frac{\rho SV}{m}\left[C_{X_T}C_\alpha+C_{Z_T}S_\alpha\right]-\frac{\rho S\bar{c}q}{4m}\left[C_{X_q}C_\alpha+C_{Z_q}S_\alpha\right] \tag{5.8}$$

$$f_{1\alpha}=\frac{\rho SV^2}{2m}\left[\left(\frac{\partial C_{X_T}}{\partial\alpha}+C_{Z_T}\right)C_\alpha+\left(\frac{\partial C_{Z_T}}{\partial\alpha}-C_{X_T}\right)S_\alpha\right]-\frac{T}{m}S_\alpha+gC_{\theta-\alpha} \tag{5.9}$$

$$f_{1q}=\frac{\rho S\bar{c}V}{4m}\left[C_{X_q}C_\alpha+C_{Z_q}S_\alpha\right] \tag{5.10}$$

$$f_{1\theta}=-gC_{\theta-\alpha} \tag{5.11}$$

$$f_{1V^2}=\frac{\rho S}{m}\left[C_{X_T}C_\alpha+C_{Z_T}S_\alpha\right]-\frac{\rho S\bar{c}q}{2mV}\left[C_{X_q}C_\alpha+C_{Z_q}S_\alpha\right] \tag{5.12}$$

$$\begin{aligned} f_{1V\alpha}=&\frac{\rho SV}{m}\left[\left(\frac{\partial C_{X_T}}{\partial\alpha}+C_{Z_T}\right)C_\alpha+\left(\frac{\partial C_{Z_T}}{\partial\alpha}-C_{X_T}\right)S_\alpha\right] \\ &-\frac{\rho S\bar{c}q}{4m}\left[\left(\frac{\partial C_{X_q}}{\partial\alpha}+C_{Z_q}\right)C_\alpha+\left(\frac{\partial C_{Z_q}}{\partial\alpha}-C_{X_q}\right)S_\alpha\right] \end{aligned} \tag{5.13}$$

$$f_{1Vq}=\frac{\rho S\bar{c}}{4m}\left[C_{X_q}C_\alpha+C_{Z_q}S_\alpha\right] \tag{5.14}$$

$$\begin{aligned} f_{1\alpha^2}=&\frac{\rho SV^2}{2m}\left[\left(\frac{\partial^2 C_{X_T}}{\partial\alpha^2}+2\frac{\partial C_{Z_T}}{\partial\alpha}-C_{X_T}\right)C_\alpha+\left(\frac{\partial^2 C_{Z_T}}{\partial\alpha^2}-2\frac{\partial C_{X_T}}{\partial\alpha}-C_{Z_T}\right)S_\alpha\right] \\ &-\frac{T}{m}C_\alpha+gS_{\theta-\alpha} \end{aligned} \tag{5.15}$$

$$f_{1\alpha q} = \frac{\rho S\bar{c} V}{4m}\left[\left(\frac{\partial C_{X_q}}{\partial \alpha} + C_{Z_q}\right)C_\alpha + \left(\frac{\partial C_{Z_q}}{\partial \alpha} - C_{X_q}\right)S_\alpha\right] \tag{5.16}$$

$$f_{1\alpha\theta} = -gS_{\theta-\alpha} \tag{5.17}$$

$$f_{1\delta_e} = \frac{\rho SV^2}{2m}\left[\frac{\partial C_{X_T}}{\partial \delta_e}C_\alpha + C_{Z_{\delta_e}}S_\alpha\right] \tag{5.18}$$

$$f_{1V\delta_e} = \frac{\rho SV}{m}\left[\frac{\partial C_{X_T}}{\partial \delta_e}C_\alpha + C_{Z_{\delta_e}}S_\alpha\right] \tag{5.19}$$

$$f_{1\alpha\delta_e} = \frac{\rho SV^2}{2m}\left[\left(\frac{\partial^2 C_{X_T}}{\partial\alpha\partial\delta_e} + C_{Z_{\delta_e}}\right)C_\alpha - \frac{\partial C_{X_T}}{\partial \delta_e}S_\alpha\right] \tag{5.20}$$

$$f_{1\delta_e^2} = \frac{\rho SV^2}{2m}\frac{\partial^2 C_{X_T}}{\partial \delta_e^2}C_\alpha \tag{5.21}$$

$$f_{2V} = \frac{\rho S}{2m}\left[C_{Z_T}C_\alpha - C_{X_T}S_\alpha\right] - \frac{\rho S\bar{c}q}{4mV}\left[C_{Z_q}C_\alpha - C_{X_q}S_\alpha\right] + \frac{T}{mV^2}S_\alpha - \frac{g}{V^2}C_{\theta-\alpha} \tag{5.22}$$

$$f_{2\alpha} = \frac{\rho SV}{2m}\left[\left(\frac{\partial C_{Z_T}}{\partial \alpha} - C_{X_T}\right)C_\alpha - \left(\frac{\partial C_{X_T}}{\partial \alpha} + C_{Z_T}\right)S_\alpha\right] - \frac{T}{mV}C_\alpha + \frac{g}{V}S_{\theta-\alpha} \tag{5.23}$$

$$f_{2q} = 1 + \frac{\rho S\bar{c}}{4m}\left[C_{Z_q}C_\alpha - C_{X_q}S_\alpha\right] \tag{5.24}$$

$$f_{2\theta} = -\frac{g}{V}S_{\theta-\alpha} \tag{5.25}$$

$$f_{2V^2} = -\frac{2T}{mV^3}S_\alpha + \frac{2g}{V^3}C_{\theta-\alpha} \tag{5.26}$$

$$\begin{aligned} f_{2V\alpha} = {} & \frac{\rho S}{2m}\left[\left(\frac{\partial C_{Z_T}}{\partial \alpha} - C_{X_T}\right)C_\alpha - \left(\frac{\partial C_{X_T}}{\partial \alpha} + C_{Z_T}\right)S_\alpha\right] \\ & - \frac{\rho S\bar{c}q}{4mV}\left[\left(\frac{\partial C_{Z_q}}{\partial \alpha} - C_{X_q}\right)C_\alpha - \left(\frac{\partial C_{X_q}}{\partial \alpha} + C_{Z_q}\right)S_\alpha\right] + \frac{T}{mV^2}C_\alpha - \frac{g}{V^2}S_{\theta-\alpha} \end{aligned} \tag{5.27}$$

$$f_{2V\theta} = \frac{g}{V^2}S_{\theta-\alpha} \tag{5.28}$$

$$\begin{aligned} f_{2\alpha^2} = {} & \frac{\rho SV}{2m}\left[\left(\frac{\partial^2 C_{Z_T}}{\partial \alpha^2} - 2\frac{\partial C_{X_T}}{\partial \alpha} - C_{Z_T}\right)C_\alpha - \left(\frac{\partial^2 C_{X_T}}{\partial \alpha^2} + 2\frac{\partial C_{Z_T}}{\partial \alpha} - C_{X_T}\right)S_\alpha\right] \\ & + \frac{T}{mV}S_\alpha - \frac{g}{V}C_{\theta-\alpha} \end{aligned} \tag{5.29}$$

$$f_{2\alpha q} = \frac{\rho S\bar{c}}{4m}\left[\left(\frac{\partial C_{Z_q}}{\partial \alpha} - C_{X_q}\right)C_\alpha - \left(\frac{\partial C_{X_q}}{\partial \alpha} + C_{Z_q}\right)S_\alpha\right] \tag{5.30}$$

$$f_{2\alpha\theta} = \frac{g}{V}C_{\theta-\alpha} \tag{5.31}$$

$$f_{2\delta_e} = \frac{\rho SV}{2m}\left[C_{Z_{\delta_e}} C_\alpha - \frac{\partial C_{X_T}}{\partial \delta_e} S_\alpha\right] \tag{5.32}$$

$$f_{2V\delta_e} = \frac{\rho S}{2m}\left[C_{Z_{\delta_e}} C_\alpha - \frac{\partial C_{X_T}}{\partial \delta_e} S_\alpha\right] \tag{5.33}$$

$$f_{2\alpha\delta_e} = -\frac{\rho SV}{2m}\left[\frac{\partial C_{X_T}}{\partial \delta_e} C_\alpha + \left(\frac{\partial^2 C_{X_T}}{\partial \alpha \partial \delta_e} + C_{Z_{\delta_e}}\right) S_\alpha\right] \tag{5.34}$$

$$f_{2\delta_e^2} = -\frac{\rho SV}{2m}\frac{\partial^2 C_{X_T}}{\partial \delta_e^2} S_\alpha \tag{5.35}$$

$$f_{3V} = \frac{\rho S\bar{c} V}{I_Y} C_{M_T} - \frac{\rho S\bar{c}^2 q}{4I_Y}\left[\Delta\bar{x}_{cg} C_{Z_q} + C_{M_q}\right] \tag{5.36}$$

$$f_{3\alpha} = \frac{\rho S\bar{c} V^2}{2I_Y}\frac{\partial C_{M_T}}{\partial \alpha} \tag{5.37}$$

$$f_{3q} = \frac{\rho S\bar{c}^2 V}{4I_Y}\left[\Delta\bar{x}_{cg} C_{Z_q} + C_{M_q}\right] \tag{5.38}$$

$$f_{3V^2} = \frac{\rho S\bar{c}}{I_Y} C_{M_T} - \frac{\rho S\bar{c}^2 q}{2I_Y V}\left[\Delta\bar{x}_{cg} C_{Z_q} + C_{M_q}\right] \tag{5.39}$$

$$f_{3V\alpha} = \frac{\rho S\bar{c} V}{I_Y}\frac{\partial C_{M_T}}{\partial \alpha} - \frac{\rho S\bar{c}^2 q}{4I_Y}\left[\Delta\bar{x}_{cg}\frac{\partial C_{Z_q}}{\partial \alpha} + \frac{\partial C_{M_q}}{\partial \alpha}\right] \tag{5.40}$$

$$f_{3Vq} = \frac{\rho S\bar{c}^2}{4I_Y}\left[\Delta\bar{x}_{cg} C_{Z_q} + C_{M_q}\right] \tag{5.41}$$

$$f_{3\alpha^2} = \frac{\rho S\bar{c} V^2}{2I_Y}\frac{\partial^2 C_{M_T}}{\partial \alpha^2} \tag{5.42}$$

$$f_{3\alpha q} = \frac{\rho S\bar{c}^2 V}{4I_Y}\left[\Delta\bar{x}_{cg}\frac{\partial C_{Z_q}}{\partial \alpha} + \frac{\partial C_{M_q}}{\partial \alpha}\right] \tag{5.43}$$

$$f_{3\delta_e} = \frac{\rho S\bar{c} V^2}{2I_Y}\frac{\partial C_{M_T}}{\partial \delta_e} \tag{5.44}$$

$$f_{3V\delta_e} = \frac{\rho S\bar{c} V}{I_Y}\frac{\partial C_{M_T}}{\partial \delta_e} \tag{5.45}$$

$$f_{3\alpha\delta_e} = \frac{\rho S\bar{c} V^2}{2I_Y}\frac{\partial^2 C_{M_T}}{\partial \alpha \partial \delta_e} \tag{5.46}$$

$$f_{3\delta_e^2} = \frac{\rho S\bar{c} V^2}{2I_Y}\frac{\partial^2 C_{M_T}}{\partial \delta_e^2} \tag{5.47}$$

The aerodynamic data C_{X_T}, C_{Z_T}, and C_{M_T} are given as look-up tables with enough resolution to capture the nonlinear behavior of the aerodynamic force and moment coefficients. In Reference 114, these aerodynamic coefficients have been modeled by the so-called "multivariate orthogonal functions". This orthogonality feature has the ability to decouple the computed regression coefficient of one function from the other functions presented in the model. Such decoupling removes any aliasing effect while qualifying each function's contribution to the overall regression model. Building the structure of this regression model was an optimization problem to minimize the so-called predicted squared error. The predicted squared error is a sum of the mean square fit error and a term proportional to the number of terms in the model. After building such a model, one can then expand these orthogonal functions into an ordinary multivariate polynomial where the total dependent aerodynamic coefficients are expressed in terms of angle of attack, sideslip angle, and control surface deflections as a finite multivariate power series as

$$C_{X_T} = \underbrace{C_x(\alpha,\delta_e)}_{\sum_{i,j=0}^{3} a_{ij}\alpha^i\delta_e^j} + \frac{\bar{c}q}{2V}\underbrace{C_{xq}(\alpha)}_{\sum_{i=0}^{4} b_i\alpha^i} = \sum_{i,j=0}^{3} a_{ij}\alpha^i\delta_e^j + \frac{\bar{c}q}{2V}\sum_{i=0}^{4} b_i\alpha^i \tag{5.48}$$

$$\begin{aligned} C_{Z_T} &= \underbrace{C_z(\alpha)}_{\sum_{i=0}^{4} f_i\alpha^i}\left[1-\left(\frac{\beta}{57.3}\right)^2\right] - 0.19\left(\frac{\delta_e}{25}\right) + \frac{\bar{c}q}{2V}\underbrace{C_{zq}(\alpha)}_{\sum_{i=0}^{4} g_i\alpha^i} \\ &= \sum_{i=0}^{4} f_i\alpha^i\left[1-\left(\frac{\beta}{57.3}\right)^2\right] - 0.19\left(\frac{\delta_e}{25}\right) + \frac{\bar{c}q}{2V}\sum_{i=0}^{4} g_i\alpha^i \end{aligned} \tag{5.49}$$

$$\begin{aligned} C_{M_T} &= \underbrace{C_m(\alpha,\delta_e)}_{\sum_{i,j=0}^{2,3} m_{ij}\alpha^i\delta_e^j} + C_{Z_T}\left(\bar{x}_{cg_r} - \bar{x}_{cg}\right) + \frac{\bar{c}q}{2V}\underbrace{C_{mq}(\alpha)}_{\sum_{i=0}^{5} n_i\alpha^i} \\ &= \sum_{i,j=0}^{2,3} m_{ij}\alpha^i\delta_e^j + C_{Z_T}\left(\bar{x}_{cg_r} - \bar{x}_{cg}\right) + \frac{\bar{c}q}{2V}\sum_{i=0}^{5} n_i\alpha^i \end{aligned} \tag{5.50}$$

The values of the regression coefficients are given in Reference 114. Unlike the look-up table structure, the multivariate orthogonal functions provide an analytical structure,

which reduce numerical errors in computing the stability and control derivatives from the aerodynamic coefficients. This polynomial formulation is used in the computation.

5.2 Local Kernel Generation

The PLTI system in Equation (5.6) provides an analytical solution for the kernels using successive substitution. Assume the velocity to be the output, then an output matrix coefficient is defined as C = [1 0 0 0]. The first PLTI system has a solution

$$V_1(t) = \int_0^t C\Phi(t-\tau)Bu(\tau)d\tau \tag{5.51}$$

where

$$\Phi(t-\tau) = e^{A(t-\tau)} \tag{5.52}$$

The characteristic equation of the longitudinal motion has two sets of conjugate complex roots. The first set represents the phugoid motion, which operates at a low frequency. This motion is also called long period motion. The second set represents the short period motion, which operates at a relatively high frequency. Total velocity and pitch angle are the significant variables with phugoid motion, while angle of attack and pitch rate are the dominant variables with short period motion. A fair assumption, therefore, is to present the total velocity or pitch angle by phugoid motion and angle of attack or pitch rate by short period motion.

By substituting, the generalized convolution solution of the total velocity is given as

$$\begin{aligned} V_1(t) = \int_0^t \{ & K_{V_{ph}} e^{-\sigma_{ph}(t-\tau)} \sin\left(\omega_{d_{ph}}(t-\tau) + \varphi_{ph}^V\right) \\ & + K_{V_{sp}} e^{-\sigma_{sp}(t-\tau)} \sin\left(\omega_{d_{sp}}(t-\tau) + \varphi_{sp}^V\right)\}\delta_e(\tau)d\tau \\ \approx & \int_0^t \left(K_{V_{ph}} e^{-\sigma_{ph}(t-\tau)} \sin\left(\omega_{d_{ph}}(t-\tau) + \varphi_{ph}^V\right)\right)\delta_e(\tau)d\tau \end{aligned} \tag{5.53}$$

where subscripts "*ph*" and "*sp*" denote phugoid and short period . Note only the phugoid contribution is retained to compute $V_1(t)$. The same procedure gives the generalized convolution solution of angle of attack as

$$\begin{aligned}\alpha_1(t) &= \int_0^t \{K_{\alpha_{ph}} e^{-\sigma_{ph}(t-\tau)} \sin(\omega_{d_{ph}}(t-\tau)+\varphi_{ph}^{\alpha}) \\ &\quad + K_{\alpha_{sp}} e^{-\sigma_{sp}(t-\tau)} \sin(\omega_{d_{sp}}(t-\tau)+\varphi_{sp}^{\alpha})\}\delta_e(\tau)d\tau \\ &\approx \int_0^t (K_{\alpha_{sp}} e^{-\sigma_{sp}(t-\tau)} \sin(\omega_{d_{sp}}(t-\tau)+\varphi_{sp}^{\alpha}))\delta_e(\tau)d\tau\end{aligned} \tag{5.54}$$

The first kernels for both V and α are thus

$$\begin{aligned}h_1^V(\tau) &= K_{V_{ph}} e^{-\sigma_{ph}(\tau)} \sin(\omega_{d_{ph}}(\tau)+\varphi_{ph}^{V}) \\ h_1^{\alpha}(\tau) &= K_{\alpha_{sp}} e^{-\sigma_{sp}(\tau)} \sin(\omega_{d_{sp}}(\tau)+\varphi_{sp}^{\alpha})\end{aligned} \tag{5.55}$$

The second kernels are calculated by adding term-by-term from the nonlinear matrices B_{xx}, B_{xu}, and B_{uu}. Many of these matrices' elements are not significant and can be ignored. For example, for the second velocity second kernel, two elements $f_{1\alpha^2}$ and $f_{1\delta_e^2}$ are significant compared to the others. Thus, the rate of velocity change is correlated to the drag coefficient, which has a quadratic form with angle of attack and elevator deflection. The drag quadratic function has a significant curvature making first order derivatives insufficient to fully describe the system. Numerical investigation of this point is discussed in detail in the next section. Assuming the two terms $f_{1\alpha^2}$ and $f_{1\delta_e^2}$ are the only sources of nonlinearity, the second kernel of the velocity is

$$V_2(t) = \underbrace{f_{1\alpha^2}\int_0^t C\Phi(t-\tau)B\alpha_1(\tau)\alpha_1(\tau)d\tau}_{V_2^{\alpha^2}(t)} + \underbrace{f_{1\delta_e^2}\int_0^t C\Phi(t-\tau)B\delta_e(\tau)\delta_e(\tau)d\tau}_{V_2^{\delta_e^2}(t)} \tag{5.56}$$

By substituting from Equation (4.55)

$$V_2^{\alpha^2}(t) = f_{1\alpha^2} K_{V_{ph}} K_{\alpha_{sp}}^2 \int_0^t e^{-\sigma_{ph}(t-\tau)} \sin\left(\omega_{d_{ph}}(t-\tau) + \varphi_{ph}^V\right) \times$$
$$\int_0^t \left(e^{-\sigma_{sp}(\tau-\tau_1)} \sin\left(\omega_{d_{sp}}(\tau-\tau_1) + \varphi_{sp}^\alpha\right)\right) \delta_e(\tau_1) \Delta(\tau-\tau_1) d\tau_1 \times \tag{5.57}$$
$$\int_0^t \left(e^{-\sigma_{sp}(\tau-\tau_2)} \sin\left(\omega_{d_{sp}}(\tau-\tau_2) + \varphi_{sp}^\alpha\right)\right) \Delta(\tau-\tau_2) \delta_e(\tau_2) d\tau_2 d\tau$$

By rearranging the integration limits in the order $d\tau \times d\tau_1 \times d\tau_2$, the multiplication of the two operators $\Delta(\tau\text{-}\tau_1)\Delta(\tau\text{-}\tau_2)$ can be replaced by setting the lower limit of the internal integration by $\max(\tau_1, \tau_2)$ instead of 0, where the operator $\max(x, y)$ refers to the maximum values between x and y. The operator $\Delta(t\text{-}\tau_i)$ also allows setting the upper limits of the external integrations by t instead of τ. The integration in Equation (5.57) yields to

$$V_2^{\alpha^2}(t) = \int_0^t \int_0^t h_{2\alpha^2}^V(t-\tau_1, t-\tau_2) \delta_e(\tau_1) \delta_e(\tau_2) d\tau_1 d\tau_2 \tag{5.58}$$

where

$$h_{2\alpha^2}^V(t-\tau_1, t-\tau_2) =$$
$$f_{1\alpha^2} K_{V_{ph}} K_{\alpha_{sp}}^2 \int_{\max(\tau_1,\tau_2)}^t e^{-\sigma_{ph}(t-\tau)} e^{-\sigma_{sp}(\tau-\tau_1)} e^{-\sigma_{sp}(\tau-\tau_2)} \sin\left(\omega_{d_{ph}}(t-\tau) + \varphi_{ph}^V\right) \tag{5.59}$$
$$\times \sin\left(\omega_{d_{sp}}(\tau-\tau_1) + \varphi_{sp}^\alpha\right) \sin\left(\omega_{d_{sp}}(\tau-\tau_2) + \varphi_{sp}^\alpha\right) d\tau$$

By integrating Equation (5.59), the second kernel due to α^2 is

$$
\begin{aligned}
h^V_{2\alpha^2}(\tau_1,\tau_2) &= \frac{f_{1\alpha^2} K_{V_{ph}} K^2_{\alpha_{sp}}}{4} e^{-\sigma_{sp}(\tau_1+\tau_1)} \left\{ \frac{1}{\widetilde{\omega}_{ph}} \sin\left(\omega_{d_{sp}}(\tau_1-\tau_2) - \varphi^V_{ph} + \widetilde{\varphi}_{ph}\right) \right. \\
&+ \frac{1}{\widetilde{\omega}_{ph}} \sin\left(\omega_{d_{sp}}(\tau_2-\tau_1) - \varphi^V_{ph} + \widetilde{\varphi}_{ph}\right) - \frac{1}{\widetilde{\omega}^+} \sin\left(\omega_{d_{sp}}(\tau_1+\tau_2) - \varphi^V_{ph} + 2\varphi^\alpha_{sp} + \widetilde{\varphi}^+\right) \\
&\left. + \frac{1}{\widetilde{\omega}^-} \sin\left(\omega_{d_{sp}}(\tau_1+\tau_2) + \varphi^V_{ph} + 2\varphi^\alpha_{sp} + \widetilde{\varphi}^-\right) \right\} \\
&- \frac{f_{1\alpha^2} K_{V_{ph}} K^2_{\alpha_{sp}}}{4} e^{-\sigma_{sp}(\tau_1+\tau_1)} e^{(2\sigma_{sp}-\sigma_{ph})\min(\tau_1,\tau_2)} \\
&\times \left\{ \frac{1}{\widetilde{\omega}_{ph}} \sin\left(\omega_{d_{sp}}(\tau_1-\tau_2) - \varphi^V_{ph} + \widetilde{\varphi}_{ph} + \omega_{d_{ph}} \min(\tau_1,\tau_2)\right) \right. \\
&+ \frac{1}{\widetilde{\omega}_{ph}} \sin\left(\omega_{d_{sp}}(\tau_2-\tau_1) - \varphi^V_{ph} + \widetilde{\varphi}_{ph} + \omega_{d_{ph}} \min(\tau_1,\tau_2)\right) \\
&- \frac{1}{\widetilde{\omega}^+} \sin\left(\omega_{d_{sp}}(\tau_1+\tau_2) - \varphi^V_{ph} + 2\varphi^\alpha_{sp} + \widetilde{\varphi}^+ + (2\omega_{d_{sp}} + \omega_{d_{ph}}) \min(\tau_1,\tau_2)\right) \\
&\left. + \frac{1}{\widetilde{\omega}^-} \sin\left(\omega_{d_{sp}}(\tau_1+\tau_2) + \varphi^V_{ph} + 2\varphi^\alpha_{sp} + \widetilde{\varphi}^- + (2\omega_{d_{sp}} - \omega_{d_{ph}}) \min(\tau_1,\tau_2)\right) \right\}
\end{aligned}
\tag{5.60}
$$

where

$$
\begin{aligned}
\widetilde{\omega}_{ph} &= \sqrt{(2\sigma_{sp} - \sigma_{ph})^2 + \omega^2_{d_{ph}}} \quad , \quad \cos(\widetilde{\varphi}_{ph}) = \frac{2\sigma_{sp} - \sigma_{ph}}{\widetilde{\omega}_{ph}} \\
\widetilde{\omega}^+ &= \sqrt{(2\sigma_{sp} - \sigma_{ph})^2 + (2\omega_{d_{sp}} + \omega_{d_{ph}})^2} \quad , \quad \cos(\widetilde{\varphi}^+) = \frac{2\sigma_{sp} - \sigma_{ph}}{\widetilde{\omega}^+} \\
\widetilde{\omega}^- &= \sqrt{(2\sigma_{sp} - \sigma_{ph})^2 + (2\omega_{d_{sp}} - \omega_{d_{ph}})^2} \quad , \quad \cos(\widetilde{\varphi}^-) = \frac{2\sigma_{sp} - \sigma_{ph}}{\widetilde{\omega}^-}
\end{aligned}
\tag{5.61}
$$

The contribution of the $f_{1\delta_e^2}$ term to the second kernel is

$$
\begin{aligned}
V_2^{\delta_e^2}(t) &= f_{1\delta_e^2} \overline{K}_{V_{ph}} \int_0^t e^{-\sigma_{ph}(t-\tau)} \sin\left(\omega_{d_{ph}}(t-\tau) + \varphi^V_{ph}\right) \delta^2_e(\tau) d\tau \\
&= f_{1\delta_e^2} \overline{K}_{V_{ph}} \int_0^t \int_0^t e^{-\sigma_{ph}(t-\tau_1)} \sin\left(\omega_{d_{ph}}(t-\tau_1) + \varphi^V_{ph}\right) \delta(t_1-\tau_2) \delta_e(\tau_1) \delta_e(\tau_2) d\tau_1 d\tau_2 \\
&= \int_0^t \int_0^t h^V_{2\delta_e^2}(t-\tau_1, t-\tau_2) \delta_e(\tau_1) \delta_e(\tau_2) d\tau_1 d\tau_2
\end{aligned}
\tag{5.62}
$$

where $\delta(\tau_1-\tau_2)$ is the impulse function. Note $\overline{K}_{V_{ph}}$ is the normalized value of $K_{V_{ph}}$ with respect to elevator deflection.

The total velocity second kernel is

$$
h^V_2(\tau_1,\tau_2) = h^V_{2\alpha^2}(\tau_1,\tau_2) + h^V_{2\delta_e^2}(\tau_1,\tau_2) \tag{5.63}
$$

The second kernel has two terms: angle of attack quadratic kernel $h^V_{2\alpha^2}(\tau_1,\tau_2)$ and elevator quadratic kernel $h^V_{2\delta_e^2}(\tau_1,\tau_2)$. Each kernel is a two dimensional surface as a function of τ_1 and τ_2. The expression of the angle of attack quadratic kernel has the short period damped frequency $\omega_{d_{sp}}$ and the phugoid damped frequency $\omega_{d_{ph}}$. The elevator quadratic kernel is an impulsive sheet over the diagonal kernel line. The boundary of this sheet has the same shape as the first order kernel.

5.3 Results and Discussion

A routine has been developed to emulate the dynamic behavior of the aircraft based on the nonlinear simulation using the Runge-Kutta 4th order logic. This routine includes many subroutines to compute: 1) trim conditions, 2) local linear model, and 3) local Volterra model. The trim condition subroutine receives the nature of the maneuver and the flight conditions (altitude, velocity, and initial angular velocities), while linear and angular acceleration are zero. Depending on the nature of the excited motion (rectilinear, pull-over, level turn, etc.), the subroutine sets some variables to specific values. For example, in the rectilinear motion, the flight path angle is zero ($\gamma = \theta-\alpha = 0$), the symmetric flight is assumed ($\beta = 0$ and $v = 0$) and all angular velocities are zero ($p = q = r = 0$). Consequently, the trim problem involves searching for the values of α, δ_e, and δ_{th} to match the derivatives of dV/dt, $d\alpha/dt$, and dq/dt to zero.

5.3.1 Local Linear and Volterra Models

Both local linear and Volterra model subroutines receive the trimming values and compute the equivalent matrices A, B, B_{xx}, B_{xu}, and B_{uu} at the equivalent trimmed states. Many of the matrix elements require aerodynamic derivatives such as $\partial C_{MT} / \partial \alpha$. These aerodynamic derivatives can be computed using a finite difference technique or analytical expressions based on the "multivariate orthogonal functions." Use of the finite difference technique may lead to round-off error at a low derivative step size or lost precision at a

high derivative step size. These types of error are more significant in the second order derivatives than the first order derivatives. In order to avoid any numerical error propagation, the analytical technique is used. For example, the generated linear and Volterra model at V = 1500 ft/s and H = 30,000 ft in a rectilinear motion is

$$A=\begin{bmatrix} -9.93\times10^{-3} & 87.22 & 0.87 & -32.17 \\ -4.30\times10^{-5} & -1.02 & 0.95 & 0 \\ 0 & -9.94 & -1.53 & 0 \\ 0 & 0 & 1 & 0 \end{bmatrix},\quad B=\begin{bmatrix} 9.13 \\ -0.11 \\ -36.82 \\ 0 \end{bmatrix}$$

$$B_{xx}=\begin{bmatrix} -3.31\times10^{-6} & -7.33\times10^{-2} & 0 & 0 & -1.29\times10^{3} & -29.08 & 0 \\ 9.55\times10^{-9} & -6.77\times10^{-4} & 0 & 0 & 1.14 & -4.18\times10^{-2} & 0 \\ 0 & -1.33\times10^{-2} & 0 & 0 & 13.96 & -1.22 & 0 \\ 0 & 0 & 0 & 0 & 0 & 0 & 0 \end{bmatrix} \tag{5.64}$$

$$B_{xu}=\begin{bmatrix} 1.22\times10^{-2} & 2.31\times10^{2} & 0 & 0 \\ -1.39\times10^{-4} & -6.44\times10^{-3} & 0 & 0 \\ -4.71\times10^{-2} & -7.50 & 0 & 0 \\ 0 & 0 & 0 & 0 \end{bmatrix},\quad B_{uu}=\begin{bmatrix} -1.04\times10^{2} \\ -2.85\times10^{-2} \\ 3.19\times10^{2} \\ 0 \end{bmatrix}$$

Note all dimensions are in feet and radians. As a nature of the rectilinear motion, some of these matrix elements are constant or zero, as an example $f_{l\theta}$ = $-gC_{\theta\text{-}\alpha}$ = $-g$. There are 40 nonzero elements, however, there are 31 varying elements left in these matrices, which change as the flight conditions change.

Figure 5.1 shows the time responses when a perturbed elevator deflection of $\delta_{el} = \Delta\delta_e$ = 1.5 deg excites both linear and Volterra models at the specific flight condition indicated. In the case of the nonlinear simulation, this perturbed deflection is added to the trim elevator deflection δ_{eo} = -2.39 deg. It is observed that there is a small lag in the position of maximum/minimum peaks between linear and nonlinear responses. On top of that, there is a noticeable difference in the steady angle of attack between linear and nonlinear. As previously shown in Chapter 4, the significant quadratic terms are responsible for producing such differences. However, qualitatively speaking, both linear

and Volterra models follow quite closely the nonlinear model in the case of angle of attack α, pitch rate q, and pitch angle θ.

In the case of the total speed V, the linear model not only fails to capture the response's amplitude, but also fails to capture the shape of response. At time t = 0.2 s, the linear model heads downward by a much less rate than the nonlinear simulation's rate. This rate keeps decreasing in the case of the linear simulation up to time t = 1.8 s, then the linear behavior heads upward; completely deviating from the nonlinear simulation. The Volterra model, on the other hand, shows a consistent behavior along with the nonlinear simulation. By the time t = 5 s, the deviation from the nonlinear simulation is -37 ft/s in the case of the linear model and -3 ft/s in the case of Volterra model, while the total perturbed velocity is -26 ft/s. The source of difference between the linear and Volterra models can be traced back to specific terms in the PLTI matrices' elements. Considering the difference in amplitude of the perturbation states, it becomes clear that the value $0.5f_{1\alpha^2} = -1.29\times10^{3}$ and $0.5f_{1\delta_e^2} = -1.04\times10^{2}$ are the most effective nonlinearities and all other terms can be neglected with respect to them. Figure 5.2 shows the simulation based on the complete or total Volterra model and the two term approximate Volterra model (only $f_{1\alpha^2}$ and $f_{1\delta_e^2}$ are nonzero).

As listed in Equation (5.63), the second kernel of the total speed has two terms. The first term is the total velocity's second kernel due to the quadratic angle of attack $h^V_{2\alpha^2}(\tau_1,\tau_2)$, which is shown in Figure 5.3. For this second kernel term, the signature of the phugoid motion appears through the diagonal line, while the signature of the short period motion appears through the cross-diagonal lines. The surface in Figure 5.3 is an oscillatory surface with $\omega_{d_{ph}}$ = 0.035 rad/s and ζ_{ph} = 0.143 over the diagonal line, which has perpendicular frequency $\omega_{d_{sp}}$ = 3.06 rad/s and damping ratio ζ_{sp} = 0.385 in the cross-diagonal direction. The second term is the total velocity's second kernel due to the quadratic elevator defelection $h^V_{2\delta_e^2}(\tau_1,\tau_2)$, which has an impulsive surface over the diagonal. The boundary of this sheet has the same shape as the total velocity's first kernel

multiplied by $f_{1\delta_e^2} = -1.04 \times 10^2$. Both terms have negative amplitudes, which is the main reason that the velocity response based on the Volterra model heads downward, consistent with the nonlinear simulation, while the velocity response based on the linear model heads upward (see Figure 5.1). Although the short period motion's frequency and damping ratio appear in the second kernel, they have almost no influence on the response. Thus, the influence of the short period motion's frequency and damping ratio characterize the cross-diagonal lines only, which scales the volume between the surface and the $\tau_1 - \tau_2$ plane. The main shape of the surface is given through the diagonal line (phugoid motion). Figure 5.4 shows the response for the same input excitation at V_o = 500 ft/s and H_o = 5 kft. As it appears, there is no significant difference between the Volterra and linear models to duplicate the nonlinear simulation. This observation indicates that the strength of the nonlinearity is a function of the operating condition.

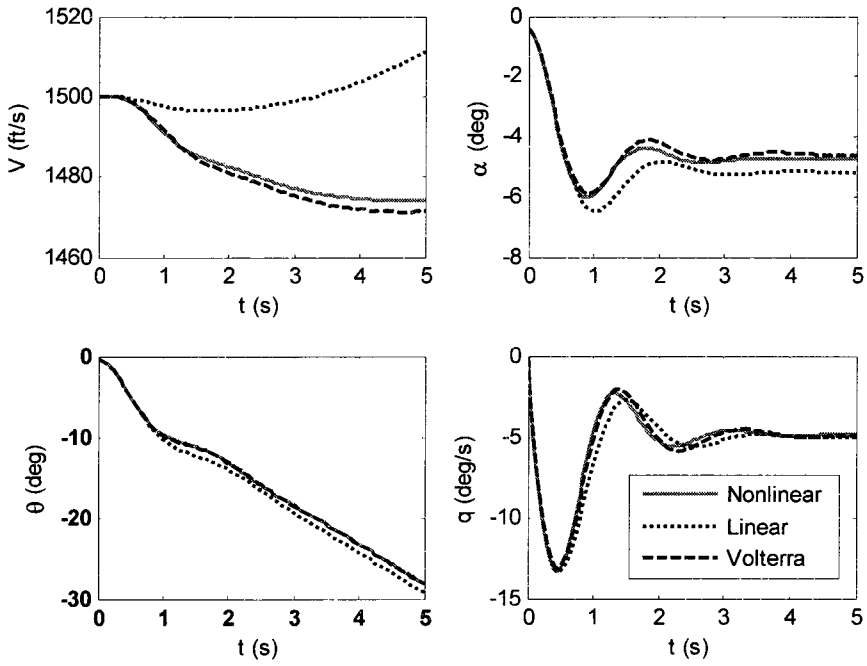

Figure 5.1 Local Linear and Volterra Models for $\Delta\delta_e$ = 1.5 deg at V_o = 1500 ft/s and H_o = 30 kft

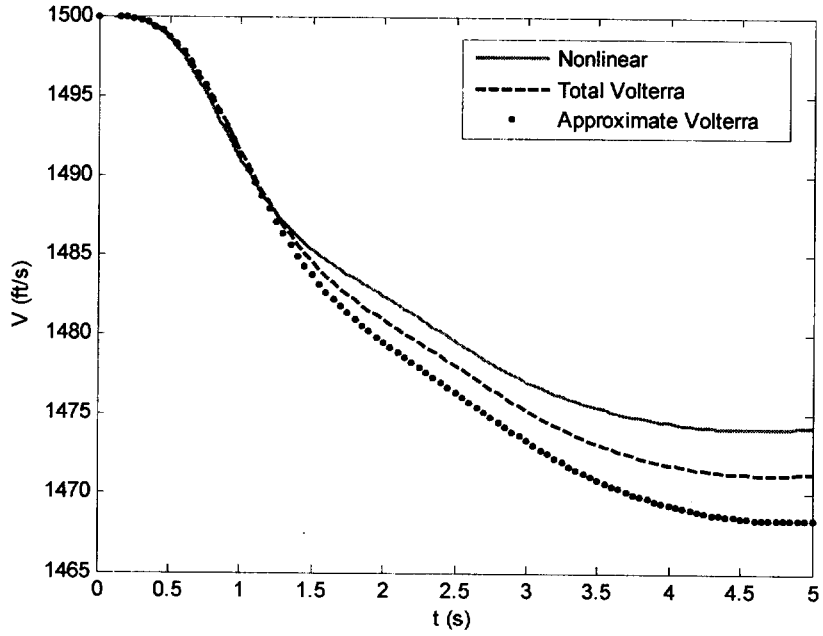

Figure 5.2 Approximate Volterra Model for $\Delta\delta_e = 1.5$ deg
at $V_o = 1500$ ft/s and $H_o = 30$ kft

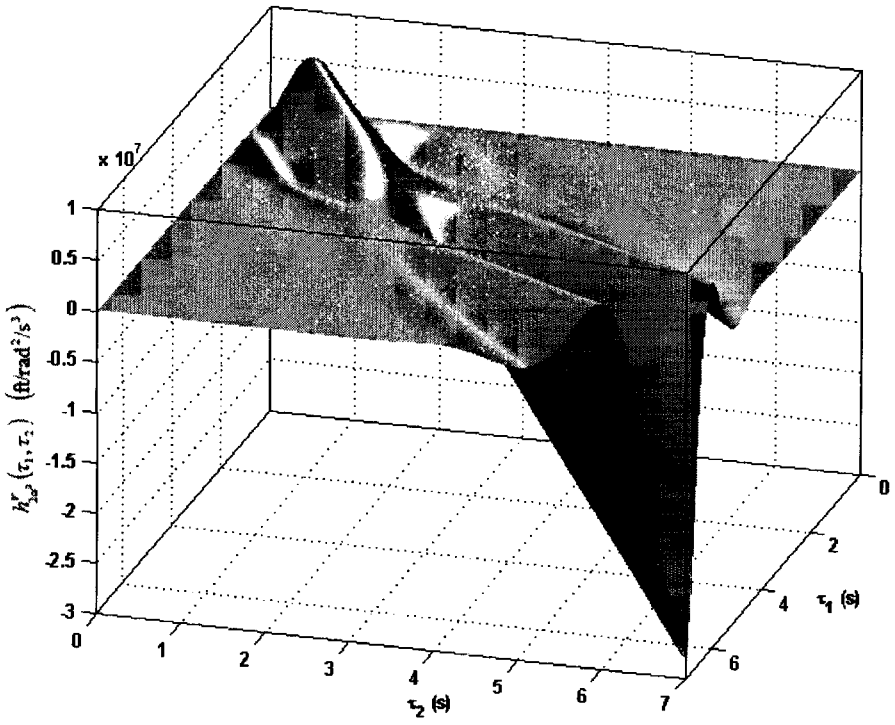

Figure 5.3 Quadratic Angle of Attack Second Order Kernel of Total Velocity
at $V_o = 1500$ ft/s and $H_o = 30$ kft

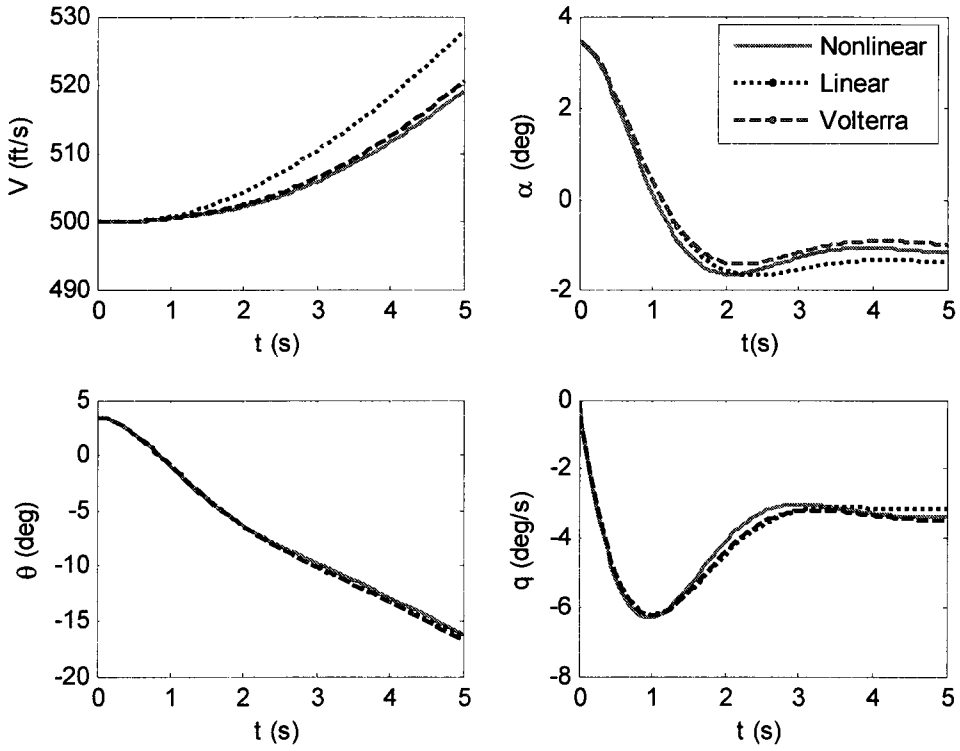

Figure 5.4 Local Linear and Volterra Models for $\Delta\delta_e$ = 1.5 deg
at V_o = 500 ft/s and H_o = 5 kft

5.3.2 Global Volterra Model

Two factors, total velocity V and altitude H or the varying parameter vector $\hat{\theta} = [V_o \quad H_o]^T$, are selected to capture the variation over the flight envelope for the rectilinear trim motion. Note, in the rectilinear motion, specifying two variables is enough to find the rest of the trimming values. The varying parameter $\hat{\theta} = [V_o \quad H_o]^T$ has velocity as one of the states, which means that the developed VPV model is quasi steady. The model is called quasi steady if the varying parameter vector includes any subset of the state vector. The high and low level of each element in the varying parameter vector $\hat{\theta}$ is set as 500 ft/s $\leq V_o \leq$ 1500 ft/s and 5,000 ft $\leq H_o \leq$ 30,000 ft.

To build a VPV model, as well as LPV model, the common technique is to generate the LPV/VPV matrices at different points over the entire flight envelope and

schedule their equivalent elements with the operating condition parameters. The choice of grid resolution, interpolation technique, and simulation step size are then a matter of concern. A grid with a high resolution yields better results, while the main disadvantage is then the consumed memory and computational cost arising from using such high-resolution tables in addition to leading to a round-off error. Using different time steps in the nonlinear simulation, there is no significant difference in the produced response for time step less than Δt = 0.1 s. The same time step is used for both LPV and VPV simulations. For grid resolution and interpolation techniques, an investigation is conducted using the input in Figures 5.5 at flight condition V_0 = 800 ft/s and H_0 = 20 kft. Three different resolutions with three different interpolation techniques have been tested as listed in Table 5.1. The results based on these grids are shown in Figures 5.6-5.8. The results show that the accuracy of the VPV model is almost the same for a grid of $N_V \times N_H = 5 \times 5$ or higher where N_V and N_H denote the number of grid points for variables V and H, respectively.

Table 5.1 Investigated Interpolation Techniques and Grid Resolutions

	$N_V \times N_H = 5 \times 5$	$N_V \times N_H = 25 \times 25$	$N_V \times N_H = 50 \times 50$
Linear Interpolation	Grid 1	Grid 4	Grid 7
Spline Interpolation	Grid 2	Grid 5	Grid 8
Mixed Interpolation	Grid 3	Grid 6	Grid 9

It is clear that linear interpolation doesn't accurately capture the variation in short period motion. For example, in cases of angle of attack and pitch rate responses, the linear interpolation provides less maximum and minimum peak overshoot than the nonlinear simulation. Such initial errors over time move the VPV propagation away from

the nonlinear simulation. In phugoid motion, the linear interpolation allows the VPV propagation to have the same qualitative response as the nonlinear simulation with a quantitative error as a consequence of the initial errors in the short period motion. The spline interpolation precisely renders the variation in the short period motion, but fails to render the phugoid motion for both V and θ. This observation concludes that spline interpolation is well suited for short period motion and linear interpolation is well suited for phugoid motion. Taking advantage of this conclusion, a mixed interpolation technique is developed. This mixed interpolation employs linear interpolation for phugoid motion, which is presented by the total velocity and pitch rate equations, while it employs spline interpolation for the short period equation or angle of attack equation. This mixed technique solves the trade-off between the two interpolation techniques delivering a better match for the nonlinear simulation. Based on this investigation, mixed interpolation with resolution $N_V \times N_H = 25 \times 25$ (Grid 6) is used throughout this chapter.

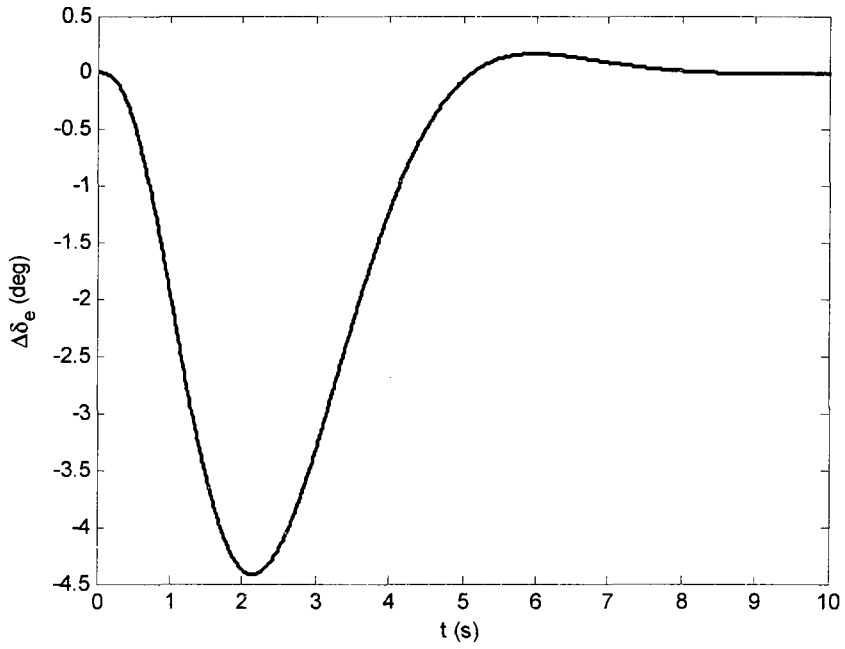

Figure 5.5 Perturbed Input I

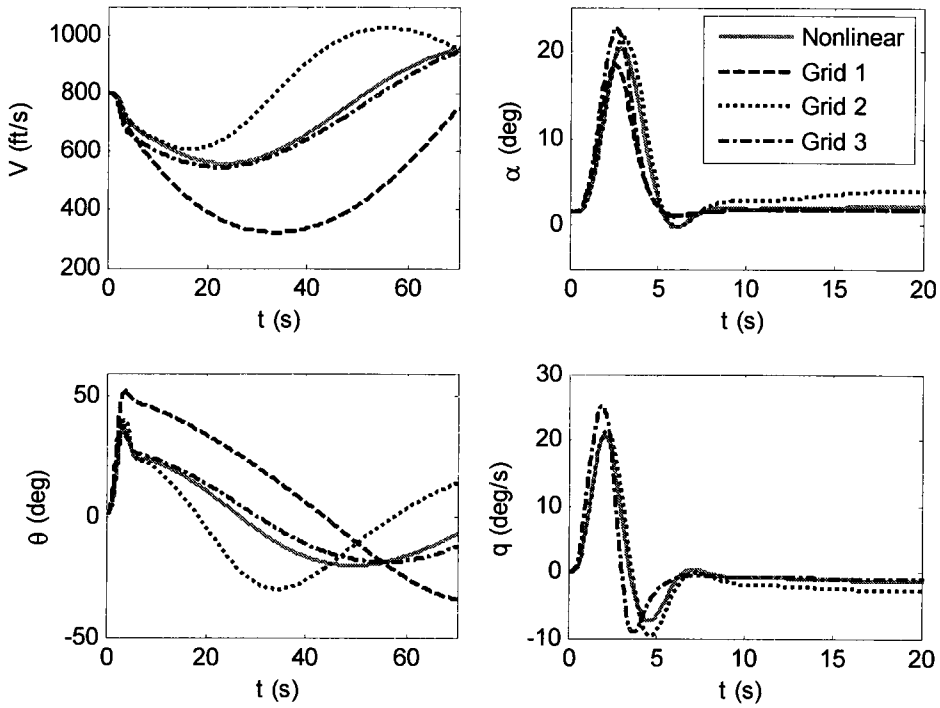

Figure 5.6 Responses of Grids 1, 2, and 3

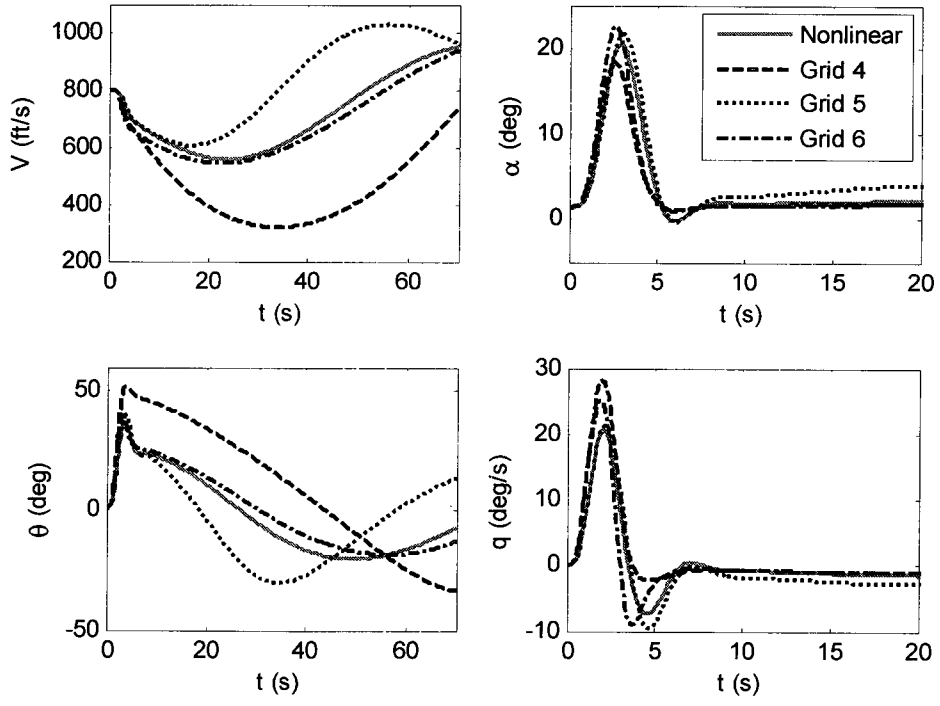

Figure 5.7 Responses of Grids 4, 5, and 6

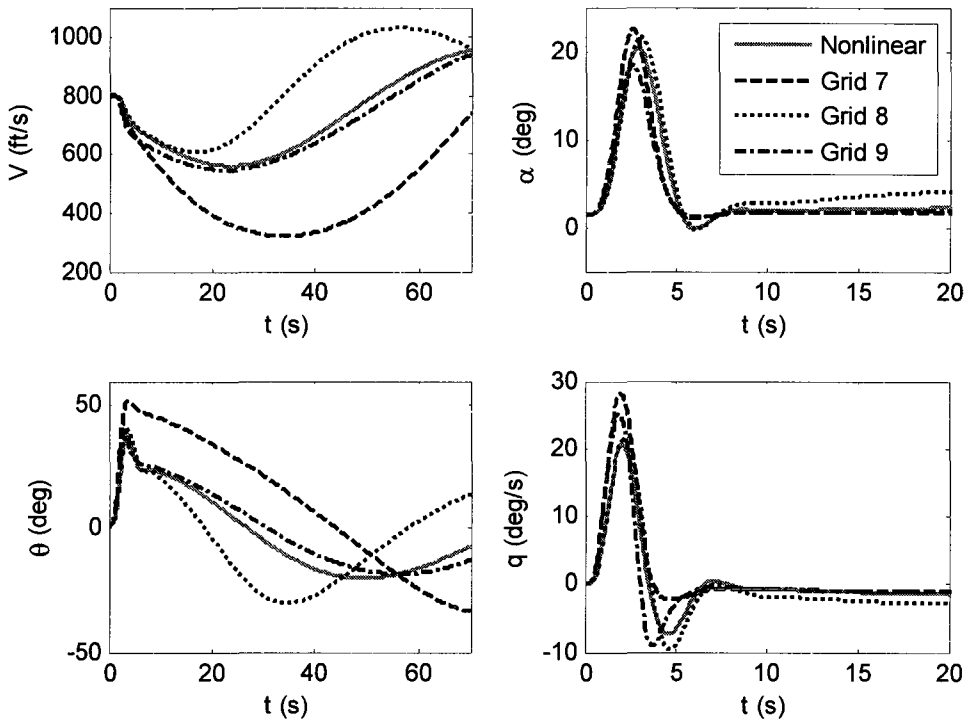

Figure 5.8 Responses of Grids 7, 8, and 9

5.3.3 Comparison to Global Linear Model

The input signal in Figure 5.5 is used to compare the LPV, VPV, and nonlinear simulations at the operating condition V_0 = 800 ft/s and H_0 = 20 kft. The input is designed to have a fast smooth change from 0 deg to -4.5 deg within 2 s. The input returns back to 0 deg by t = 5 s. This input moves the aircraft over the flight envelope as shown in Figure 5.9. At the first 5 seconds, this input excites the short period mode of the aircraft producing an oscillatory change in both angle of attack ($\Delta\alpha_{max} \approx 20$ deg) and pitch rate ($\Delta q_{max} \approx 20$ deg/sec). Consequently, the pitch angle increases by $\Delta\theta_{max} \approx 40$ deg producing a high rate of decrease in the kinetic energy (total speed), while the altitude is almost constant. When the input signal settles down to zero again, both angle of attack α and pitch rate q settle to their initial trimming value. The total speed V and pitch angle θ start then to oscillate slowly interchanging between kinetic and potential energy that occurs when the aircraft attempts to reestablish the equilibrium balance between lift,

weight, thrust, and drag (see Figure 5.10). Since the operating condition (V_o = 800 ft/s and H_o = 20 kft) has a stable phugoid mode, the generated trajectory is a slowly shrinking helix; heading toward this operating condition.

The linear model shows a significant inability to capture total velocity response during the input excitation period. The velocity response based on the LPV simulation indicates that velocity is almost constant at the first 3 s, while the VPV and nonlinear simulation show a high drop in the velocity within the same period. The parametric variation of the drag and lift coefficients (C_D and C_L) with angle of attack, shown in Figure 5.11 for the first 3 seconds, explains why LPV modeling is not enough to capture the dynamics. The LPV technique considers the local slope at t = 0 s, relatively low, to launch the simulation. Such a low initial drag coefficient rate of change induces a velocity with almost zero rate of change. Over time, this slope is then updated by the parameter varying process and a correction to the velocity and altitude response eventually happens, which is the reason that the LPV approach is still able to capture the behavior. The error propagation, however, because of using first derivatives only, makes the LPV simulation shift from the nonlinear simulation by Δt = 11 s for the first minimum peak overshoot. Unlike the LPV approach, the VPV model uses a second order approximation, which is well suited for the drag variation with the angle of attack α (see Figure 5.11). The variation in the lift coefficient C_L with the angle of attack α, on the other hand, can be fairly well approximated by a linear model. For this reason, there is no significant difference between LPV and VPV responses with the nonlinear simulation for the angle of attack's response.

The input in Figure 5.12 moves the aircraft over the track shown in Figure 5.13 with the trim condition being V_o = 1000 ft/s and H_o = 17.5 kft. The variation of this input is sharper than the variation in input I. The response based on this input signal is shown in Figure 5.14 indicating that the LPV model delivers a close result to the VPV model, which means that the waveform of the input signal has an influence on the strength of the

nonlinearity. The amplitude of the input II is less than the amplitude of the input I during the first five seconds. This fact indicates that the quadratic elevator nonlinearity's contribution is much less in case of input II. The quadratic angle of attack nonlinearity, on the other hand, is proportional to the short period motion, and this amplitude for input II is less than that for input I. In this way, VPV methodology has a capability to increase or decrease the nonlinearity impact with the input's waveform.

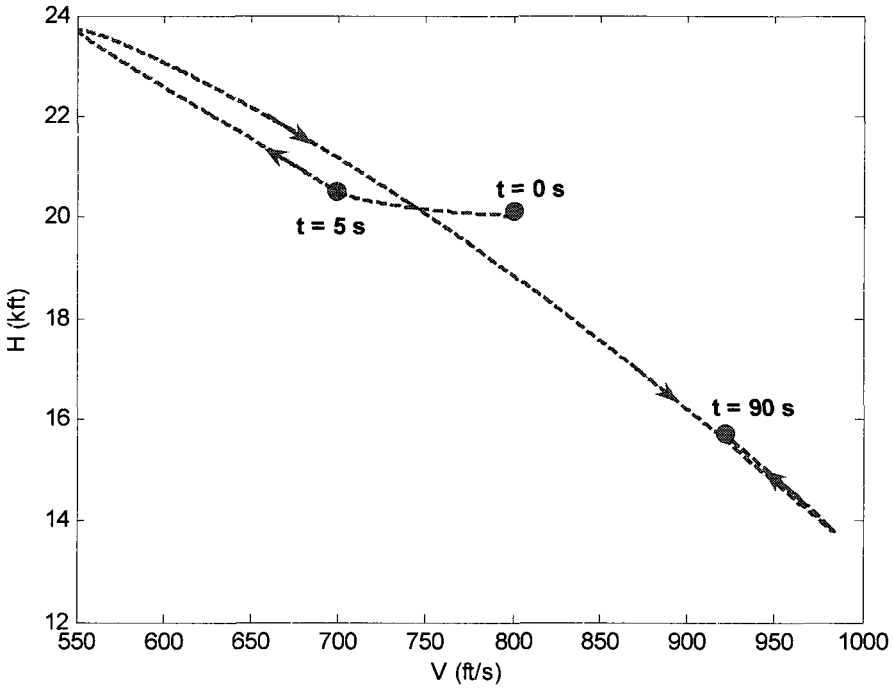

Figure 5.9 Aircraft Trajectory of Input I

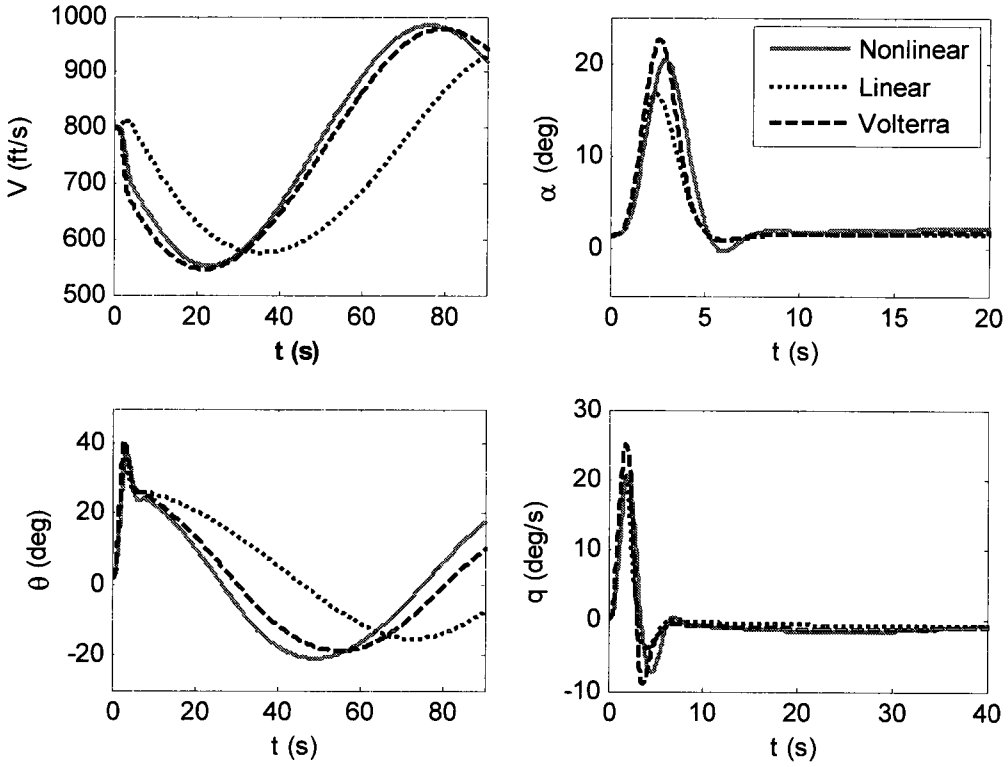

Figure 5.10 Aircraft Response of Input I

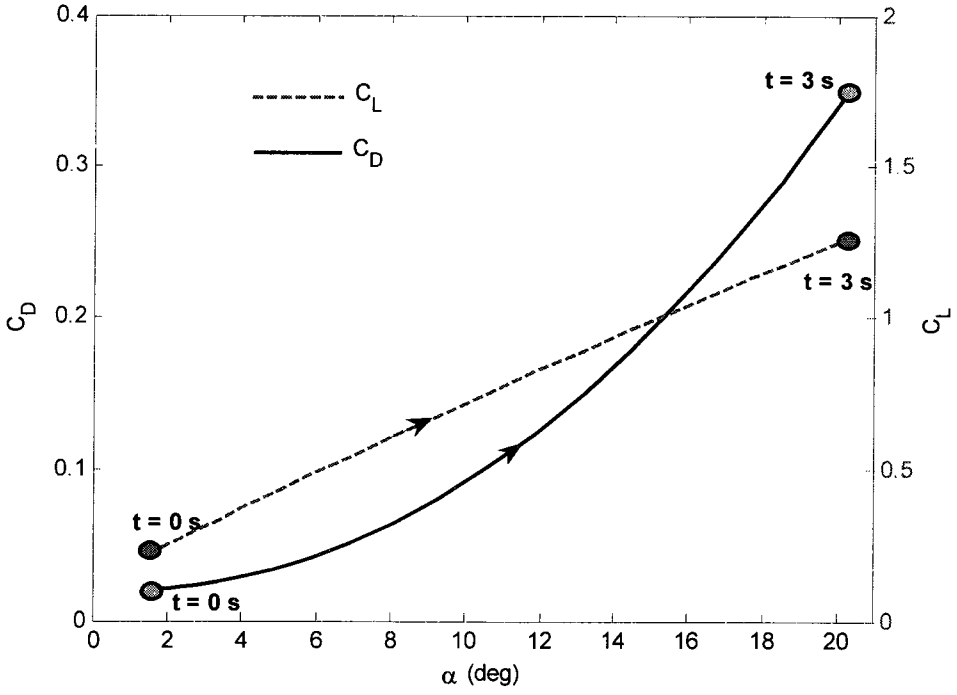

Figure 5.11 Parametric Variation of Drag and Lift Coefficients with Angle of Attack

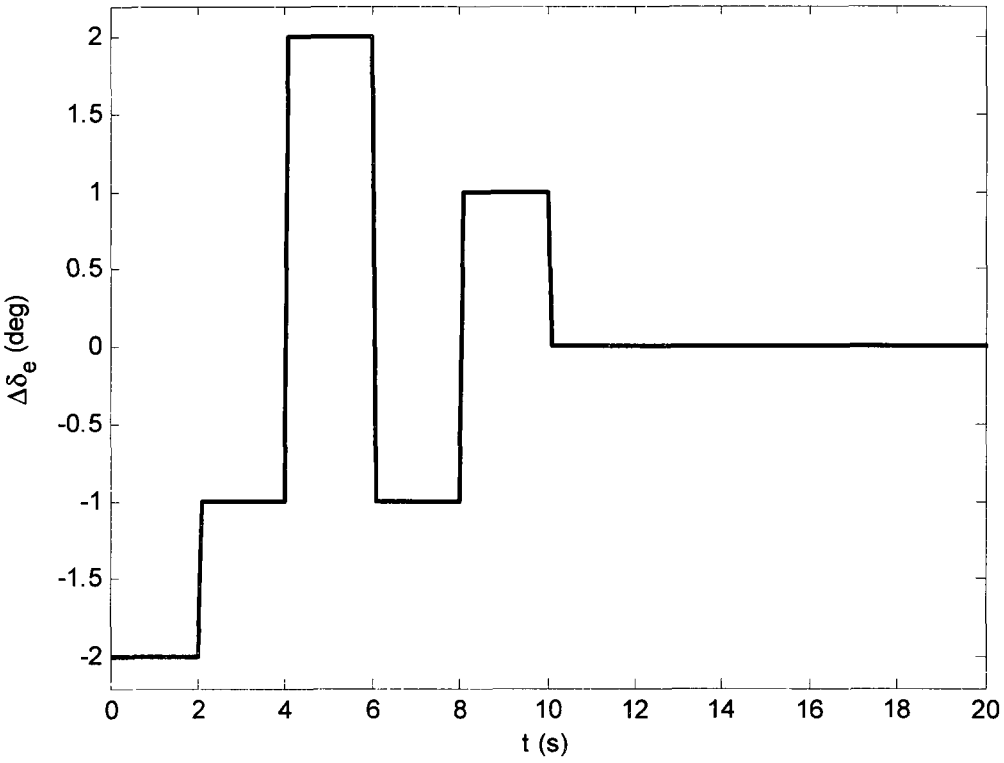

Figure 5.12 Perturbed Input II

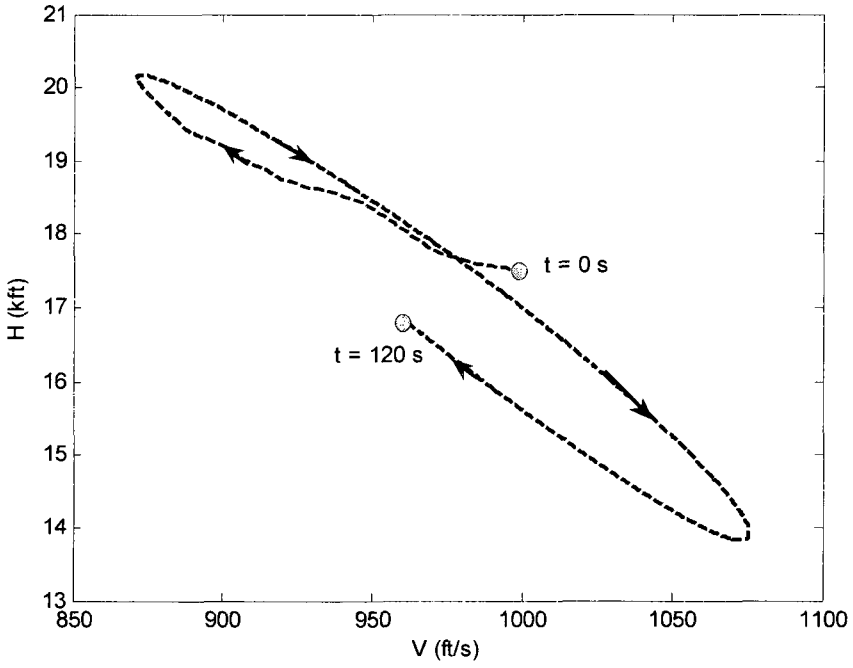

Figure 5.13 Aircraft Trajectory of Input II

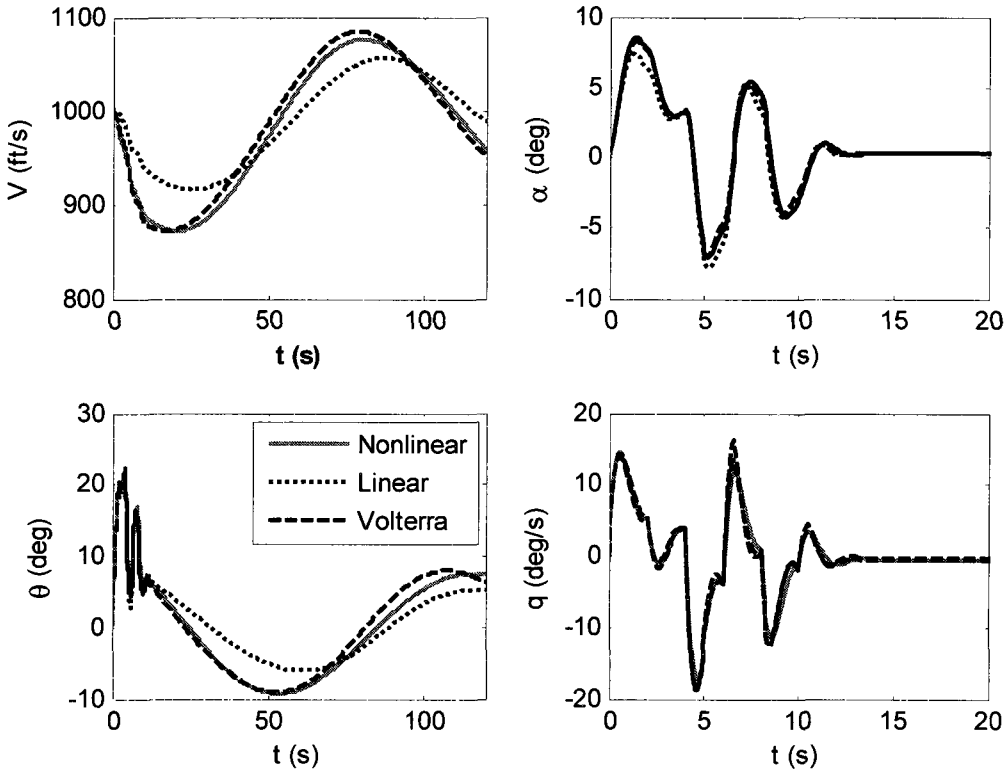

Figure 5.14 Aircraft Response of Input II

5.3.4 Global Kernels

Analysis of flight vehicle dynamic behavior, based on the Volterra model kernels, is addressed in this subsection. Although a differential form of Volterra theory using mixed interpolation was implemented for simulation accuracy purposes, the integral form can also be used in creating the global model. The primary intent here is dynamic analysis based on the analytical kernel framework. For that reason, the analytical expression of the first and second Volterra kernels (see Equations (5.55) and (5.63)) are computed at each operating condition. In this way, new dimensions are added to the series kernels. For example, the first kernels will have three arguments, $h_1(t, V_0, H_0)$, instead of one, $h_1(t)$, where V_o and H_0 represent the operating point around which the sub-model is constructed. The hyper-surface representing the first kernels $h_1^V(t, V_o, H_o)$ and

$h_1^{\alpha}(t,V_o,H_o)$ can not be fully plotted in three dimensions. For visualization, a set of slices is shown in Figures 5.15-5.18. These slices are taken to be at the middle of the selected operating space (500 ft/s ≤ V_o ≤ 1500 ft/s and 5 kft ≤ H_o ≤ 30 kft).

The waveforms of $h_1^V(t,V_o,H_o=17.5\,\text{kft})$ in Figure 5.15 and $h_1^{\alpha}(t,V_o,H_o=17.5\,\text{kft})$ in Figure 5.16 capture the variation of the first kernels with velocity. In the case of the total velocity's first kernel h_1^V, up to altitude H_o = 22 kft, increasing the velocity makes the system less oscillatory (decreasing $\omega_{d_{ph}}$) with more damping (increasing ζ_{ph}). When the altitude is more than H_o = 22 kft, increasing the velocity increases $\omega_{d_{ph}}$ and reduces ζ_{ph} up to a critical speed (≈ 600 ft/s) followed by an opposite variation. After this critical velocity, increasing the velocity reduces $\omega_{d_{ph}}$ and increases ζ_{ph}. The amplitude of h_1^V increases with velocity, which means the velocity responds more sensitively to the elevator deflection at a high velocity. On the other hand, increasing the velocity makes the angle of attack's first kernel h_1^{α} more oscillatory (increasing $\omega_{d_{sp}}$) with a slight reduction in the damping (ζ_{sp} is almost constant). The amplitude of angle of attack first kernel h_1^{α} decreases with the operating velocity, indicating less sensitivity to the elevator deflection.

Figures 5.17 and 5.18 show the influences of altitude variation on h_1^V and h_1^{α} at V_o = 1000 ft/s. For the total velocity's first kernel h_1^V, up to V_o = 700 ft/s, increasing the altitude reduces the damping (decreasing ζ_{sp}) and slightly increases the $\omega_{d_{sp}}$ up to a critical altitude (≈ 25 kft) followed by opposite influences. The amplitude of total velocity's first kernel h_1^V increases with altitude indicating more sensitivity to the elevator deflection. When the velocity is more than V = 700 ft/s, increasing the altitude slightly increases $\omega_{d_{sp}}$ and reduces ζ_{sp}. The angle of attack first kernel h_1^{α}, on the other hand, receives reductions in the damping ζ_{sp} and frequency $\omega_{d_{sp}}$ associated with a slight reduction in the amplitude as H_o increases.

The global second kernel of the total velocity, as an example, includes two components $h_{2\alpha^2}^V(\tau_1,\tau_2,V_o,H_o)$ and $h_{2\delta_e^2}^V(\tau_1,\tau_2,V_o,H_o)$. Both terms have a four-

dimensional space. Figures 5.19-5.24 show the contour plots of different slices of the hyper-surface of $h^V_{2\alpha^2}(\tau_1,\tau_2,V_o,H_o)$ describing its variation with the operating velocity V_o and altitude H_o. The variation of the surface $h^V_{2\alpha^2}(\tau_1,\tau_2,V_o,H_o)$ at constant V_o and H_o has a low frequency $\omega_{d_{ph}}$ waveform with a damping ratio ζ_{ph} over the diagonal line. The surface has an orthogonal waveform with a relatively high frequency $\omega_{d_{sp}}$ and high damping ratio ζ_{sp}. Combining the two waveforms constructs the surface, which can be described through a set of primary convex and concave signatures over the diagonal line ($\tau_1 = \tau_2$) and a set of the secondary convex and concave signatures over the off-diagonal lines ($\tau_1 = \tau_2 + \tau_c$ and $\tau_c \neq 0$). Because the cross-diagonal waveform has a relatively high damping ratio, the primary convex and concave set is the most significant part of the surface. Consider the first concave signature, which has an elliptical projection over the τ_1-τ_2 plane (see Figures 5.19-5.24). The semi-major axis of this τ_1-τ_2 projected ellipse lies over the diagonal line ($\tau_1 = \tau_2$) with a slope of 45 deg, while the semi-minor axis lies over the cross-diagonal line. The length of the semi-major axis is defined by the phugoid frequency at this operating condition to be $\pi/\omega_{d_{ph}}$ (half cycle) and the semi-minor axis is defined by the short period frequency at this operating condition to be $\pi/\omega_{d_{sp}}$ (half cycle). The variation of the hyper-surface $h^V_{2\alpha^2}(\tau_1,\tau_2,V_o,H_o)$ with operating velocity and altitude could be described by the variation of the first concave signature.

The surface of the quadratic elevator component $h^V_{2\delta_e^2}(\tau_1,\tau_2,V_o,H_o)$ is an impulsive hyper-surface over the diagonal line ($\tau_1 = \tau_2$). Since it is hard to visualize such an impulsive surface, the gain of this quadratic elevator component is used herein to be an indication of the strength of the quadratic elevator nonlinearity. Figure 5.25 shows the variation of the quadratic elevator component's gain $f_{1\delta_e^2}\overline{K}_{V_{ph}}$ with the flight condition. It is clear that increasing the altitude and decreasing the velocity increases the strength of the quadratic elevator nonlinearity. This conclusion also explains the difference between the aircraft responses in Figures 5.1 and 5.4.

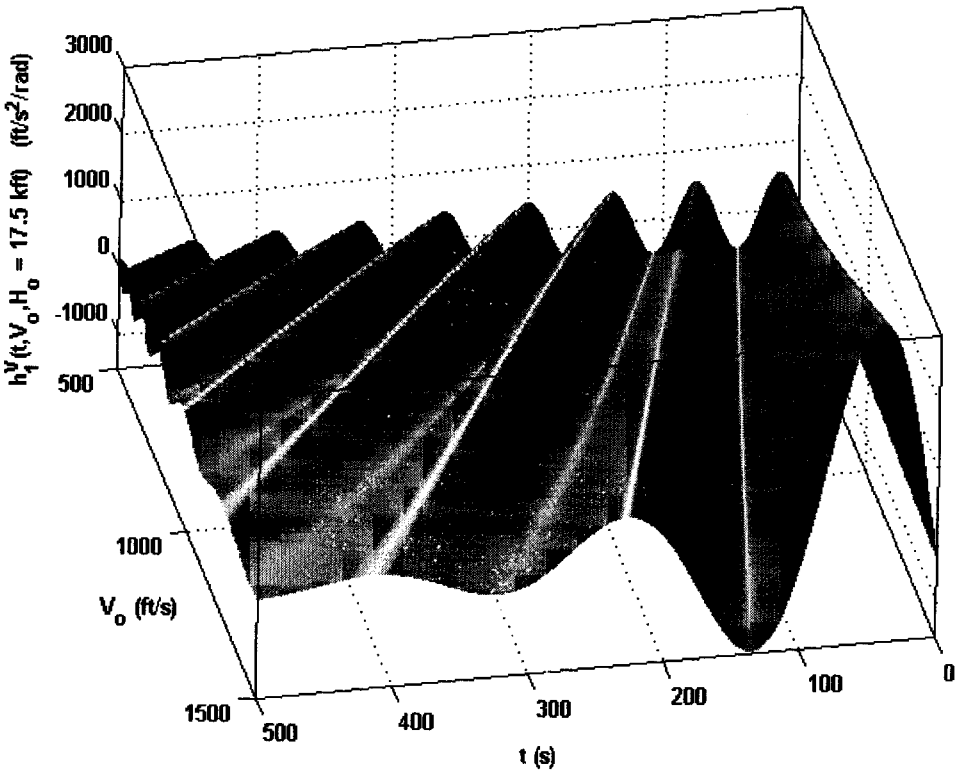

Figure 5.15 Total Velocity First Kernel at H_o = 17.5 kft

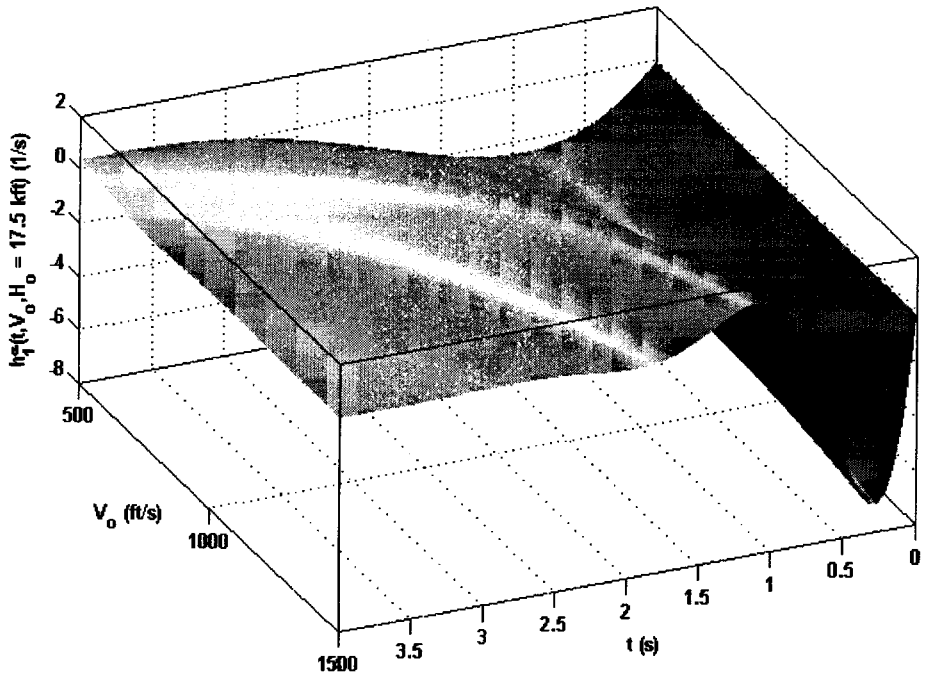

Figure 5.16 Angle of Attack First Kernel at H_o = 17.5 kft

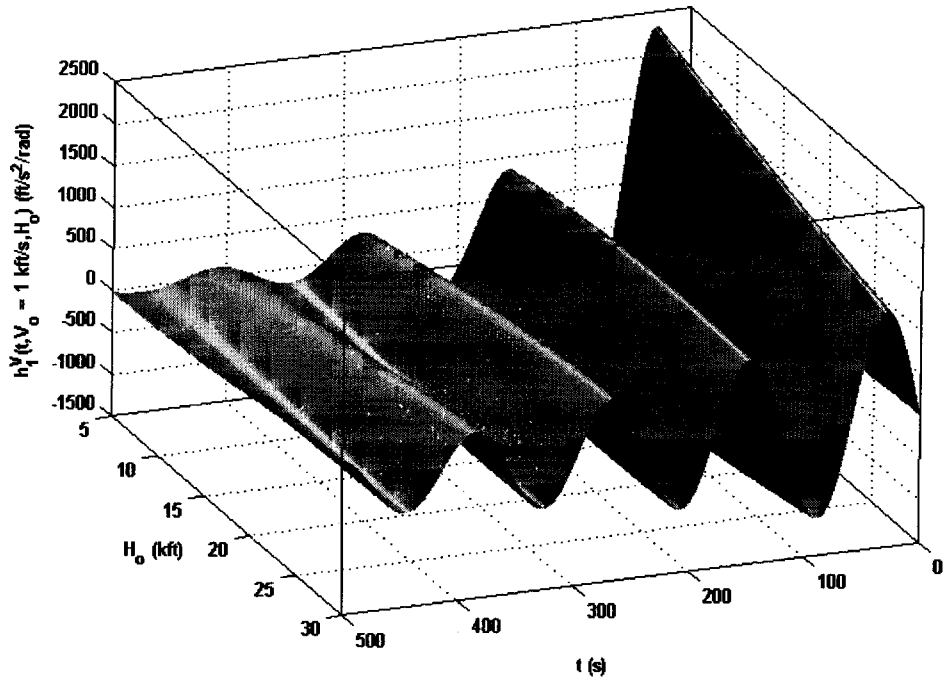

Figure 5.17 Total Velocity First Kernel at V_o = 1000 ft/s

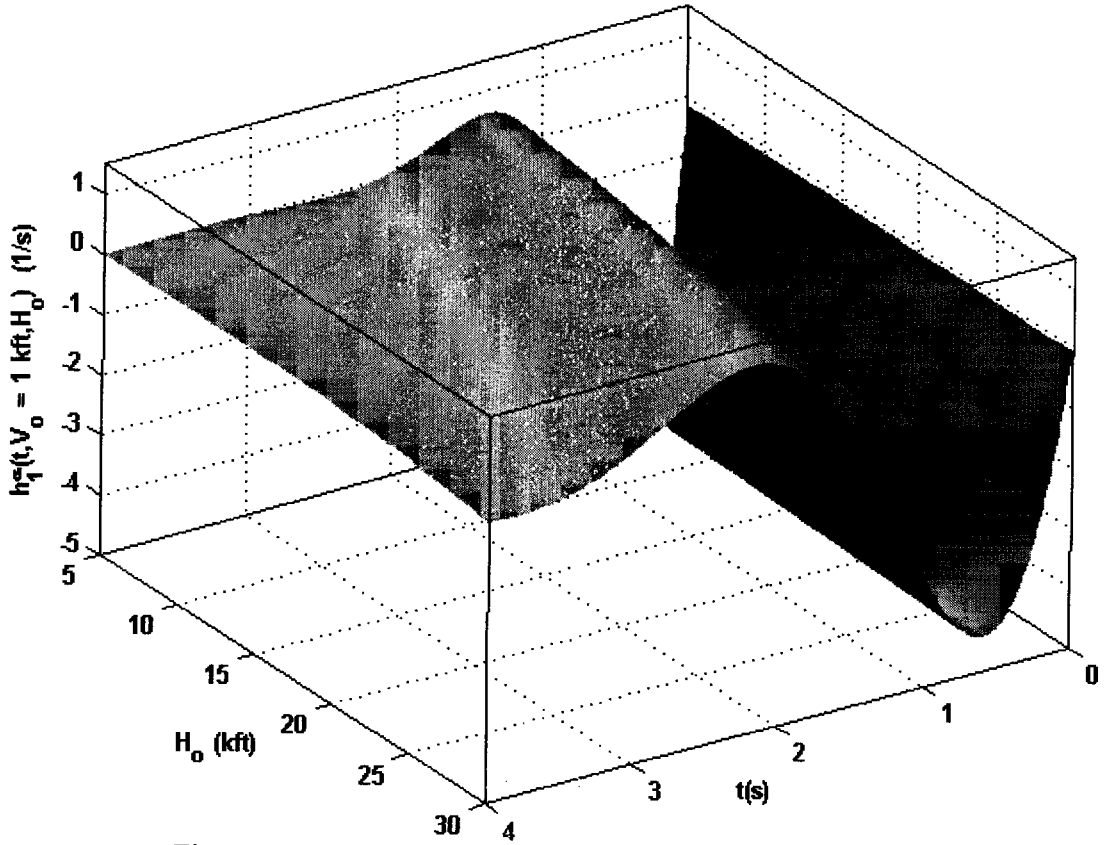

Figure 5.18 Angle of Attack First Kernel at V_o = 1000 ft/s

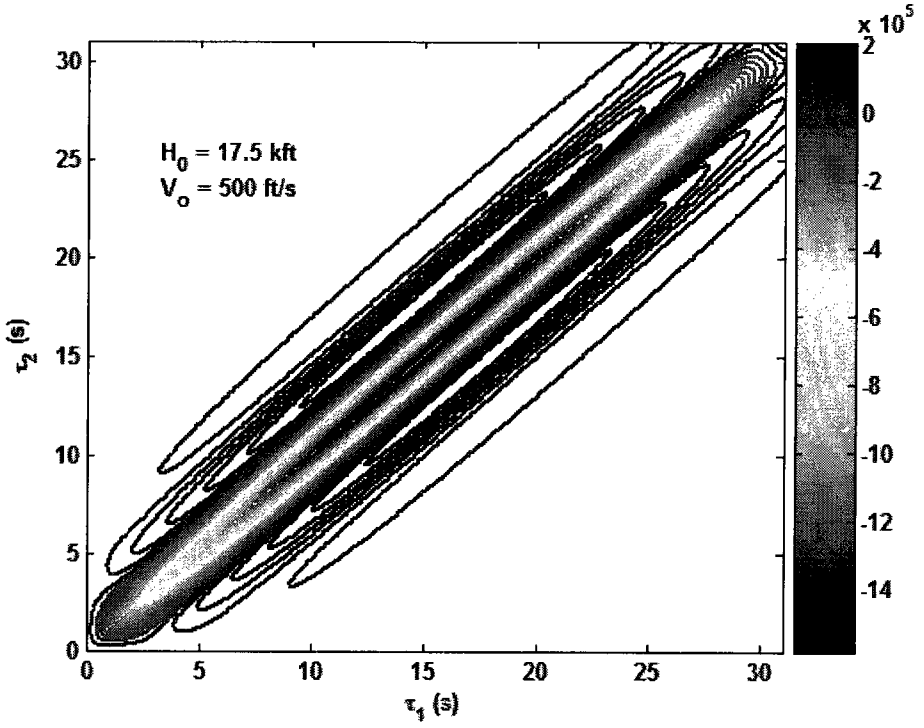

Figure 5.19 Quadratic Angle of Attack Second Kernel of Total Velocity at H_o = 17.5 kft and V_o = 500 ft/s

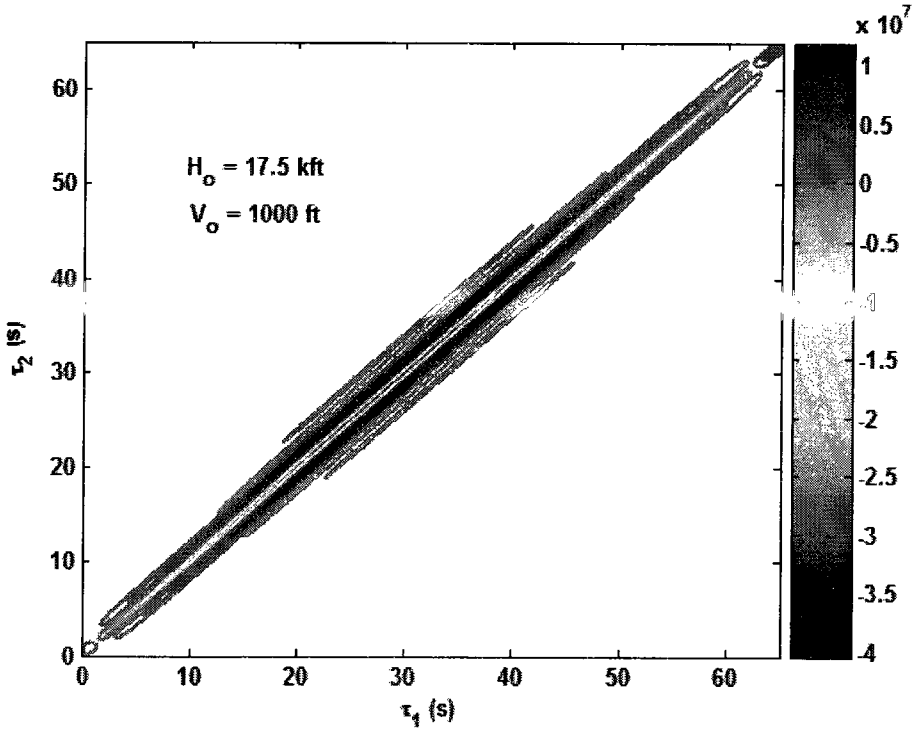

Figure 5.20 Quadratic Angle of Attack Second Kernel of Total Velocity at H_o = 17.5 kft and V_o = 1000 ft/s

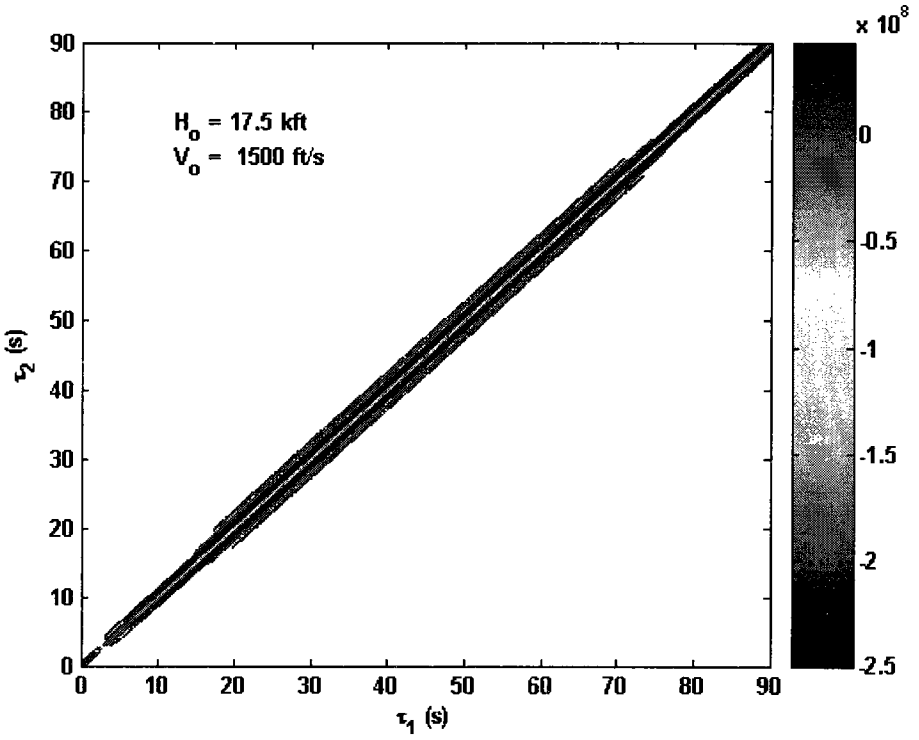

Figure 5.21 Quadratic Angle of Attack Second Kernel of Total Velocity at H_o = 17.5 kft and V_o = 1500 ft/s

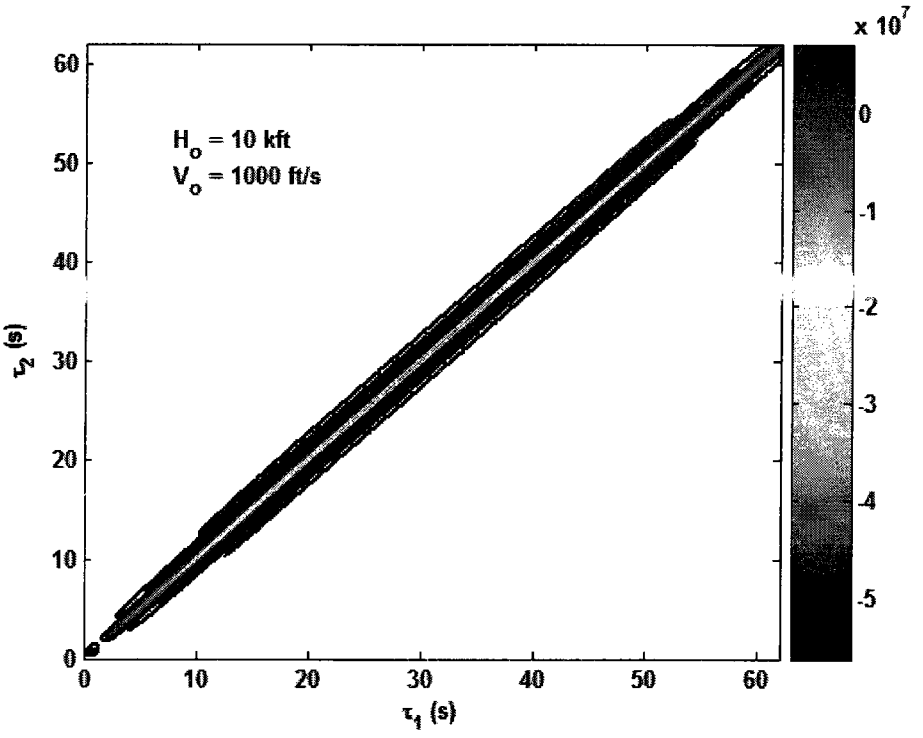

Figure 5.22 Quadratic Angle of Attack Second Kernel of Total Velocity at H_o = 10 kft and V_o = 1000 ft/s

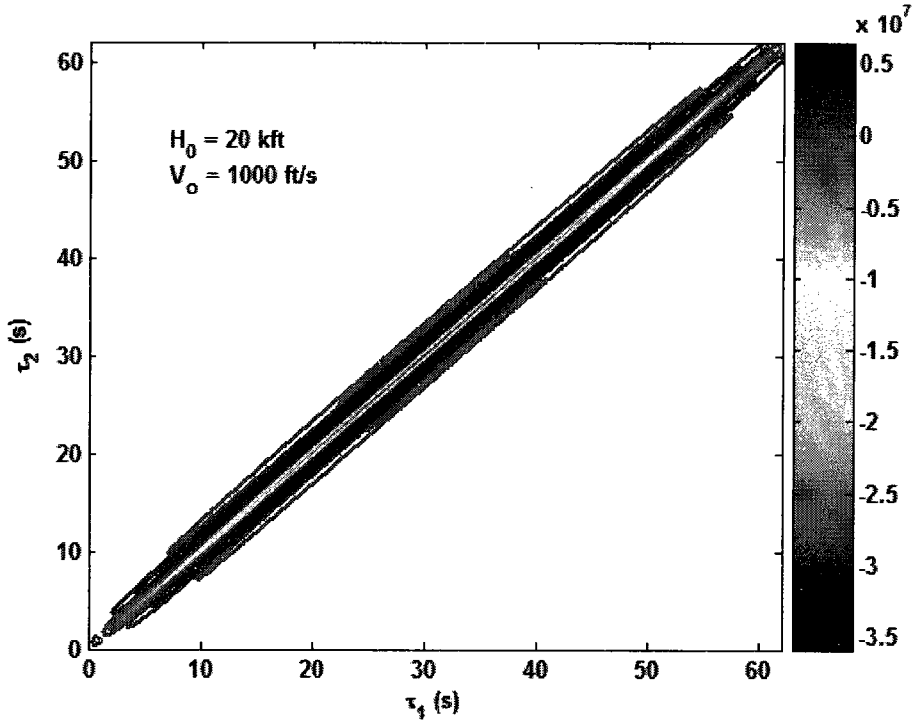

Figure 5.23 Quadratic Angle of Attack Second Kernel of Total Velocity at H_o = 20 kft and V_o = 1000 ft/s

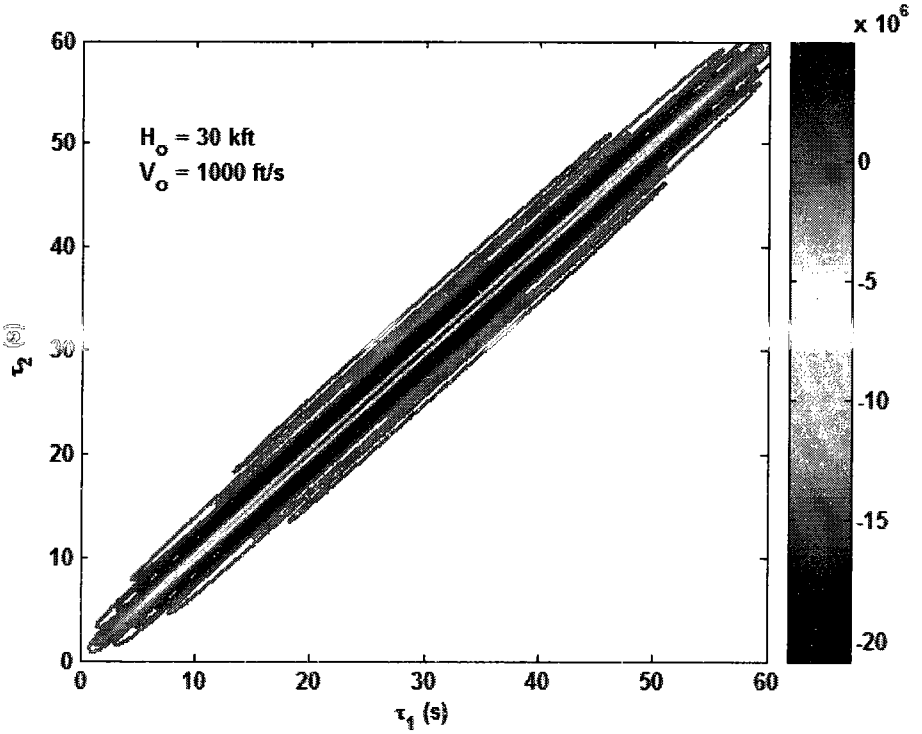

Figure 5.24 Quadratic Angle of Attack Second Kernel of Total Velocity at H_o = 30 kft and V_o = 1000 ft/s

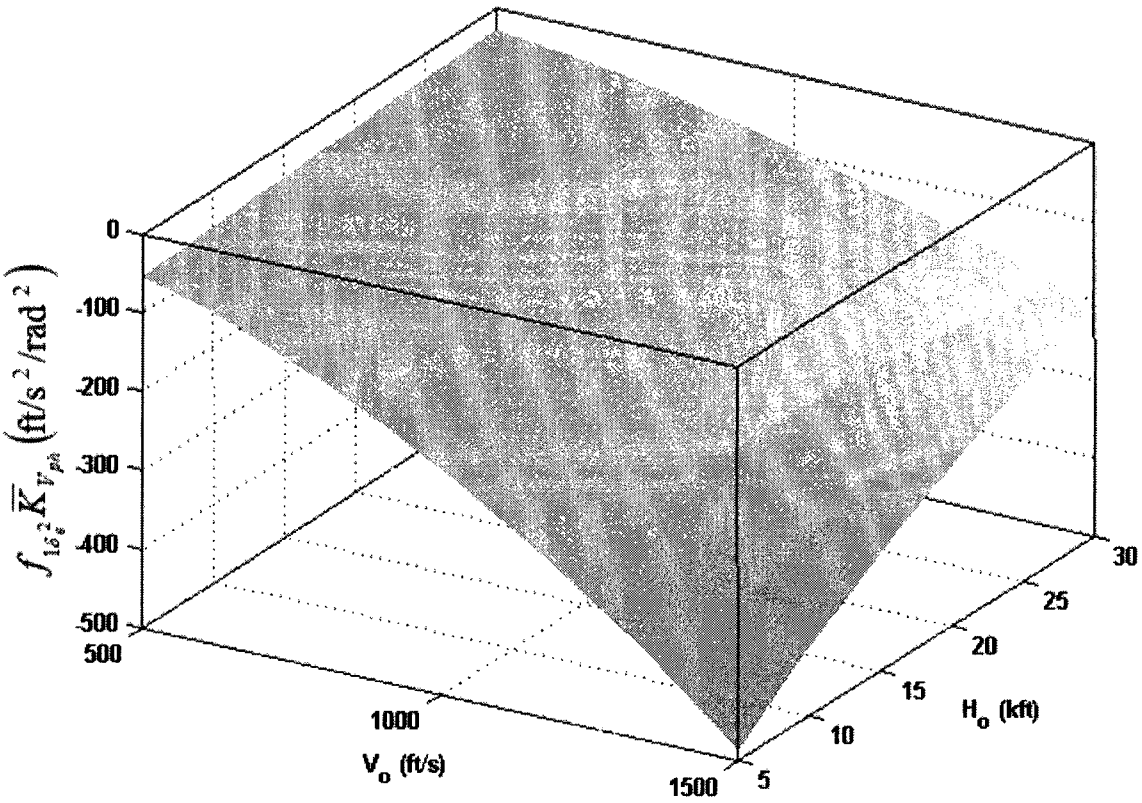

Figure 5.25 Variation of Quadratic Elevator Kernel's Gain of Total Velocity

CHAPTER 6

CONCLUSIONS AND RECOMMENDATIONS

6.1 Conclusions

The objectives of this dissertation were 1) reducing the computational cost of applying Volterra theory for high strength nonlinearities as in the aircraft dynamics case, 2) developing a nonlinear cause-and-effect parametric study for the low order atmospheric flight motions, that can be used as a foundation to qualify the high performance aircraft, and 3) constructing a global model, which has the capability to duplicate the aircraft nonlinear behavior across a wide array of operating conditions. Considerable efforts were focused on meeting these objectives and much success was achieved in all areas. The new techniques have been developed for constructing mathematical solutions from the governing relationships describing the aircraft dynamic behavior using Volterra theory. These techniques include the Piecewise Volterra Approach, the Nonlinear Cause-and-Effect Analysis, and the Volterra Parameter-Varying Approach. These methods were applied to low and high order atmospheric flight dynamic systems. Numerical and analytical solutions for such atmospheric flight dynamic systems show the capability of Volterra-based models to duplicate the aircraft's dynamic behavior. The solutions were used to obtain valuable insight and understanding to predict and analyze the aircraft dynamic behavior beyond that attainable by the linear theory or the nonlinear simulation. Overall, this dissertation has made significant and unique contributions to flight dynamics.

The piecewise Volterra approach proves the universality of a Volterra model by decomposing the nonlinearity into weaker component nonlinearities appearing in several operational sub-regions, which only require a low order truncated series. The approach has successfully captured the limit cycle and amplitude hysteresis behavior when applied

to an approximate low order nonlinear pitch-plunge model. However, there is no systematic way to assemble all these sub-regions together. That requires a bio-logic interaction to define the range of each sub-region. The cause-and-effect analysis provides a procedure to analytically assemble the constituents of the dynamic response of simple low order nonlinear systems using the variational method. The procedure provides closed-form expressions for the convolution integral kernels, which in turn lead to expressions for the time response for a step input. The explicit nature of the relational expressions allows cause-and-effect insights between nonlinearities present in the state space model and corresponding response traits. Application to single state and dual state uniaxial aircraft motion exposed the source of differences between nonlinear and linear responses, specifically initial departure time, maximum and steady offsets, differences in settling times, and oscillation frequency and phase shifts. The procedure has only been developed for first and second order single degree of freedom systems. Volterra parameter-varying approach has been developed as a systematic procedure to model a computationally complex and large envelope airframe system. In a comparison with the global linear varying model, it can be inferred that the Volterra varying model approach has more capability to replicate the dynamic behavior of a particular system, because of its ability to render the inherent nonlinearities in the system. This systematic approach has less error during switching between different flights regimes. The technique was successfully applied to a nonlinear longitudinal motion model for the F-16. This technique can be extended and applied to more general dynamic system evolutions.

The proposed approaches in this dissertation not only provide an acceptable accuracy level to duplicate the dynamic behavior, but also a theoretic framework by presenting the solution as a set of kernels. These kernels are a unique signature of the system and they can be used for understanding the way in which the change of basic parameter characteristics from one flight regime to another in the flight envelope can lead to significant change in system behavior. The proposed analytical Volterra-based model

offers an efficient nonlinear preliminary design tool in qualifying the aircraft responses before computer simulation is invoked or available.

6.2 Recommendations

Several extensions to this dissertation and its contents are recommended as future activities. Considerable work in this dissertation involves the flight mechanics application. Applying the same techniques to other dynamic systems could be an interesting topic for the nonlinear dynamics research community. The proposed procedures have been applied with time domain analysis. An extension to the Laplace domain or frequency response analysis may lead to the development of equivalent dynamics and control techniques for purposes of model reductions and control design. Also, an extension of this framework to multi-axis motions is of future interest.

REFERENCES

1. Kokotovic, P., "Singular Perturbation and Order Reduction In Control Theory-An Over View" Automatica, Vol. 12, No. 2, 1976.
2. Genesio, R., and Milanese, M., "A Note on The Derivation and Use of Reduced Order Models," IEEE Transactions on Automatic Control, Vol. 21, No. 1, 1976.
3. Hickin, J., and Sinha, N., "Model Reduction for Linear Multivariable Systems," IEEE Transctions on Automatic Control, Vol. 25, No. 6, 1980
4. Roskam, J., "Airplane Flight Dynamics and Automatic Controls," University of Kansas, Lawerance, Kansas, 1979.
5. Stevens, B. and Lewis, F., "Aircraft Control and Simulation," John Wiley & Sons, New York, 1992.
6. McRuer, D., Ashkenas, I., and Graham, D., "Aircraft Dynamics and Automatic Control," Princeton University Press, Princeton, New Jersey, 1973.
7. Etkin, B., "Dynamics of Atmospheric Flight," John Wiley & Sons, New York, New York, 1972.
8. Ashkenas, I., and McRuer, D., "Approximate Airframe Transfer Functions and Application to Single Sensor Control Systems," WADC-TR-58-82, Wright Air Development Center, Wright-Patterson AFB, Ohio, June, 1958.
9. Pearce, B., Johnson, W., and Siskind, R., "Analytical Study of Approximate Longitudinal Transfer Functions for a Flexible Airframe," ASD-TDR-62-279, Aeronautical Systems Division, Wright-Patterson AFB, Ohio, June 1962.
10. Newman, B., and Schmidt, D., "Numerical and Literal Aeroelastic-Vehicle-Model Reduction for Feedback Control Synthesis," Journal of Guidance, Control, and Dynamics, Vol. 14, No. 5, 1991, pp. 943–953.

11. Newman, B., "Aerospace Vehicle Model Simplification for Feedback Control," Ph.D. Dissertation, School of Aeronautics and Astronautics, Purdue Univiversity, West Lafayette, Indiana, 1992.

12. Livneh, R., and Schmidt, D. K., "New Literal Approximations for the Longitudinal Dynamic Characteristics of Flexible Flight Vehicles," Proceedings of the AIAA Guidance, Navigation, and Control Conference, Hilton Head, South Carolina August, 1992.

13. Livneh, R., "Improved Literal Approximations for the Lateral-Directional Dynamics of Rigid Aircraft," Proceedings of the AIAA Guidance, Navigation, and Control Conference, Baltimore, Maryland, August, 1995.

14. Newman, B. and Kassem, A., "Analytical Relationships for Linear Quadratic Aeroelastic Flight Control Eigenvalues," Journal of Guidance, Control, and Dynamics, Vol. 20, No.6, 1997, pp. 1149-1156.

15. Kassem, A., "Approximate Analytical Relationships for Linear Optimal Aeroelastic Flight Control Laws," Ph.D. Dissertation, Aerospace Department, Old Dominion University, Norfolk, Viriginia, 1998.

16. Phillips, W., "Phugoid Approximation for Conventional Airplanes," Journal of Aircraft, Vol. 37, No. 1, January-February, 2000, pp. 30-36.

17. Phillips, W., "Improved Closed-Form Approximation for Dutch Roll," Journal of Aircraft, Vol. 37, No. 3, May-June, 2000, pp. 484-490.

18. Ananthkrishnan, N. and Unnikrishnan, S., "Literal Approximation to Aircraft Dynamic Modes," Journal of Guidance, Control, and Dynamics, Vol. 24, No. 6, November-December, 2001, pp. 1196-1203.

19. Ananthkrishnan, N. and Ramadevi, P., "Consistent Approximations to Aircraft Longitudinal Model," Journal of Guidance, Control, and Dynamics, Vol. 25, No. 4, July-August, 2002, pp. 820-824.

20. U.S. Dept. of Defense, Military Standard: Flying Qualities of Piloted Aircraft, MIL-STD-1797A, January, 1990.

21. Hodgkinson, J., "Aircraft Handling Qualities," AIAA Education Series, 1999.

22. Hodgkinson, J., LaManna, W., and Heyde, J., "Handling Qualities of Aircraft with Stability and Control Augmentation Systems - A Fundamental Approach," Journal of the Royal Aeronautical Society, February, 1976.

23. Bacon, B. and Schmidt, D., "Fundamental Approach to Equivalent Systems Analysis," Journal of Guidance, Control, and Dynamics, Vol. 11, No. 6, November-December, 1988, pp. 527-534.

24. Newman, B., "Proposed Flying Quality Metrics and Simulation Studies for Elastic Vehicles," AIAA-1996-3423, Proceedings of the AIAA Atmospheric Flight Mechanics Conference, San Diego, CA, July 1996.

25. Tischler, B. and Barlow, B., "Dynamic Analysis of the Flat Spin Mode of a General Aviation Aircraft," Journal of Aircraft, Vol. 19, No. 3, 1982, pp. 198-205.

26. Tischler, B. and Barlow, B., "Determination of the Spin and Recovery Characteristics of a General Aviation Design ," Journal of Aircraft, Vol. 18, No. 4, 1981, pp. 238-244.

27. Stengel, F. and Nixon, B., "Stalling Characteristics of a General Aviation Aircraft," Journal of Aircraft, Vol. 19, No. 6, 1982, pp. 425-434.

28. Aouf, N., Boulet, B., and Botez, R., "Model and controller reduction for flexible Aircraft Preserving Robust Performance," IEEE Transactions on Control Systems Technology, Vol. 10, No. 2, 2002, pp.229-237.

29. Newman, B. and Schmidt, D., "Truncation and Residualization with Weighted Balanced Coordinates," Journal of Guidance, Control, and Dynamics, Vol. 17, No. 6, November-December, 1994, pp. 1299-1307.

30. Joshi, S. and Kelkar, A., "On Longitudinal Control of High Speed Aircraft in the Presence of Aeroelastic Modes," NASA-TM-110254, Langley Research Center, Hampton, Virginia, May, 1996.

31. Prudehomme, S., "Reduction for Aeroelastic Aircraft Control Design: a Practical Approach," AIAA-1995-3308, Proceedings of the AIAA Atmospheric Flight Mechanics Conference, Baltimore, Maryland, August 1995.

32. Robinson, A., "Survey of Dynamic Analysis Methods for Flight Control Design," Journal of Aircraft, Vol. 6, No. 2, 1969, pp. 81-98.

33. Sobel, K. and Shapiro, E, "Application of Eigenstructure Assignment to Flight Control Design: Some Extensions," Journal of Guidance, Control, and Dynamics, Vol. 19, No. 1, 1987, pp. 73-81.

34. Stevens, B., Lewis, F., Al-Sunni , F., "Aircraft Flight Controls Design Using Output Feedback," Journal of Guidance, Control, and Dynamics, Vol. 15, No. 1, 1992, pp. 238-246.

35. Satoh, A. and Sugimoto, K., "Partial Eignenstructure Assignment Approach for Robust Flight Control," Journal of Guidance, Control, and Dynamics, Vol. 27, No. 1, 2004, pp. 145-150.

36. Yomchinda, T., Horn, J., and Cameron, N., "Integrated Flight Control Design and Handling Qualities Analysis for a Tilt Rotor Aircraft," AIAA-2009-6058, Proceedings of the AIAA Guidance, Navigation, and Control Conference, Chicago, Illinois, August, 2009.

37. Guckenheimer, J. and Holmes, P., "Nonlinear Oscillations, Dynamical Systems and Bifurcation of Vector Fields," Springer-Verlag Berlin and New York., 1983.

38. Hale, J. and Kocak, H., "Dynamics and Bifurcations," Springer-Verlag, Berlin and New York, 1991.

39. Carroll, V. and Mehra, K., "Bifurcation Analysis of Nonlinear Aircraft Dynamics," Journal of Guidance, Control and Dynamics, Vol. 5, No. 5, 1982, pp. 529-536.

40. Planeaux, B., Beck, A., and Baumann, D., "Bifurcation Analysis of a Model Fighter Aircraft with Control Augmentation," AIAA-1990-2836, Proceedings of the AIAA Atmospheric Flight Mechanics Conference, Portland, Oregon, August, 1990.

41. Guicheteau, P., "Bifurcation Theory in Flight Dynamics: An Application to a Real Combat Aircraft," Proceedings of the International Council of the Aeronautical Science, ICAS Paper 116 (90-5.10.4), September 1990.

42. Jahnke, C. and Culick, C., "Application of Bifurcation Theory to High Angle of Attack Dynamics of the F-14," Journal of Aircraft, Vol. 31, No. l, 1994, pp. 26-34.

43. Mehra, K., Woburn, M., Prasanth, K., and Woburn, M., "Bifurcation and Limit Cycle Analysis of Nonlinear Pilot Induced Oscillations," AIAA-1998-4249, Proceedings of the AIAA Atmospheric Flight Mechanics Conference, Boston, Massachusetts, August, 1998.

44. Goman, G., Zagainov, I., and Khramtsovsky, V., "Application of Bifurcation Methods to Nonlinear Flight Dynamics Problems", Progress in Aerospace Sciences Journal, Vol. 33, No. 9-10, 1997, pp. 539-586.

45. Sinha, N. and Ananthkrishnan, N., "Use of the Extended Bifurcation Analysis for Flight Control Law Design," AIAA-2002-249, Proceedings of the AIAA Aerospace Sciences Meeting, Reno, Nevada, January 2002.

46. Sinha, N., Jangid, M., and Ananthkrishnan, N., "Automated Gain Scheduling for Level Flight Stability Augmentation Using Continuation Techniques," AIAA-2003-5315, Proceedings of the AIAA Atmospheric Flight Mechanics Conference, Austin, Texas, August, 2003.

47. Richardson, T., Lowenberg, M., Bernardo, M., and Charles, G., "Design of a Gain-Scheduled Flight Control System Using Bifurcation Analysis," Journal of Guidance, Control, and Dynamics, Vol. 29, No. 2, 2006, pp. 444-453.

48. Newman, B., "Dynamics and Control of Limit Cycling Motions in Boosting Rockets," Journal of Guidance, Control, and Dynamics, Vol. 18, No. 2, 1995, pp. 280-286.

49. Duda, H., "Prediction of Pilot-in-the-Loop Oscillations Due to Rate Saturation," Journal of Guidance, Control, and Dynamics, Vol. 20, No. 3, 1997, pp. 581-587.

50. Klyde, H., McRuer, T., and Myers, T., "PIO Analysis with Actuator Rate Limiting," AIAA-1996-3432, Proceedings of the AIAA Atmospheric Flight Mechanics Conference, San Diego, California, July, 1996.

51. Mehra, K., Washburn, B., and Carrol, V., "A Study of the Application of Singular Perturbation Theory," NASA CR-3167, AMES Research Center, Muffed field, California, 1979.

52. Go, T. and Lie, F., "Analysis of Wing Rock Due to Rolling Moment Hysteresis," Journal of Guidance, Control, and Dynamics, Vol. 31, No. 4, 2008, pp. 849-857.

53. Ardema, M. and Rajan, N., "Slow and Fast State Variables for Three-Dimensional Flight Dynamics," Journal of Guidance, Control, and Dynamics, Vol. 8, No. 4, July-August, 1985, pp. 532-535.

54. Volterra, V., "Theory of Functionals and of Integral and Integro-Differential Equations," Dover Publications, New York, New York, 1959.

55. Wiener, N., "Response of a Nonlinear Device Noise," Massachusetts Institute of Technology Radiation Laboratory Rept. 165, Cambridge, Massachusetts, 1942.

56. Brilliant, M., "Theory of the Analysis of Nonlinear Systems," Massachusetts Institute of Technology Radiation Laboratory, Rept. 345, Cambridge, Massachusetts, 1958.

57. George, D., "Continuous Nonlinear Systems," Massachusetts Institute of Technology Radiation Laboratory, Rept. 355, 1959.

58. Rugh, W., "Nonlinear System Theory: The Volterra/Wiener Approach," John Hopkins Univ. Press, Baltimore, Maryland, 1981.

59. Schetzen, M., "The Volterra and Wiener Theories of Nonlinear Systems," Wiley-Interscience, New York, 1980.

60. Brus, L., "Nonlinear Identification of an Anaerobic Digestion Process," Proceedings of 2005 IEEE Conference on Control Application, IEEE Publications, Piscataway, NJ, Aug. 2005, pp. 137–142.

61. Gray, S. and Nabet, B., "Volterra Series Analysis and Synthesis of a Neural Network for Velocity Estimation," IEEE Transactions on Systems, Man, and Cybernetics, Vol. 29, No. 2, 1999, pp. 190–197.

62. Alper, P., "A Consideration of the Discrete Volterra Series," Automatic Control, IEEE Transactions on, Vol. 10, No. 3, 1965, pp. 322-327.

63. Zhang, H., Zhang, C., Chen, Z., and Xiang, W., "OFS Model-Based Adaptive Control for Block-Oriented Non-Linear Systems," Transactions of the Institute of Measurement and Control Journal, Vol. 28, No. 3, May 2006, pp. 206–118.

64. Franz, M., and Scholkopf, B., "A Unifying View of Wiener and Volterra Theory and Polynomial Kernel Regression," Neural Computation Journal, Vol. 18, No. 12, 2006, pp. 3097–3118.

65. Soni, A., "Control-Relevant System Identification Using Nonlinear Volterra and Volterra Laguerre Models," Ph.D. Dissertation, School of Engineering, University of Pittsburgh, Pittsburgh, PA, 2006.

66. Asyali, M. and Juusola, M., "Use of Meixner Functions in Estimation of Volterra Kernels of Nonlinear Systems with Delay," IEEE Transactions on Bio-Medical Engineering, Vol. 52, No. 2, 2005, pp. 229–237.

67. Marmarelis, V., "Nonlinear Dynamic Modeling of Physiological Systems," Wiley, New York, 2004.

68. Fliess, M., Lamnabhi, M., and Lamnabhi-Lagarrigue, F., "An Algebraic Approach to Nonlinear Functional Expansions," Circuits and Systems, IEEE Transactions on, Vol. 30, No. 8, 1983, pp. 554 – 570.

69. Smith, W., and Rugh, W., "On the Structure of a Class of Nonlinear Systems," IEEE Transactions on Automatic Control, Vol. 19, No. 6, 1974, pp. 701-706.

70. Ku, Y., and Wolff, A., "Volterra-Wiener Functionals for the Analysis of Nonlinear Systems," Journal of the Franklin Institute, Vol. 281, No.1, 1966, pp. 9-26.

71. Chua, L., Ng, C., "Frequency-Domain Analysis of Nonlinear Systems: General Theory," IEE Journal on Electronic Circuits and Systems, Vol. 3, No. 2, 1979, pp. 165-185.

72. Flake, R., "Volterra Series Representations of Time-Varying Nonlinear Systems," Proceedings of the Second International Congress of IFAC, Butterworth, London, 1963.

73. Lesiak, C. and Krener, A., "The Existence and Uniqueness of Volterra Series for Nonlinear Systems," IEEE Transactions on Automatic Control, Vol. 23, No. 6, 1978, pp. 1090-1095.

74. Parente, R., "Nonlinear Differential Equations and Analytic System Theory," SIAM Journal on Applied Mathematics, Vol. 18, No. 1, 1970, pp. 41-66.

75. Selivanov , M. and Chernoivan , Y., "A Combined Approach of the Laplace Transform and Pade Approximation Solving Viscoelasticity Problems" International Journal of Solids and Structures, Vol. 44, No. 1, 2007, pp. 66-76.

76. Peddanarappagari, V. and Brandt-Pearce, M., "Volterra Series Transfer Function of Single-Mode Fibers," Lightwave Technology, IEEE Transaction, Vol. 15, No. 12, 1997, pp. 2232 – 2241.

77. Brockett, R., "Volterra Series and Geometric Control Theory," Automatica Vol. 12, No. 2, 1976, pp. 167-176.

78. Krener, A., "Linearization and Bilinearization of Control Systems," Proceedings of the 1974 Allerton Conference on Circuit and System Theory, Urbana-Champaign, Illinois, 1974.

79. Brewer, J., "Kronecker Products and Matrix Calculus in System Theory," IEEE Transactions on Circuits and Systems, Vol. 25, No. 9, 1978, pp. 772-781.

80. Vande, N., Nijmeijer, H., and Van-Campen, D., "A Volterra Series Approach to the Approximation of Stochastic Nonlinear Dynamics," Journal of Nonlinear Dynamics Vol. 27, 2002, pp. 397-409.

81. Wouw, N., Nijmeijer, H., and Campen, H.," On the Nonlinear System Identification of a Class of bilinear Dynamical Models," COC2000, IEEE 2nd Control of Oscillations and Chaos Conference, Petersburg, Russia, July 5-7, 2000.

82. Gilbert, E., "Functional Expansions for the Response of Nonlinear Differential Systems," IEEE Transactions on Automatic Control, Vol. 22, No. 6, 1977, pp. 909-921.

83. Stalford, H., Baumann, W. T., Garrett, E., and Herdman, T., "Accurate Modeling of Nonlinear System Using Volterra Series Sub-models," Proceedings of the 6th American Control Conference, Minneapolis, Minnesota, July 1987.

84. Baumann, W., Herdman, T., Stalford, H., and and Garrett, E., "A Volterra Series Sub-model Approach to Modeling Nonlinear Aerodynamics System," TM-88-FIGC, Air Force Wright Aeronautical Laboratories, Wright-Patterson, Ohio, 1988.

85. Herdman, T., "An Application of Volterra Series to Large Amplitude Maneuvers," TM-83-173, Air Force Wright Aeronautical Laboratories, Wright-Patterson, Ohio, 1983.

86. Silva, W., "A Methodology for Using Nonlinear Aerodynamics in Aeroservoelastic Analysis and Design," Technical Memorandum 104087, NASA Langley Research Center, Hampton, Virginia, 1991.

87. Silva, W., "Discrete-Time Linear and Nonlinear Aerodynamic Impulse Responses for Efficient CFD Analyses," Ph.D. Dissertation, College of William and Mary, Williamsburg, Virginia, 1997.

88. Silva, W., "Application of Nonlinear Systems Theory to Transonic Unsteady Aerodynamic Responses," Journal of Aircraft, Vol. 30, No. 5, 1993, pp. 660–668.

89. Silva, W., "Simultaneous Excitation of Multiple-Input Multiple-Output CFD-Based Unsteady Aerodynamic Systems," AIAA-2007-1988, Proceedings of the 48th AIAA/ASME/ASCE/AHS/ASC Structures, Structural Dynamics, and Materials Conference, Honolulu, Hawaii, April 2007.

90. Silva, W., "Simultaneous Excitation of Multiple-Input/Multiple- Output CFD-Based Unsteady Aerodynamic Systems," Journal of Aircraft, Vol. 45, No. 4, July–Aug. 2008, pp. 1267–1274.

91. Silva, W., Hajj, M., and Prazenica, R., "Recent Applications of the Volterra Theory to Aeroelastic Phenomena," IMAC XXIII: Conference and Exposition on Structural Dynamics, Orlando, Florida, January, 2005.

92. Prazenica, R., Reisenthel, P., Kurdila, A., and Brenner, M., "Volterra Kernel Extrapolation for Modeling Nonlinear Aeroelastic Systems at Novel Flight Conditions," Journal of Aircraft, Vol. 44, No. 1, 2007, pp. 149–162.

93. Lind, R., Prazenica, R., Brenner, M., and Baldelli, D., "Identifying Parameter Dependent Volterra Kernels to Predict Aeroelastic Instabilities," AIAA Journal, Vol. 43, No. 12, 2005, pp. 2496–2502.

94. Lind, R., Prazenica, R., and Brenner, M., "Estimating Nonlinearity Using Volterra Kernels in Feedback with Linear Models," Nonlinear Dynamics, Vol. 39, 2005, pp. 3–23.

95. Lucia, D. and Beran, P., "Reduced-Order Model Development Using Proper Orthogonal Decomposition and Volterra Theory," AIAA Journal, Vol. 42, No. 6, 2004, pp. 1181–1190.

96. Lucia, D., Beran, P., and Silva, W., "Aeroelastic System Development Using Proper Orthogonal Decomposition and Volterra Theory," Journal of Aircraft , Vol. 42, No. 2, 2005, pp. 509–518.

97. Marzocca, P., Librescu, L., and Silva, W., "Aeroelastic Response of Nonlinear Wing Sections Using a Functional Series Technique," AIAA Journal, Vol. 40, No. 5, 2002, pp. 813–824.

98. Marzocca, P., Silva, W., and Librescu, L., "Nonlinear Open-/Closed-Loop Aeroelastic Analysis of Airfoils via Volterra Series," AIAA Journal, Vol. 42, No. 4, 2004, pp. 673– 686.

99. Milanese, A., "Volterra Series Revisited, with Applications in Nonlinear Structural Dynamics and Aeroelasticity," Ph.D. Dissertation, Department of Mechanical and Aeronautical Engineering, Clarkson University, April 2009.

100. Suchomel, C., "An Evaluation of Volterra Series Using a Large Amplitude Aircraft Maneuver," Air Force Wright Aeronautical Laboratories, TM-86-FIGC. 1986.

101. Suchomel, C., "Nonlinear Flying Qualities-One Approach," AIAA-1987-347, Proceedings of the AIAA 25th Aerospace Sciences Meeting, AIAA, New York, Jan. 1987.

102. William, L., Garrard, L., and John, J., "Design of Nonlinear Flight Control System," Automatica, Vol. 13, 1977, pp. 497-505.

103. Stalford, H., "Application of the Estimation-Before-Modeling EBM System Identification Method to the High angle of Attack/Sideslip flight of the T-2C jet trainer aircraft," Naval Air Development Center Report NADC-76097-30, April 1979.

104. Mohler, R., "Nonlinear Stability and Control Study of Highly Maneuverable High Performance Aircraft, " OSU-ECE Report NASA 93-03, Oregon State University, Department of Electrical and Computer Engineering, Corvallis, OR, 1993.

105. Omran, A. and Newman B.," Piecewise Global Volterra Nonlinear Modeling and Characterization for Aircraft Dynamics," AIAA Journal of Guidance, Control, and Dynamics, 2009, Vol. 32, No. 3, pp. 749-759.

106. Omran, A., and Newman, B., "Global Aircraft Dynamics Using Piecewise Volterra Kernels," AIAA Atmospheric Flight Mechanics Conference and Exhibit, Honolulu, HI, USA, August 18-21., 2008.

107. Omran, A., and Newman, B., "Aircraft Volterra Parameter-Varying Modeling Approach," AIAA Atmospheric Flight Mechanics Conference and Exhibit, Toronto, Ontario, Canada, August 2-5, 2010.

108. Omran, A., and Newman, B., "Nonlinear Analytical Multi-Dimensional Convolution Solution of the Second Order System," Journal of Nonlinear Dynamics, Vol. 62, No. 4, pp. 799-819.

109. Omran, A., and Newman, B., "Analytical Nonlinear Analysis Methodology for Reduced Aircraft Dynamical Systems," ICAS2010 Annual International Council of the Aeronautical Sciences Conference, Nice, France, September 19-24, 2010.

110. Omran, A., and Newman, B., "Nonlinear Cause-Effect Analysis for a Second Order System using Volterra Kernels,"ACC2010, IEEE American Control Conference, Baltimore, Maryland, June 30 - July 2, 2010.

111. Omran, A., and Newman, B., "Analytical Response for the Prototypic Nonlinear Mass-Spring-Damper System," ESDA2010 Proceedings of the ASME2010 10th Biennial Conference on Engineering System Design and Analysis, Istanbul, Turkey, July 12-14, 2010.

112. Omran, A., and Newman, B., "On Dynamical Assembly of Nonlinear Uniaxial Atmospheric Flight Mechanics," AIAA Atmospheric Flight Mechanics Conference and Exhibit, Chicago, Illinois, August 10-13, 2009.

113. Nguyen, L., Ogburn, M., Gilbert, W., Kibler, K., Brown, P., and Deal, P., "Simulator Study of Stall/Post-Stall Characteristics of a Fighter Airplane with Relaxed Longitudinal Static Stability," NASA TP-1538, 1979, NASA Langley Research Center, Hampton, Virginia, 1979.

114. Morelli, E. A., "Global Nonlinear Parametric Modeling with application to F-16 Aerodynamics," Proceedings of the American Control Conference, Philadelphia, Pennsylvania, June, 1998.

VITA

Ashraf Omran was born on April 5th 1980 in Cairo, Egypt. He earned his B.S. degree with honors from the Aerospace Engineering Department at Cairo University in June 2002 and he was ranked as second out of 140 students. He received the undergraduate excellence scholarship at Cairo University each year from 1997 to 2002. After this, he served as a teaching assistant at Cairo University, 2002-2006. In 2006, Ashraf earned his M.S. degree in Aerospace Engineering in the field of flight mechanics and control. His thesis is entitled "Kinematics, Dynamics, and Control of Flight Simulator Manipulators" and was supervised by Dr. Ayman Kassem. Five journal articles have been published out of his thesis research. After this, Ashraf joined the Aerospace Engineering Department at Old Dominion University with an awarded Research Assistantship. In 2010, he earned the Ph.D. degree in Aerospace Engineering at Old Dominion University under the supervision of Professor Brett Newman in the field of flight dynamics and control. Six proceedings, two journal articles and his Ph.D. dissertation are published and presented from the work. There are two other journal articles under review. Ashraf is now a research scientist at Old Dominion University.